

NOVEL PACKAGING DESIGNS FOR IMPROVEMENTS
IN AIR FILTER PERFORMANCE

Except where reference is made to the work of others, the work described in this dissertation is my own or was done in collaboration with my advisory committee.
This dissertation does not include proprietary or classified information.

Ryan Anthony Sothen

Certificate of Approval:

W. Robert Ashurst
Assistant Professor
Chemical Engineering

Bruce J. Tatarchuk, Chair
Professor
Chemical Engineering

Mario R. Eden
Associate Professor
Chemical Engineering

Daniel Harris
Associate Professor
Mechanical Engineering

George T. Flowers
Dean
Graduate School

NOVEL PACKAGING DESIGNS FOR IMPROVEMENTS
IN AIR FILTRATION PERFORMANCE

Ryan Anthony Sothen

A Dissertation
Submitted to
the Graduate Faculty of
Auburn University
in Partial Fulfillment of the
Requirements for the
Degree of
Doctor of Philosophy

Auburn, Alabama

August 10th, 2009

NOVEL PACKAGING DESIGNS FOR IMPROVEMENTS
IN AIR FILTRATION PERFORMANCE

Ryan Anthony Sothen

Permission is granted to Auburn University to make copies of this dissertation at its discretion, upon request of individuals or institutions and at their expense.
The author reserves all publication rights.

Signature of Author

Date of Graduation

VITA

Ryan A. Sothen was born and raised by James E. and Lois R. Sothen in Charleston, West Virginia. He began his collegiate studies in the Department of Chemical Engineering at Virginia Polytechnic Institute & State University (Virginia Tech). During his time at Virginia Tech, he worked outside the classroom as an analytical chemist for Dominion Semiconductor and performed undergraduate research on polymeric materials for Dr. Donald Baird. Ryan completed his Bachelor of Science in the Spring of 2004, and subsequently enrolled in the Chemical Engineering Graduate Program at Auburn University during the Fall of 2004.

DISSERTATION ABSTRACT

NOVEL PACKAGING DESIGNS FOR IMPROVEMENTS
IN AIR FILTRATION PERFORMANCE

Ryan Anthony Sothen

Doctor of Philosophy, August 10, 2009
(B.S., Virginia Polytechnic Institute & State University, 2004)

234 Typed Pages

Directed by Bruce J. Tatarchuk

Adsorbent entrapped media, such as microfibrinous materials engineered at Auburn University, provide a novel method to effectively remove harmful airborne contaminants such as volatile organic compounds and particulate matter from polluted indoor air. These dual-functioning materials are limited in their use as air filters due to their high pressure drops and relatively small loading of adsorbent material. Utilization of a pleated filter design is a common approach in the air filtration industrial to increase the available media and reduce the pressure drop of a media. A second technique was developed to greatly increase the capacity and further reduce the pressure drop by employing numerous pleated filters into a single filter unit known as a Multi-Element Structured Array (MESA).

A comprehensive pressure drop model was constructed to understand the working parameter space within these filter designs. The model was formulated on fundamental fluid dynamics equations such as Bernoulli's Equation and empirical data obtained on custom-made filter units. The working models were shown to be successful in replicating over 1500 data points spanning 20 pleated filters and 32 MESA units.

Several niche filtration designs were envisioned during the development of the model. These designs were subsequently tested to demonstrate their performance advantage over standard HVAC pleated designs based on dirt holding and power consumption. It was determined that MESA architectures can be utilized to provide equal or superior particulate removal efficiency while operating at only 20% of the power of a traditional pleated filter.

ACKNOWLEDGMENTS

The author would like to express his sincere gratitude to Dr. Bruce J. Tatarchuk for his guidance throughout the course of my graduate studies. I would like to acknowledge the US Army (TARDEC) for funding the research presented in this dissertation. I would also like to thank my committee members Dr. Mario Eden, Dr. W. Robert Ashurst, Dr. Daniel Harris, and Dr. Christopher Roy for their time and efforts to ensure the compilation of this work.

Special thanks are in order for all of my past and present CM³ colleagues. In particular, I would like to acknowledge the members of the filtration group. My upmost appreciations are in order to Mr. Ron Putt and Mr. Amogh Karwa for their assistance in helping me with laboratory and theoretical issues as well as Mrs. Yanli “Joyce” Chen for her assistance with laboratory experimentation over the last six months. I would like to thank the following members of the Faculty and Staff who have helped me greatly during my time at Auburn: Mrs. Sue Ellen Abner, Mr. Dwight Cahela, Mrs. Karen Cochran, Mrs. Jennifer Harris, Dr. Lewis Payton, Dr. Christopher Roberts, Mrs. Megan Schumacher, and Mr. Brian Scweiker. Lastly, I would like to thank Dr. Donald Baird and Dr. Y. A. Liu for supporting and encouraging me to continue my education career after completion of my Bachelor of Science at Virginia Tech.

Style manual or journal used: *HVAC & R Research*
Computer software used: *Microsoft Word*

TABLE OF CONTENTS

LIST OF FIGURES	xiii
LIST OF TABLES	xxii
Chapter I: Introduction to Air Filtration	1
I.1 Motivation	1
I.2. Microfibrous Media	3
I.3. Influence of Pressure Drop within a HVAC System	5
Chapter II: Background & Experimental for Modeling Initial Pressure Drop	8
II.1. Previous Pleated Filter Models	8
II.1.1. Chen et al	8
II.1.2. Rivers & Murphy	10
II.1.3. Del Fabbro et al	10
II.1.4. Caeser and Schroth	11
II.1.5. Tronville and Sala	12
II.1.6. Raber	13
II.2. Objectives of Current Modeling Efforts	14
II.3 Theory	15
II.3.1. Forchheimer-extended Darcy's Law	16
II.3.2. Mechanical Energy Balance / Bernoulli's Equation	17
II.3.3. Equation of Continuity	21
II.3.4. Momentum Balance	22

II.4. Experimental Setups.....	22
II.4.1. Media Test Rig.....	22
II.4.2. Filtration Test Rig	24
II.5. Data Acquisition.....	30
II.5.1. Media Pressure Drop Curves.....	30
II.5.2. Filter Pressure Drop Curves	30
II.5.3. Media Thickness	34
Chapter III: Initial Pressure Drop Modeling of Pleated Filters.....	35
III.1 Introduction.....	35
III.1.1. Pleated Filter Schematics	35
III.1.2. Parameters.....	38
III.1.3 Proposed Flow through a Pleated Filter.....	39
III.1.4 Modeling a Pleated Filter.....	40
III. 2. Identifying the Constants	43
III. 2.1. Media Constants & Thickness	43
III. 2.2. Grating Coefficient of Friction (K_G).....	46
III. 2.3. Pleat Tip Assumption.....	50
III. 2.4. Pleat Coefficient of Friction (K_P)	51
III. 2.5. Reevaluate the Pleat Tip Contraction and Expansion.....	58
III.3. Utilization and Discussion of the Model	60
III. 3.1. Pleating Curve.....	60
III. 3.2. Location of the Optimal Pleat Count	63
III. 3.3. Influence of Design Parameters	64

III. 3.4. Limitations of the Model	77
Chapter IV. Initial Pressure Drop of Multi-Element Structured Arrays	78
IV.1. Introduction.....	78
IV.1.1. Multi-Element Structured Arrays Schematic.....	78
IV.1.2. Parameters.....	80
IV.1. 3. Proposed Flow through a MESA.....	82
IV.1. 4. Modeling a Multi-Element Structured Arrays	84
IV.2. Multi-Filter Bank Experimental	85
IV.2. 1. Entrance Coefficient of Friction (K_{CB}).....	86
IV.2. 2. Exit Coefficient of Friction (K_{EB}).....	89
IV.2.3. Slot Coefficient of Friction (K_S).....	91
IV.3. Discussion Utilizing the Model	98
IV.3.1. Achievement of Objectives.....	98
IV.3.2. The Pleating Curve of a MESA	99
IV.3.3. Locating the Optimal Pleat Count	102
IV.3.4. Influence of Design Parameters	102
Chapter V: Theory & Experimental for Air Filtration Performance	117
V.1. Introduction.....	117
V.2. Theory	117
V.2.1. Previous Research concerning Dirt Loading of Air Filters.....	117
V.2.2. Particulate Removal Efficiency by Fibrous Media	119
V.3. Experimental	122
V.3.1. Test Rig and Equipment.....	122

V.3.2. Experimental Data Acquisition	130
V.3.2.1. Volumetric Flow	130
V.3.2.2. Pressure Drop across Filtration Section	134
V.3.2.3. Particle Count.....	134
V.3.3. Testing Procedures	136
V.3.3.1. Initial Pressure Drop	136
V.3.3.2 Testing Procedure for Dirt Loading	138
V.3.3.3. Removal Efficiency Testing.....	141
Chapter VI: Filtration Performance of Novel, Single Element Designs.....	143
VI.1. Introduction.....	143
VI.2. Materials and Methods	143
VI.3. Results and Discussion	144
VI.3.1. Initial Resistance.....	144
VI.3.2. Dirt Loading.....	147
VI.3.3. Estimations of Useful Lifetime and Power Consumption	160
Chapter VII: Filtration performance of Multi-Element Structured Arrays.....	165
VII.1. Introduction	165
VII.2. Particulate Removal Efficiency of a MEFPB.....	165
VII.2.1. Materials	166
VII.2.2. Results and Discussion	166
VII.3. Dirt Loading of MESA's	170
VII.3.1. Materials	170
VII.3.2. Results and Discussion	170

VII.3.2.1. Influence of Pleat Count within an MESA.....	170
VII.3.2.2. Influence of Element Count	173
VII.3.2.3. Power Consumption Analysis	176
VII.4. Preferential Element Alignment within a MESA.....	177
VII.4.1. Materials and Methods	177
VII.4.2. Results and Discussion.....	179
VII.4.2.1. Initial Pressure Drop.....	179
VII.4.2.2. Dirt Loading	181
Chapter VIII: Conclusions and Future Work.....	192
VIII.1. Conclusions.....	192
VIII.2. Future Work	193
V.III.1. Utilization of Fairings	194
V.III.2. Media Compression versus Permeability.....	194
V.III.3 Pyramid Filter	195
References.....	196
Appendix A.....	197
A.1 Rotameter Calibration	199
A.2 Calibration of Pressure Transducers	202
A.3 Construction of Filter Holder.....	204
A.4 Construction of MESA Unit	204
A.5 Weight Increase of ASHRAE Dust under Atmospheric Conditions	206
A.6 Observed Flow Channeling due to Pleat Tip Blockage	207
A.7 Determination of Ramping Rate	208

Appendix B: Nomenclature	211
B.1 Arabic Symbols	211
B.2 Greek Symbols	212
B.3. Subscripts	212

LIST OF FIGURES

Figure 1.1: Typical “U” Pleating Curve	7
Figure 2.1: Sudden Contraction Diagram	19
Figure 2.2: Sudden Expansion Diagram	19
Figure 2.3: Gradually Contraction Diagram	20
Figure 2.4: Grating Diagram.....	20
Figure 2.5: Duct Diagrams.....	21
Figure 2.6: General Schematic of Media Test Rig	23
Figure 2.7: Control Pressure Drop Curve for Media Test Rig.....	24
Figure 2.8: General Schematic of Blower Test Rig.....	25
Figure 2.9: Flow Distribution at 40 Hz Before (A) and After (B).....	26
Figure 2.10: Coefficient of Variance	28
Figure 2.11: Control Pressure Drop Curve for Filter Test Rig	29
Figure 2.12: Measurement Path for the Vane Anemometer	31
Figure 2.13: Velocity Measurement Comparison.....	33
Figure 2.14: Pressure Measurement Comparison	34
Figure 3.1: Pleated Filter Illustration	36
Figure 3.2: Illustration of Pleat Dimensions	37
Figure 3.3: Pleat Tip Illustration.....	38
Figure 3.4: Flow Pattern	40

Figure 3.5: Control Volume of a Downstream Pleat	41
Figure 3.6: Media Resistance Curves	44
Figure 3.7: Darcy's Law Analysis of Media Resistance.....	46
Figure 3.8: Illustration of Grating Schemes.....	47
Figure 3.9: Pressure Drop Curves for Various Frontal Blockages	47
Figure 3.10: Computed Grating Resistances	48
Figure 3.11: Effects of Front Grating Modification.....	49
Figure 3.12: Effects of Back Grating Modification	50
Figure 3.13: Pressure Drop Curves for a 20"x20"x1" FM1 Filter with 42 Pleats	52
Figure 3.14: Pleat Coefficient Graph for a 20"x20"x1" FM1 Filter with 42 Pleats	53
Figure 3.15: Pleat Coefficient Plots for 20"x20"x1" Filters.....	54
Figure 3.16: Pleat Coefficient Graph	56
Figure 3.17: A Linear Pleat Coefficient Plot	57
Figure 3.18: Correlation Plot between Empirical and Modeled Pleat Coefficients.....	58
Figure 3.19: Modified Correlation Plot	59
Figure 3.20: Pleating Curve and Individual Resistances	61
Figure 3.21: Optimal Pleat Count Location.....	64
Figure 3.22: Effects of Face Velocity on Pleating Curve	67
Figure 3.23: Effects of Media Thickness on Pleating Curve	68
Figure 3.24: Effects of Media Thickness on Model's Derivatives	70
Figure 3.25: Modeled Pleat Tip Contribution to Total Resistance 20"x20"x1" Filters.....	71
Figure 3.26: Modeled Effects of Filter Depth on Pleating Curve.....	72
Figure 3.27: Effects of Filter Depth on Model Derivatives	73

Figure 3.28: Effects of Filter Depth on Performance Curve.....	74
Figure 3.29: Effects of Media Resistance on Pleating Curve	75
Figure 3.30: Effects of Media Resistance on Model’s Derivatives	76
Figure 4.1: General Schematic of a Multi-Element Structured Array	79
Figure 4.2: Array Configurations (A) “W” (B) “WV” Configuration (C) “WW”	80
Figure 4.3: General Diagram of Multi-Filter Array.....	82
Figure 4.4: Proposed Flow Profile	83
Figure 4.5: Illustration and Schematic of Flow within a Normal (A) and Contraction Modified Array (B)	87
Figure 4.6: Measured Pressure Drop for a Normal and Modified Array.....	88
Figure 4.7: Observed and Modeled Pressure Drop Differences	89
Figure 4.8: Illustration and Schematic of Flow within a Normal (A) and Expansion Modified Array (B).....	90
Figure 4.9: Measured Pressure Drop for a Normal and Modified Array.....	90
Figure 4.10: Observed and Modeled Pressure Drop Differences	91
Figure 4.11: Pressure Drop Curves for a WV Array of 1” Filters	92
Figure 4.12: Slot Coefficient Graph for a WV Array of 1” Filters.....	93
Figure 4.13: Slot Coefficient Plots for Various Configurations	95
Figure 4.14: Slot Coefficient Graph.....	97
Figure 4.15: Observed versus Modeled Slot Coefficient.....	98
Figure 4.16: Correlation Plot between Observed and Modeled Data	99
Figure 4.17: Multi-element structured array Pleating Curve	100
Figure 4.18: Percentage Contribution of (A) Single Filter and (B) “W” Array	101
Figure 4.19: Effects of Element Count on MESA Pleating Curve	104

Figure 4.20: Effect of Element Count on Contribution of the pressure drop	105
Figure 4.21: Effects of Element Count on MESA Performance Curve.....	106
Figure 4.22: Effects of Element Width on MESA Performance Curve.....	108
Figure 4.23: Effect of Element Width on Contribution	109
Figure 4.24: Effects of Element Depth on MESA Performance Curve.....	110
Figure 4.25: Effect of Element Depth on Contribution	111
Figure 4.26: Effects of Media Constants on MESA Pleating Curve	112
Figure 4.27: Effects of Media Thickness on MESA Pleating Curve.....	114
Figure 4.28: Effects of Velocity on MESA Pleating Curve.....	115
Figure 5.1: General Trend in Filter Loading.....	119
Figure 5.2: Impaction Mechanism for Particulate Capture.....	121
Figure 5.3: interception Mechanism for Particulate Capture.....	121
Figure 5.4: Particulate Capture by Brownian Motion.....	122
Figure 5.5: Schematic of Full Scale Test Rig	123
Figure 5.6: upstream Picture of the Test Rig	123
Figure 5.7: Downstream Picture of the Test Rig	124
Figure 5.8: Removal Efficiency of Upstream Filters.....	125
Figure 5.9: TSI 8108 Large Particle Generator Schematic.....	128
Figure 5.10: Schematic and Picture of Sealing System	130
Figure 5.11: Blower and Tap Configuration.....	133
Figure 5.12 Face Velocity Calibration Curve for Test Rig's Orifice Plate	134
Figure 5.13: Comparison of Upstream and Downstream Counting Probes.....	136
Figure 5.14: Alignment and Clamping System.....	137

Figure 5.15: Loading Tray with leveling Tool.....	140
Figure 6.1: Pleating Curve for 24"x24"x1" Filters at 500 fpm: Filters composed of 411 SF media.....	145
Figure 6.2: Pleating Curve for 24"x24"x2" Filters at 500 fpm: Filters composed of 411 SF media	146
Figure 6.3: Pleating Curve for 24"x24"x4" Filters at 500 fpm Filters composed of 411 SF media.....	146
Figure 6.4: Dirt Loading for 24"x24"x1" Filters	148
Figure 6.5: Normalized Loading Profiles of 24"x24"x1" Filters	149
Figure 6.6: Depth Filtration Regime for 20 and 28 Pleat Filter.....	150
Figure 6.7: Schematic of Preferential Loading. (A) Low and (B) High Beta Angle.....	151
Figure 6.8: Normalized Loading Profiles of Select 24"x24"x1" 411SF Filters with Transition Lines	152
Figure 6.9: Normalized Loading Profiles of 24"x24"x1" Filters composed of 355H Filter Media	153
Figure 6.10: Dirt Loading for 24"x24"x2" Filters	154
Figure 6.11: Normalized Dirt Loading for 24"x24"x2" Filters	155
Figure 6.12: Dirt Loading for 24"x24"x4" Filters	156
Figure 6.13: Normalized Dirt Loading for 24"x24"x2" Filters	157
Figure 6.14: Relationship between Pleating Angle and Transition Point.....	158
Figure 6.15: Average Power Consumption of 24"x24"x1" Filters.....	161
Figure 6.16: Average Power Consumption of 24"x24"x1" Filters.....	162
Figure 6.17: Average Power Consumption of 24"x24"x1" Filters.....	163
Figure 7.1: Removal Efficiency of a Single Filter and MESA.....	167
Figure 7.2: Removal Efficiency of a Single Element during Loading Conditions.....	168

Figure 7.3: Removal Efficiency of a MESA during Loading Conditions	168
Figure 7.4: Quality Factor Analysis.....	169
Figure 7.5: Total Dirt Holding Capacity of V MESA with Various Pleat Counts	171
Figure 7.6: Normalized Dirt Holding Capacity of V MESA with Various Pleat Counts	172
Figure 7.7: Total Dirt Loading of Various Element Count Systems	173
Figure 7.8: Normalized Loading Profile of a Various Element Count Systems with emphasis placed on the Depth Loading Regime.....	174
Figure 7.9: Normalized Loading Profile of a Various Element Count Systems with emphasis placed on the Cake Loading Regime	176
Figure 7.10: Power Consumption of MESAs' and Single Filter	177
Figure 7.11: Horizontally-Oriented (Left) & Vertically-Oriented (Right) Banks	178
Figure 7.12: Clean Resistance of DP 4-40 Elements Loaded Vertically and Horizontally into a V MESA Configuration.....	180
Figure 7.13: Clean Resistance of DP 95 Elements Loaded Vertically and Horizontally into a W MESA Configuration.....	180
Figure 7.14: Dirt Loading of DP 4-40 Elements Loaded Vertically and Horizontally into a V MESA Configuration.....	182
Figure 7.15: Dirt Loading of DP 95 Elements Loaded Vertically and Horizontally into a W MESA Configuration.....	182
Figure 7.16: Schematic of Pleat Nomenclature	184
Figure 7.17: View of Inline Loaded pleats	185
Figure 7.18: View of Shielded Loaded pleats.....	185
Figure 7.19: Air Permeability of Sample Obtained from Vertical MESA	186
Figure 7.20: Air Permeability of Sample Obtained from Horizontal MESA	187
Figure 7.21: Adhesive Squares and Removed Dirt from top and bottom Pleat Sides of a Horizontally Oriented MESA after Dirt Loading	189

Figure 7.22: Adhesive Squares and Removed Dirt from inline Side of Vertically Oriented MESA after Dirt Loading	190
Figure 7.23: Adhesive Squares and Removed Dirt from Shielded Side of Vertically Oriented MESA after Dirt Loading	190
Figure 7.24: Weighed Pulled per Layer of Adhesive Backing	191
Figure A1: Rotameter Calibration Set-Up	200
Figure A2: Rotameter Calibration Curve.....	201
Figure A.3: Calibration Tube.....	202
Figure A4: Calibration Curve for Pressure Transducer #1	203
Figure A5: Calibration Curve for Pressure Transducer #2	203
Figure A6: 24”x24”x2” Filter Holder	204
Figure A7: MESA Housing Schematic.....	205
Figure A.8: ASHRAE Dust Water Uptake over Time.....	207
Figure A.9: Upstream Pleat Tip after Dust Loading.....	208
Figure A.10: Downstream Pleat Tip after Dust Loading	208
Figure A.11: Variation in Pressure Measurements due to Incrementing Rate	210

LIST OF TABLES

Table 1.1: Minimum Efficiency Removal Value and Typical Filtration Platform.....	2
Table 3.1: Summary of Media Constants and Thickness	45
Table 3.2: Summary of Filters Employed.....	53
Table 3.3: Summary of Pleat Coefficients	55
Table 4.1: Blockage (F_B) Tabulations.....	82
Table 4.2: Alpha Tabulations (in radians)	82
Table 4.3: Summary of Elements used in Slot Coefficient Study	94
Table 4.4: Summary of Observed Slot Coefficients and R^2 Fit.....	96
Table 4.5: MESA vs. Single Filter Comparison	106
Table 4.6: Summary of Design Parameters and Effects due to their Increase.....	116
Table 5.1: ASHRAE Dust Size Distribution.....	127
Table 5.2: Average Velocity and Coefficient of Variation within Test Rig.....	128
Table 6.1: Critical Parameters of Filters Utilized	144
Table 6.2: Interval Loading Rate for 24"x24"x2" 411SF Filter with 15 Pleats	159
Table 6.3: Interval Loading Rate for 24"x24"x2" 411SF Filter with 20 Pleats	159
Table 6.4: Interval Loading Rate for 24"x24"x2" 411SF Filter with 40 Pleats	159
Table 6.5: Estimated Lifetime Costs for 24"x24"x1" Filters	161
Table 6.6: Estimated Lifetime Costs for 24"x24"x2" Filters	162
Table 6.7: Estimated Lifetime Costs for 24"x24"x4" Filters	163
Table 7.1: Transition Point of V MESA and Single Elements	172
Table 7.2: Associated Costs	177
Table A1: Experimental Data	201

CHAPTER I: INTRODUCTION TO AIR FILTRATION

I.1 Motivation

Adverse health effects stemming from poor indoor air quality (IAQ) has become a prominent concern since the implementation of energy efficiency buildings in response to the energy crisis of the 1970s (Kay et al. 1991, Moffat 1997). The decreased exchange between inside and outside air due to thicker insulation and improved passageway seals has created an environment where indoor air pollutants can reach levels that are ten times greater than ambient outdoor conditions (Meckler 1991). The decline in IAQ has been linked to increases in asthma, allergies, lung/respiratory cancer, and other pulmonary diseases (Godish 2001). Poor IAQ is also a primary cause for personal discomforts such as headaches; fatigue; dizziness; nausea; and irritation of skin, eyes, throat, and lungs that affects the quality of life and worker performance (Moffat 1997). The foremost indoor air pollutants are volatile organic compounds (VOC's), ozone, nitrogen oxides, carbon monoxide, and particulate matter less than 10 microns in diameter (Liu and Lipták 2000). Since the average American spends an estimated 90% of their time indoor (EPA 2009), effective air filtration is needed to eliminate these harmful contaminants from human living environments.

Traditionally, home filters have consisted of a panel units composed of loose fitting fiberglass fibers. The purpose of these filters was the removal of particles before they damaged the working machinery of the air handler. Also, the filter prevented the cooling coils from becoming clogged with dirt which decreases the efficiency of the heat

exchangers (Robinson and Ouellet 1999, Waring and Siegel 2008). Panel filters, however, offer little in terms of removing the serious health affecting particles that are below 10 micron. Table 1; obtain from the American Society of Heating, Refrigeration, and Air-conditioning Engineers (ASHRAE) Standard 52.2; highlights some of the common air filters and their ability to remove particulate matter.

Table 1: Minimum Efficiency Removal Value (MERV) and Typical Filtration Platform

MERV Rating	0.3 to 1.0 Micron	1.0 to 3.0 Micron	3.0 to 10.0 Micron	Filter Type
1	n/a	n/a	< 20%	Panel
2	n/a	n/a	< 20%	Panel
3	n/a	n/a	< 20%	Panel
4	n/a	n/a	< 20%	Panel
5	n/a	n/a	20 - 35 %	Cartridge Filter
6	n/a	n/a	35 - 50%	Cartridge Filter
7	n/a	n/a	50 - 70%	Cartridge Filter
8	n/a	n/a	> 70%	Pleated Filter
9	n/a	< 50 %	> 85%	Pleated Filter
10	n/a	50 - 60 %	> 85%	Pleated Filter
11	n/a	65 - 80 %	> 85%	Box Filter
12	n/a	> 80%	> 90%	Box Filter
13	<75%	> 90%	> 90%	Bag Filter
14	75 - 85%	> 90%	> 90%	Bag Filter
15	85 - 95%	> 90%	> 90%	Bag Filter
16	> 95%	> 95%	> 95%	Bag Filter

Although higher MERV rated filters excel at removing particulate matter, they can not remove VOC's and other airborne molecular contaminants. A second filtration system, such as a packed bed or monolith, must be employed in order to successfully remove the non-particulate contaminants. A third option is the utilization of microfibrinous media which has been previously shown to remove many of the airborne molecular contaminants listed above. Kalluri (2008) demonstrated the ability of microfibrinous media to remove ozone from a polluted air stream. Kennedy (2007) and Queen (2005)

employed microfibrinous materials in cathode air filters and fire masks for the successful removal of VOC's. Catalytic oxidation of carbon monoxide to the more benign carbon dioxide has also been achieved through the use of microfibrinous media (Karanjjikar 2005).

I.2. Microfibrinous Media

Microfibrinous Media (MfM) was developed in 1987 for use in chemical and electrochemical applications by Auburn University's Department of Chemical Engineering and the Space Power Institute. The media is a sinter-locked matrix of fibers with diameters typically ranging between two and twenty microns. Matrices can be constructed with metal, ceramic, or polymer fibers through a traditional wet-laid paper manufacturing process. (Tatarchuk et al. 1992, 1994). As the technology developed, the microfibrinous frameworks were used to entrap particles below 300 microns for use in catalytic and adsorptive applications. The resulting composite structures were known as Microfibrinous Sorbent-Supported Media (MSSM) (Harris et al. 2001).

The ability to be wet-laid and entrap microscopic particles bestows several key attributes to the media that enhances its utility in sorbent and catalytic processes. The decreased particle size allows molecules to diffuse into a sorbent's innermost structure at a higher rate leading to higher utilization, smaller mass transfer zones, and shorter critical bed depths compared to packed beds and monoliths (Harris et al. 2001, Kalluri 2008). In turn, lower amount of costly catalytic material is needed to achieve the same performance. The wet-lay process creates a homogeneous material that reduces channeling effects typically associated with the use of sub-millimeter particulate supports (Kalluri 2008). This assists with preventing the premature breakthrough of the pollutant

through the system. The wet-laid process also allows for customizable void volumes ranging between 30% to 98% (Marrion et al. 1994).

Although MSSM possesses a high contacting efficiency, the drawback to its utilization as a filtration media is a large pressure drop and relatively low loading capacity of adsorbent material. The large resistance of the media is due to the combinational effects of flow through the porous structure and drag forces present on the embedded particles. The matrix must be composed of micron diameter fibers in order to entrap the desired range of micro-sized adsorbent particles. The pressure drop of the media has an inverse quadratic relationship with both fiber radius and particle diameter; thus, the resistance quickly rises as smaller particles and fibers are employed (Cahela and Tatarchuk 2001). Capacity of the media remains low due to the thinness of the material and low concentration of support within matrix. The thickness and support concentration parameters can be adjusted to increase capacity, but each will cause the pressure drop of the media to increase in a linear fashion as describe by Darcy's Law.

Darcy's Law states that the force required to move a fluid through a porous media is directly proportional to the media thickness (L), the superficial velocity through the media (V_s), and the permeability constant of the media (K_m).

$$-\Delta(P + \rho gh) = \frac{\mu L}{K_m} V_s \quad (1.1)$$

The forces acting on the fluid are pressure (P) and a potential force created on a height of fluid (h) by the acceleration of gravity (g). The viscosity and density of the fluid flowing through the media is denoted by μ and ρ respectively. With no elevation change through the media, the equation can be reduced and rearranged to give the following linear form:

$$\Delta P = \frac{\mu L}{K_m} V_s \quad (1.2)$$

The term $\mu L/K_m$ is known as the Darcy's constant. Darcy's Law is generally considered valid only in the regime of creeping flow (Reynolds Numbers < 1) (Perry and Green 1997). An increase in media thickness or decrease in permeability created by an increase support concentration will lead to a higher pressure drop of the MSSM material.

I.3. Influence of Pressure Drop within a HVAC System

Proper design of flow resistance is of particular importance in air filtration applications where a large pressure drop can overload the air handler unit and reduce or prevent air flow. More importantly, pressure drop is directly related to the energy consumption of the system. The pressure-volume work of the system can be computed by (Rudnick 2008):

$$E = \Delta P Q t \eta_B^{-1} \quad (1.3)$$

The simple calculation states that the energy (E) required to move the air is the product of the volumetric flow rate (Q) of air moved, the resistance (ΔP), time of operation (t), and the efficiency of the air handler (η_B). The energy consumption to move the air accounts for 81% of the total expense in an HVAC system with procurement and additional operational costs such as labor accounting for the remaining 19% (Arnold et al. 2005). A significant pressure drop will render a MSSM filtration media impractical due to substantial operational costs or unfeasible because of the mechanical limitations of the air handler.

Pleated filters are a platform for improved pressure drop performance and enhanced capacity of microfibrous materials. The performance enhancements result from

transforming the flat material into a three-dimensional, corrugated structure to increase the available media area. The additional area extends the capacity of a filter as well as lowers the pressure drop by slowing down the velocity through the porous material. The addition of each pleat, however, introduces a new source of resistance due to increased surface-fluid friction. The reduction in pressure drop through the media is steadily counteracted by a rise in the flow resistance because of increased friction in the pleat. Due to the exchange of media-induced flow resistance loss for pleat-induced pressure losses, a pleated filter will experience a minimal resistance corresponding to an optimal pleat count and media area.

Previous research by Chen et al. (1996), Del Fabbro et al. (2002), Caesar and Schroth (2002), and Tronville and Sala (2003) each presented plots of pressure drop versus pleat count that demonstrated this tradeoff behavior (Figure 1.1). Chen labeled the lower pleat count region to the left of the optimal number as the media-dominated regime. A filter was listed in the viscosity-dominated regime when it possessed more than the optimal number of pleats. Although the previous research identified that an optimal pleat count existed, a detailed understanding of the influential design parameters and the impact of their variation was not well established.

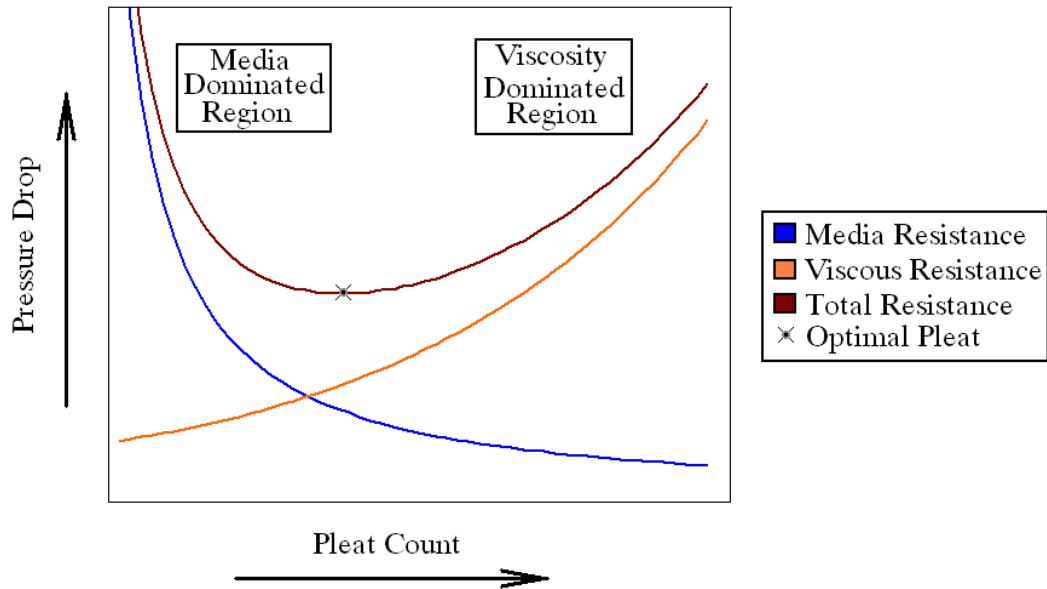


Figure 1.1: Typical “U” Pleating Curve

A need exists for an accurate pressure drop model to assist in designing more efficient pleated filters. A thorough understanding of the design parameters and their influence on the overall pressure drop would lead to better predictions regarding the minimum initial pressure drop or maximum filtration area while maintaining an acceptable initial resistance that a filter could obtain. A model could be further used to establish preferred media properties with respect to permeability versus thickness; thus, it could serve as a design tool for media construction as well. The end benefits to a filtration design are an increase in dirt holding capacity, improvement in removal efficiency, and reduction of operational energy costs.

CHAPTER II: BACKGROUND AND EXPERIMENTAL FOR MODELING INITIAL PRESSURE DROP

II.1. Previous Pleated Filter Models

Various models have been published that calculate the flow resistance encountered within a pleated filter. Chen et al., Rivers & Murphy, Tronville & Sala, Caesar & Schroth, Del Fabbro et al., and Raber have each suggested that a pleated filter can be modeled by the general formula:

$$\Delta P_f = K_{GEO} V_F^2 + K_M V_M \quad (2.1)$$

The equation states that the total pressure drop across the filter (ΔP_f) is a second order polynomial composed of a geometric and media term. The geometric term is equal to the squared face velocity into the filter (V_F) multiplied by a geometry coefficient (K_{GEO}). The media term is composed of the media velocity (V_M) times the media coefficient (K_M). The media velocity is calculated by dividing the face volumetric flow by the available filtration area. The following sections briefly discuss each researcher's work and their methods to model a pleated filter.

II.1.1. Chen et al.

Chen et al. (1995) calculated the pressure drop of a rectangular pleated filter through the use of a nine-node finite numerical method. The flow resistance upstream and downstream was computed by the Navier-Stokes equation. The pressure loss

through the media was estimated by Darcy-Lapwood-Brinkman equation with the media constant (K) experimentally determined.

$$\Delta P_f = \Delta P_M + \Delta P_C = K\mu V_M + \left(\frac{P_h - M_t}{\frac{1}{4} P_o^2} \right) \mu V_C \quad (2.2)$$

The research proposed that the optimal pleat count existed when the resistance of the media equaled that of the viscous effects. This computation is displayed by Equation 2.3 and is rearranged into a general correlation as shown. Once the correlation coefficient (C) is calculated, the optimal pleat count can be computed for a given media.

$$\frac{\Delta P_{fo}}{\Delta P_M} = 1 + \frac{\Delta P_C}{\Delta P_M} = 1 + C \left(\frac{8}{K} \frac{P_h^2}{(\frac{1}{2} P_o - M_t)^3} \right) \quad (2.3)$$

Besides experimentally determining the media coefficient (K), all work presented in the first study was theoretical. When Chen et al. (1996) subsequently investigated the flow resistance through a triangular pleated filter, the research concluded that the face velocity explored in the first study [<100 feet per minute (fpm)] was not a reasonable operational value. The use of Darcy-Lapwood-Brinkman equation was found to be invalid in the new operational velocity range. The researcher replaced the equation with a semi-empirical model:

$$\frac{\Delta P_f}{\Delta P_M} = 1 + M_1 \left(\frac{2}{\frac{1}{2} P_o \Delta P_M} \right) + M_2 \left(\frac{2}{\frac{1}{2} P_o \Delta P_M} \right)^2 \quad (2.4)$$

The last term in Equation 2.4 is proposed to account for viscous effects that stem from the directional flow change inside the pleat. Chen concludes that the angle of change is influenced by the media's resistance; therefore, M_2 must be empirically solved for each media type used.

II.1.2. Rivers & Murphy

Rivers and Murphy (2000) proposed a modified version of Equation 2.1 that could be used to model the total pressure drop through any air filter.

$$\Delta P_f = K_G V_f^N + f(V_m, \mu, \alpha_{SM}, \beta, M_t, R_f, Kn, M) \quad (2.5)$$

The work primarily focused on estimating the media's resistance. In particular, the research investigated how the compression of an HVAC media led to non-linear rises in resistance as face velocity was increased. The model provides great detail into predicting media performance based on the media design parameters of media velocity, viscosity, volumetric solid fraction, media non-uniformity, media thickness, fiber radius, Knudsen number, and dust load (denoted in order as $V_m, \mu, \alpha_{SM}, \beta, M_t, R_f, Kn, M$). To account for the influence of geometric factors, the model relies on two non-transferable factors lumped into a bulk term ($K_G V_f^N$) that must be empirically fit for each filter. The process first determined ΔP_f versus face velocity for a filter, and then Equation 2.5 was rearranged into a linear form to solve the constants N and K_G . Reported N values varied from 1.15 to 3.74 while the K_G values were not discussed. The model can not be use in a predictive capacity since the factors must be empirically determined for each filter.

II.1.3. Del Fabbro et al.

Del Fabbro et al. (2002) focused on modeling pressure loss created within a pleated filter composed of HEPA and low efficiency filter medium. The research initially attempted to compare experimental data to a computational fluid dynamic (CFD) model. The CFD model was ultimately deemed too computational expensive and difficult for the accuracy of results it provided. The study turned to a semi-empirical, dimensionless model that identified and utilized the following eight critical design parameters: pressure

drop, filtration velocity, media resistance, media thickness, density, viscosity, pleat height, and pleat opening.

The model could theoretically predict pressure drop through a pleated filter if the critical parameters are known or specified; however, the model was shown to be incapable of accurately predicting the experimental data presented by Del Fabbro. The results displayed significant positive and negative deviations between experimental and modeled data with divergences as large as 100 Pa (0.4" H₂O) and 500 Pa (2" H₂O). Beyond the strong deviations, the flow conditions studied were far below a normal filter's operating range. The maximum, modeled face velocity of 15 cm/s (30 fpm) was an order of magnitude below standard operational conditions. The study also failed to account for the pressure drop associated with the filter's housing.

II.1.4. Caeser and Schroth

Caeser and Schroth (2002) created a three termed model for predicting pressure drop in deep-pleated (4 to 12 inches) filters. The three resistances were the influence of airflow in and out of the pleats, through the pleats, and through the media. The airflow in and out of the pleats was modeled by a coefficient of friction. A reduced Navier-Stokes equation was used to compute pressure drop through the pleats. The media's resistance was calculated by Darcy's Law. The total resistance of a filter was the summation of the three terms.

Although the methodology employed by Caeser and Schroth was unique, the research overall had several deficiencies. The coefficient of friction listed in the research resembles a sudden contraction modified by a second parameter. The second parameter was listed as a function of entry and exit edge sharpness, yet a means to calculate the

second parameter was not presented. The study focused on deep-pleated HEPA and ULPA that are commonly built with metal spacers/combs to keep the pleats from collapsing, yet the model lacks a method to account for the influence of these additional structures. Several assumptions are postulated to reduce the Navier-Stokes equation into a more computationally simple form. The validity of these assumptions was never proven against experimental data.

II.1.5. Tronville and Sala

Tronville and Sala (2003) expanded on Equation 2.1 by proposing two new formulas to calculate the coefficients. Following the research of Rivers and Murphy, the pressure drop for flow through the media ($1/K_c$) was modeled by the Carmen-Kozeny equation with the solid mass fraction (α) described by the Natanson – Pich function. The parameter D_c is the pore hydraulic diameter and Δz is the thickness of the filter. The geometric resistance coefficient ($1/K_{air}$) was based on the pleat count per unit length (σ) raised to an empirically determined power N multiplied by the face velocity. Equation 2.6 is the end result of substituting the new coefficients into Equation 2.1. The two unknowns (N and D_c) can be solved by plotting a second-degree polynomial to experimental data obtained for a filter.

$$-\frac{\Delta P}{\Delta z} = \left(\frac{1}{K_{air}} + \frac{1}{K_c} \right) \mu U_D = \left(U_D \sigma^N + \frac{2f(\alpha)}{\sigma \Delta z D_c^2} \right) \mu U_D \quad (2.6)$$

The research only empirically determined the coefficients for a single filter. The authors assume that determining the parameter N at one pleat configuration would allow them to assess geometry resistance effects at all pleat arrangements. The minipleat style filter in this study possessed 304 pleats per meter, yet the model makes predictions for

pleat counts upwards of 1000 pleats per meter. With no supplementary experimental data to back this claim, the assumption that the model is capable of making this prediction becomes questionable. Furthermore, the model makes no concessions to account for filter housing or variations in filter depth.

II.1.6. Raber

Raber (1982) attempted to establish the effects of dirt loading on the flow resistance within a pleated filter. The media's resistance was experimentally identified by testing a small media sample to determine the impact of dust loading on the pressure drop. The term was found to be a second order polynomial that increased as the sample was loaded with dirt. The geometric resistances were numerically calculated from the momentum balance based on a characteristic half-pleat control volume. The half pleat was divided into five elements, and the total resistance across the half-pleat was calculated by sequentially solving the momentum balance with the conservation of mass equation and the media influence polynomial.

To assess the validity of the calculations, Raber built four 24"x24"x12" (HxWxD) prototype filters that possessed 16 pleats. The filters were tested at a face velocity of 500 fpm and loaded with dust until a final resistance of 1" H₂O was reached. The prototypes were not accurately modeled by the calculation. The initial deviations were approximately 0.05" H₂O to 0.1" H₂O and grew beyond 0.2"H₂O as the filters were loaded.

A probable source of error is the elimination of the friction term from the momentum balance. The research dismisses the friction losses due to the relatively moderate velocities encountered within the pleat. The moderate velocities, however, are

the product of employing 128 square feet of media to reduce the face velocity from 500 fpm to 3.9 fpm. The assumption's dismissal becomes increasingly debatable when attempting to model shallower filters with substantially higher pleat velocities.

Although Raber does not incorporate friction losses into his model, he does outline seven areas that would be associated with friction loss. This outline, described in Section 3.I.C, serves as the basis for the flow pattern used in this research.

II.2. Objectives of Current Modeling Efforts

The overarching goal of this work is the formulation of a model that meets the key objectives described below. The study was deemed necessary since the prior models often fail to achieve two or more of these requirements. The sixth objective is unique to this research, and no previous work regarding this subject was found.

1. Predictive

The model should be capable of predicting total pressure drop based solely on geometric design and media properties. The use of non-transferable factors should not be utilized. In particular, a model should not need empirical pressure drop versus face velocity data from a fully-constructed filter in order to make predictions.

2. Full Accounting of Design Parameters

The model should meticulously account for all previously identified contributing design parameters. The inability to properly assess the design parameters results in misattributed resistances and erroneous predictions. The most commonly ignored design parameters are the contribution of pleat tips to the overall resistance and the effect of structural elements within the filter.

3. Accurate

The ability to accurately predict a desired behavior is the primary objective of any modeling endeavor. A model should be able to predict the initial pressure drop of a filter to within $\pm 10\%$ for a given operational velocity.

4. Experimentally Verified

An empirical model should be based upon observed data covering a wide range of all design variables. A theoretical model needs to be tested against a similarly diverse field of design variables.

5. Computationally Benign

The model allows for quick calculations to improve the utility of the model. Long computation times and exceeding complex mathematics can hinder the usefulness of a predictive model.

6. Adaptable

The model should be able to make predictions for a single pleated filter as well as a Multi-Element Structured Arrays (MESA's). Multi-Element Structured Arrays are a novel filtration platform that incorporates numerous filter elements together to further reduce the pressure drop and drastically increase the available media area. The model should fulfill requirements 1 through 5 for both types of filtration systems.

II.3. Theory

The following equations are used in the research and modeling efforts: Forchheimer-extended Darcy's Law, Bernoulli's Equation, the Equation of Continuity, and the Momentum Balance. Several previously published coefficients of friction are employed in conjunction with Bernoulli's equation.

II.3.1. Forchheimer-extended Darcy's Law

The high operational velocities associated with a particulate air filter often result in non-linear deviations from Darcy's Law for flow through the media (Rivers & Murphy 2000, Chen et al. 1996). Rivers & Murphy concluded that the deviations were the product of media compression due to the air's inertial force being sufficient to compress the fibers together. Although Darcy's Constant should be slightly decreased due to the overall reduction in length of the porous media, the compression changes the internal void volume and tortuosity of the media leading to higher superficial velocities, decreased permeability, and an overall increase in Darcy's Constant.

A practical method to account for the non-Darcian behavior is the addition of a second-order term to Darcy's Law (Scheidegger 1974). Equation 2.7 is known as a Forchheimer-extended Darcy's law. The "A" term is equivalent to the Darcy's Law constant ($\mu L/K_m$). The "B" constant accounts for the non-linear deviation due to inertial effects.

$$\Delta P = AV_M + BV_M^2 \quad (2.7)$$

Numerous theoretical equations exist that attempt to relate the physical significance of the second media constant, but these theories require extensive knowledge of the media's fiber dimensions and packing densities (Rivers & Murphy 2000). The research presented by Rivers and Murphy demonstrates the complexity and difficulty in accurately modeling media performance with these theories. Since the primary objective of the research is to identify and determine the resistances created by the geometric design parameters and not the media formulation, it is preferable to model the media constants by a quick, empirical approach that will not introduce as much theoretical error.

The second order term also allows the model to account for the presence of particle matter embedded within the fibrous framework.

II.3.2. Mechanical Energy Balance / Bernoulli's Equation

The mechanical energy balance is a summation of kinetic, potential, mechanical, compressive, and viscous energy terms. Bernoulli's Equation is a specialized case of the mechanical energy balance. Bernoulli's Equation assumes incompressible, steady-state flow while maintaining a control volume with stationary, solid boundaries (Perry and Green 1997). Bernoulli's Equation is:

$$P_1/\rho + \alpha_v V_1^2/2 + gZ_1 + \delta W_s = P_1/\rho + \alpha_v V_2^2/2 + gZ_2 + L_v \quad (2.8)$$

Rearranging similar terms:

$$\Delta(P/\rho + \frac{1}{2}\alpha V^2 + gZ) = \delta W_s - L_v \quad (2.9)$$

Equation 2.5 states the change in pressure, kinetic energy, and potential energy is equal to the mechanical energy (δW_s) added to the system minus the viscous losses (L_v). The term alpha (α_v) is the ratio of velocity cubed over the average velocity cubed. Alpha assumes a value of unity for turbulent flow. Bernoulli's Equation can be further simplified by eliminating elevation change within the control volume and removing all mechanical work. The following equation results when applied between two points:

$$\Delta P = P_1 - P_2 = \frac{1}{2}\rho (V_2^2 - V_1^2) + L_v \quad (2.10)$$

The viscous loss term (L_v) accounts for the change of mechanical energy into heat due to viscous forces. The term is also referred to as the minor or miscellaneous losses. Denoting the viscous losses as minor or miscellaneous is misleading because they are frequently the primary resistance forces within a system (Perry and Green 1997).

There are two methods to account for the losses: equivalent length or velocity head. The

later will be used in this dissertation. The L_v term can be reported in equivalent number of velocity heads.

$$L_v = \frac{1}{2} \rho K V^2 \quad (2.11)$$

The K value is referred to as either the velocity head loss coefficient or the coefficient of friction. Although the viscous losses can be theoretically computed by simultaneously solving both the mechanical energy balance and momentum balance for the given control volume, they are most often determined through experimental measurements (Bird et al. 2001, Perry and Green 1997). The coefficient is required to be a dimensionless function of either geometry, Reynolds number, or both. The importance of the Reynolds number increases in laminar flow due to the rise in friction at the boundaries (Bird et al. 2001). The V term is an arbitrary, reference velocity on which the coefficient is based.

The present research makes use of the following five previously researched friction coefficients: sudden contractions, sudden expansions, gradually contractions, flow across a perforated plate, and flow through a duct. Each coefficient's formula, general control volume schematic, and reference velocities are presented below.

1. Coefficient of Friction for a Sudden Contraction

Idelchik (1994)

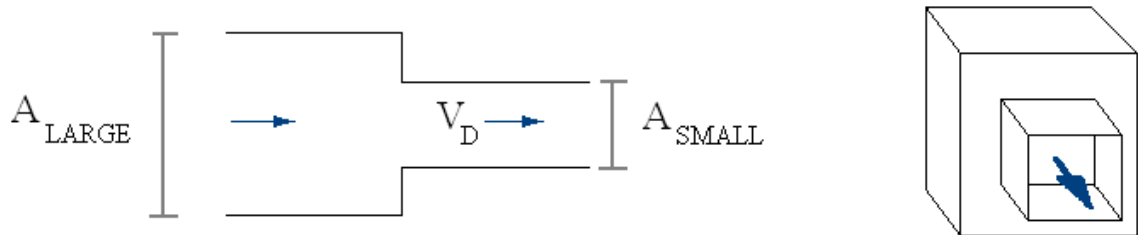


Figure 2.1: Sudden Contraction Diagram

$$K_C = \frac{1}{2} \left(1 - \frac{A_{SMALL}}{A_{LARGE}} \right)^{0.75} \quad (2.12)$$

(Based on downstream velocity)

2. Coefficient of Friction for a Sudden Expansion

Idelchik (1994)

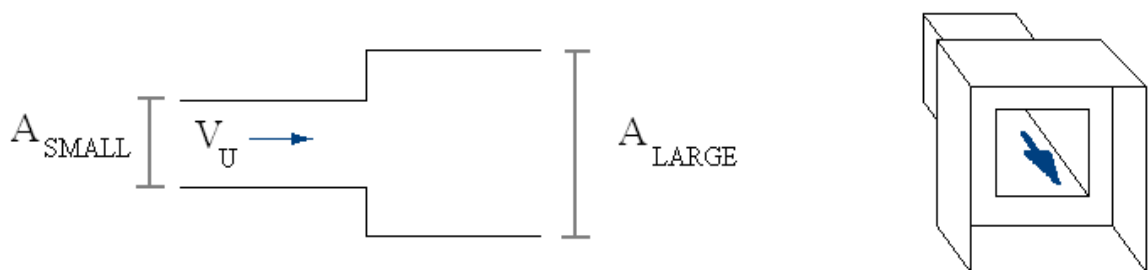


Figure 2.2: Sudden Expansion Diagram

$$K_E = \left(1 - \frac{A_{SMALL}}{A_{LARGE}} \right)^2 \quad (2.13)$$

(Based on upstream velocity)

3. Coefficient of Friction for a Gradually Contraction

Fried and Idelchik (1989)

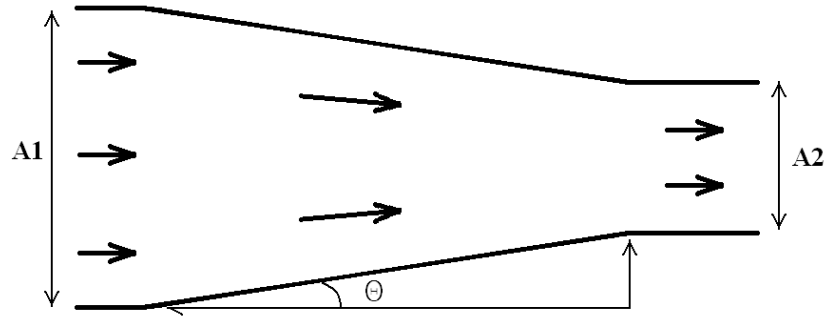


Figure 2.3: Gradually Contraction Diagram

$$K_{GC} = [(-0.0125N^4 + 0.0224N^3 - 0.00723N^2 + 0.00444N - 0.00745)(A^3 - 2\pi A^2 - 10A)] \quad (2.14)$$

$$A = 0.01745\theta \quad (\text{where } \theta \text{ is in radians})$$

$$N = A_2 / A_1$$

(Based on upstream velocity)

4. Coefficient of Friction for Flow Across a Perforated Plate

Idelchik (1994)

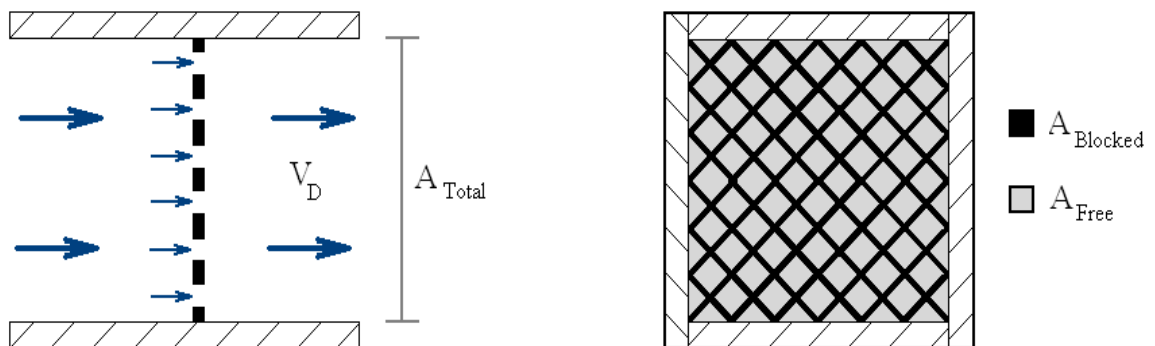


Figure 2.4: Grating Diagram

$$K_G = \left(1.707 - \frac{A_{FREE}}{A_{TOTAL}} \right) \left(\frac{A_{FREE}}{A_{TOTAL}} \right)^{-2} \quad (2.15)$$

(Based on downstream velocity)

5. Darcy-Weisbach Equation: Flow in a Duct with Smooth Walls

Idelchik (1994)

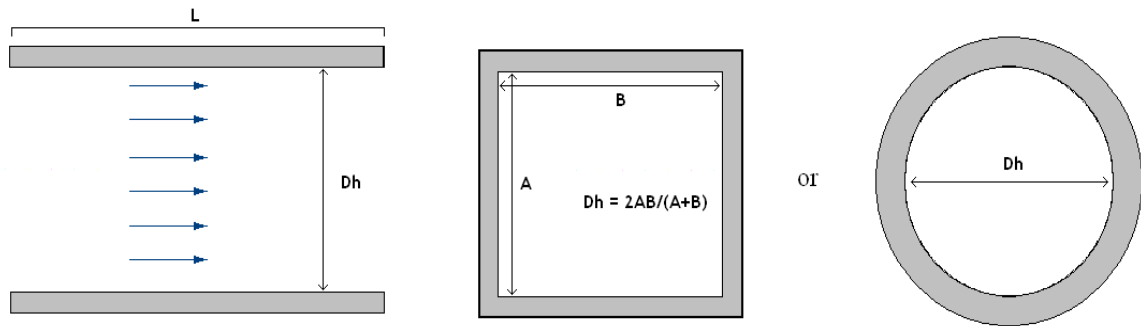


Figure 2.5: Duct Diagrams

$$K_T = \left(\frac{L}{D_h} \right) \lambda \quad (2.16)$$

(Based on flow velocity)

$$\lambda = \frac{64}{\text{Re}} \quad \text{Re} < 2000 \text{ (Laminar Regime)}$$

$$\lambda = \left[\frac{1}{(1.8 \times \log(\text{Re}) - 1.64)^2} \right] \quad \text{Re} > 4000 \text{ (Turbulent Regime)}$$

$$\text{Re} = \frac{VD_h}{\nu} \quad (2.17)$$

Tabular data is available in the Handbook of Hydraulic Resistance (Idelchik 1994) for computing λ in the transitional regime defined by Reynolds number between 2000 and 4000.

II.3.3. Equation of Continuity

The equation of continuity is based on the conservation of mass (Perry and Green 1997). The equation denotes that mass flow entering and leaving a control volume is equal. When constant density is assumed, the equation can be written as:

$$V_1 A_1 = V_2 A_2 \quad (2.18)$$

II.3.4. Momentum Balance

Although not extensively used in the study, the momentum balance is:

$$\frac{d}{dt}\Gamma = \rho_1 V_1^2 A_1 u_1 - \rho_2 V_2^2 A_2 u_2 + P_1 A_1 u_1 - P_2 A_2 u_2 + F_s + mg \quad (2.19)$$

The balance asserts that the change of momentum is the difference between the amount of momentum carried into the system by the fluid and the pressure acting on the fluid versus the momentum carried out by the fluid and the pressure acting on the outlet fluid (Bird et al. 2001). Addition factors such as the force of gravity on the fluid's mass and the force of system's surfaces on the fluid (F_s) are factored into the balance.

II.4. Experimental Setups

Two separate test rigs were constructed and used to measure pressure drop performance across a media sample and a filtration system. A general description of the test rigs, control runs, and equipment verification are provided in this section.

II.4.1. Media Test Rig

The media constants were determined using a 1-inch circular diameter duct powered by house air at 100 psig (Figure 2.6). The duct length to diameter ratio was sufficiently long (48-to-1) to ensure no entrance effects. A media sample was held in place by two plates tightened together by four nut and bolt assemblies. A twelve inch outlet section was located downstream of the media sample to prevent additional pressure loss due to a sudden expansion out of the tube.

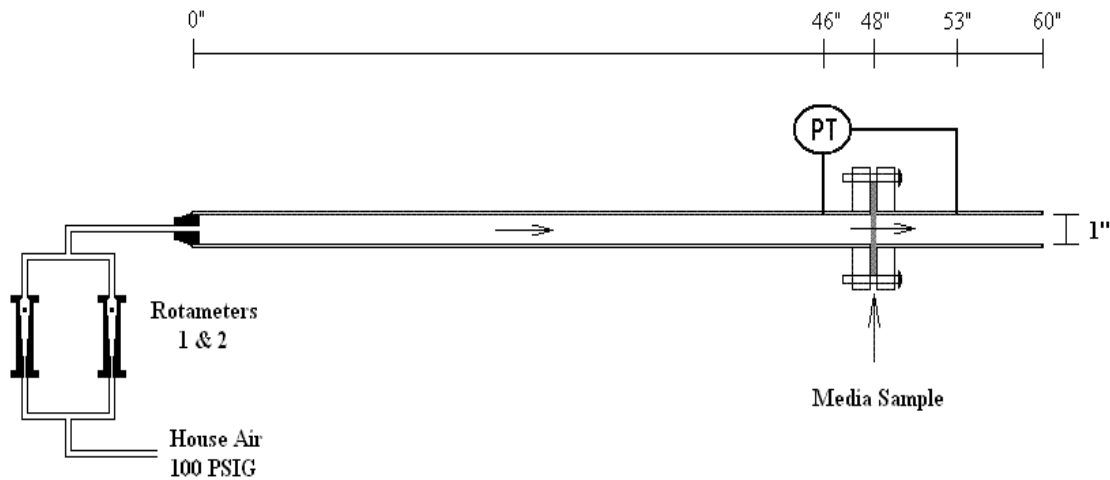


Figure 2.6: General Schematic of Media Test Rig

Airflow to the rig was controlled by two rotameters. The rotameters were connected in series to produce a stable, controllable volumetric flow between 0 and 160 SCFH. This correlated to a maximum superficial velocity of 488.9 fpm within the one inch test rig. The rotameters were calibrated by a volumetric displacement test (See appendix for calibration procedure and results). Resistance measurements were obtained with an Omega Model PX154–010DI differential pressure transmitter connected to a pressure tap located two inches upstream and five inches downstream of the media sample. The taps had a one-eighth inch diameter and were drilled flush with the inner tube diameter to prevent increased friction. The pressure transmitter had a range of -1.0 to 10" H₂O with a resolution of 0.001" H₂O.

A control test performed on the media test rig resulted in 0.003" H₂O of pressure drop at the maximum volumetric flow. The measured resistance follows the Darcy-Weisbach Equation (Eq. 2.16) for flow in a circular pipe with a smooth interior. The measured and calculated values are shown in Figure 2.7. The step-shaped appearance of

the measured data was the product of the differential pressure transmitter's resolution of 0.001" H₂O. The slope shifts in the calculated plot were due to the transition from laminar to turbulent flow.

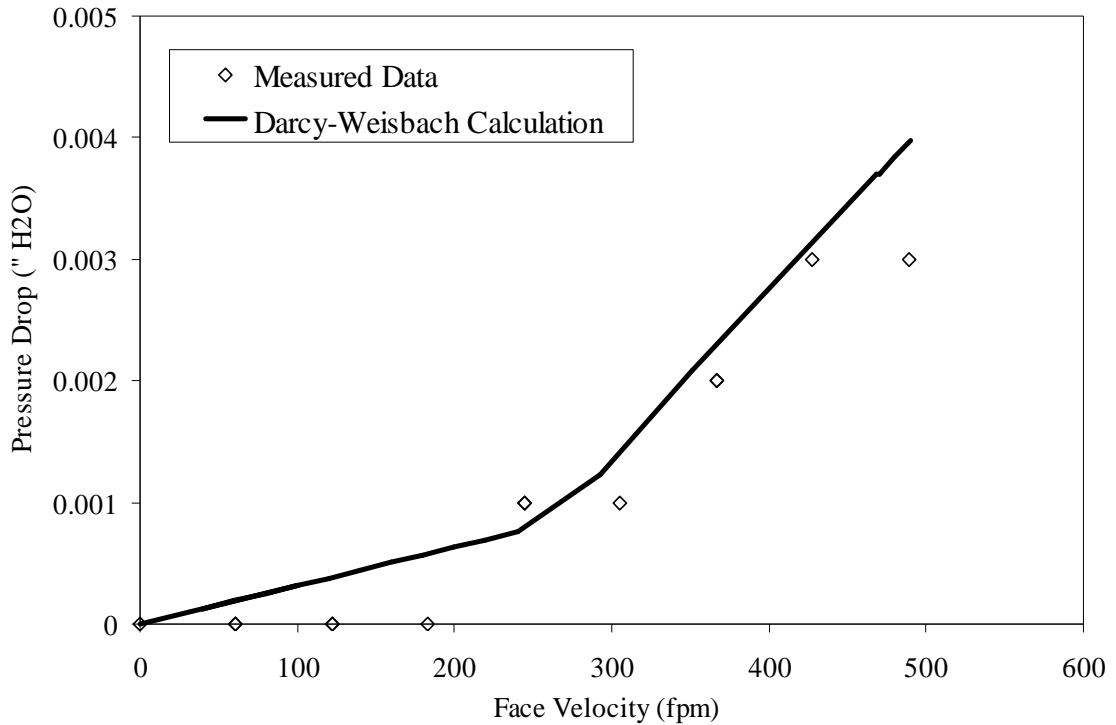


Figure 2.7: Control Pressure Drop Curve for Media Test Rig

II.4.2. Filtration Test Rig

A general schematic of the filtration test rig is depicted by Figure 2.8. The test rig was composed of the following eight subunits: (1) blower, (2) blower sleeve, (3) three-way transition, (4) baffles, (5) air straighteners, (6) main duct, (7) filter box, and (8) outlet duct. The primary building material was 5/8" thick particle board. The subunits were fastened by nut and bolt fixtures. All joints were sealed with a polymer glue gun. The edge of each section was fitted with 1/4" foam weather-stripping. After tightening the bolts to compress the weather-stripping, the resulting seal produced no noticeable leaks.

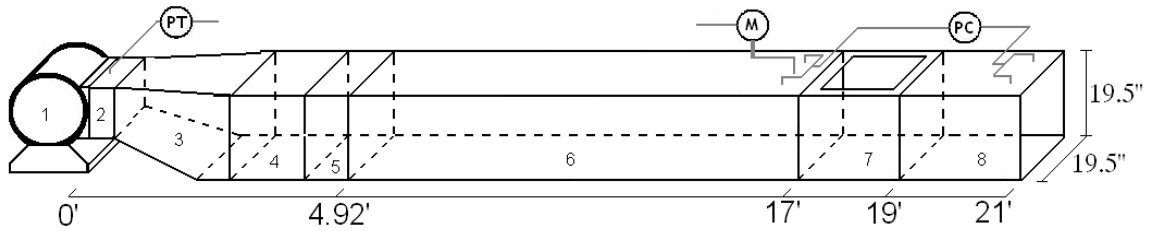


Figure 2.8: General Schematic of Blower Test Rig

The air handler used was a Dayton System with a 15" impellor powered by a 3 Hp Hitachi motor. The motor was controlled by a Hitachi frequency drive with a range of zero to sixty hertz at 0.1 Hz increments. The outlet port dimensions for the blower were 16" x 11.5".

A sleeve served as a connecting segment between the blower and the three-way transition. The sleeve was attached to the blower's outlet port. A pressure tap, located on the sleeve, coupled with a pressure transducer monitored resistance across the blower. Once inside the three-way transition, the cross-sectional dimensions expanded from 16" x 11.5" to 19.5" x 19.5" (H x W). The three-way transition then connected to the baffles.

The baffles were composed of 4 vertical planks followed by 4 horizontal planks. This created an outlet composed of twenty-five squares. The allowable flow to each square was controlled by the position of the vertical and horizontal planks. The baffles were followed by the flow straighteners. The first straightener was a perforated metal plate that blocked fifty percent of the cross-sectional area. The second straightener was a heavy mesh screen. The airflow passed from the straighteners into the main duct. The main duct was composed of three extensions. It had a length of twelve feet with internal dimensions of 19.5" x 19.5" (H x W).

The baffles, flow straighteners, and main duct served to delivery a uniformly-distributed airflow into the filter box. The baffles directed large quantities of air to the desired segments of the duct. The straighteners assisted with leveling the flow by introducing a considerable resistance into the system. The length of the main duct allowed the air to evenly disperse. The before-and-after effects of adding these subunits are highlighted below. The figure was created by measuring velocity at each point depicted by the 7x7 grid with a hot-wire anemometer (Extech Model # 407123). Without any duct modifications, the blower delivered a heavily concentrated volumetric flow to the left-hand side of the ductwork. The distribution system eliminated this “hot spot” and reduced the variation between the maximum and minimum localized velocity by an order of magnitude.

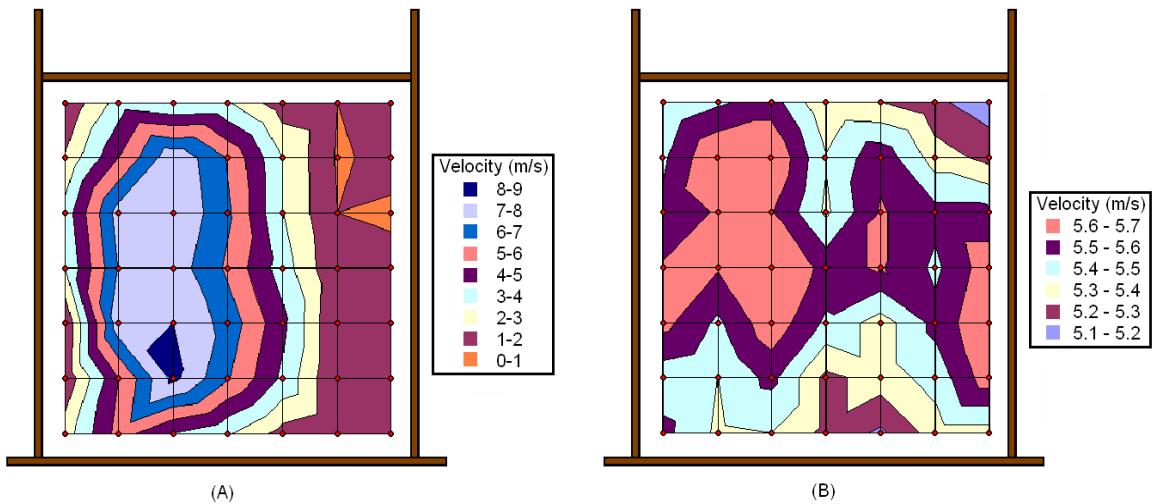


Figure 2.9: Flow Distribution at 40 Hz Before (A) and After (B)

Once it had traveled through the main duct, the air entered into the filter box. The filter box could be loaded with a single filter or a multi-element pleated filter array. The filter box had the following dimensions: 19.5”x19.5”x 24” (HxWxL). The top of the filter box contained a window in order to observe that the pleat’s integrity remained intact

throughout the experiments. The filter box was followed by the outlet section. The 24” long outlet section prevented an increase in pressure drop due to sudden expansion out into the room.

A metal strip was positioned four inches from the front of the filter box to secure a single filter into position. The strip had a height of 1/8” that allowed it to fit behind the filter’s housing without interfering with the pressure measurements. For array tests, the filters were held together and sealed into place using duct tape. No additional support was needed to keep the filter array in position due to the tight fit of the filter box.

Pressure drop across the filtration section was monitored by a Dywer Mark II monometer and an Invensys Foxboro IDP10 differential pressure transmitter. The equipment was connected upstream into the duct by three pressure taps located ten inches before the filter test box. A 1/8” pressure tap located in the center of the duct was connected to the manometer. The manometer’s second connection was left open to the room’s atmosphere. The other two pressure taps were evenly spaced across the top of the duct. The taps had a 1/4” opening within the duct that reduced to a 1/8” tube fitting. All taps were drilled flush to the ducts interior wall to prevent additional friction. The two taps were connected together via a “T” junction. The line was then ran to the differential pressure transmitter. The transmitter’s outlet was connected to a second “T” junction. The “T” split lines were connected downstream to pressure taps located six inches before the duct outlet. The dual tap configuration was a method to average the pressure drop readings.

Air to the blower was drawn from the room. All tests were performed in an environment of approximately 20°C (68 °F) and elevation of 215 meters (705 ft) above

sea level; therefore, the density of air was assumed to possess a constant value of 1.16 kg/m³ (0.0725 lb/ft³) throughout the experiments.

The ASHRAE 52.2 Standard provided an outline for certifying an acceptable flow distribution and pressure drop across an empty test section. The flow distribution test, outlined in Section 5.2, consisted of a nine-point test at three volumetric flow rates (472, 1970, and 2990 cfm) (ASHRAE 2007). A nine square grid was bracketed off at the outlet of the duct with a thin metal wire. The average velocity was taken at the center of each grid square for one minute. The test was repeated three times at each square. The square's velocity value was composed of the average from the three tests. The coefficient of variance was computed between all nine squares at a given volumetric flow rate. The coefficient of variance was defined as the standard deviation between the nine points divided by the mean. The coefficient of variance must be less than ten percent to pass. Data and the coefficients of variance for the ductwork utilized in this study were presented in Figure 2.10. The velocities units were listed in meter per second (m/s).

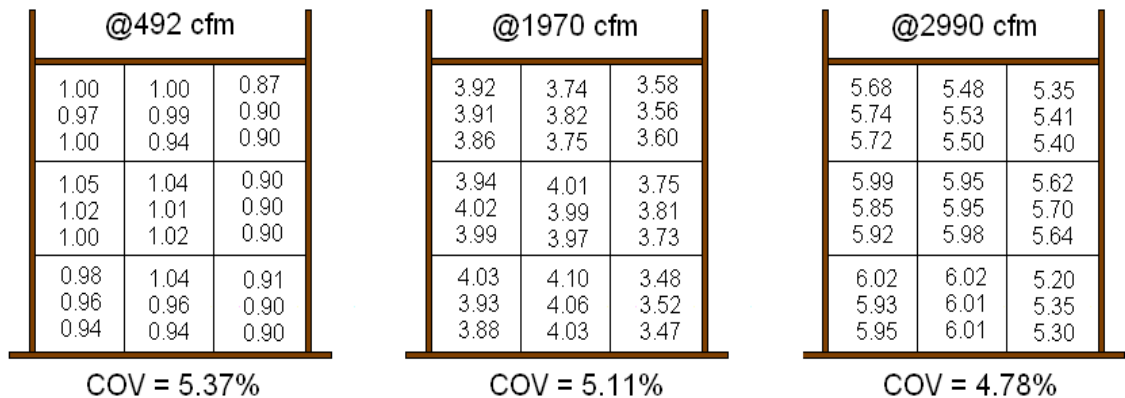


Figure 2.10: Coefficient of Variance

Section 5.16.2 of ASHRAE Standard 52.2 states that the pressure drop across the test section at 1970 cfm (500 fpm in a 2' x 2' duct) shall be less than 0.03" H₂O (ASHRAE

1999). The test rig's recorded pressure drop was approximately 0.001" H₂O at the volumetric flow of 1970 cfm.

As with the media test rig, the pressure drop between the pressure taps was adequately calculated by the Darcy-Weisbach equation. The results of the control run and the calculated values were presented in Figure 2.11. The step-like distribution of the measured values was due to the pressure transmitter's resolution of 0.001" H₂O. The transition from laminar to turbulent flow was not observed in the control plot because it occurred at 24 fpm. Since the flow was primarily turbulent in the ductwork, the alpha term in Bernoulli's Equation equaled unity.

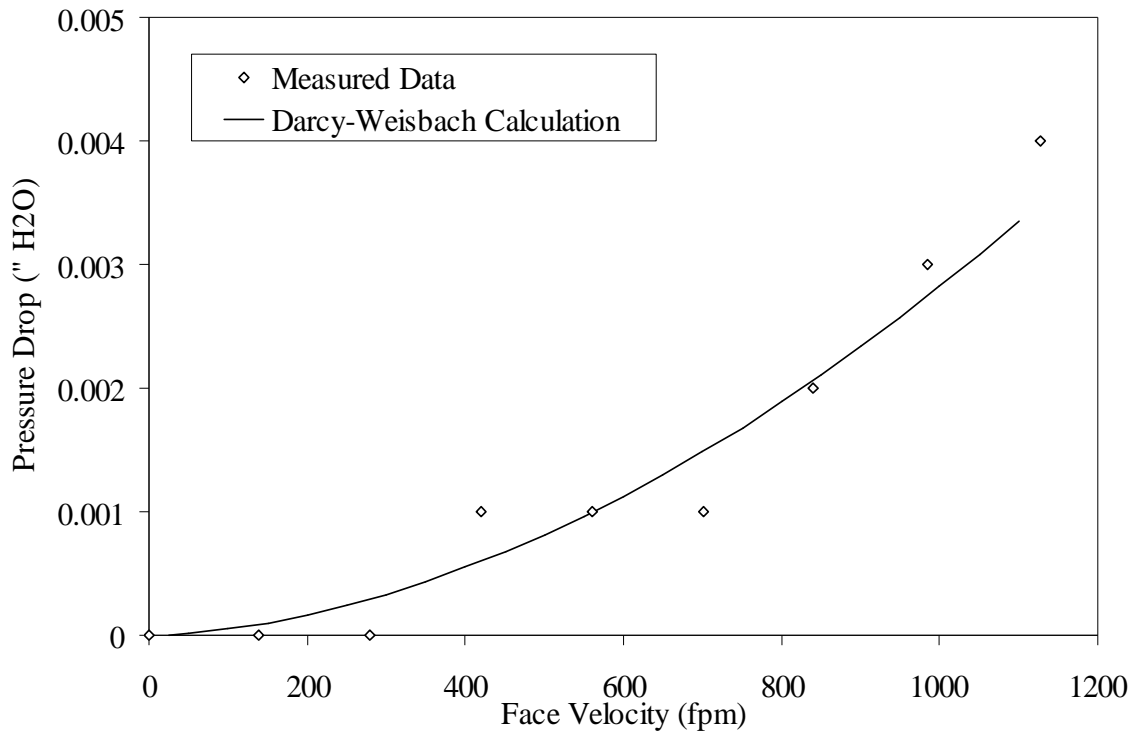


Figure 2.11: Control Pressure Drop Curve for Filter Test Rig

II.5. Data Acquisition

II.5.1. Media Pressure Drop Curves

Three pressure drop runs were performed on each media sample. The first run consisted of 35 data points, the second run 12 data points, and the third run 11 data points. A data point consisted of setting the rotameter to a flow rate and recording the corresponding pressure drop. Each run used a different strategy for incrementing the rotameters to randomize the data collection.

II.5.2. Filter Pressure Drop Curves

All data collected during a single filter experiment followed the manner described below unless stated otherwise. The blower frequency was first set at 5 hertz, and the flow was allowed to equilibrate. The pressure drop across the blower was measured by the pressure transducer. The pressure drop across the filtration section was measured by the differential pressure transmitter and manometer. An average velocity was measured with an Extech Model 451104 vane-anemometer over a thirty second period by uniformly moving the meter over the path indicated below at the outlet of the test rig. This measurement technique was based on the ASHRAE 52.2 velocity uniformity test.

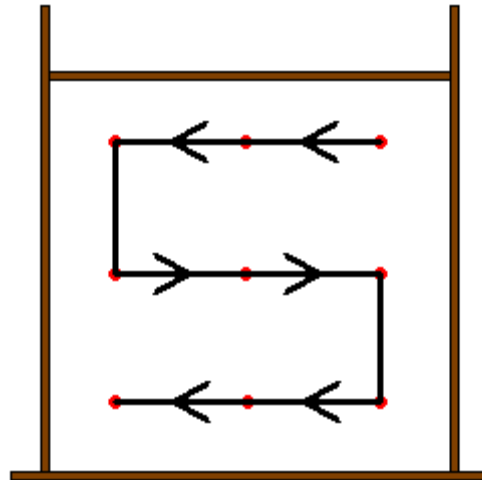


Figure 2.12: Measurement Path for the Vane Anemometer

The measurements were repeated at the following frequencies in the order listed: 10, 15, 20, 25, 30, 35, 40, 37.5, 32.5, 27.5, 22.5, 17.5, 12.5, and 7.5 hertz. The test was repeated up to three times on certain filters, but multiple runs were ultimately abandoned due to time constraints. Frequencies above forty hertz were not measured during single filter tests because they corresponded to velocities greater than 1000 fpm. Frequencies below five hertz were not measured in either filter arrangement because the blower was not able to overcome the initial flow resistance created by the test rig; therefore, there was no flow in the ductwork.

For the multi-element test, data was collected in the same manner up until 35 hertz. Frequencies larger than 35 hertz corresponded to face velocities greater than 1000 fpm. The frequency was then decreased in a following manner: 33.7, 32.5, 31.3, 28.7, 27.5, 26.3, 23.7, 22.5, 21.3, 18.7, 17.5, 16.3, 13.7, 12.5, 11.3, 8.7, 7.5, and 6.3 hertz. Only the pressure drop measurements were recorded as the frequency was decreased.

This was done to save time on data recording since the velocity could be accurately calculated from the blower curve based on pressure drop data (Figure 2.13).

Once the data was collected for a filter or array, a pressure drop curve was created by plotting pressure drop versus face velocity. A regression line was fitted to each pressure drop curve for use in data analysis. The fitted line helped alleviate individual data discrepancies. The Darcy-Weisbach equation was used to remove the background noise from the measurements.

As stated, the velocity values were computed from the blower curve in multi-filter tests. The volumetric flow could be calculated based on the pressure drop across the blower and frequency setting by the following series of equations:

- | | | |
|------|---|----------------------------|
| i) | $RPM = 37.75 \times \text{Setting (Hz)}$ | Rate per Minute |
| ii) | $k = RPM / 2265 \text{ (Hz)}$ | k Factor |
| iii) | $\Delta P_{60\text{Hz}} = \Delta P_{\text{blower}} / k^2$ | Pressure Drop at 60 Hz |
| iv) | $V_{60\text{ Hz}} = -25.32\Delta P_{60\text{Hz}}^2 - 389.08\Delta P_{60\text{Hz}} + 5185.5$ | Volumetric Flow at 60 Hz |
| v) | $V = kV_{60\text{ Hz}}$ | Volumetric Flow at Setting |

Once the volumetric flow was known, the face velocity was calculated by dividing the volumetric flow by allowable flow area. Figure 2.13 was a comparison of 189 velocities measured by the vane-anemometer and the resulting calculations from the blower curve.

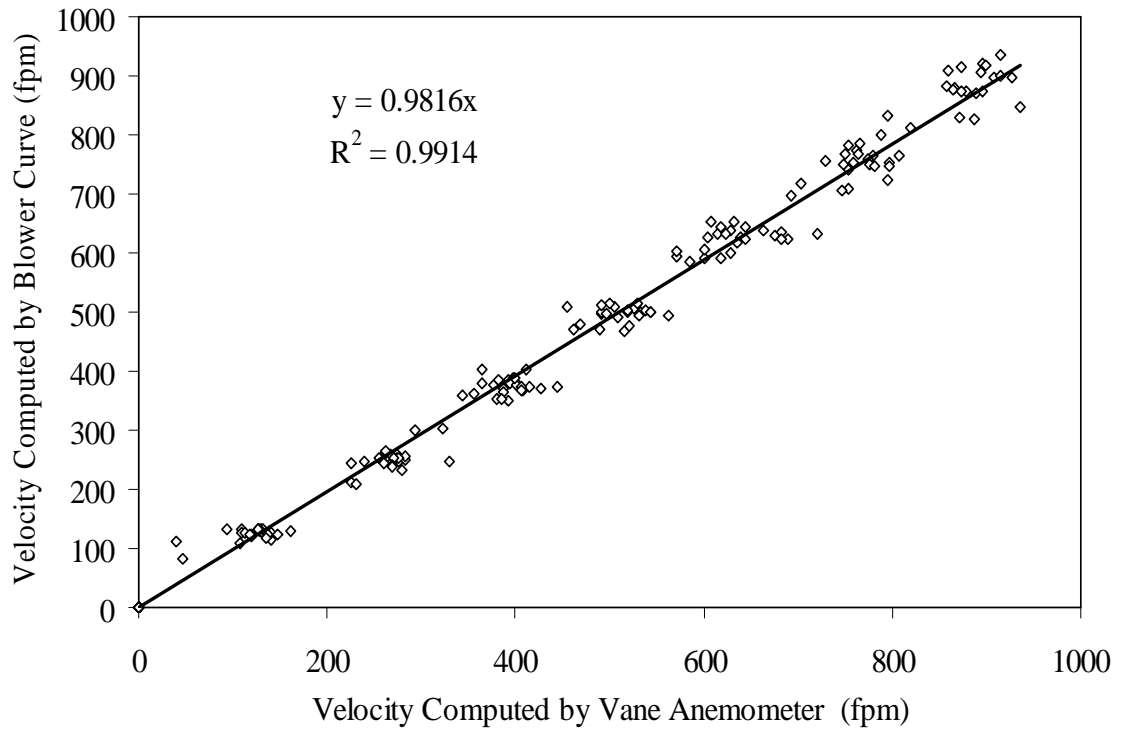


Figure 2.13: Velocity Measurement Comparison

The measurement comparison between the differential pressure transmitter and the manometer was shown in Figure 2.14. The meters showed a one-to-one correspondence. The figure developed a plateau-shaped distribution as pressure drop increased. This was due to the gradual decrease in manometer resolution at readings above 0.1" H₂O.

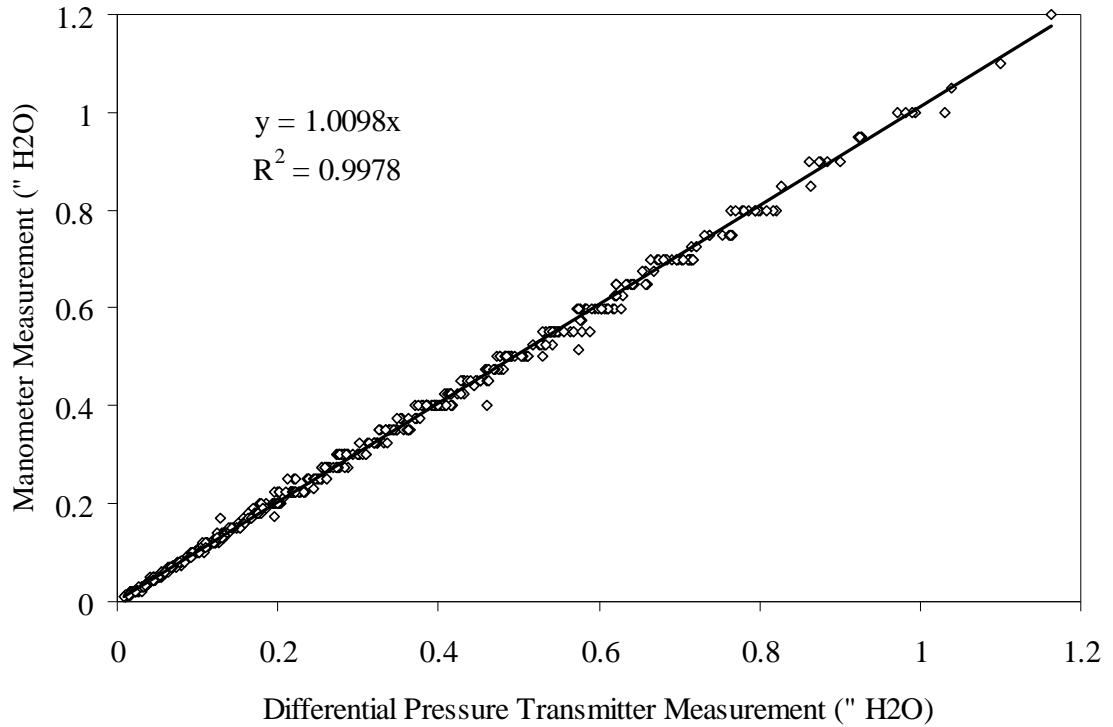


Figure 2.14: Pressure Measurement Comparison between Manometer and Transmitter

II.5.3. Media Thickness

The media thickness was determined with a micrometer. A given media was layered twenty times, and the thickness was measured. The test was repeated twice, and the average thickness of a single layer was calculated from the three tests.

CHAPTER III: INITIAL PRESSURE DROP MODELING OF PLEATED FILTERS

III.1. Introduction

III.1.1. Pleated Filter Schematics

The following schematics (Figure 3.1, 3.2, & 3.3) are provided to familiarize the reader with the dimensions and nomenclature used throughout the research to describe a pleated filter. Figure 3.1 is an illustration of a filter with nine pleats. The symbols F_D , F_H , and F_W stand for filter depth, filter height, and filter width. A filter will often be referred to as an “X” inch filter. This size dimension denotes the filter depth. The face dimensions (F_H and F_W) remain constant throughout the research involving a single pleated filter. In the orthogonal view, the top of the filter is shown as partially removed to expose the pleat’s geometry.

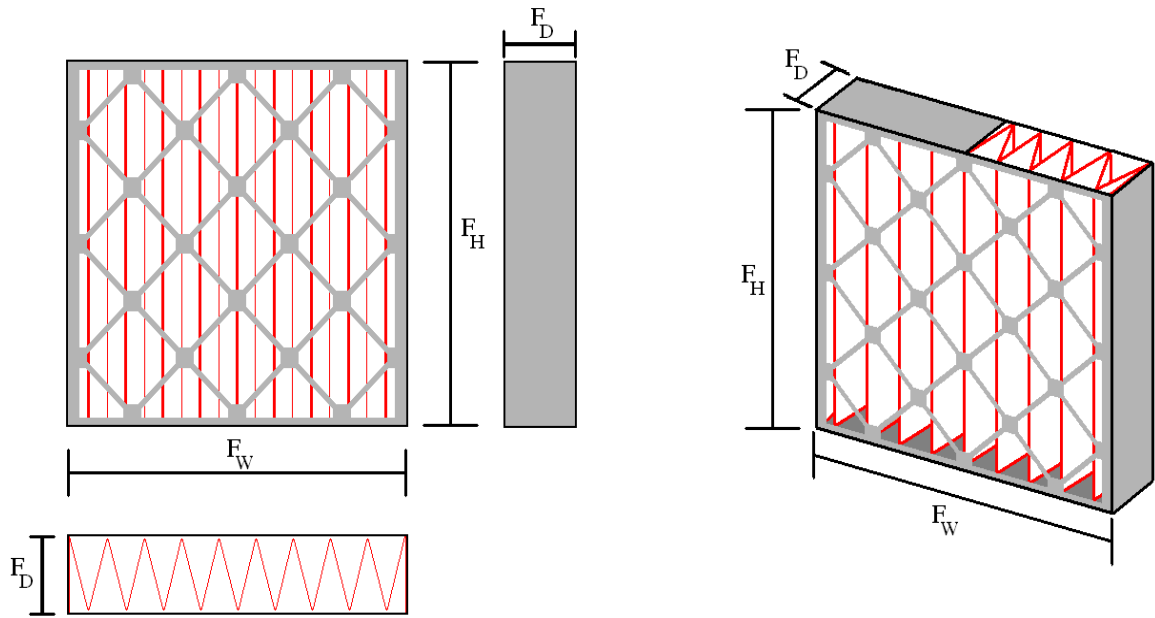


Figure 3.1: Pleated Filter Illustration

A more detailed view of the pleat structure is presented in Figure 3.2. Because of the technique used to construct a pleated filter, the pleat length (P_L) is the same dimension as the filter depth. The pleat depth (P_D) is therefore shorter than the overall depth of the filter. The allowable flow area into the pleat is slightly less than the pleat opening (P_O) due to the fractional blockage created by the pleat tip (P_T). The pleat pitch, also called pleat angle, is denoted by the Greek letter Beta. The pleat height, which is not shown, runs the span of the pleat tip and is equivalent to the filter height.

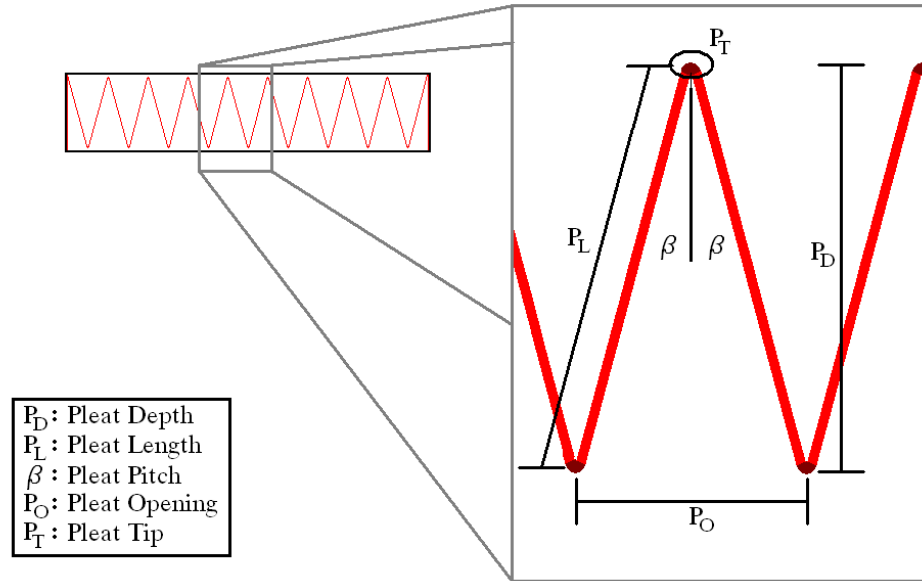


Figure 3.2: Illustration of Pleat Dimensions

Figure 3.3 is an illustration of a pleat tip formation from a flat sheet of media. A pleat tip is modeled as a rounded peak created by folding the media around a pinch point. The pinch point is indicated by the square box. The label M_T represents the media's thickness. The effective flow area blocked by the tip is indicated by label A_T (Area of Pleat Tip). The label M_E is the approximate length of material used in the creation of the pleat tip. The angle γ is solely used in calculations.

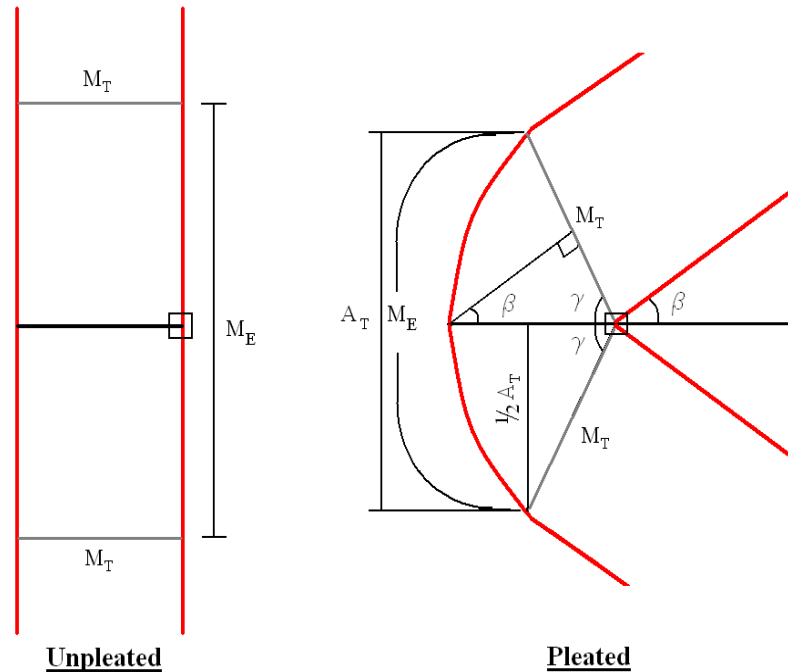


Figure 3.3: Pleat Tip Illustration

III.1.2. Parameters

Most of the filter's parameters are defined by the ductwork employed or the end user. The remaining parameters are dependent on the defined parameters.

Filter Parameters

Filter Height (F_H):	Dictated by the Duct Height
Pleat Height (P_H):	Dictated by the Duct Height
Filter Width (F_W):	Dictated by the Duct Width
Filter Depth (F_D):	Specified by the User
Pleat Length (P_L):	Specified by the User (Equivalent to Filter Depth)
Pleat Count:	Specified by the User
Grating Blockage:	Specified by the User
Media Thickness (M_T):	Specified by the User (Property of Media)
Permeability:	Specified by the User (Property of Media)

Pleat Parameters

Pleat Tip	= $2\sin(\gamma)\text{Media Thickness}$
Pleat Opening	= Filter Width / Pleat Count
Pleat Pitch [β]	= $\sin^{-1}(\frac{1}{2} \text{Pleat Opening} / \text{Pleat Length})$
Gamma [γ]	= $\pi/2 - \text{Pleat Pitch}$
Media Loss (A_T)	= $2(\text{Media Thickness}) \times \text{Gamma}$

III.1.3. Proposed Flow through a Pleated Filter

The modeling efforts began by defining a pathway for air to flow through a filter. The pathway chosen, first proposed by Raber (1982), consisted of air traveling through seven regions of varying cross-sectional area to pass through a pleated filter. A uniform flow profile is assumed to exist in the upstream duct before the filter. A typical pleated filter employs a grating that increases the structure integrity of the filter and the pleats. The flow is contracted by the grating resulting in an increased velocity. The air expands back out after the grating, yet it is quickly contracted as it is channeled around the pleat tips and into the pleats.

Once in the filter's pleats, the air begins to split and change directions to allow entrance into the media at an angle perpendicular to the media's surface. The air expands out onto the media's surface area after the directional change. The proposed flow pattern through the filter's pleats is very similar to the flow in a converging or diverging wye.

The fourth region is the media's accessible surface area. The area does not include the small portion of the media that will be pinched shut in the pleat tips. The air flow then follows a similar, albeit reversed, path out of the filter system into the downstream duct after flowing through the media.

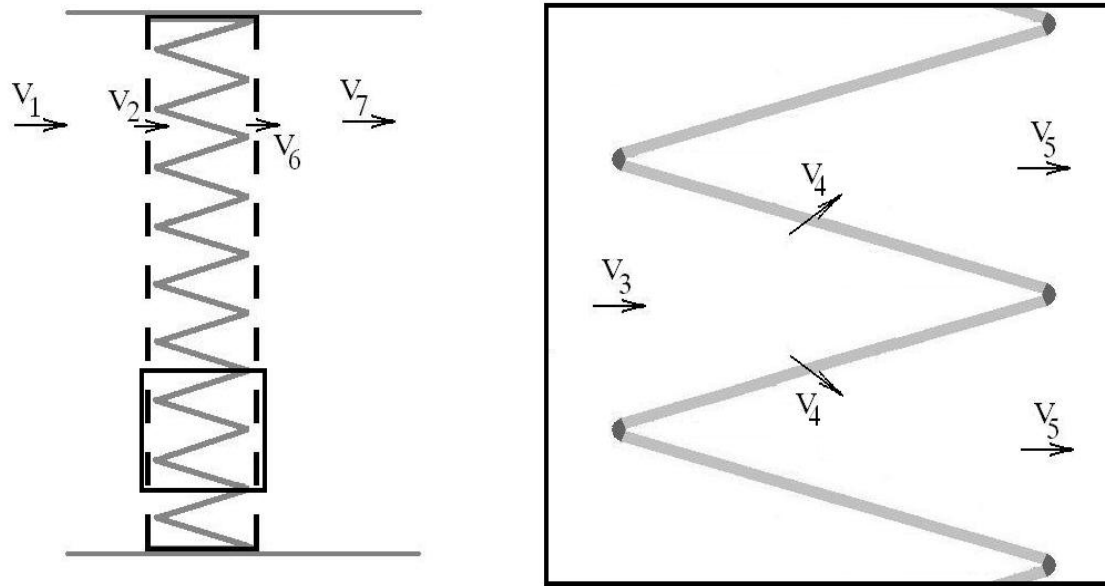


Figure 3.4: Flow Pattern

Area Calculations:

- i) Area 1 (Area 7): *Duct Width x Duct Height*
- ii) Area 2 (Area 6): *(Filter Width x Filter Height) x (1 - % Blocked)*
- iii) Area 3 (Area 5): *(Filter Width x Filter Height) – Pleat Count x Pleat Tip x Pleat Height*
- iv) Area 4: *(Pleat Count x Pleat Height) x (2 Pleat Length – Media Loss)*

III.1.4. Modeling a Pleated Filter

The total pressure drop through a pleated filter was modeled as a summation of individual resistances. The individual resistances were formulated by applying Bernoulli's Equation or Forchheimer-extended Darcy's Law to the seven proposed flow areas. The singular parts were summed together in the same way that electronic resistances can be added in series. This method was previously used by Idelchik (1994) to model an electrostatic filter and is similar in nature to the three-tiered modeled proposed by Caeser and Schroth (2002).

- | | | |
|------|---|--|
| i) | Across Front Grating: | $\Delta P_1 = \frac{1}{2} \rho [(V_2^2 - V_1^2) + K_G V_2^2]$ |
| ii) | Flow from Grating to Pleat Inlet: | $\Delta P_2 = \frac{1}{2} \rho [(V_3^2 - V_2^2) + K_C V_3^2]$ |
| iii) | Flow from Pleat Inlet to Media Surface: | $\Delta P_3 = \frac{1}{2} \rho [(V_4^2 - V_3^2) + K_{P1} V_3^2]$ |
| iv) | Flow through Media: | $\Delta P_4 = A V_4 + B V_4^2$ |
| v) | Flow from Media Surface to Pleat Outlet: | $\Delta P_5 = \frac{1}{2} \rho [(V_5^2 - V_4^2) + K_{P2} V_5^2]$ |
| vi) | Expansion from Pleat Outlet into Grating: | $\Delta P_6 = \frac{1}{2} \rho [(V_6^2 - V_5^2) + K_E V_5^2]$ |
| vii) | Across Back Grating: | $\Delta P_7 = \frac{1}{2} \rho [(V_7^2 - V_6^2) + K_G V_6^2]$ |

$$\Delta P_T = \sum \Delta P_i = \Delta P_1 + \Delta P_2 + \Delta P_3 + \Delta P_4 + \Delta P_5 + \Delta P_6 + \Delta P_7 \quad (3.1)$$

K_C , K_E , and K_G were modeled as previous published coefficients of friction computed by Equations 2.12, 2.13, and 2.15. K_{P1} and K_{P2} are unique friction coefficients for flow in the upstream and downstream pleats for which no previous formula could be found; thus, a new formula had to be developed. A coefficient's formula can be identified by simultaneously solving the mechanical energy balance and the momentum balance. Figure 3.5 is a pleat control volume for the downstream pleat.

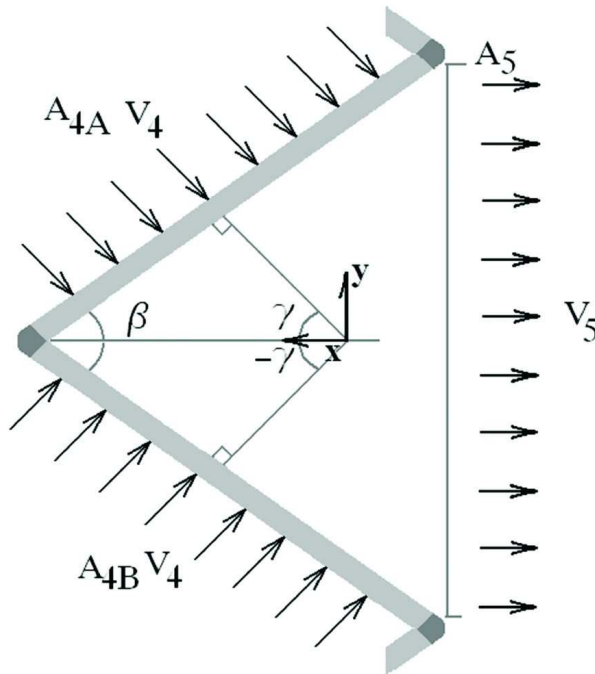


Figure 3.5: Control Volume of a Downstream Pleat

Momentum Balance

$$d\Gamma/dt = [V_4 W_4 + P_4 A_4] U_i - [V_5 W_5 + P_5 A_5] U_i + F_{s \rightarrow f} + mg$$

Force of Fluid on the Solid

Forces in y-Direction

$$F_y = \frac{1}{2} (V_4 W_4 + P_4 A_4) \cos(\beta) + \frac{1}{2} (V_4 W_4 + P_4 A_4) \cos(-\beta) - 0 = 0$$

Forces in x-Direction

$$F_x = (V_4 W_4 + P_4 A_4) \sin(\beta) - (V_5 W_5 + P_5 A_5)$$

$$F_x = \rho V_4^2 A_4 (A_5 / A_4) + P_4 A_4 (A_5 / A_4) - \rho V_5^2 A_5 - P_5 A_5$$

$$F_x = \rho (V_4^2 - V_5^2) A_5 - (P_5 - P_4) A_5$$

$$F_{f \rightarrow s} = (F_x^2 + F_y^2)^{1/2}$$

Assuming $F_{f \rightarrow s}$ is zero

$$0 = \rho (V_4^2 - V_5^2) A_5 - (P_5 - P_4) A_5$$

$$(P_5 - P_4) = \rho (V_4^2 - V_5^2)$$

Mechanical Energy Balance

$$\frac{1}{2} (V_5^2 - V_4^2) + (1/\rho)(P_5 - P_4) + L_v = 0$$

$$L_v = \frac{1}{2} (V_4^2 - V_5^2) - (1/\rho)(P_5 - P_4)$$

Substituting in Momentum Balance Solution

$$L_v = \frac{1}{2} (V_4^2 - V_5^2) - (1/\rho)[\rho(V_4^2 - V_5^2)]$$

$$L_v = \frac{1}{2} (V_5^2 - V_4^2)$$

$$V_4^2 = (V_5 A_5 / A_4)^2$$

$$L_v = \frac{1}{2} V_5^2 (1 - (A_5 / A_4))$$

$$k \approx [1 - (A_4 / A_5)^2] \approx [1 - (1/\beta)^2]$$

where the reference velocity is V_4

The solution indicates that the coefficient is a function of the pleat pitch (β). As will be shown in Section 3.II.D, the solution does not directly correspond to the observed data. Possible sources of error can be found in two simplifying assumptions. First, the force of the fluid on the surface ($F_{f \rightarrow s}$) can not be readily neglected as proposed. Second, assuming air will enter and exit the media at a strictly perpendicular angle is questionable.

The pleat coefficients were determined in an empirical manner since the two balances could not be simultaneously solved. Experimentally, the individual contributions of K_{p1} and K_{p2} could not be separated and analyzed due to the upstream and downstream pleat symmetry. The two coefficients were therefore combined into a single

coefficient (K_P) since they share identical geometries and experience the same velocities. The newly formed pleat coefficient was then substituted in their place.

With the equation of continuity assumed valid, the series can be simplified by replacing all downstream velocities with their reciprocal upstream velocities. The seven terms can be summed and rearranged into the following model:

$$\Delta P_F = \frac{1}{2} \rho [(2K_G)V_2^2 + (K_C + K_E + K_P)V_3^2] + AV_4 + BV_4^2 \quad (3.2)$$

The first four terms represent the geometric contribution and the last two terms denote the media influence; thus, the equation can be rewritten to resemble Equation 2.1.

III.2. Identifying the Constants

The objective of the experimental program was to verify the validity of utilizing previously published coefficients to model particular aspects of the filter design as well as to empirically determine a new coefficient for friction encountered in the pleat. Since the media constants will be unique and vary with the media used in the filter, the approach began by measuring the media constants (A & B) and thickness of the materials utilized in the research. The previous published coefficients (K_G , K_C , and K_E) were then shown to be applicable. The pleat coefficient for a single filter was empirically determined from empirical ΔP_T versus face velocity data. This technique was based on Rivers and Murphy's approach to identify the constants N and K_G from their model. A more universal coefficient was developed by determining K_P for a multitude of filter designs.

III.2.1. Media Constants & Thickness

The research utilized five types of media. For future identification purposes, the media types will be referred to in this dissertation by FM1, FM2, FM3, FM4, or FM5.

Figure 3.6 presents the flow resistance versus face velocity results obtained from flat media sheets. The points on the graph represent the experimentally collected data. The lines are second-order polynomials fitted by Excel by applying a least-square regression line.

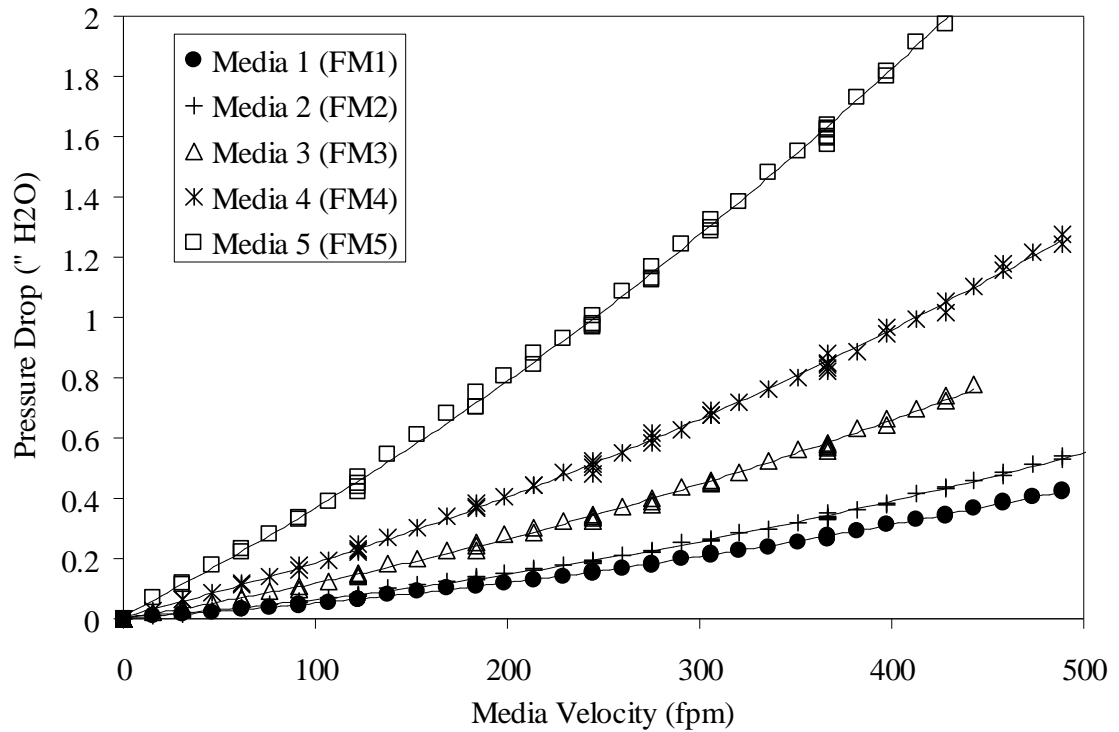


Figure 3.6: Media Resistance Curves

The media constants were determined from the polynomial fits. A table of each media parameters and degree of fit is shown below. As previously observed by Chen et al. (1996), the second order coefficient B is sufficiently smaller than the first order coefficient. The average thickness of each media type is also listed in Table 3.1.

Table 3.1: Summary of Media Constants and Thickness

Media (-)	Thickness (in) / [mm]	A x 10 ⁻⁴ (" H ₂ O * min / ft)	B x 10 ⁻⁷ ("H ₂ O * min ² / ft ²)	R ² (-)
FM1	0.0193 / [0.5 mm]	4.09 x 10 ⁻⁴	8.94 x 10 ⁻⁷	0.9990
FM2	0.0194 / [0.5mm]	4.87 x 10 ⁻⁴	11.59 x 10 ⁻⁷	0.9988
FM3	0.0625 / [1.6 mm]	9.73 x 10 ⁻⁴	17.28 x 10 ⁻⁷	0.9983
FM4	0.0398 / [1 mm]	15.89 x 10 ⁻⁴	19.18 x 10 ⁻⁷	0.9989
FM5	0.0417 / [1.1 mm]	32.88 x 10 ⁻⁴	29.25 x 10 ⁻⁷	0.9990

Figure 3.7 shows how the utilization of Darcy's Law to describe the media resistance at the typical operational velocities will result in modeling errors. Darcy's Law remains valid at low velocities as seen in Graph A, but deviations begin to arise between observed and predicted values when face velocities extended beyond approximately 150 fpm. It is commonplace for the media velocity to be above 150 fpm since HVAC filters often operate at 500 fpm face velocity. A pleating factor greater than 3.33 would be needed in order to lower the face velocity of a 20"x20" filter below 150 fpm. Graph B is an attempt to fit the linear Darcy's Law to the entire velocity range for FM1 and FM5 media. Both attempts show an R-square value below the average value of 0.999 observed in Figure 3.6 when utilizing Forchheimer's Equation.

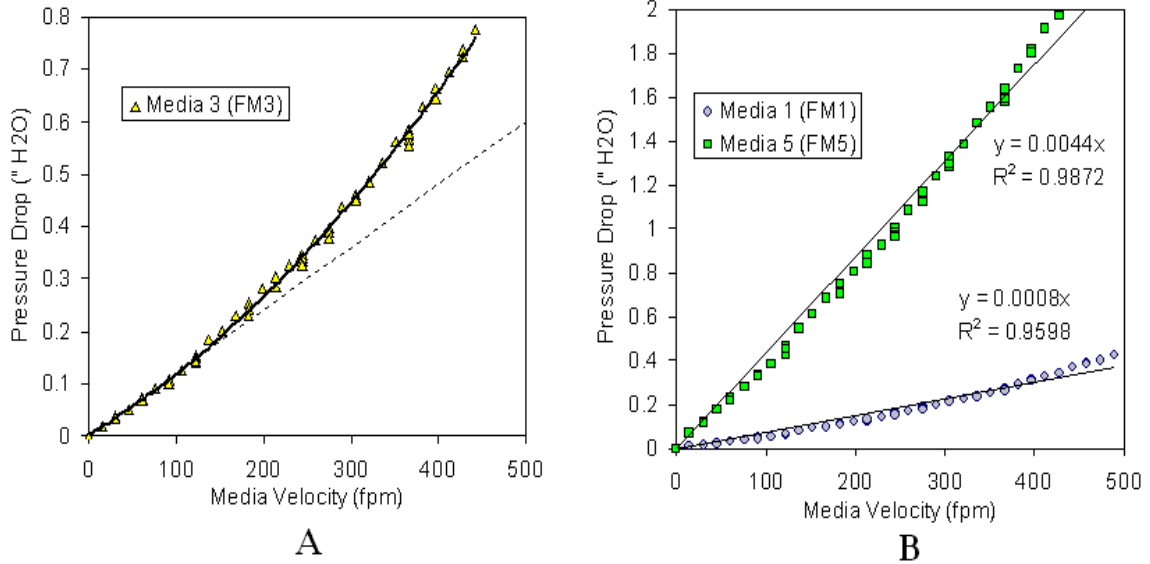


Figure 3.7: Darcy's Law Analysis of Media Resistance

III.2.2. Grating Coefficient of Friction (K_G)

The Handbook of Hydraulic Resistance computes the coefficient of friction for fluid flowing through a shaped, perforated plate by Equation 2.14. In order to verify that the filter housing could be modeled by the same formula, the frame was mechanically altered and the corresponding measured pressure deviation was compared to the calculated deviation.

The filter utilized in the grating experiments consisted of a FM2 media with 22 pleats per filter and nominal dimensions of 20"×20"×1". The filter's standard housing was composed of a diamond grid that blocks 34.5% of the flow area. Additional grating was uniformly added to the filter's front to increase the blocked flow area from 34.5% to 59.4%. Subsequently, the filter's grating was removed resulting in only 16.0% of the flow area blocked. The appearance of the different grating schemes is visible below.

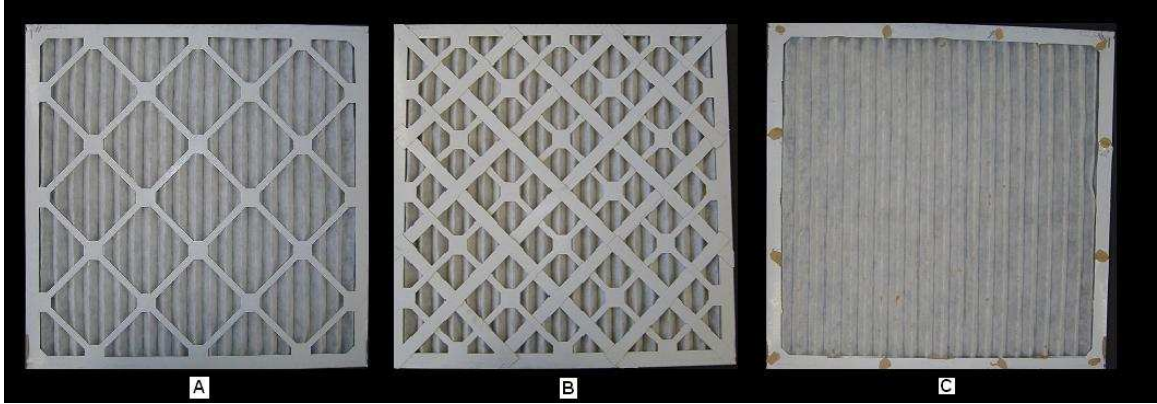


Figure 3.8: Illustration of Grating Schemes
 (A) Normal Filter (B) High Blockage Filter (C) Low Blockage Filter

A pressure drop versus face velocity curve was experimentally observed for each grating configuration. The curves were plotted in Figure 3.9. The markers represented the observed data and the solid lines were Excel-fitted regression lines.

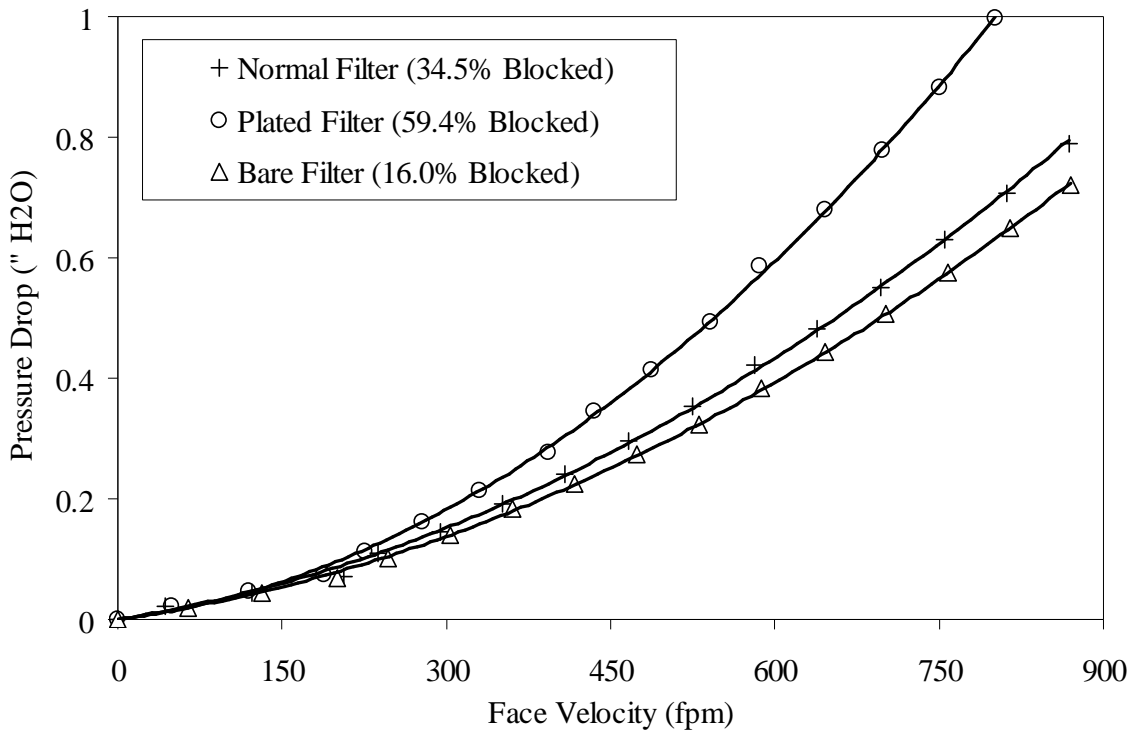


Figure 3.9: Pressure Drop Curves for Various Frontal Blockages

The validity of using Equation 2.14 was proven by comparing the increase in resistance of the observed system (Figure 3.9) to the increase in resistance of the

computed system (Figure 3.10). Figure 3.10 was constructed by using Equation 2.11

with the following K_G values to estimate the resistance created by the grating by itself:

For Normal Blockage:	$K_G = (1.707 - 0.655)/(0.655)^{-2} = 2.50$
For Low Blockage:	$K_G = (1.707 - 0.840)/(0.840)^{-2} = 1.23$
For High Blockage:	$K_G = (1.707 - 0.406)/(0.406)^{-2} = 7.89$

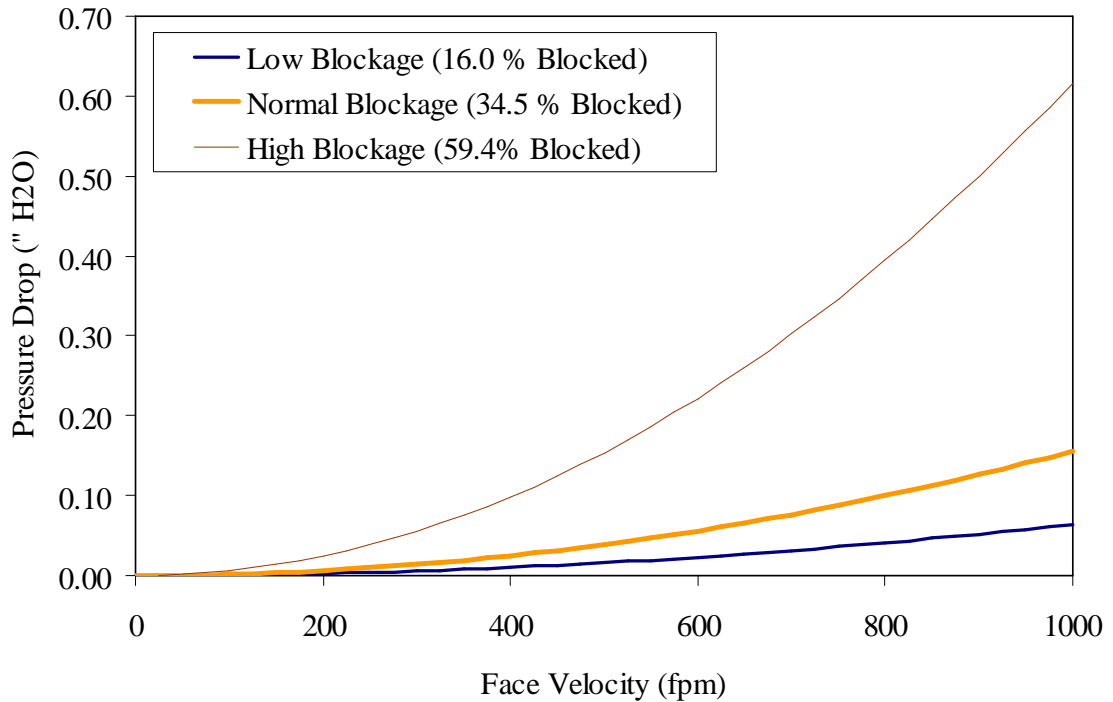


Figure 3.10: Computed Grating Resistances

The observed pressure increase between the curves in Figure 3.9 was generated solely by the grating modification since the same filter was utilized in all three tests. The magnitude of the increase was quantified by using the Low Blockage curve as a reference. Likewise, the resistance increase in Figure 3.10 was the product of an equal percentage blockage increase. The extent of the increase was gauged using the Low Blockage as a baseline. If Equation 2.14 adequately described the resistance created by the grating, then the resistance rise in both systems would be identical. As portrayed in Figure 3.11, the overlap of the observed and computed pressure drop rises indicated that

Equation 2.11 in conjunction with Equation 2.14 properly predicted the resistance behavior of the grating.

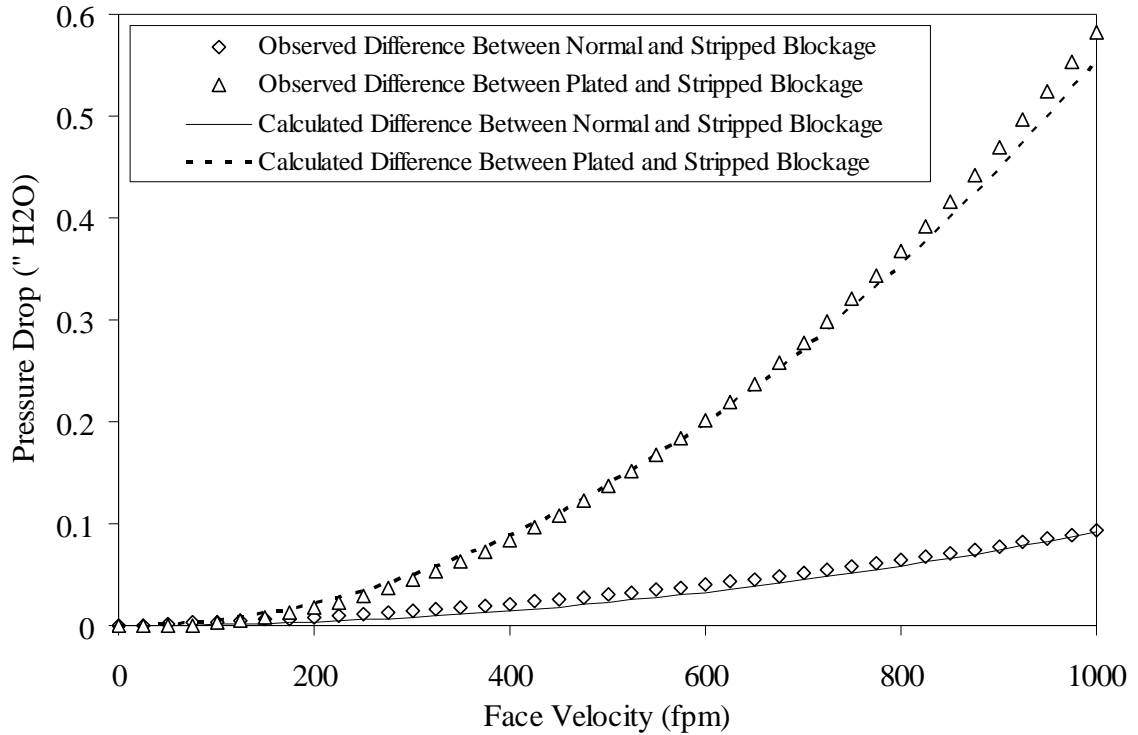


Figure 3.11: Effects of Front Grating Modification

A similar test was performed by modifying the grating on the back of a filter. The results from the back modification test are shown in Figure 3.12. The markers again designated the observed pressure difference while the solid line denoted the calculated predictions. As shown, modification of the housing at the back of the filter produced a nearly identical result.

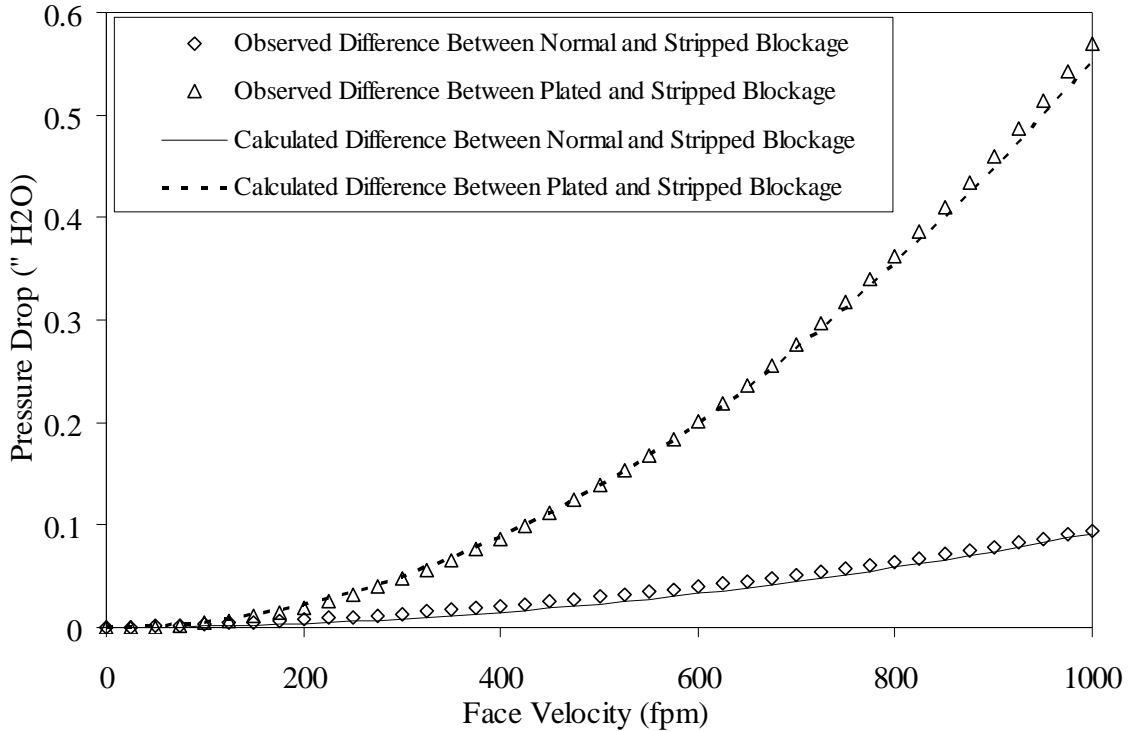


Figure 3.12: Effects of Back Grating Modification

III.2.3. Pleat Tip Assumption

The contraction and expansion into and out of the pleats is assumed to be accurately modeled by Equation 2.11 using friction coefficients computed by Equations 2.12 and 2.13. It is exceedingly difficult to experimentally alter a pleat tip and analyze the resulting contribution to flow resistance without inadvertently affecting other resistances. The assumption that a pleat tip acts as a non-porous wall is based on Darcy's Law. When a media is pleated, the porous material is folded on top of itself creating a pleat tip of increased thickness and/or decreased permeability. Either an increase in media thickness or a decrease in permeability will result in a path of greater flow resistance according to Darcy's constant. Air flow through the pleat tip is therefore assumed to be blocked due to this heightened resistance and will be channeled around the

tips and into the pleats. This assumption was previously incorporated into the research of Caesar and Schroth (2002) and stated by Raber (1982).

III.2.4. Pleat Coefficient of Friction (K_P)

The pleat coefficient for a specific filter was determined by obtaining ΔP_T versus face velocity data over a range of velocities. The model was rearranged into the following linear form:

$$\Delta P_T - \frac{1}{2} \rho [(2K_G)V_2^2 + (K_C + K_E)V_3^2] + BV_4 + AV_4^2 = \frac{1}{2} \rho K_P V_3^2 \quad (3.3)$$

V_i values were computed from the face velocity using the equation of continuity. The coefficients K_G , K_C , K_E , A , and B were calculated by methods previously discussed. The friction created by the pleating was empirically determined by subtracting all known flow resistances from the experimentally measured total pressure drop. The resulting difference was then plotted versus the reference velocity term ($\frac{1}{2} \rho V_3^2$). The pleat coefficient can then be inferred from the slope.

Figure 3.13 graphically showcases this methodology for a FM1 filter with 42 pleats and nominal dimensions of 20" x 20" x 1". The dashed line is a least-squared regression fitted to the experimentally measured pressure drop versus face velocity data. The solid line is a model compilation of the known pressure drops due to the flow through the media, blockage created by the filter grating, and the channeling due to pleat tip contraction and expansion. The hyphenated line represents the observed difference between the least-squared regression and the modeled line. It is equivalent to the left-hand side of Equation 3.3.

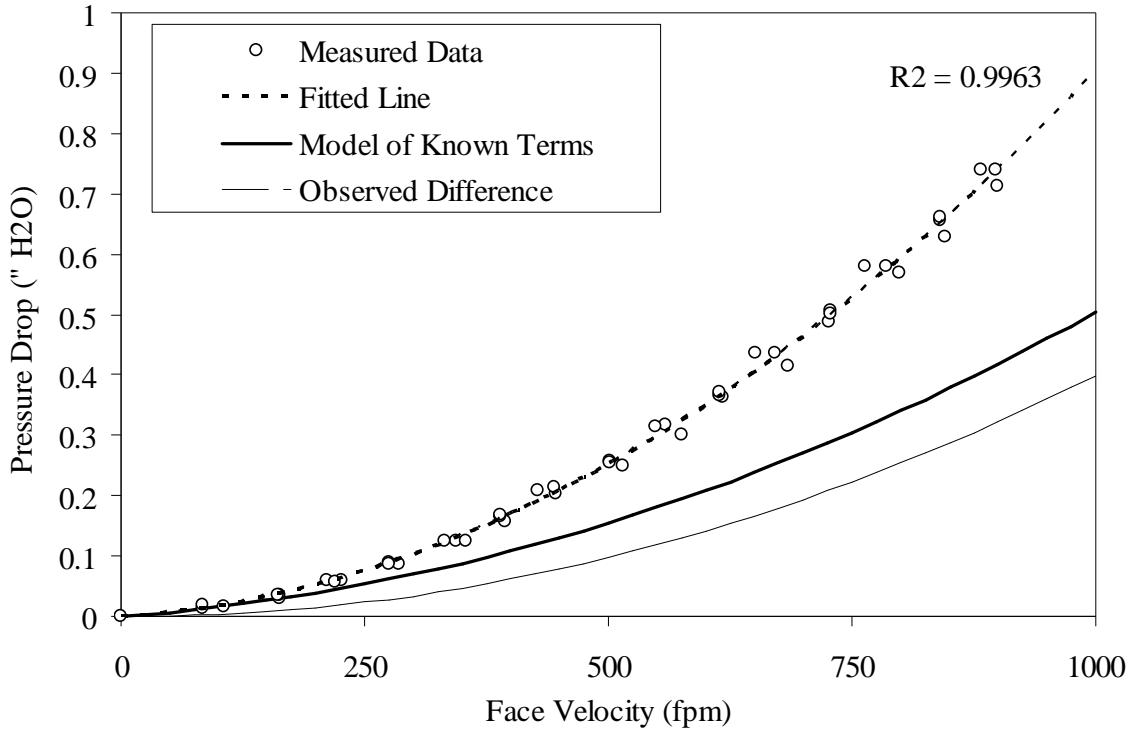


Figure 3.13: Pressure Drop Curves for a 20''x20''x1'' FM1 Filter with 42 Pleats

A linear trend resulted when plotting the observed difference versus $\frac{1}{2}\rho V_3^2$ for the filter (Figure 3.14). A regression line forced through zero was fitted using Excel. The slope of the line equated to the pleat coefficient of friction. The resulting coefficient is only valid for a filter with identical design parameters. In order to acquire a more universal coefficient for the model, the pleat coefficient needed to be determined for a wide range of parameter space covering various pleat counts, filter depths, media thicknesses, permeability, and face velocities. The following table itemized the twenty filter variations used to determine the pleat coefficient. The pleat coefficient for each filter was determined by the same method outlined above. All filters used in this study were manufactured by Quality Filters, Inc. in Robertsdale, Alabama.

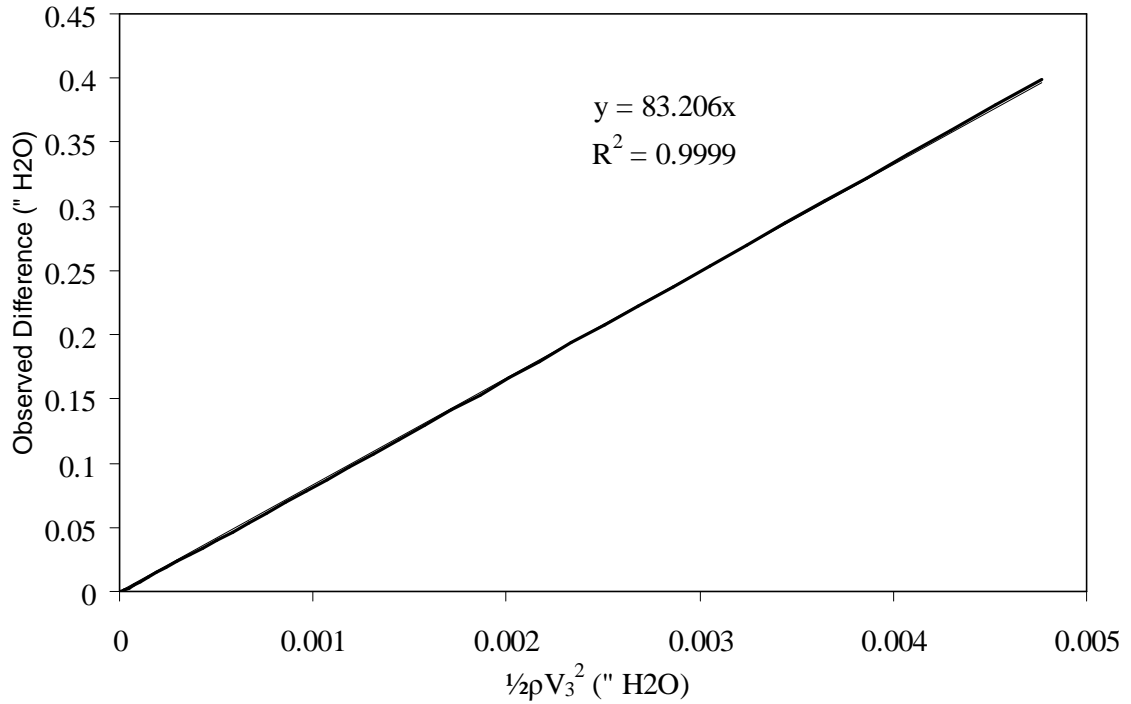


Figure 3.14: Pleat Coefficient Graph for a 20''x20''x1'' FM1 Filter with 42 Pleats.

Table 3.2: Summary of Filters Employed

Filter	Depth	Width	Height	Pleat Count	Media Type
A	0.85" (1")	19.5" (20")	19.5" (20")	22	FM2
B	1.75" (2")	19.5" (20")	19.5" (20")	16	FM2
C	0.85" (1")	19.5" (20")	19.5" (20")	14	FM1
D	0.85" (1")	19.5" (20")	19.5" (20")	19	FM1
E	0.85" (1")	19.5" (20")	19.5" (20")	23	FM1
F	0.85" (1")	19.5" (20")	19.5" (20")	28	FM1
G	0.85" (1")	19.5" (20")	19.5" (20")	32	FM1
H	0.85" (1")	19.5" (20")	19.5" (20")	37	FM1
I	0.85" (1")	19.5" (20")	19.5" (20")	42	FM1
J	0.85" (1")	19.5" (20")	19.5" (20")	47	FM1
K	0.85" (1")	19.5" (20")	19.5" (20")	55	FM1
L	1.75" (2")	19.5" (20")	19.5" (20")	19	FM1
M	1.75" (2")	19.5" (20")	19.5" (20")	34	FM1
N	3.5" (4")	19.5" (20")	19.5" (20")	19	FM1
O	0.85" (1")	19.5" (20")	19.5" (20")	19	FM3
P	0.85" (1")	19.5" (20")	19.5" (20")	32	FM3
Q	1.75" (2")	19.5" (20")	19.5" (20")	19	FM3
R	1.75" (2")	19.5" (20")	19.5" (20")	32	FM3
S	1.75" (2")	19.5" (20")	19.5" (20")	56	FM5
T	3.5" (4")	19.5" (20")	19.5" (20")	12	FM4

The resulting coefficient plots for all 20"x20"x1" FM1 filters with pleat counts varying between 14 and 55 pleats per filter are graphed in Figure 3.15. The equation listed beside each plot indicates the pleat coefficient value and the degree of fit. As expected, the pleat coefficient's magnitude increased as more pleats were incorporated into a filter due to heighten friction inside the pleat. Table 3.3 presents an inventory of the filters, geometric parameters, calculated pleat coefficients, and R-squared fit.

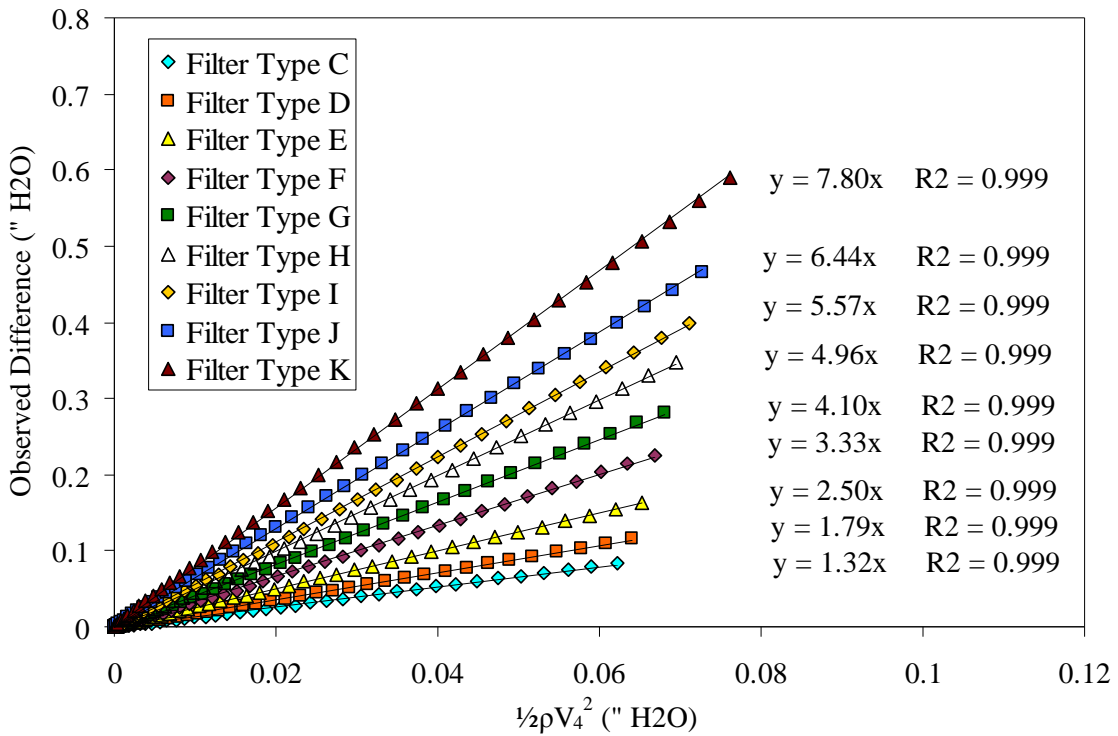


Figure 3.15: Pleat Coefficient Plots for 20"x20"x1" Filters

Table 3.3: Summary of Pleat Coefficients

Filter (-)	Pleats (-)	P _O (ft)	P _D (ft)	P _L (ft)	P _H (ft)	Beta (rad)	K _p (-)	R ² (-)
A	22	0.074	0.061	0.071	1.625	0.521	2.083	0.9761
B	16	0.102	0.137	0.146	1.625	0.348	1.893	0.9498
C	14	0.116	0.042	0.071	1.625	0.819	1.329	0.9991
D	19	0.086	0.057	0.071	1.625	0.604	1.791	0.9998
E	23	0.071	0.062	0.071	1.625	0.499	2.501	0.9998
F	28	0.058	0.065	0.071	1.625	0.410	3.335	0.9995
G	32	0.051	0.067	0.071	1.625	0.358	4.104	0.9998
H	37	0.044	0.068	0.071	1.625	0.310	4.960	0.9997
I	42	0.039	0.068	0.071	1.625	0.273	5.573	0.9999
J	47	0.035	0.069	0.071	1.625	0.244	6.442	0.9998
K	55	0.030	0.070	0.071	1.625	0.209	7.802	0.9997
L	19	0.086	0.140	0.146	1.625	0.293	2.311	0.9794
M	34	0.048	0.144	0.146	1.625	0.164	5.867	0.9974
N	19	0.086	0.289	0.292	1.625	0.147	3.506	0.9992
O	19	0.086	0.059	0.071	1.625	0.604	1.837	0.9932
P	32	0.051	0.067	0.071	1.625	0.358	3.938	0.9737
Q	19	0.086	0.140	0.146	1.625	0.293	2.466	0.9612
R	32	0.051	0.144	0.146	1.625	0.174	5.116	0.9979
S	56	0.029	0.145	0.146	1.625	0.099	10.066	0.9906
T	12	0.135	0.284	0.292	1.625	0.232	1.881	0.9850

Based on this data, an empirical coefficient of friction for flow through a pleat was formulated. Coefficients of friction are functions of Reynolds number, dimensionless geometric ratios, or both. Reynolds number has a prominent effect on the coefficient only when laminar flow is present. The flow was almost always turbulent for the test conditions encountered; therefore, the K_p coefficient was based solely on geometric configuration.

From the partial solution to the momentum and mechanical energy balanced provided earlier, the pleat coefficient should be related to the function $(1/\beta)^2$. Figure 3.16 is a plot of each experimentally-determined coefficient versus the function. The function does not have a direct correlation to the observed coefficients. In particular, three distinct

trends were observed indicating an additional factor must be included. This discrepancy is to be expected due to simplifying assumptions that were made in order to simultaneously solve the mechanical and momentum balances. A general power law trend was visualized between the function and the pleat coefficient. The dashed lines were functions possessing the generic formula $y=mx^{0.67}$.

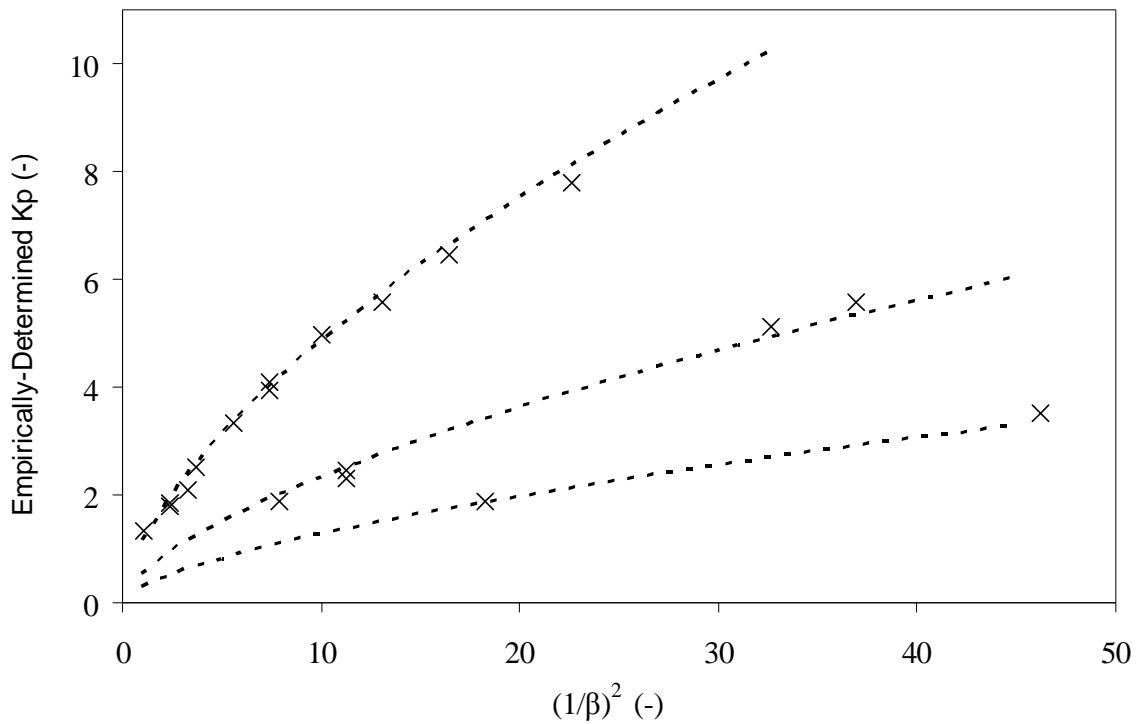


Figure 3.16: Pleat Coefficient Graph

The formula was reduced to contain only the $1/\beta$ term in order to simplify the modeled coefficient. The scaling component Z was chosen to be $4/3$ ($x^2 * x^{0.67} \approx x^{4/3}$) to eliminate the power law fit. For future reference, the function $(1/\beta)^{4/3}$ will be referred to by the Greek letter χ . The plotted data was further refined by indicating the data points that corresponded to 1", 2", and 4" deep filters. Figure 3.17 was the resulting graph.

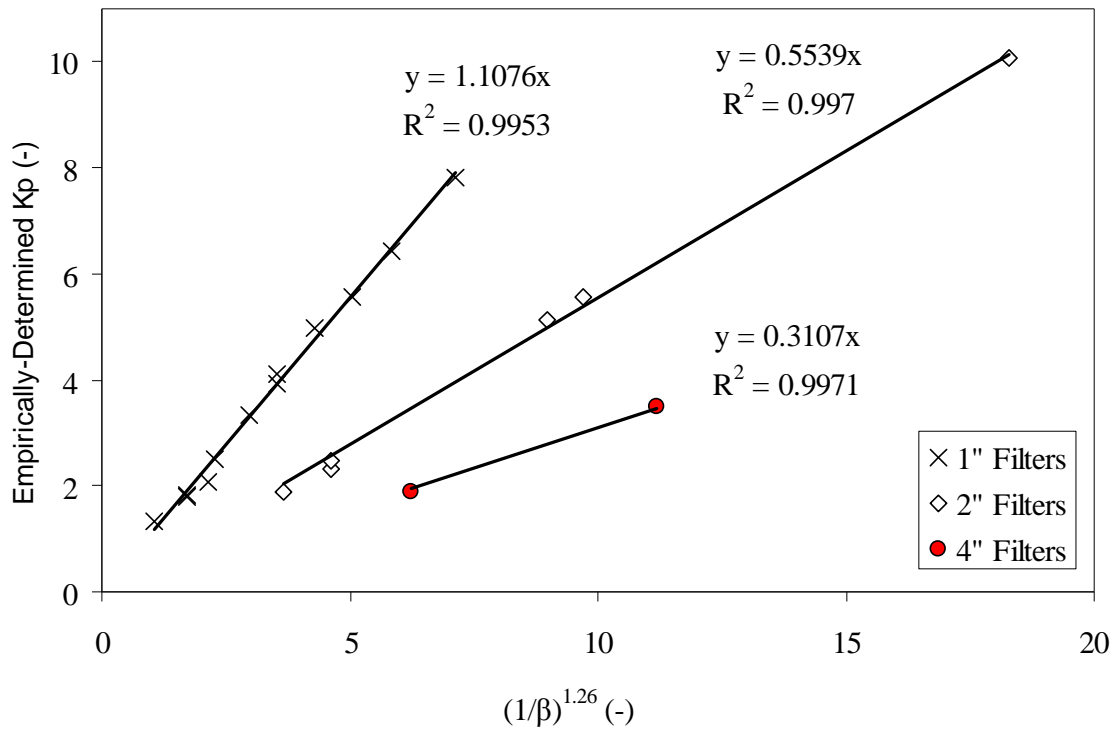


Figure 3.17: A Linear Pleat Coefficient Plot

Figure 3.17 indicates that the depth of the filter is an influential factor in determining the pleat coefficient. Unlike the one inch filters, the pleat coefficients for the two and four inch are greatly overestimated by χ alone. It is hypothesized that χ corresponds to the resistance created by the turn and separation of air in the pleat, but it does not fully account for the area available to make this maneuver. Due to the increased spacing within the two and four inch filters, the air flow is allowed to gradually slow and expand which reduces friction. This in turn leads to a lower pleat coefficient. The pleat coefficient is accurately modeled by adding a dimensionless coefficient η to account for the available area for the pleats to occupy.

$$K_p = \eta\chi \quad (3.4)$$

$$\chi = (1/\beta)^{4/3} \quad (3.5)$$

$$\eta = 0.11(F_{HD}/F_D) \quad (3.6)$$

$$F_{HD} = (2F_H F_D) / (F_H + F_D) \quad (3.7)$$

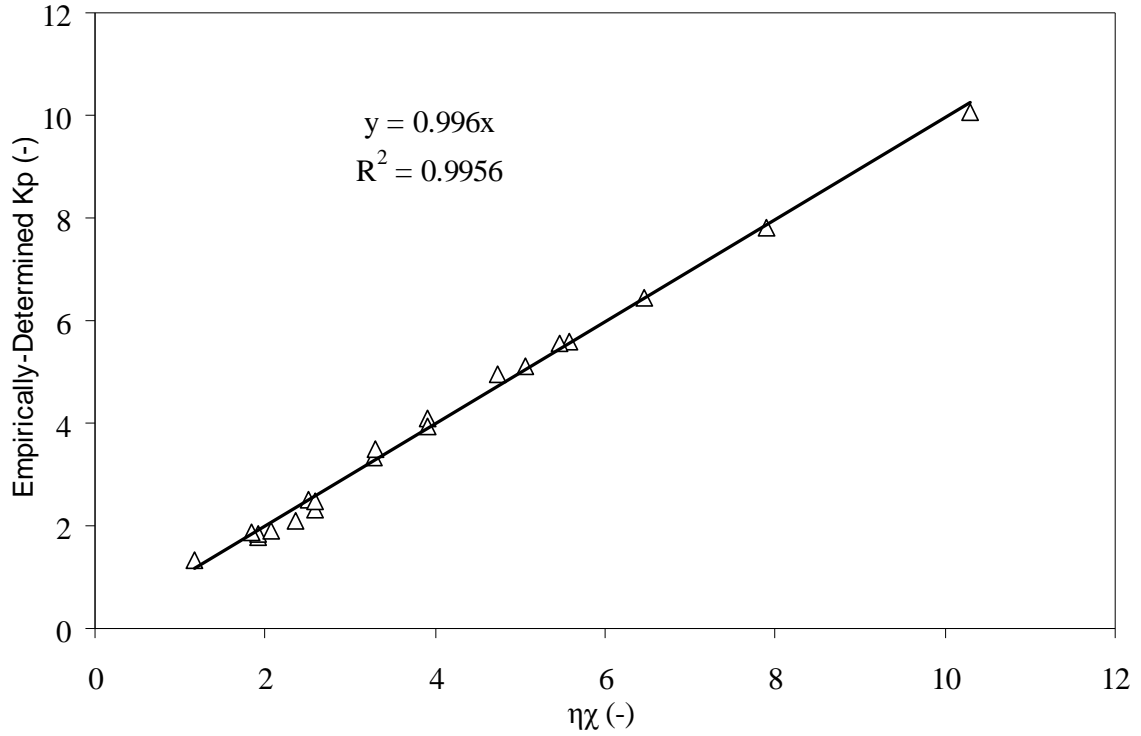


Figure 3.18: Correlation Plot between Empirical and Modeled Pleat Coefficients

III.2.5. Reevaluate the Pleat Tip Contraction and Expansion

The model assumed the contraction and expansion created by the pleat tip was adequately modeled by Equation 2.12 & 2.13. The model and experimental data were reanalyzed while ignoring the pleat tip contribution. Returning to the proposed model (Equation 3.2), exclusion of the pleat tips removes the coefficients K_C and K_E as well as the velocities into the pleats (V_3) and out of the pleats (V_5). The reformulated model can be written as:

$$\Delta P_T = \frac{1}{2} \rho [(2K_G + K_P)V_2^2] + AV_3 + BV_3^2 \quad (3.8)$$

Using same method as described in Section D, the model was rearranged into a linear form and the pleat coefficient of friction was empirically-determined for a given filter based on experimental resistance data. The most accurate coefficient of friction formula was determined to be:

$$K_p = 0.07903(F_{HD}/F_D)(1/\beta)^{1.29} \quad (3.9)$$

The following graph shows the results between the empirically-determined and modeled pleat coefficients.

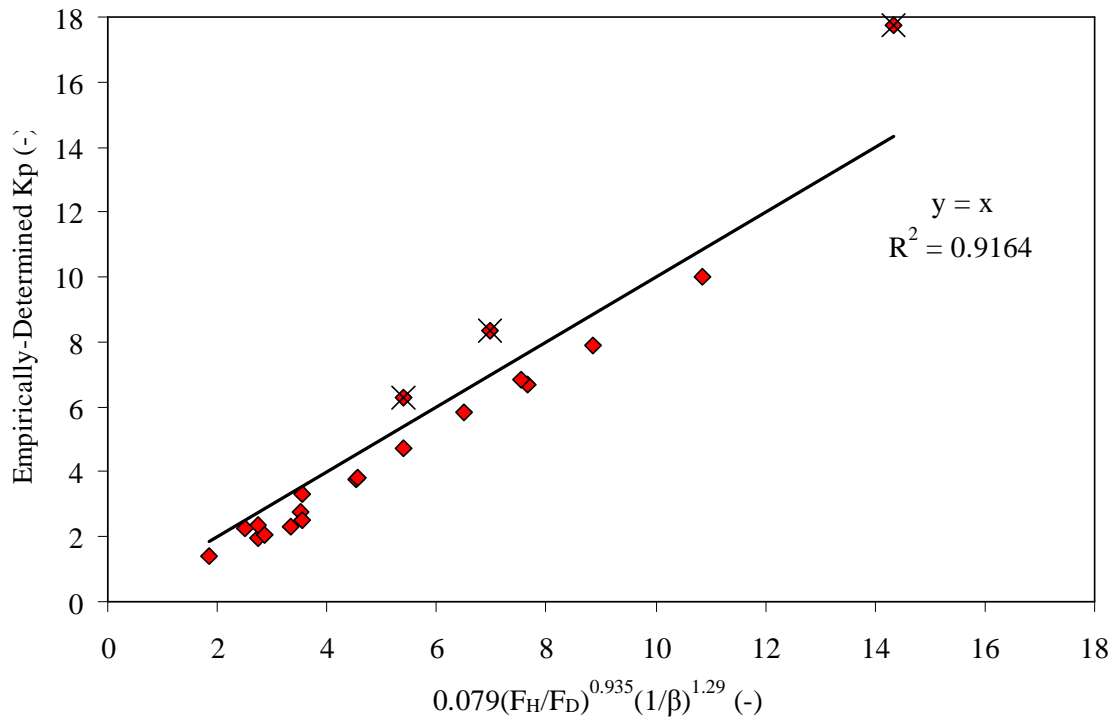


Figure 3.19: Modified Correlation Plot

The pleat coefficient could not be properly fitted after the pleat tips were excluded. A telling aspect was found in the three points denoted with an “X”. These three markers showed the largest deviation from the model. These markers correspond to filters type P, R, and S (going left to right on the graph). These filters possessed the largest pleat tip blockage. Filters P and R were built with the thicker FM3 media and had a pleat count of 32. Filter S used the 1 mm thick FM5 media with 56 pleats. Since the effects of the pleat tip were being adsorbed into the pleat coefficient, it was natural to observe a higher than average pleat coefficients in filters with a larger pleat tip blockage.

This result furthered strengthened the assumption that pleat tips play an active role in the pressure drop.

During the subsequent research presented in Chapter V through VII, the channel of particulate matter around the pleat tip can be visualized when a filter is subjected to dust loading. This indicates that the air flow is diverging around the material and not passing through the tip. The Appendix showcases the occurrence of the channeling through a series of photographs.

III.3. Utilization and Discussion of the Model

III.3.1. Pleating Curve

A conventional pleating “U” curve was generated by modeling the 20”x20”x1” filters with FM1 media constants. The graph, Figure 3.20, was calculated by holding velocity constant at 500 fpm and varying the pleat count from twelve to sixty pleats per filter. The model predictions were plotted as lines while the circles represent the observed total pressure drop for filter types C through K. The modeled resistances due to the pleat contraction and expansion were left off the graph for clarity because their contribution was very small (< 0.002 ” H₂O). The observed pressure losses were fitted with error bars signaling plus or minus five percent of their value. The total modeled resistance fell within the error bars of the experimental data.

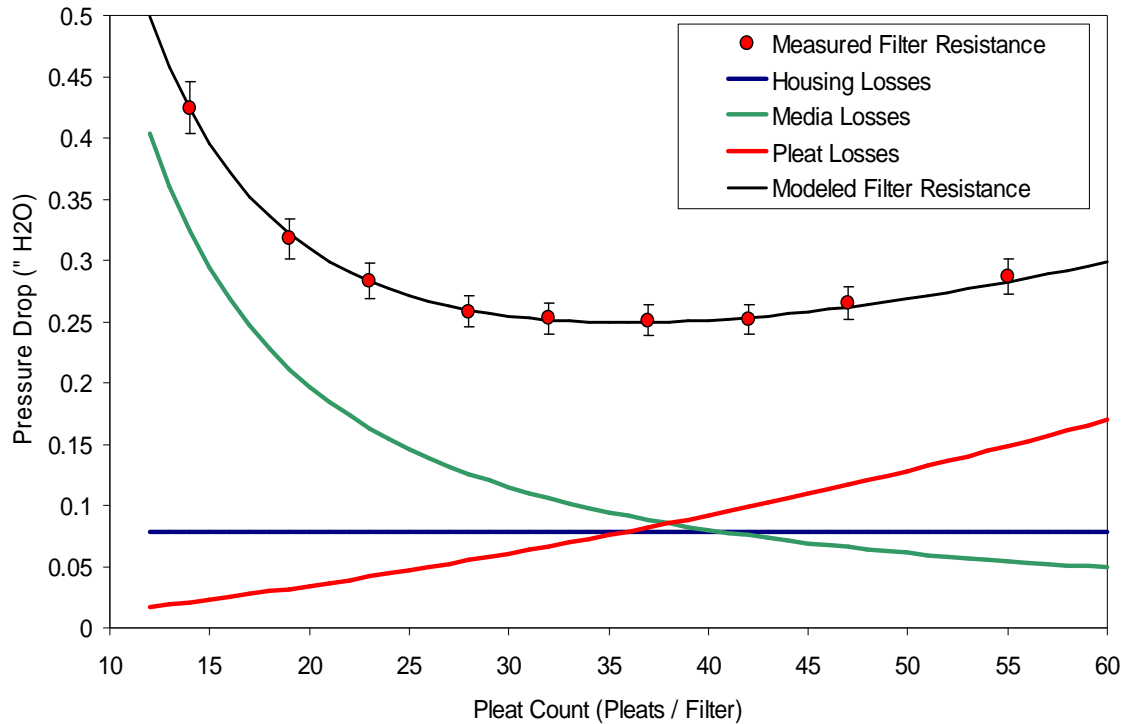


Figure 3.20: Pleating Curve and Individual Resistances

The modeling results of Figure 3.20 confirm previously published general trends regarding pleated filters. The resistance versus pleat count graph clearly indicates a lowest obtainable resistance (LOR) corresponds to an optimal pleat count. The LOR occurred due to the tradeoff of media resistances for viscous resistances as the pleat count was increased. The graph also partly corroborated with Chen's assertion that pleat tip blockage could be ignored; however, FM1 was a thin media (~ 0.5mm) and the same claim can not be made for all media types.

A novel feature of the model is the inclusion of a distinct term for the housing losses. Previous research usually ignores the housing effects or their influence is masked because they are simply combined in with the geometric losses. This has a two-fold disadvantage from a filter design perspective. First, the housing resistance is wrongfully attributed to other geometric design parameters such as pleat height or pleat pitch. This

artificially augments the actual influence of these geometric parameters leading to errors in design estimates. Second, the nature of the housing resistance acts in a different manner than the other geometric losses. The structural pressure drop serves as a fixed resistance and does not change with pleat count. All other geometric resistances increase with pleat count. A small increase due to the incorporation of the grating losses into the geometric resistances becomes further skewed as pleat count rises. By identifying and separating the grating contribution, the model provides a better understanding of the individual resistances allowing enhanced analysis, improved design, and increased performance.

The model also identifies various design strategies that could minimize material costs, minimize energy consumption, or maximize a filter's useful life while maintaining an acceptable initial pressure drop. Figure 3.20 indicates the presence of a semi-flat valley between 27 and 47 pleats where these design goals can be exploited. The initial pressure drop hovers around the acceptable starting resistance of 0.25" H₂O in this valley. At the low pleat count end, a filter with 27 pleats can be constructed that will perform at an adequate pressure drop without incurring a higher production cost due to increased material costs. This is the traditional design point of most filter manufacturers. A more energy efficient filter can be constructed by increasing pleat count to the LOR of 36 pleats. By increasing the pleat count further, the high end count of the valley offers the largest filtration area that can be incorporated into the filter without sufficiently increasing the initial pressure drop. The ability to locate and work within this valley demonstrates the utility of an accurate pressure drop model to a filter designer.

III.3.2. Location of the Optimal Pleat Count

Although it can be used as a general heuristic, the optimal pleat count does not simply exist where the media and geometric resistances are equal. The optimal pleat count in Figure 3.20 is 36 pleats, yet the media and pleat resistances are equal at 38 pleats. The lowest obtainable resistance and the optimal pleat count occur when the total pressure drop's rate of change with respect to pleat count is zero. Since Equation 3.2 is composed of polynomials, the model can be broken down into individual terms and the first derivative with respect to pleat count can be readily computed.

1st Derivative:

$$\frac{\partial \Delta P_F}{\partial P_C} = \frac{\partial(\rho K_G V_1^2)}{\partial P_C} + \frac{\partial(\frac{1}{2} \rho K_C V_3^2)}{\partial P_C} + \frac{\partial(\frac{1}{2} \rho K_E V_3^2)}{\partial P_C} + \frac{\partial(\frac{1}{2} \rho K_P V_3^2)}{\partial P_C} + \frac{\partial(AV_4)}{\partial P_C} + \frac{\partial(BV_4^2)}{\partial P_C}$$

(3.10)

$$\frac{\partial \Delta P_T}{\partial P_C} = \text{Term 1} + \text{Term 2} + \text{Term 3} + \text{Term 4} + \text{Term 5} + \text{Term 6}$$

The grating contribution's (Term 1) first derivative is zero because it is not a function of pleat count. The first derivative of the viscous/geometric effects (Terms 2, 3, and 4) are always positive while the media resistances (Terms 5 and 6) have continuously negative first derivatives with respect to pleat count. Since the left hand side of Equation 3.10 equals zero at the optimal pleat count, it can be rearranged to give Equation 3.11. Equation 3.11 and Figure 3.21 clearly indicates the balance between viscous and media-dominated resistances.

$$\left[\frac{1}{2} \rho \frac{\partial(\rho K_C V_3^2 + K_E V_3^2 + K_P V_3^2)}{\partial P_C} \right] = \frac{\partial(AV_4 + BV_4^2)}{\partial P_C} \quad (3.11)$$

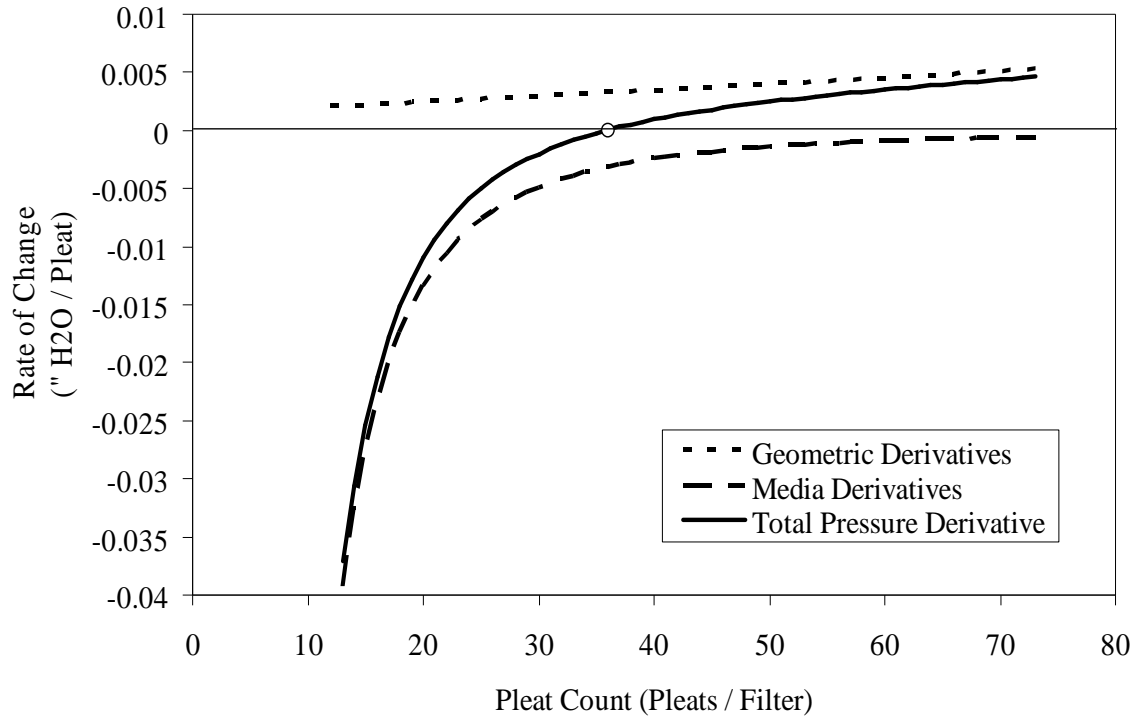


Figure 3.21: Optimal Pleat Count Location

III.3.3. Influence of Design Parameters

The model has established the ability to accurately portray the cause and effect relationship of adding more pleats to a filter design. It can also be used to calculate the optimal pleat count and determine the magnitude of the viscous and media derivatives. Pleat count, however, is just one of the many design factors that can be manipulated in a filter. Previous models identified the following design variables within a pleated filter: pleat count, face velocity, filter height, filter width, filter depth, fluid density, fluid viscosity, solid volume fraction, media thickness, fiber radius, Knudsen number, media permeability, and dirt loading. In this section, the model will be employed to investigate the influence of face velocity, filter depth, media thickness, and media constants. The remaining variables were not directly examined due to reasons described below.

Solid volume fraction, fiber radius, Knudsen number, and media permeability were lumped together as general media constants in this research. The individual effects of each variable can be related to the empirical constants through theoretical equations such as the Carmen-Kozeny (Rivers and Murphy 2000) or the porous media permeability (PMP) equation (Cahela and Tatarchuk 2001). By studying the response of the generic media constants, one can deduce the effects these parameters would have on the overall performance.

The influence of density and viscosity can also be readily factored in, but their effects were not analyzed in this study. A change in these fluid properties has an identical influence on both the viscous and media terms, and thus shifts the whole “U” curve up or down. Furthermore, it would be more beneficial to study the effect of temperature on performance since density and viscosity are dependent on the temperature of the fluid. Although this was not explored either, a general assessment would be a rise in temperature will result in a decrease in air density and as thus a decrease in the overall flow resistance of a filtration system. This observation was previously made in *Filters and Filtration Handbook* (Dickenson 1992). The model could also theoretically be utilized to study pleated filters in other filtration projects with different fluids such as water or oils. Last, the effect of dirt loading will be discussed in Chapters 5 through 7.

1. Effects of Face Velocity

Face velocity universally influences both the viscous and media terms much like air density and viscosity. Unlike the fluid properties, face velocity is an operational condition that is more readily controlled by the system user. HVAC systems primarily run at a set velocity of 300 fpm for residential homes or 500 fpm for commercial

buildings, but other applications that utilize pleated filter operate at different ranges. Cathode air filters, for example, typically run at 0 to 200 fpm depending on the fuel cell power output. It is intuitive from Equation 2.1 that increasing the face velocity will result in a higher resistance; however, the general impacts of face velocity on the pleating curve have not previously been reported.

The effects of face velocity were study by modeling a 20"x20"x1" FM1 media filter as air speeds rose from 100 fpm up to 700 fpm. At low face velocities, the curve resembles more of a line than the traditional "U" shape. The curve gains its distinctive profile by increasing face velocity that in turn heightens both viscous and media effects. The optimal pleat count is shifted to a lower pleat count because the viscous terms are second order functions of velocity; thus, they are able to overtake the media effects in a lower pleat count regime.

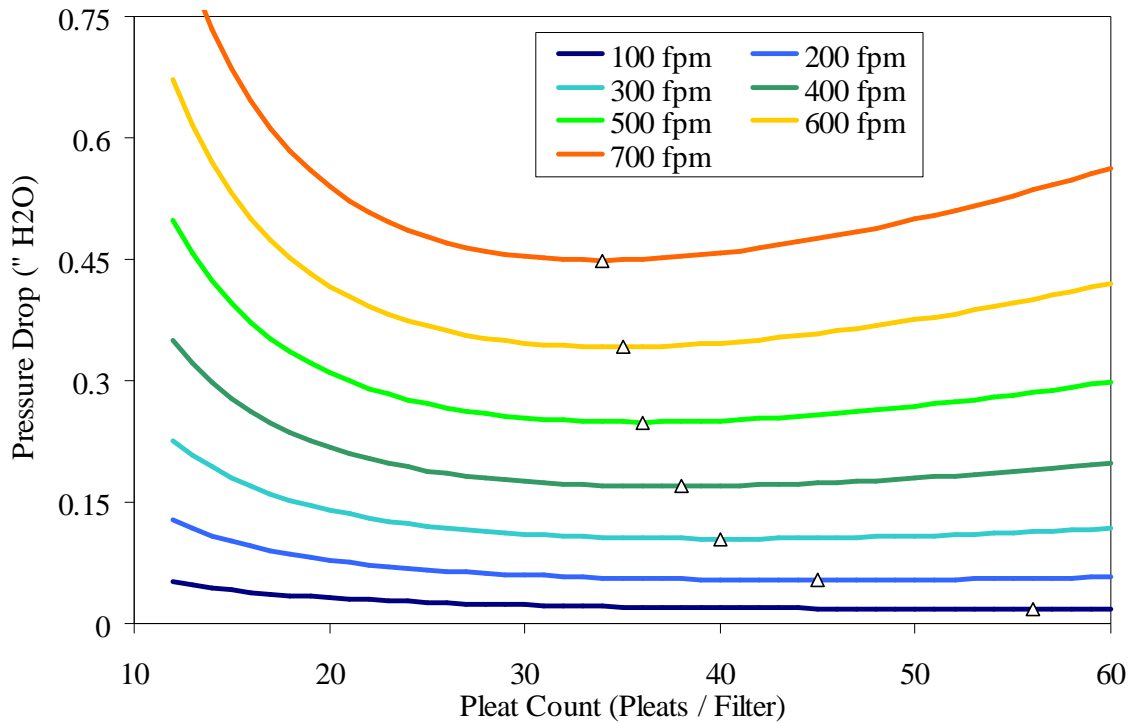


Figure 3.22: Effects of Face Velocity on Pleating Curve

Common blowers typically operate at set face velocity, but energy efficient variable air volume (VAV) HVAC systems will cycle between 100 and 700 fpm throughout the course of the day. In a similar fashion, compressors on fuel cells will ramp up and down based on the required power load. Since the optimal pleat count varies with face velocity, the model can be used as a design tool to construct a filter with a pleat count corresponding to the lowest energy cost over the course of the operation.

2. Effects of Media Thickness

To examine the effects of various media thicknesses on the pressure drop behavior of a pleated filter, individual pleating curves were generated for various thicknesses between 0.5 and 3.5 mm while holding the other design parameters constants. The model makes predictions based on a set flow rate (500 fpm), pleat length (2"

nominal), and fixed resistance through the media. A fixed resistance means the overall resistance for flow across the media is constant. Idealistically, this occurs when an increase in thickness is counteracted by increase in permeability to maintain a set pressure drop across the media according to Darcy's Law. A fixed resistance can simply be modeled by keeping the media constants steady ($A=10 \times 10^{-4}$ and $B=17.5 \times 10^{-7}$) since Darcy's Law is not utilized. Modeling a fixed resistance system allows the individual effect of media thickness to be discerned without observing additional phenomena. The "Δ" marks the optimal pleat count for each plot.

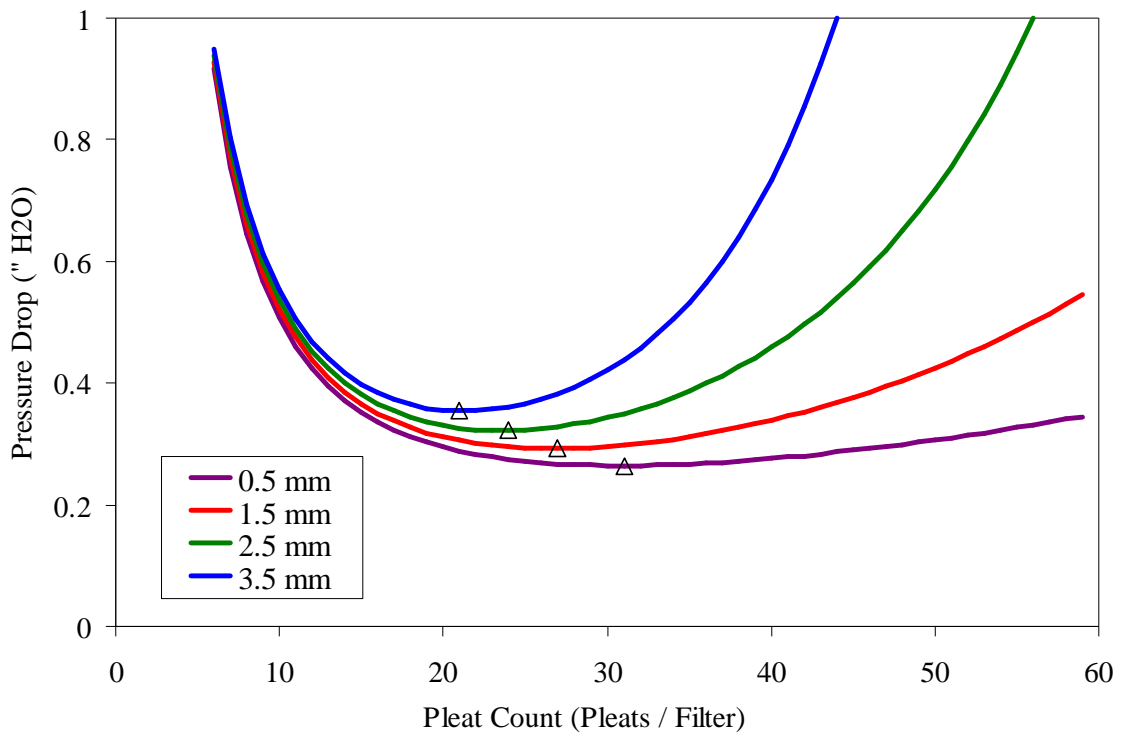


Figure 3.23: Effects of Media Thickness on Pleating Curve

An increased media thickness steepens the viscous-regime and raises the overall resistance of the U curve due to a two-prong effect. The obvious reason for the shift is a thicker media creates a larger pleat tip blockages and higher resistances. The more

influential effect, however, is a heightened rate of closure for the pleat opening. A thicker media occupies more space within a filter and allows fewer pleats to be placed into a filter before the pleat openings become constrained. The synergy of these two influences sizably increases the magnitude of the geometric terms leading to the sharp rise in the viscous-dominated region. This causes the optimal pleat count to occur at a much lower available media. Since optimal pleating occurs at a lower count, the filter can not amass a sufficient filtration area to decrease the media velocity. The corresponding heighten pressure drop through the media causes the overall resistance to remain high.

The leftward shift of the optimal pleat count and the overall increase in the lowest obtainable pressure drop can be visualized by studying the derivatives of Figure 3.23. Figure 3.24 shows the sizable increase of the viscous derivatives as thicker media is employed. Only one media derivative is presented because media thickness barely affects the media terms. A slightly change in the media terms does occur from the increased media area consumed to make the thicker pleat tips, but this negligible effect can be seen by the convergence of each plot's media-dominated section in Figure 3.23.

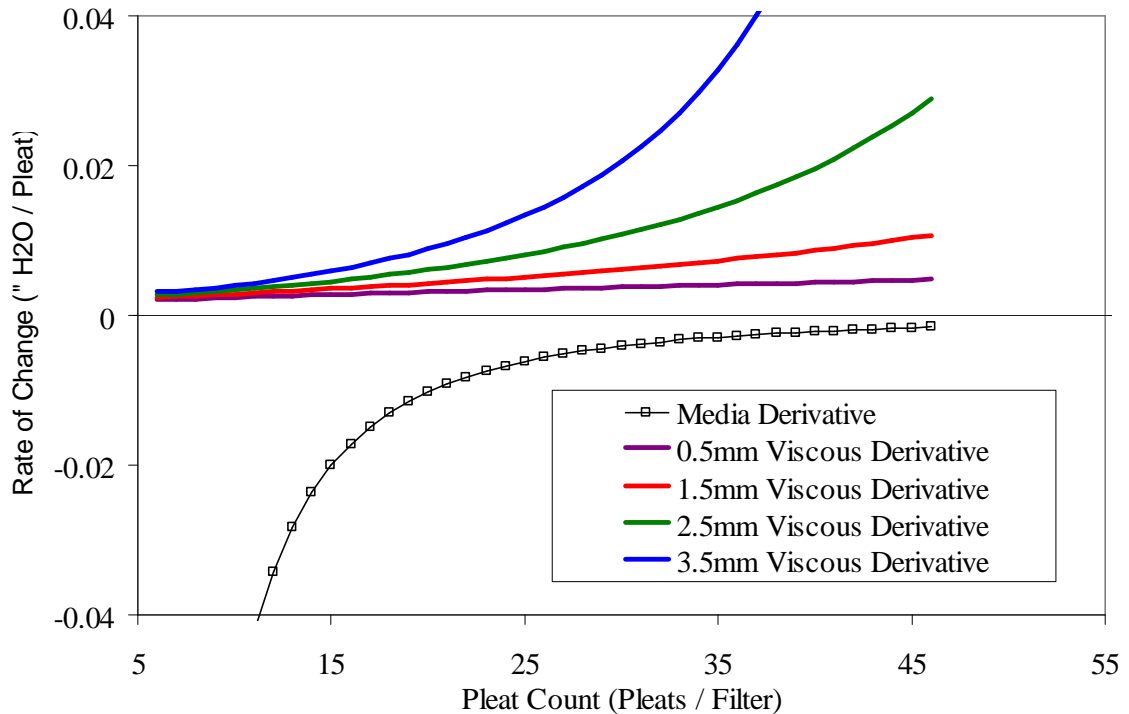


Figure 3.24: Effects of Media Thickness on Model's Derivatives

Several of the previous published studies neglect the effects of pleat tip blockage into and out of the pleats. Chen et al. (1996) states that the flow resistance due to the media tips can be ignored in triangular pleat systems. This assumption holds approximately true for a thin media. The pleat tip blockage for a 0.5 mm thick media never accounts for more than two-thirds of a percent of the total pressure loss (Figure 3.25). The same can not be said for a thicker media. A filter composed of 3.5 mm thick media will accrue roughly ten percent of its total pressure drop from entering and exiting the pleat tips. Figure 3.25 is compiled from data generated while modeling Figure 3.23.

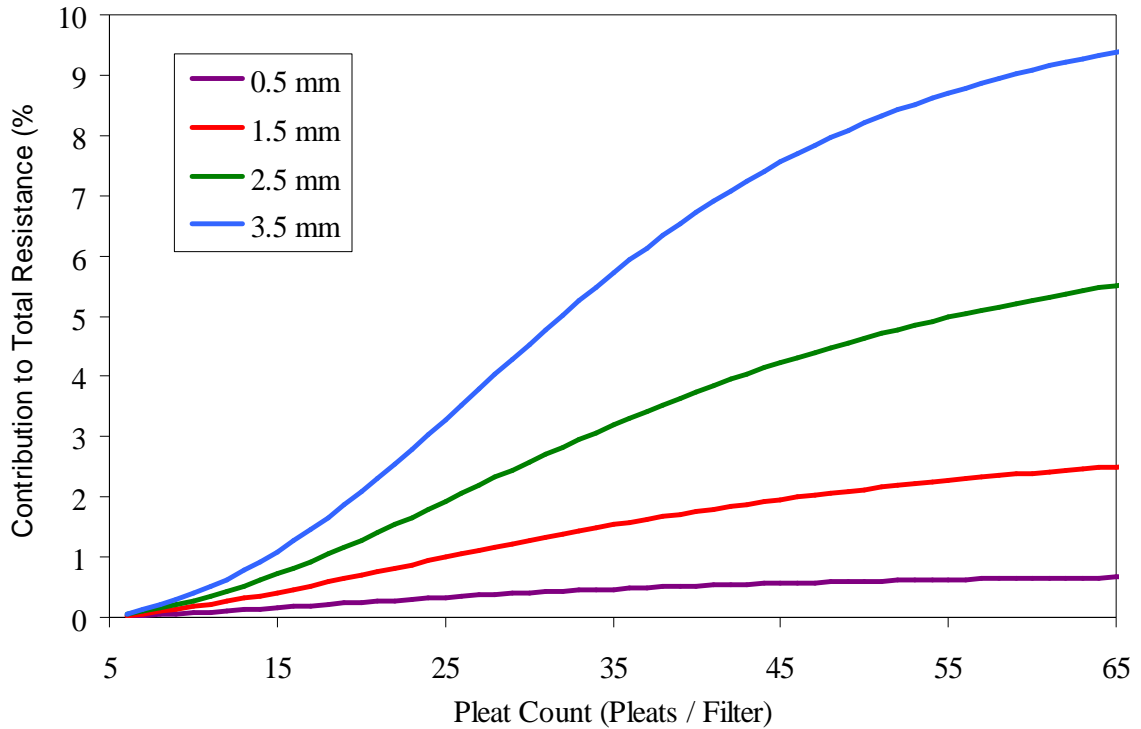


Figure 3.25: Modeled Pleat Tip Contribution to Total Resistance
20"x20"x1" Filters at 500 fpm

3. Effects of Filter Depth

The model was employed to study the effects created by varying the filter depth while holding constant the flow rate (500 fpm), media constants ($A = 10 \times 10^{-4}$; $B = 17.5 \times 10^{-7}$), and media thickness (0.5 mm). Increasing filter depths directly translates to increasing pleat length. The results presented in Figure 3.26 indicate that increasing filter depth decreases the optimal pleat count and lowest obtainable resistance. This observation was previously made in Chen's research.

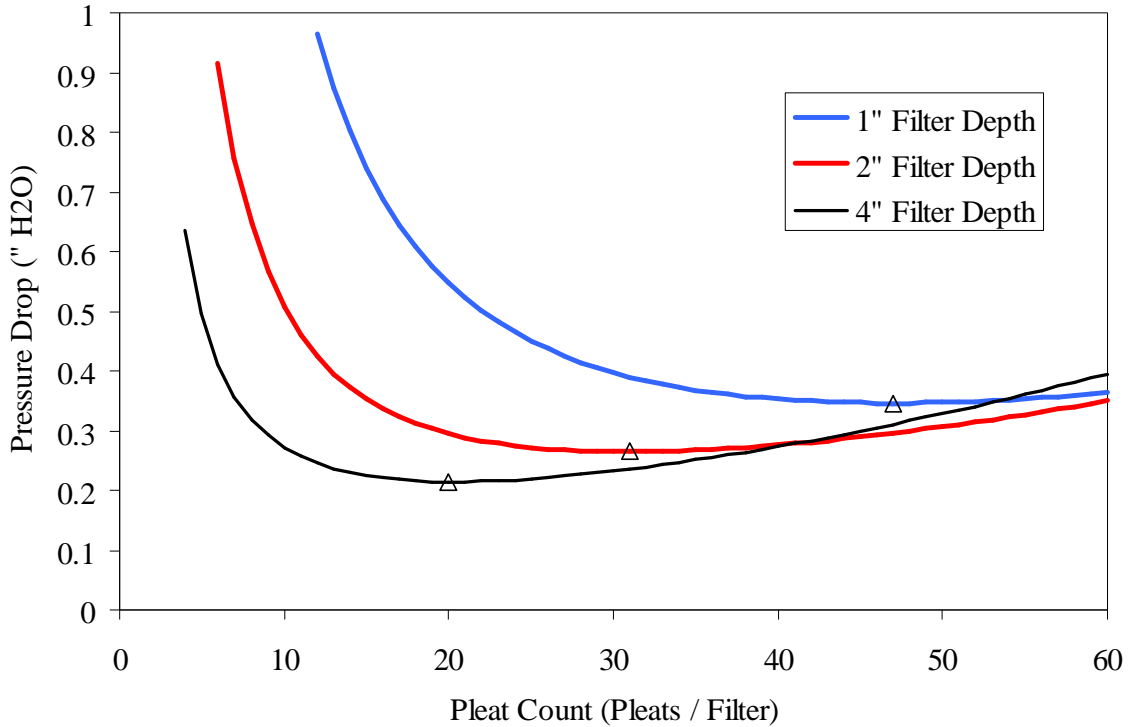


Figure 3.26: Modeled Effects of Filter Depth on Pleating Curve

A variation of filter depth impacts both the media and the viscosity terms. The additional pleat length increases the available filtration area and quickly removes the influence of the media term at a low pleat count. This leads to a decreased LOR because the viscous terms' magnitudes are relatively small at the low pleat counts. As pleat count rises, the growth of pleat resistance in deeper filters outpaces the shallower filters due to heighten friction. This contributes to the steeper pressure rise in the viscosity-dominated region.

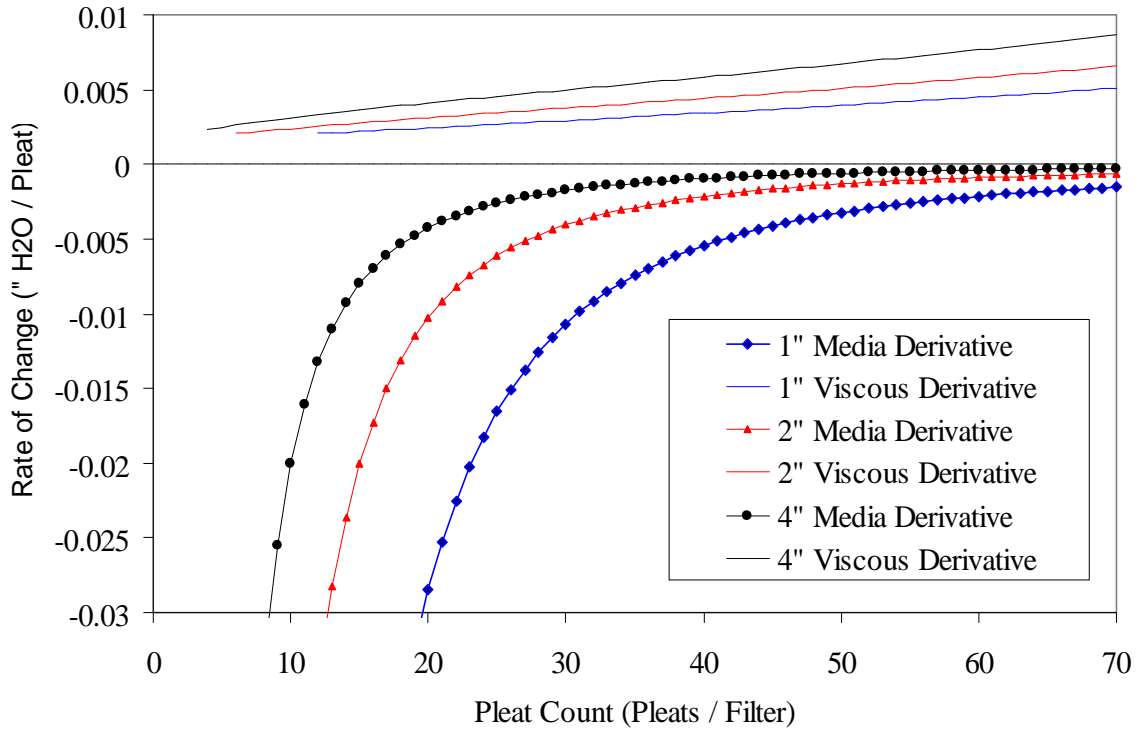


Figure 3.27: Effects of Filter Depth on Model Derivatives

Although the influences of filter design variables on total pressure drop are conventionally plotted versus pleat count, it is beneficial to compare resistances versus available filtration area when dealing with variations in filter depth. The real design issue centers not on the number of pleats that can be incorporated into a filter but on the available filtration area of the filter. Pleat count usually directly translated to available filtration area, but this is not true in filters of different depths. The same pleat count in a 4" deep filter translates to four times the area of its 1" counterpart.

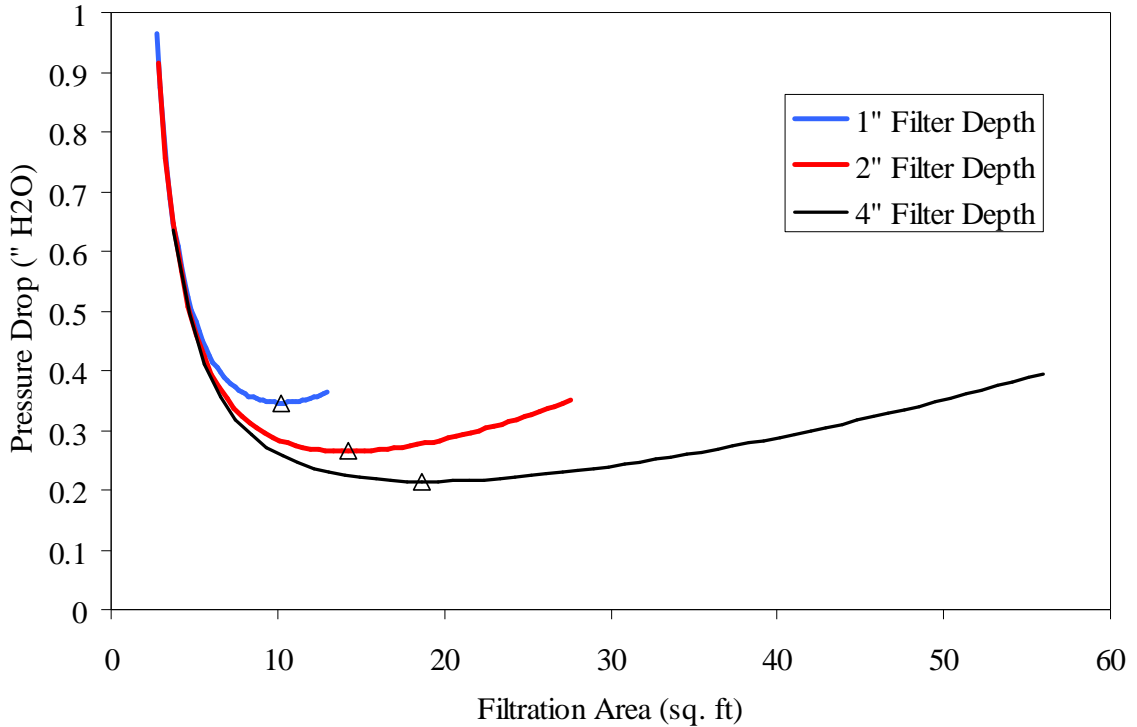


Figure 3.28: Effects of Filter Depth on Performance Curve

As seen in Figure 3.28, increasing filter depth reduces total pressure drop while greatly increasing the available filtration area. The previous plot is misleading in the fact that it appears that a 1" and 2" filter, given the right number of pleats, can operate at a lower resistance than a 4" filter. The 4" filter is clearly able to operate at a lower pressure drop over the entire range of available media area.

4. Effects of Media Constants

Figure 3.29 was generated by varying the media constants at a fixed flow rate (500 fpm), media thickness (0.0032 ft [1 mm]), and pleat length (1.75 inches nominal) while increasing pleat count. The "Δ" marks the optimal pleat count.

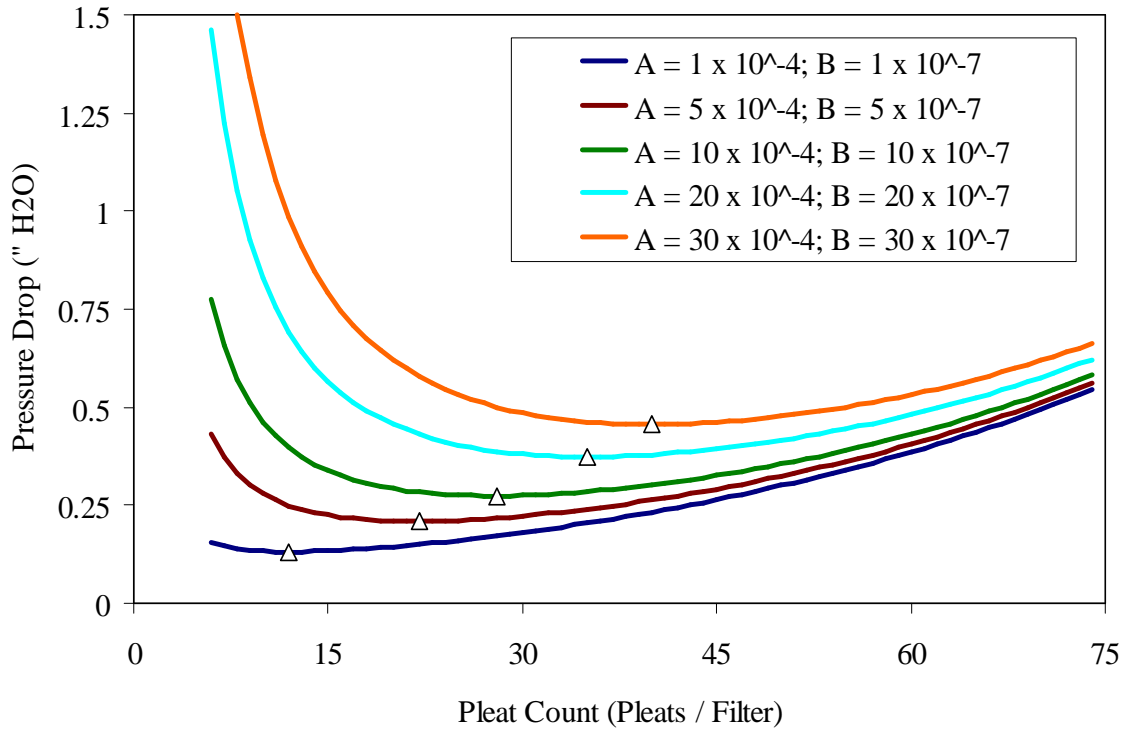


Figure 3.29: Effects of Media Resistance on Pleating Curve

Figure 3.29 indicates that an increase in the media constants results in a higher optimal pleat count and higher optimal resistance. A change in the media resistance solely influences the media term and has no bearing on the filter's viscous terms unlike media thickness, face velocity, and pleat length. The media term's derivative is therefore greatly increased while the viscous term remains the same (Figure 3.30). The optimal pleating arrangement must be shifted right to allow room for the magnitude of the viscosity's derivative to counteract the increase in the media derivative. Even though this shift increases the available filtration space, it still does not provide sufficient area to reduce the media velocity and the overall media resistance. The result is an increase in optimal resistance. It should be noted that the plots begin to converge in the viscosity-

dominated region. This is expected because the media term eventually approaches zero as pleat count increases; thus, eliminating the effects of media resistance from the plots.

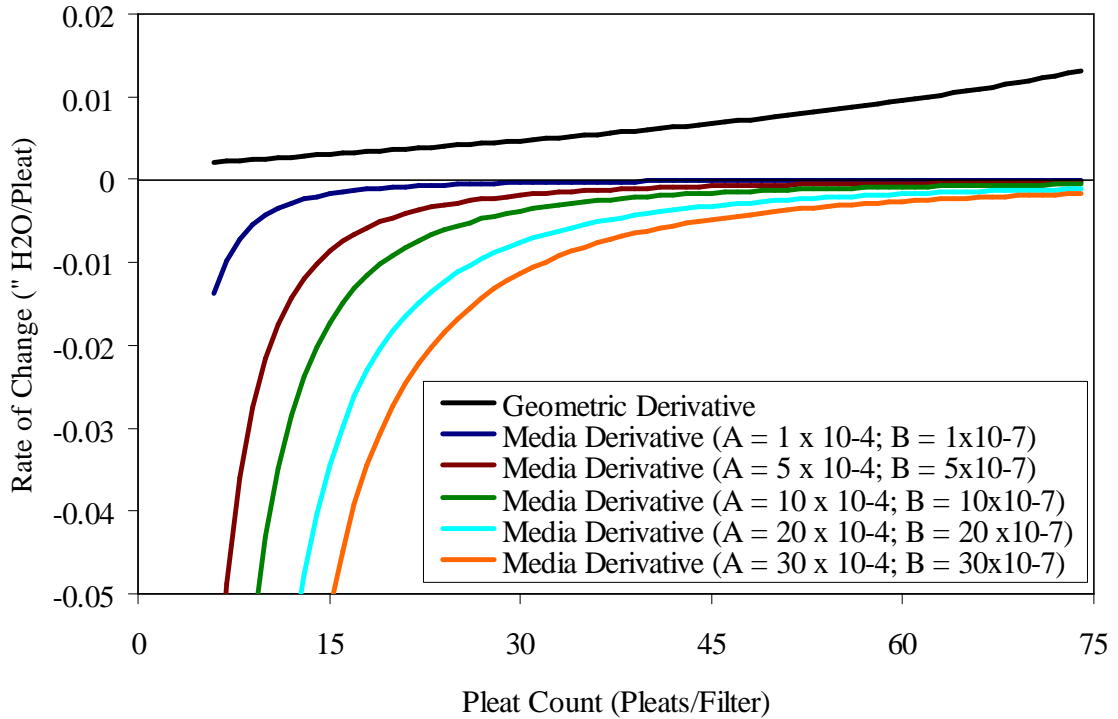


Figure 3.30: Effects of Media Resistance on Model's Derivatives

An interesting media design paradox occurs between media permeability and media thickness. A decrease in media thickness leads to a smaller LOR as shown in the media thickness section. In order to create a thinner media, the material must be compressed. Compression leads to a decrease in media permeability and an increase in the media constants. An increase in media constants results in a rise in the LOR. Thus, it is uncertain if compressing the media will lead to an overall reduction or increase in the lowest obtainable resistance. Future research will be performed to study the impact of media compression on media constants.

III.3.4. Limitations of the Model

Although constructed over a wide range of parameter space, it should be noted that there are limitations to the accuracy of the model as a design tool. The pleat coefficient is based on experimental data obtained for 20" x 20" face dimensions. The model, in theory, should be applicable to other filter dimensions but additional research needs to be conducted. Filter with depths greater than four inches were not studied. Only general estimations of viscous effects created by filters with depths greater than four inches can be made based on observed trends. The same statement can be said about pleat counts above 60 per filter and media thickness above 2 mm. The experimental data upon which the research was based did not explore face velocities above 1000 fpm, yet HVAC filters do not typically operate above 500 fpm so this is only a minor limitation.

CHAPTER IV: INITIAL PRESSURE DROP OF MULTI-ELEMENT STRUCTURED ARRAYS

IV.1. Introduction

Multi-Element Structured Arrays (MESA's) are a novel platform that integrates multiple pleated filter elements into a single filtration system. The MESA's concept is an extension of the pleated filter design. A pleated filter extends the media area and reduces the resistance by transforming a flat material into a three dimensional filter. The MESA takes a flat, pleated filter and turns it into a three dimensional array of filters to further extend the filtration area and reduce the pressure drop. The idea is a derivation of the common V-Bank filtration systems utilized to house mini-pleat filtration media. Unlike V-Banks, MESA's use off-the-shelf filter element that can be inserted into the array's framework.

IV.1.1. Multi-Element Structured Array Schematic

Figure 4.1 showcases the major dimensions and parameters of a Multi-Element Structured Array. All parameters associated with a single filter remain unchanged. A triangular "slot" is created when the filters are angled into place. The slot's dimensions depend on the number of elements used. A general schematic of a two element array is shown below, but the same nomenclature can be applied to arrays with additional elements. Included in Figure 4.1 is a photograph of two elements loaded into a clear, polycarbonate filter box.

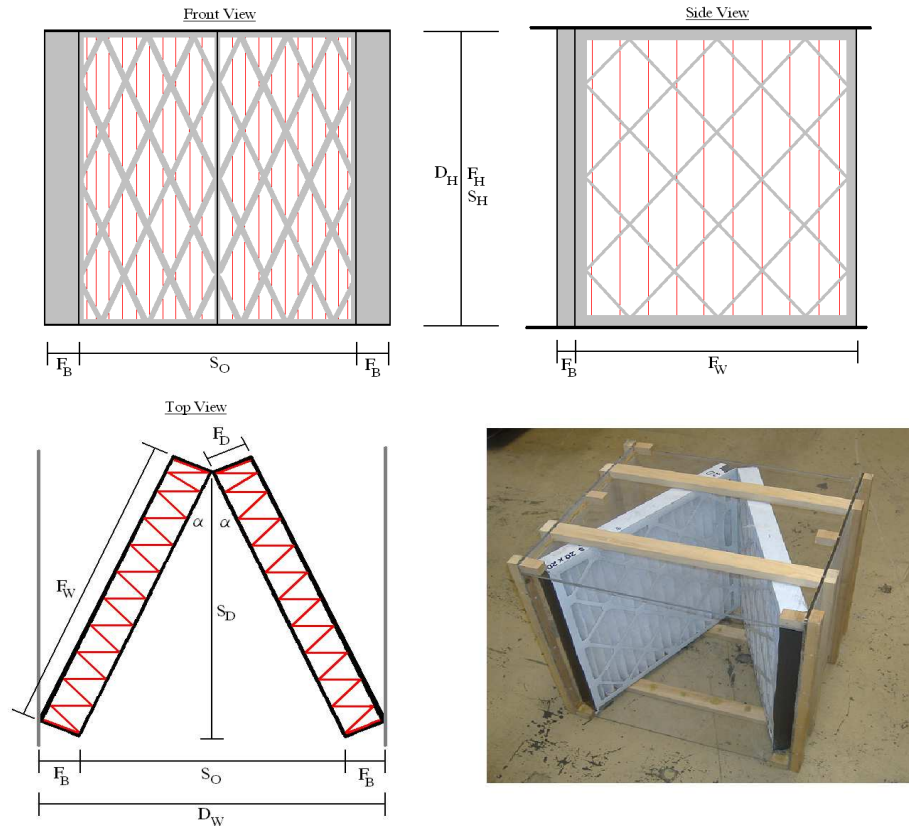


Figure 4.1: General Schematic of a Multi-Element Structured Array

The schematic above depicts a filter box loaded with two 20"x20"x2" filter elements. An array constructed with two filters will be referred to as possessing a "V" configuration. Three additional array configurations were utilized in this chapter. For future reference, arrays configurations will be designated based on their appearance as illustrated in Figure 4.2.

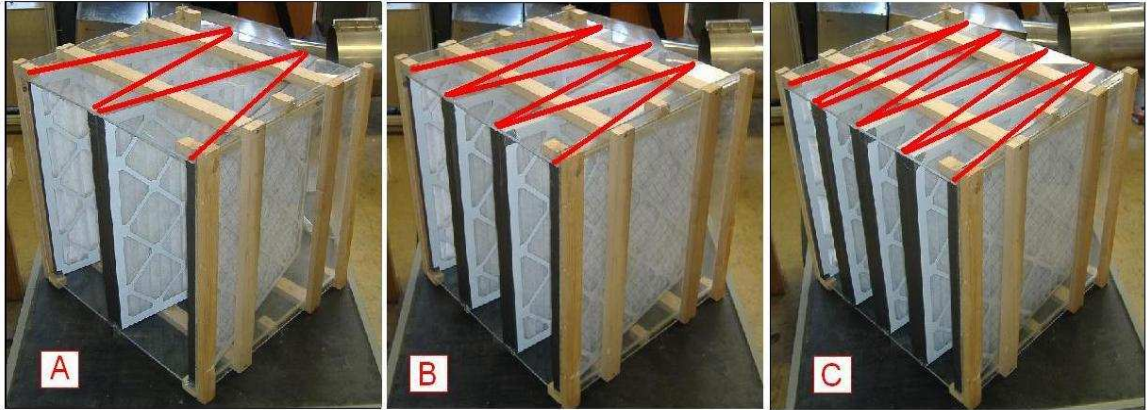


Figure 4.2: Array Configurations (A) “W” (B) “WV” Configuration (C) “WW”

IV.1.2. Parameters

The system parameters of a Multi-Element Structured Array are specified by the user’s needs or dictated by the ductwork. The pleat parameters are calculated in the same manner outlined in Chapter 3. The slot parameters are functions of the system parameters and can be solved by a system of equations.

System Parameters

Filter Height (F_H):	Dictated by the Duct Height
Pleat Height (P_H):	Dictated by the Duct Height
Filter Width (F_W):	Dictated by the User
Slot Height (S_H):	Dictated by the User (equal to Filter Width)
Filter Depth (F_D):	Specified by the User
Pleat Length (P_L):	Specified by the User (equal to Filter Depth)
Pleat Count:	Specified by the User
Grating Blockage:	Specified by the User
Media Thickness (M_T):	Specified by the User (Property of Media)
Permeability (A & B):	Specified by the User (Property of Media)
Element Count (E_C)	Specified by the User

Slot Parameters

Edge Blockage (F_B)	Solved by System of Equation
Slot Pitch [α]	Solved by System of Equation
Slot Opening (S_O)	= Duct Width / # Filters – 2 x Edge Blockage
Slot Depth (S_D)	= $\sin^{-1}(1/2 \text{Slot Opening} / \text{Filter Width})$

Blockage System of Equations

Figure 4.3 is a general V array schematic used to solve the system of equations.

The element count, the duct's dimension, and the depth of each filter element are known.

The remaining dimensions of the array can be simultaneously solved by the following set of equations.

<u>Known:</u>	Duct Width (D_W) Element Count (E_C) Filter Depth (F_D) Filter's Width (F_W)
<u>Computed:</u>	Opening (B_O) = Duct Width / # Filters
<u>Unknown:</u>	Slot Pitch (α) Element Blockage (F_B) Space Variable (F_E)
<u>Three equations:</u>	(I) $\cos(\alpha) = F_B / F_D$ (II) $\cos(1/2\pi - \alpha) = F_B / F_E$ (III) $\sin(\alpha) = 1/2 B_O / (F_W + F_E)$

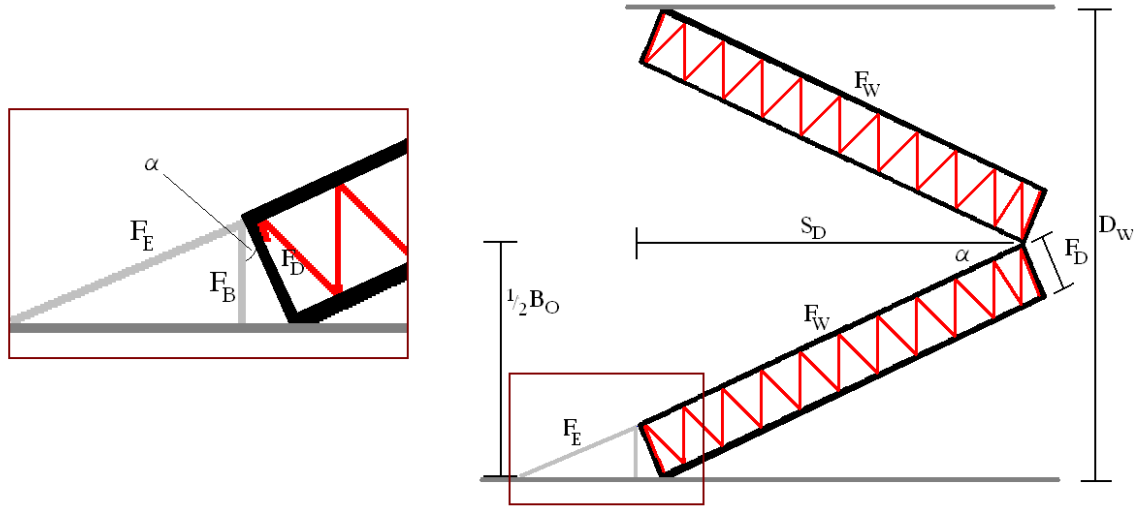


Figure 4.3: General Diagram of Multi-Filter Array

Table 4.1: Blockage (F_B) Tabulations

Element Width	Element Depth	V Array	W Array	WV Array	WW Array
19.5"	1"	0.0628'	0.0693'	0.0703'	0.0706'
19.5"	2"	0.1324'	0.1439'	0.1454'	n/a
19.5"	4"	0.2753'	0.2909'	n/a	n/a
14.5"	1"	0.0552'	0.0680'	0.0698'	0.0704'
9.5"	1"	n/a	0.0639'	0.0685'	0.0698'

Table 4.2: Alpha Tabulations (in radians)

Element Width	Element Depth	V Array	W Array	WV Array	WW Array
19.5"	1"	0.479	0.209	0.124	0.082
19.5"	2"	0.447	0.259	0.169	n/a
19.5"	4"	0.337	0.073	n/a	n/a
14.5"	1"	0.677	0.284	0.167	0.110
9.5"	1"	n/a	0.432	0.162	0.078

IV.1.3. Proposed Flow through a Multi-element structured array

In order to develop the model, a pathway for airflow through the array had to be proposed. The path consisted of eleven areas of varying accessibility for air to flow through a MESA (Figure 4.4). The upstream flow in the duct is assumed uniform. The air velocity increases at the front of the array due to the contraction created by the

element's edges. The air is channeled around the edges and into the array's slot(s). In the slot, the air diverges and expands as it reaches the face of each filter element.

While in the filter element, the air is assumed to flow in an identical path outlined in the single filter flow profile (Chapter III.1.3). The air is contracted due to the filter housing and pleat tip blockage. It then travels down the filter's pleats before entering the media. The air passes through the media and out of the filter element in a reverse manner. The air converges as it exits the elements and enters into the downstream slot. The exit from the array causes a further increase in area and velocity decrease. The air finally uniformly redistributes in the downstream duct.

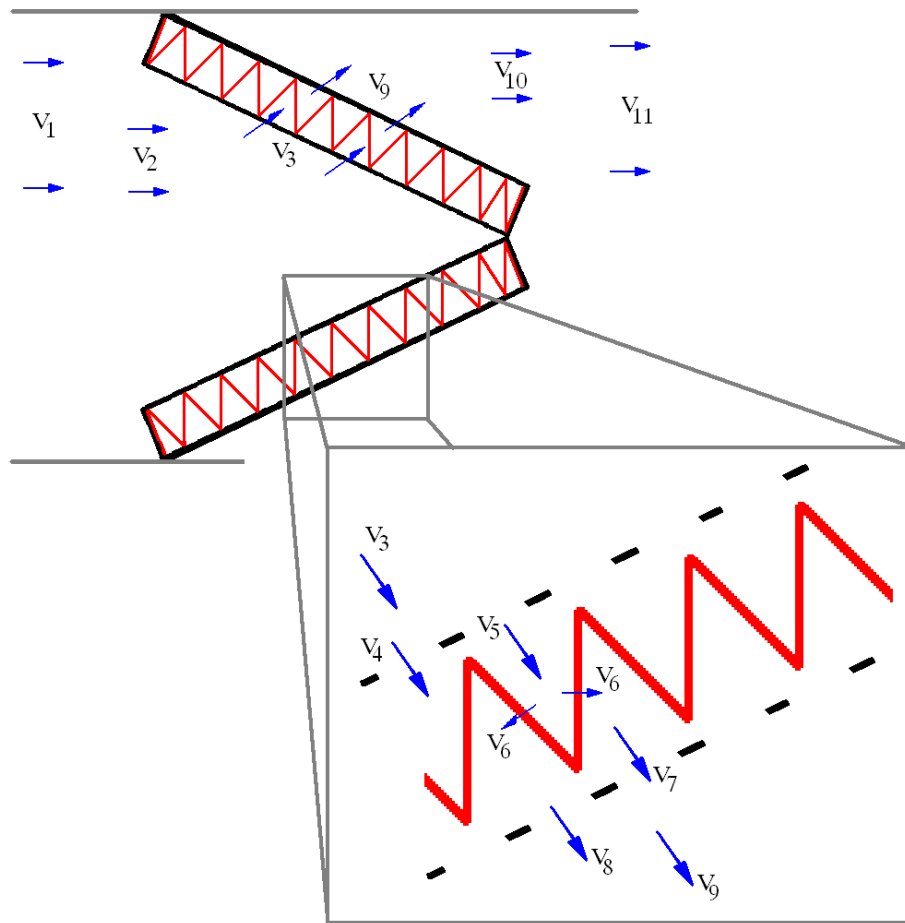


Figure 4.4: Proposed Flow Profile

Area Calculations:

Area 1 (Area 11):

Duct Width x Duct Height

Area 2 (Area 10):

(Duct Width x Duct Height) – (Edge Blockage x Element Height x # Element)

Area 3 (Area 9):

Element Width x Element Height x #Element

Area 4 (Area 8):

[Element Width x Element Height x (1 -% Blockage)] x #Element

Area 5 (Area 7):

[(Element Wid. x Element Ht.) – # Pleat x Pleat Tip x Pleat Height] x # Element

Area 6:

[(Pleat Count x Pleat Height) x (2 Pleat Length – Media Loss)] x # Element

IV.1.4. Modeling a Multi-Element Structured Array

The MESA model was developed as an extension of the single pleated filter model. The total flow resistance through a Multi-Element Structured Array was compiled as a summation of eleven discrete resistances. The individualistic resistances were formulated by applying Bernoulli's equation or Forchheimer-extended Darcy's Law to each of the eleven flow sections.

Flow into Slot:	$\Delta P_1 = \frac{1}{2} \rho [(V_2^2 - V_1^2) + K_{CB} V_2^2]$
Flow from Slot Inlet to Filter Face:	$\Delta P_2 = \frac{1}{2} \rho [(V_3^2 - V_2^2) + K_{S1} V_3^2]$
Across Front Grating:	$\Delta P_3 = \frac{1}{2} \rho [(V_4^2 - V_3^2) + K_G V_3^2]$
Flow from Grating to Pleat Inlet:	$\Delta P_4 = \frac{1}{2} \rho [(V_5^2 - V_4^2) + K_{CP} V_5^2]$
Flow from Pleat Inlet to Media Surface:	$\Delta P_5 = \frac{1}{2} \rho [(V_6^2 - V_5^2) + K_{P1} V_5^2]$
Flow through Media:	$\Delta P_6 = A V_6 + B V_6^2$
Flow from Media Surface to Pleat Outlet:	$\Delta P_7 = \frac{1}{2} \rho [(V_7^2 - V_6^2) + K_{P2} V_7^2]$
Expansion from Pleat Outlet into Grating:	$\Delta P_8 = \frac{1}{2} \rho [(V_8^2 - V_7^2) + K_{EP} V_7^2]$
Across Back Grating:	$\Delta P_9 = \frac{1}{2} \rho [(V_9^2 - V_8^2) + K_G V_9^2]$
Flow from Filter Face to Slot Outlet:	$\Delta P_{10} = \frac{1}{2} \rho [(V_{10}^2 - V_9^2) + K_{S2} V_{10}^2]$
Flow out of Slot:	$\Delta P_{11} = \frac{1}{2} \rho [(V_{11}^2 - V_{10}^2) + K_{EB} V_{11}^2]$

$$\Delta P_T = \sum \Delta P_i = \Delta P_1 + \Delta P_2 + \Delta P_3 + \Delta P_4 + \Delta P_5 + \Delta P_6 + \Delta P_7 + \Delta P_8 + \Delta P_9 + \Delta P_{10} + \Delta P_{11}$$

(4.1)

Terms ΔP_3 through ΔP_9 were previously identified and verified in the single filter section. (Of note: the nomenclature for coefficients K_C and K_E were changed to K_{CP} and K_{EP} to indicate the sudden contraction or expansion due to the pleat tips). K_{CB} and K_{EB} also referred to a sudden contraction and expansion, but these coefficients referenced the flow change in and out of the array.

The new coefficients K_{S1} and K_{S2} accounted for friction encountered in the slot(s) upstream and downstream of the filters. The slot(s) can be thought of as macro-pleats due to their similar geometry; therefore, it is not surprising that the momentum and mechanical energy balance could not be simultaneously solved for the slot(s) geometry either. The partial solution to the balances indicated the coefficient should be a function of slot pitch (α).

An empirical approach was taken to distinguish the coefficients due to the inability to theoretically solve for them. The two constants were merged into one coefficient (K_S) since the individual influences of K_{S1} and K_{S2} could not be separated and discerned. After making the appropriate substitutions and utilizing the upstream/downstream symmetry, the series of equations were reduced and re-written into the following Multi-Element Structured Array model:

$$\Delta P_T = \frac{1}{2} \rho [(K_{CB} + K_{EB})V_2^2 + (2K_G + K_S)V_3^2 + (K_{CP} + K_{EP} + K_P)V_5^2] + AV_6 + BV_6^2 \quad (4.2)$$

IV.2. MESA Experimental

The experimental objective was to verify the use of the nine parameters that comprise the Multi-Element Structured Array model. A , B , K_G , K_{CP} , K_{EP} , and K_P were proven valid or empirical determined by the research presented in the previous chapter. The present objective was to establish the model's remaining three terms: K_{CB} , K_{EB} , and

K_S . The coefficients K_{CB} and K_{EB} were proven to be accurately model by a sudden contraction or a sudden expansion coefficient by mechanically altering an array's blockage and measuring the responding deviation in pressure. The slot coefficient (K_S) was empirically developed by an analogous methodology used to formulate the pleat coefficient. The process examined 32 arrays employing assorted media types, element depths, element widths, pleat counts, and element counts to devise a robust coefficient.

IV.2.1. Entrance Coefficient of Friction (K_{CB})

The added resistance for entering the array can accurately be calculated by Equation 2.11 using a friction coefficient computed by Equation 2.12. This assessment was authenticated by modifying the blockage created by the front edge of the elements and comparing the corresponding resistance to the computational predications. Unlike the experimental approach used to verify the filter grating, the contraction created by the array's edge could not be modified by adding extra blockage. Several modifications to increase the flow blockage were envisioned, yet each modification had secondary influences that skewed other resistances or geometries. Instead of trying to increase the blockage and monitor the responding pressure increase, the effects of the blockage were removed and the decrease in resistance was observed.

The array's entrance blockage was eliminated by adding a long, gradual contraction to the front of the array. The gradual slope of the contraction removed the air friction normally encountered when reducing the allowable flow area. Thus, the sudden contraction and the resistance of the contraction were removed from the total pressure drop. The overall drop in resistance was then compared to the expected resistance

computed by the sudden contraction coefficient (Equation 2.12) with the ratio $A_{\text{FREE}}/A_{\text{TOTAL}}$ equal to A_2/A_1 .

Figure 4.5 illustrates a normal array configuration and the modified design. The transition was created by adding a 19.5" (H) by 23" (W) board to each front edge. The boards are highlighted below in blue. The boards were taped to the duct walls and the element's front edge to eliminate additional friction due to uneven surfaces. The filter array had to be slightly positioned into the outlet section of the test rig to accommodate the additional length of the front transitional boards, yet all elements of the system remained between the pressure taps.

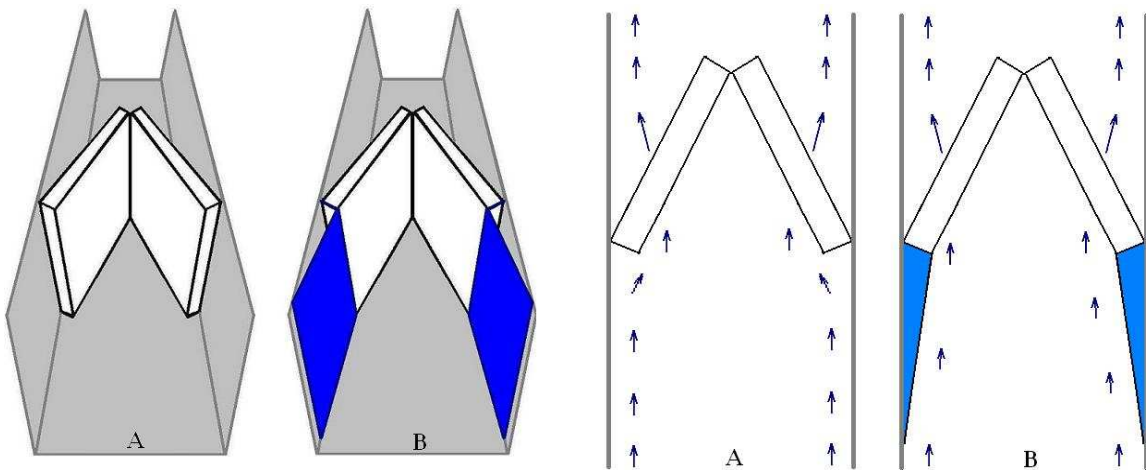


Figure 4.5: Illustration and Schematic of Flow within a Normal (A) and Contraction Modified Array (B)

The experimental procedure was similar in manner to the one used in the grating coefficient tests. A pressure drop curve was first recorded for the normal array geometry, and then a second pressure drop curve was measured for the modified array entrance. The test was conducted on a “V” configuration array using elements with depths of two and four inches. Figure 4.6 graphs the experimentally recorded data for a normal and

modified “V” array constructed with 4” deep filter elements. The data points in the enlarged area were outfitted with error bars of ± 0.002 ” H₂O.

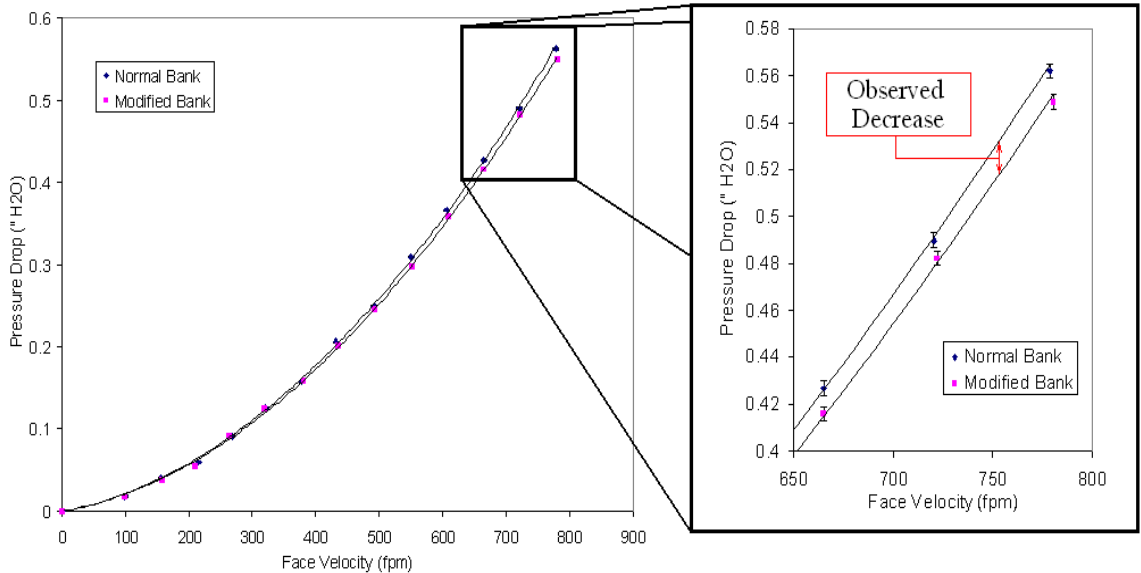


Figure 4.6: Measured Pressure Drop for a Normal and Modified Array

Since the gradual contraction was of significant length and the overall decrease in area remained small, the coefficient of friction and pressure drop of the transition were approximately zero.

$$A = 0.01745(\sin^{-1}(0.275/1.625)) = 0.141$$

$$N = (1.625 - .275*2)/1.625 = 0.66$$

$$K_{GC} = [(-0.0125N^4 + 0.0224N^3 - 0.00723N^2 + 0.00444N - 0.00745)(A^3 - 2\pi A^2 - 10A)]$$

$$K_{GC} = 5.5 \times 10^{-3} \approx 0$$

This meant that the observed decrease in resistance from Figure 4.6 could be directly compared to the calculated resistance of the array blockage. The observed decrease due to the modification closely correlated to the expected resistance created by a sudden contraction (Figure 4.7); therefore, the viscous loss equation combined with the friction coefficient for a sudden contraction accurately modeled the pressure drop created by the elements edge walls.

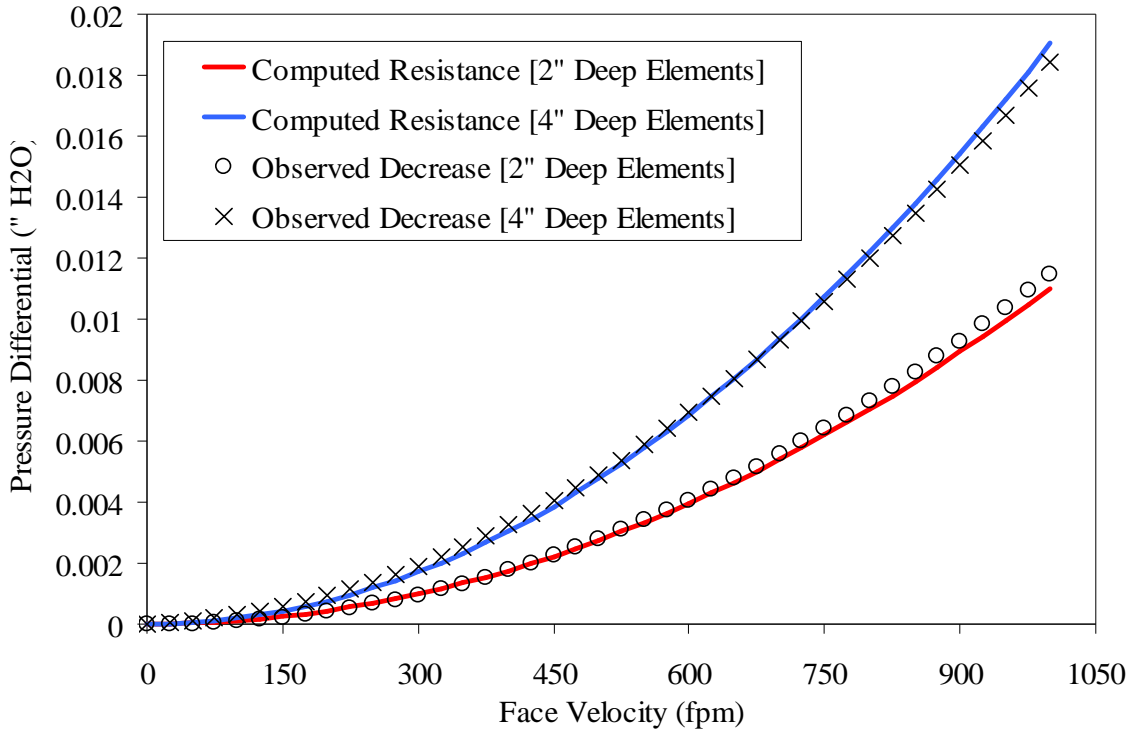


Figure 4.7: Observed and Modeled Pressure Drop Differences

IV.2.2. Exit Coefficient of Friction (K_{EB})

An analogous test was performed to verify the use of a sudden contraction (Equation 2.11) to model the pressure loss when air exits from the filter array. A normal pressure drop curve was measured followed by a second pressure drop curve for a modified design. The modified outlet design changed the sudden expansion into a gradually transition. Since the same array is used in both experiments, the observed difference between the two configurations can be compared to the calculated pressure drop expected by a sudden expansion. The array was modified by adding a tail fin composed of two 19.5" (H) by 23" (W) boards to the back of the filter's edges. Figure 4.8 provides a general set-up for the experiment while Figure 4.9 presents the results.

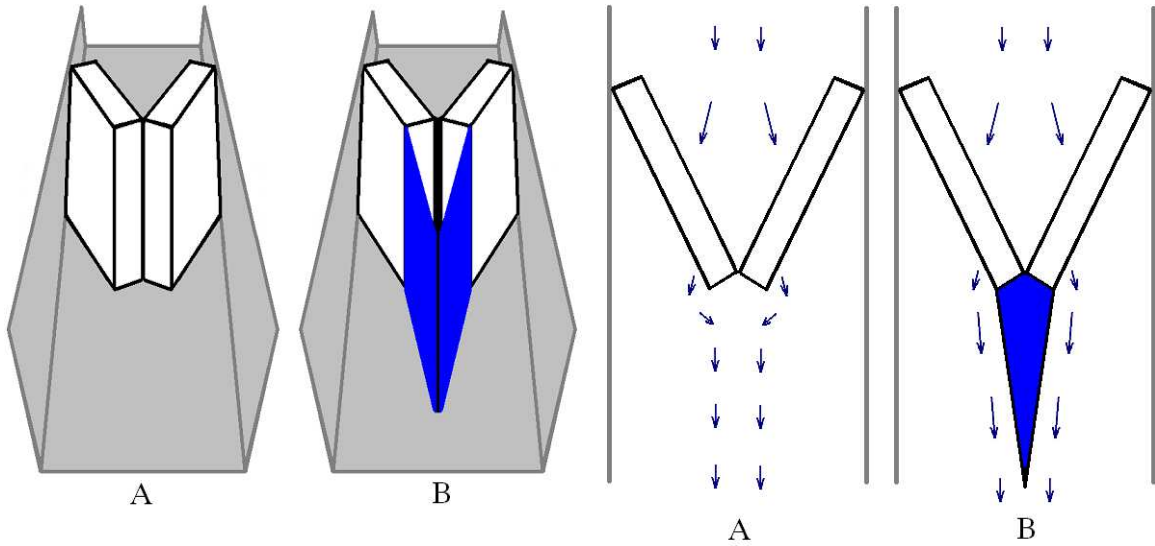


Figure 4.8: Illustration and Schematic of Flow within a Normal (A) and Expansion Modified Array (B)

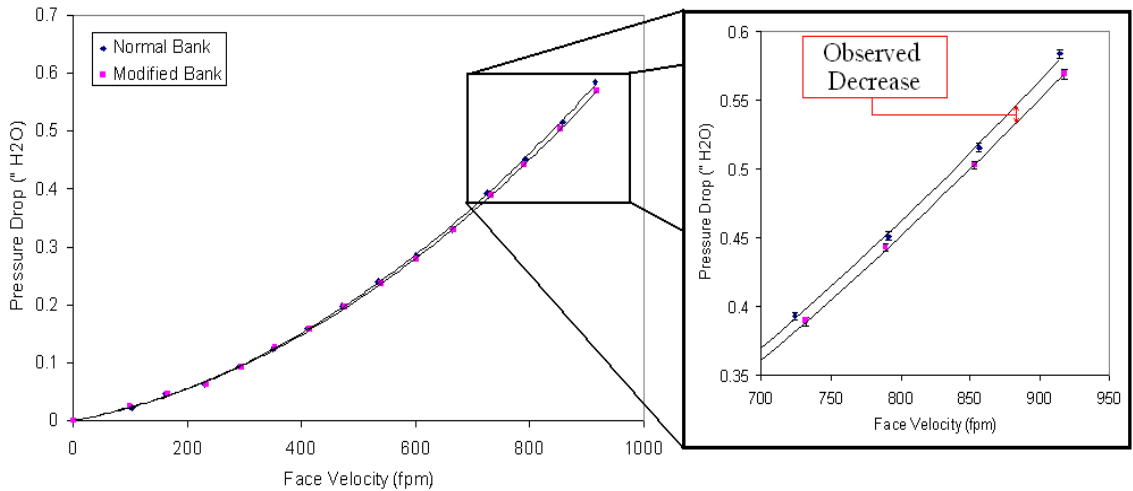


Figure 4.9: Measured Pressure Drop for a Normal and Modified Array

The experiment was performed on a “V” array loaded with 4 inch filters. Figure 4.10 indicates that the expansion out of the array can accurately be modeled by a sudden expansion coefficient due to the good correlation between the computed and observed pressure differences.

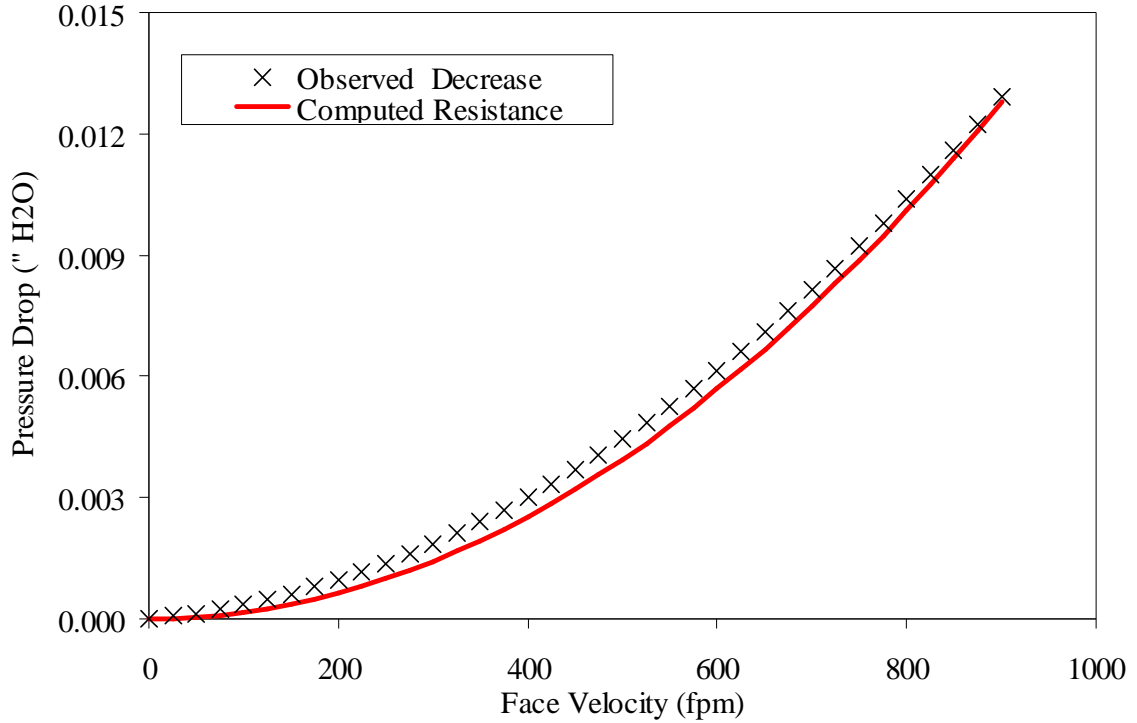


Figure 4.10: Observed and Modeled Pressure Drop Differences

IV.2.3. Slot Coefficient of Friction (K_S)

The slot friction coefficient was formulated through the use of empirical data spanning 32 MESA systems. Equation 4.2 was reorganized into the following form:

$$\{\Delta P_T - \frac{1}{2} \rho [(K_{C1} + K_{E2})V_2^2 + (2K_G)V_3^2 + (K_{C2} + K_{E1} + K_P)V_5^2] + BV_6 + AV_6^2\} = K_S (\frac{1}{2}\rho V_3^2) \quad (4.3)$$

Data relating ΔP_T versus face velocity data was acquired for a specific array. All velocities in the above equation were calculated from the face velocity using the equation of continuity. The friction coefficients were calculated based on known geometric dimensions, and the media constants were experimentally determined. The slot coefficient for a particular array was solved by plotting the calculated values on the left-

hand side versus the reference velocity term ($\frac{1}{2}\rho V_3^2$). The process was repeated for various element types to improve the versatility of the coefficient.

The following graph demonstrated the procedure for a filtration array loaded with six, 20"x20"x1" elements. Each element contained 32 pleats and was constructed with FM1 media (Filter Type G). The black circles marked experimentally measured pressure drop versus velocity data. The dashed line was a least-squared fit to the experimentally measured data. The solid, black line was the modeled pressure loss due to known coefficients. The hyphenated line represented the unaccounted pressure drop. It was created by subtracting the solid line from the dashed line.

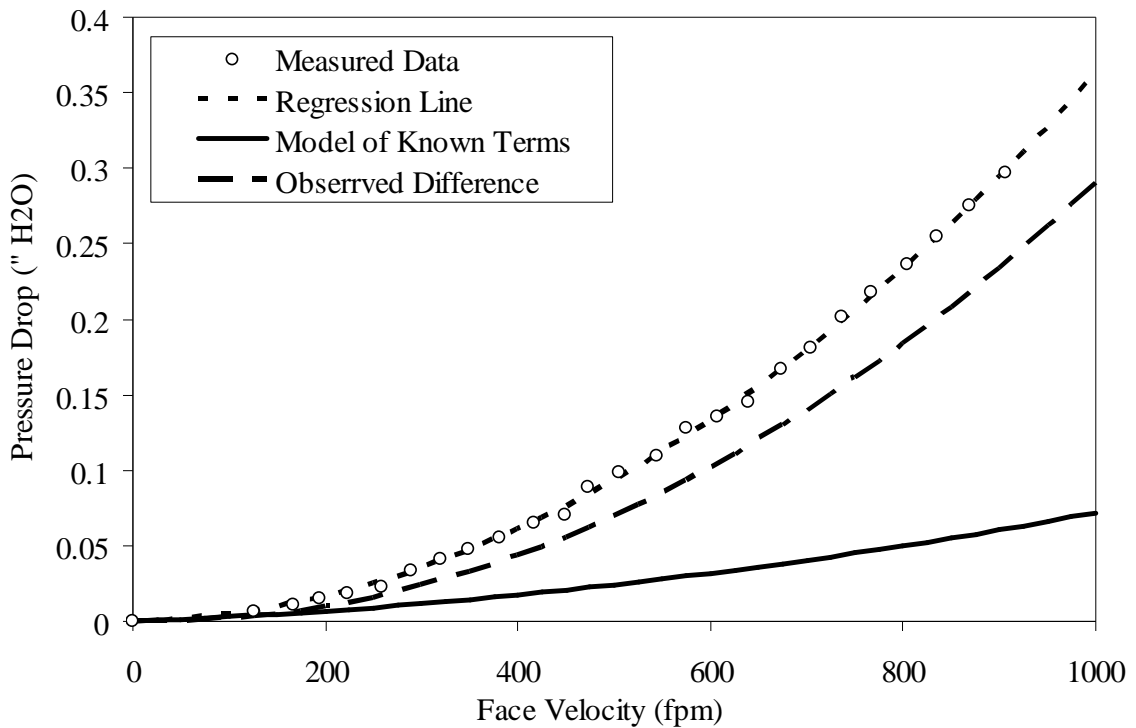


Figure 4.11: Pressure Drop Curves for a WV Array of 1" Filters

The hyphenated line was plotted versus $\frac{1}{2}\rho V_3^2$ in Figure 4.12 below. A linear line forced through the origin was fitted by Excel. The slot coefficient was calculated as

172.2 from the plot's slope. This particular slot coefficient is only valid for a "WV" array configuration employing 20"x20"x1" elements.

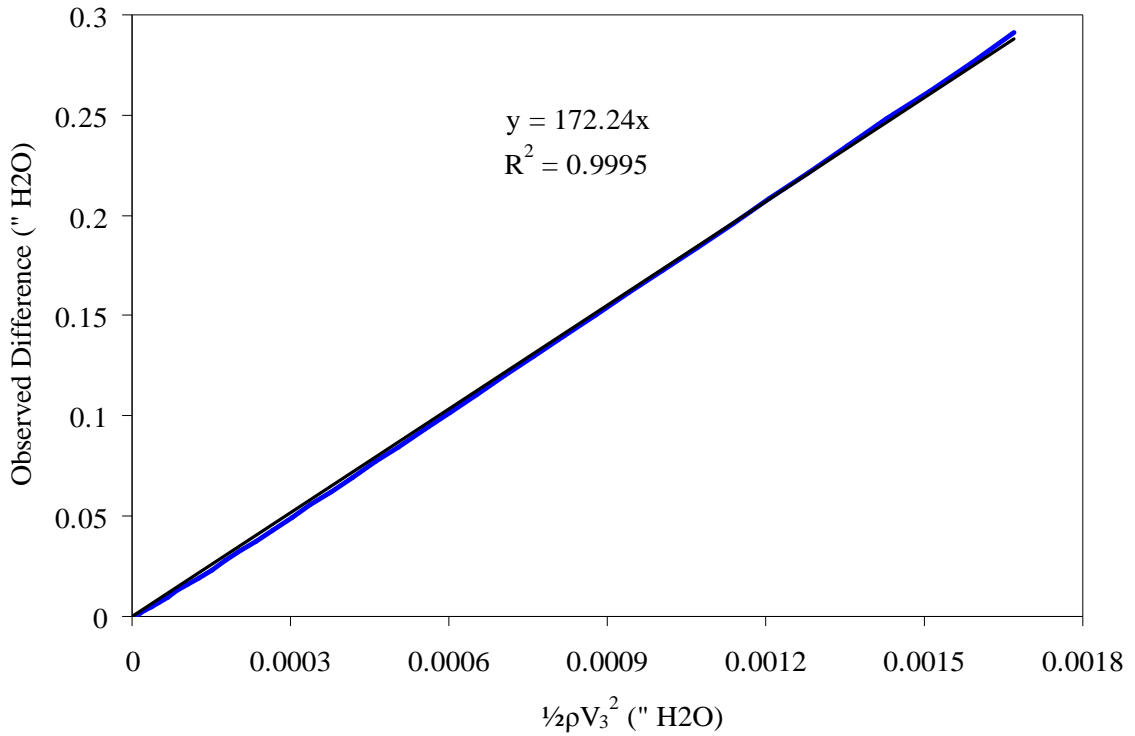


Figure 4.12: Slot Coefficient Graph for a WV Array of 1" Filters

Thirty-two filtration arrays were utilized to investigate the effects of design variation on the slot coefficient. The following table compiled the element types and configurations used. All filter elements were modeled as single, pleated filters in the previous chapter except for Type X and Y. Type X and Y possessed widths less than 19.5" and were unable to be loaded as a single filter.

Table 4.3: Summary of Elements used in Slot Coefficient Study

Filter	Depth	Width	Height	Pleat Count	Media Type	Combinations
D	0.85" (1")	19.5" (20")	19.5" (20")	19	FM1	2x , 4x, 6x, & 8x
G	0.85" (1")	19.5" (20")	19.5" (20")	32	FM1	2x , 4x, 6x, & 8x
J	0.85" (1")	19.5" (20")	19.5" (20")	47	FM1	2x , 4x, 6x, & 8x
B	1.75" (2")	19.5" (20")	19.5" (20")	16	FM2	2x , 4x, & 6x
L	1.75" (2")	19.5" (20")	19.5" (20")	19	FM1	2x , 4x, & 6x
S	1.75" (2")	19.5" (20")	19.5" (20")	56	FM5	2x , 4x, & 6x
N	3.5" (4")	19.5" (20")	19.5" (20")	19	FM1	2x & 4x
T	3.5" (4")	19.5" (20")	19.5" (20")	12	FM4	2x & 4x
X	0.85" (1")	9.5" (10")	19.5" (20")	17	FM1	4x, 6x, & 8x
Y	0.85" (1")	14.5" (10")	19.5" (20")	17	FM1	2x , 4x, 6x, & 8x

The slot coefficient results obtained by loading a filter box with two, four, six and eight Type J filters is plotted in Figure 4.13. Each line was a least-square regression line forced through zero. The slope and degree of fit is presented to the right of each line. As expected, the coefficient rose as more filters were added into the array owing to an increase in friction. This frictional increase occurred because an identical volumetric quantity of air was attempting to flow through a reduced area. The slot of the 20"x20"x1" V array, for example, has approximately 1.3 times the open volume of the a 20"x20"x1" WW array's slot. The reduced flow area increases the average velocity in the slot as well as heightened fluid-fluid interaction within the slot. Friction is increased by forcing the air to make a sharper turn before entering into the individual elements in higher count arrays. Table 4.4 listed all computed slot coefficients and their degree of fit.

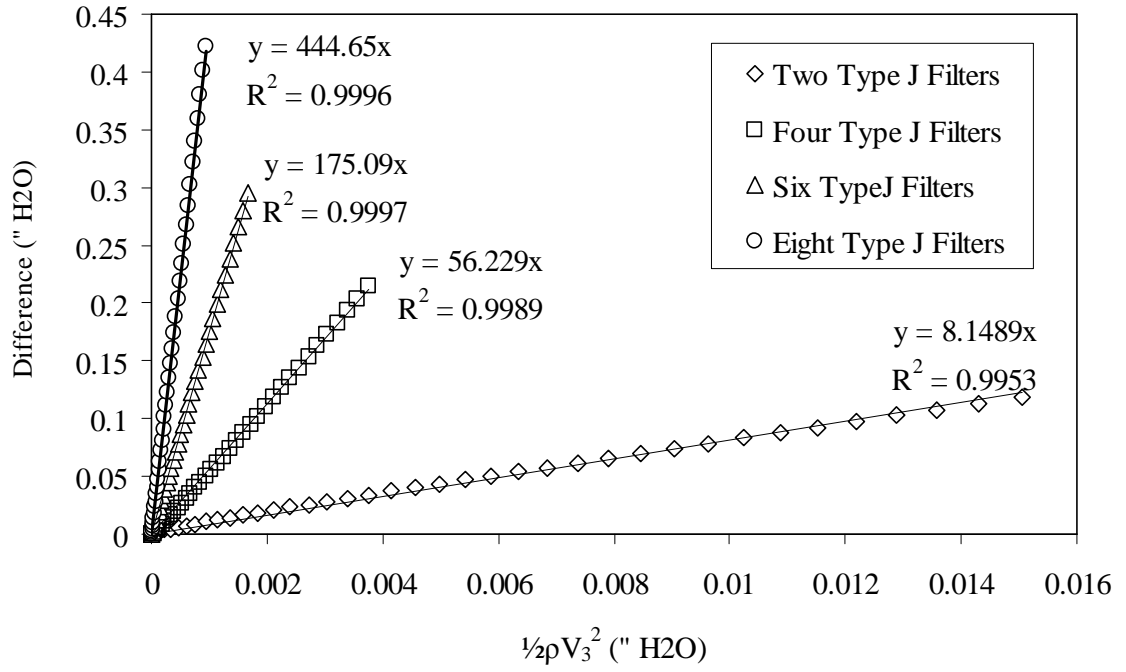


Figure 4.13: Slot Coefficient Plots for Various Configurations

Table 4.4: Summary of Observed Slot Coefficients and R² Fit

System	Element Count (-)	Slot Opening (ft)	Slot Length (ft)	Slot Depth (ft)	Alpha (rad)	Ks (-)	R2 (-)
D - V	2	1.499	1.625	1.442	0.479	7.658	0.9980
D - W	4	0.674	1.625	1.590	0.209	49.620	0.9998
D - WV	6	0.401	1.625	1.613	0.124	153.890	0.9975
D - WW	8	0.265	1.625	1.620	0.082	399.590	0.9982
G - V	2	1.499	1.625	1.442	0.479	8.435	0.9996
G - W	4	0.674	1.625	1.590	0.209	56.966	0.9990
G - WV	6	0.401	1.625	1.613	0.124	172.190	0.9995
G - WW	8	0.265	1.625	1.620	0.082	408.040	0.9977
J - V	2	1.499	1.625	1.442	0.479	8.449	0.9956
J - W	4	0.674	1.625	1.590	0.209	56.529	0.9990
J - WV	6	0.401	1.625	1.613	0.124	175.400	0.9997
J - WW	8	0.265	1.625	1.620	0.082	444.960	0.9996
B - V	2	1.360	1.625	1.476	0.432	9.020	0.9901
B - W	4	0.525	1.625	1.604	0.162	93.882	0.9967
B - WV	6	0.251	1.625	1.620	0.077	388.000	0.9985
L - V	2	1.360	1.625	1.476	0.432	11.270	0.9990
L - W	4	0.525	1.625	1.604	0.162	105.760	0.9995
L - WV	6	0.251	1.625	1.620	0.077	439.850	1.0000
S - V	2	1.360	1.625	1.476	0.432	6.859	0.9999
S - W	4	0.525	1.625	1.604	0.162	80.104	0.9967
S - WV	6	0.251	1.625	1.620	0.077	386.710	0.9987
N - V	2	1.074	1.625	1.534	0.337	22.591	0.9985
N - W	4	0.231	1.625	1.621	0.071	390.700	0.9997
T - V	2	1.074	1.625	1.534	0.337	20.765	0.9893
T - W	4	0.231	1.625	1.621	0.071	344.317	0.9970
X - W	4	0.685	0.792	0.714	0.447	14.479	0.9999
X - WV	6	0.405	0.792	0.765	0.258	40.558	0.9999
X - WW	8	0.267	0.792	0.780	0.169	93.643	0.9993
Y - V	2	1.515	1.208	0.231	0.677	3.418	0.9974
Y - W	4	0.676	1.208	0.716	0.284	26.593	0.9999
Y - WV	6	0.402	1.208	0.766	0.167	89.383	0.9987
Y - WW	8	0.265	1.208	0.780	0.110	218.180	0.9987

The partial solution to the mechanical and momentum balances for a slot was used as a starting point for modeling the slot coefficient. The solution $(1/\alpha)^2$ was plotted below versus the empirically-determined coefficients.

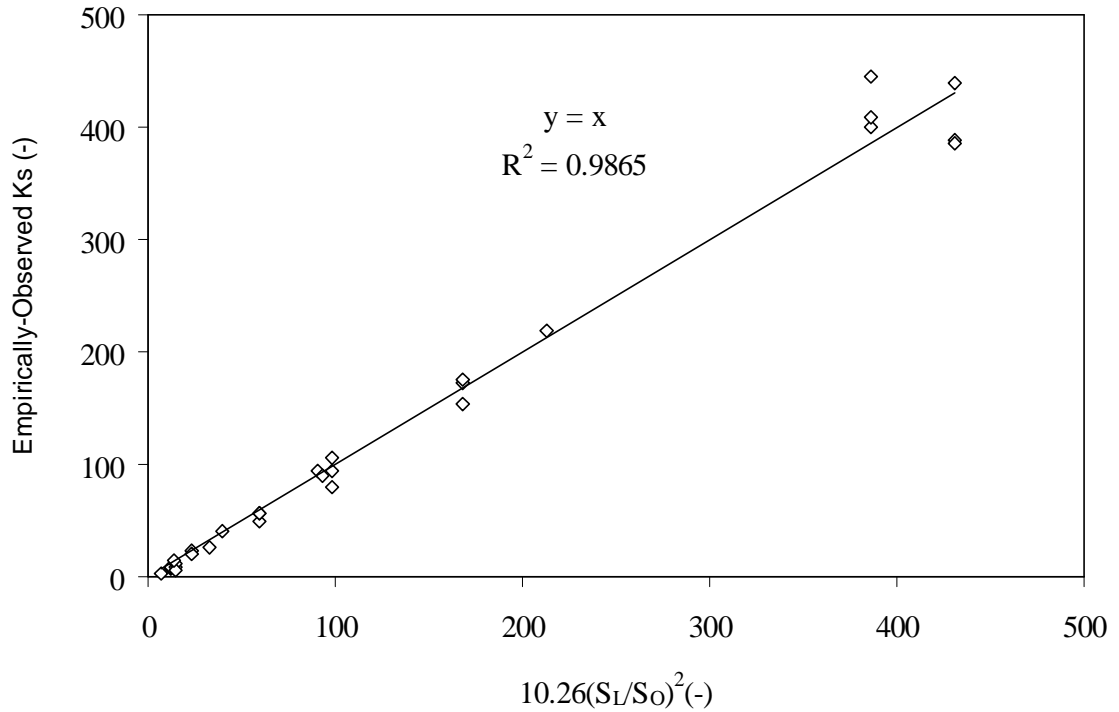


Figure 4.14: Slot Coefficient Graph

The modeled formula showed a linear relationship to the empirically-observed coefficient. An oddity occurred involving both observed slot coefficients for array systems consisting of four, 4” elements. Each array possessed an unusually low coefficient. These coefficients were tagged by the solid, black diamonds. One possible reason for the divergence was that by loading four, 4” filters into a box an abnormal flow pattern was created due to approximately 70% of the duct being blocked by the array’s front edges. The extreme flow pattern could have been inducing other unforeseen effects within the system that was not able to be accounted for by the model.

The slot coefficient was reevaluated with the two abnormal values removed. The main reason for this was the impracticality of packaging 4” filters into a “W” array. The average pressure loss in such a configuration at 500 fpm was 0.6” H₂O. The same amount of media could be loaded into an array utilizing 1” or 2” deep elements while

maintaining a total pressure drop below 0.25” H₂O. It is therefore more beneficial to possess a slot coefficient that could accurately describe the useful arrays instead of a coefficient that attempted to model all systems with less accuracy. After the removal of the two abnormal values, the slot coefficient was determined as:

$$K_s = 2.575(1/\alpha)^2 \quad (4.4)$$

with V_3 as the Reference Velocity

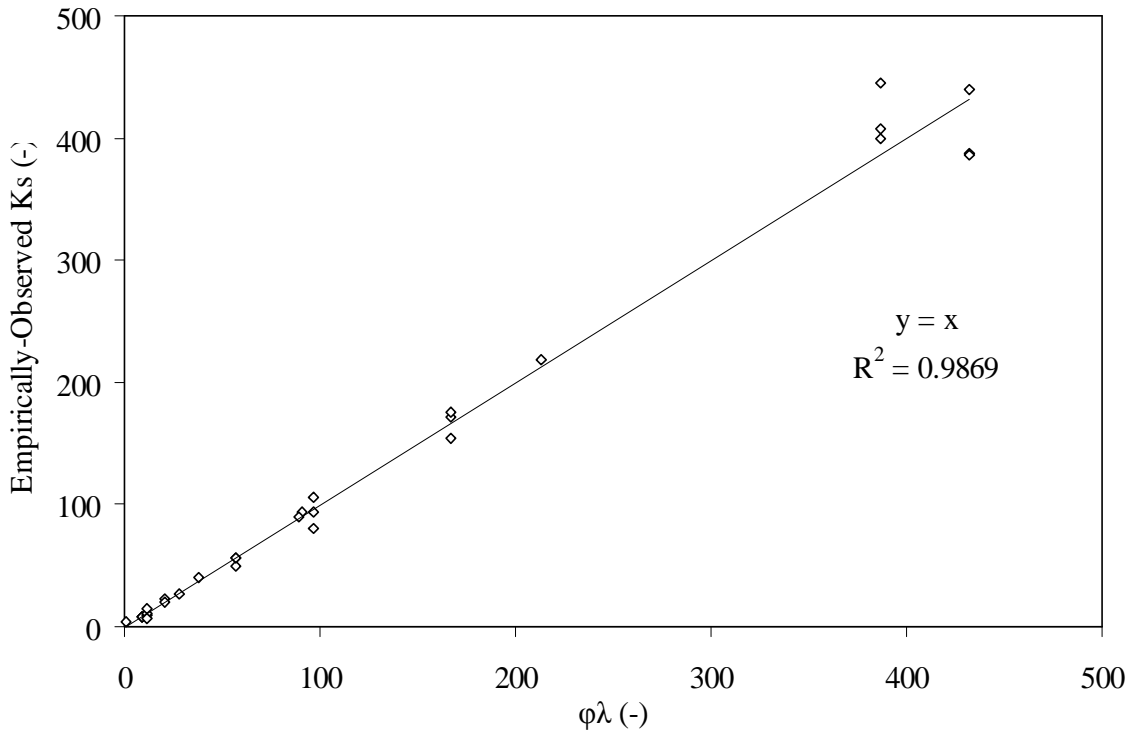


Figure 4.15: Observed versus Modeled Slot Coefficient

IV.3. Discussion Utilizing the Model

IV.3.1. Achievement of Objectives

The one-to-one correlation on over 1500 data points demonstrates the two models’ ability to calculate resistance as a function of face velocity. The inner dashed lines in Figure 4.16 equal $\pm 5\%$ from unity and the outer dashed lines correspond to $\pm 10\%$ from unity. The empirical pleat coefficient was formulated on 680 individual data points spanning twenty design variations. The slot’s friction coefficient was devised from 750

data points encompassing thirty different array architectures. The models accounted for all known pleated filter parameters and are fully capable of making predictions based solely on empirical data pertaining to the media constants. All geometric coefficients are based on physical design variables without the use of non-transferable factors.

Theoretical equations relating media constants to media properties such as fiber diameter and void volume could readily be incorporated to make the model fully independent of empirical data. The model is composed entirely of polynomials allowing for quick analysis and estimations times.

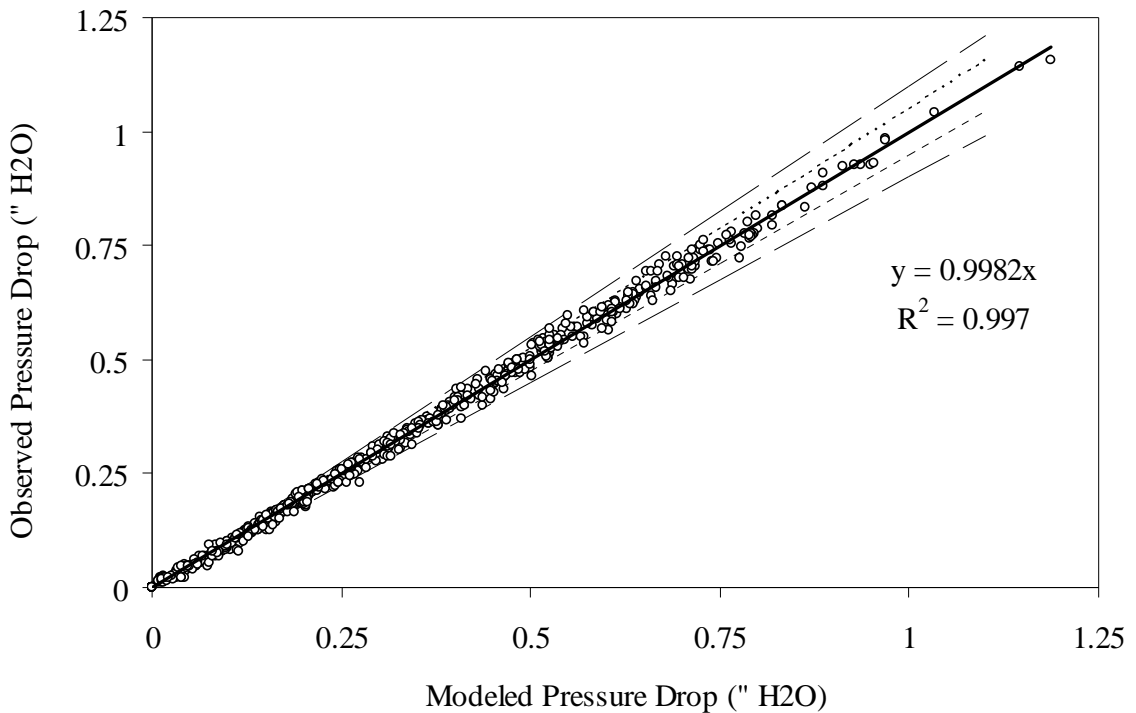


Figure 4.16: Correlation Plot between Observed and Modeled Data

IV.3.2. The Pleating Curve of a Multi-Element Structured Array

The array model was employed to study the effects created by increasing pleat count within a multi-element array. Figure 4.17 displays a “W” array configuration loaded with 20”x20”x1” FM1 media filter elements to illustrate the resistances

encountered within an array. The red circles were experimentally observed values with error bars of $\pm 5\%$. The individual plots for pleat contraction, pleat expansion, array contraction, and array expansion were removed for clarity. Since each term by itself contributed less than 0.003" H₂O of resistance, they were summed and plotted as the cumulative resistance entitled "Miscellaneous."

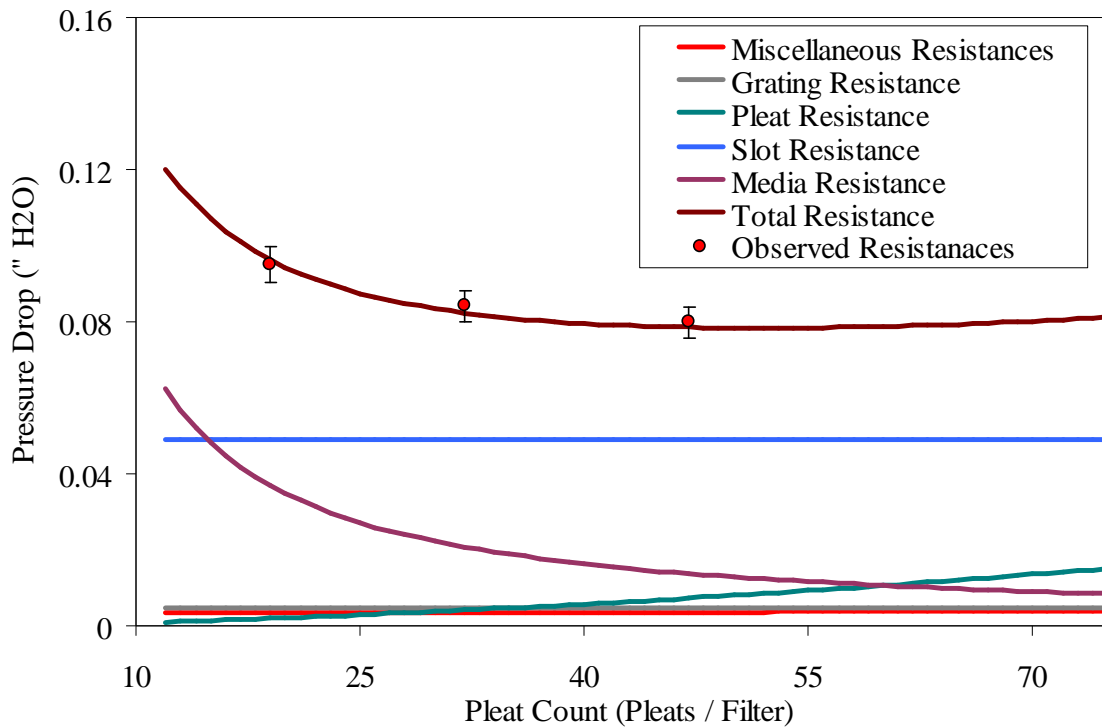


Figure 4.17: Multi-element structured array Pleating Curve

The resistance behavior of a Multi-Element Structured Array partially mimics the trends observed in a single filter's pleating curve, yet the overall magnitude of the pressure drop and the contributing factors are substantially different. Foremost, the total flow resistance is between one-third to one-half the resistance of a single 20"x20"x1" FM1 media filter over the same range of pleat counts. The pleat and media terms no longer serve as the primary contributor to pressure drop. Likewise, the impact of the

grating has been heavily reduced. The slot resistance now accounts for the bulk of the overall resistance. Just like the grating term, the slot term acts as a fixed resistance and is not a function of pleat count. The contraction and expansion into and out of the MESA also act as fixed resistances. The filtration system still trades media losses for pleat induced resistances, and the optimal pleat count is dependent upon these terms. Below is a graphical representation of the percentage contribution to the total resistance from each resistance term. The chart was compiled from data obtained at the optimal pleat count in Figures 3.20 and 4.17.

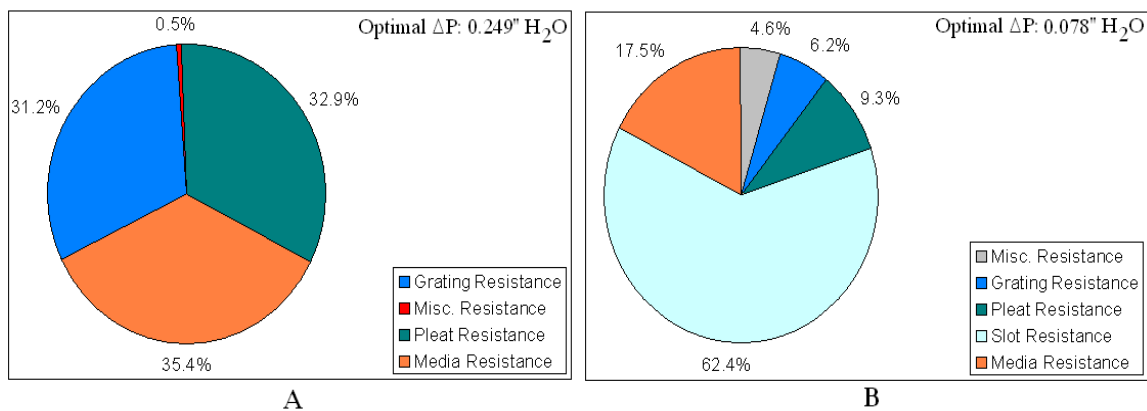


Figure 4.18: Percentage Contribution of (A) Single Filter and (B) "W" Array

The reduction in the grating, pleat, and media term are the product of incorporating multiple filters to reduce the face velocity into each element. Since the grating and pleat terms are second order polynomial functions of face velocity, decreasing the airflow into each element by one-fourth results in a 16-fold decrease in their resistance. A one-fourth reduction in face velocity results in a 4 to 16-fold reduction of the media term depending on the media constants. Likewise, the utilization of eight elements would result in a 64-fold decrease in elemental resistances.

Slowing the face velocity into the elements grants an array a unique range of benefits. MESA's can serve as a platform to house high-resistance media that would be otherwise impractical to use. Furthermore, an array can employ any media type and operate at a vastly decreased resistance over a traditional pleated filter. With the reduction of the element's viscous effects, the individual filters can be pleated to a much higher extent before reaching a limiting resistance.

IV.3.3. Locating the Optimal Pleat Count

The MESA model is simply an extension of the single filter's model. The three terms italicized below are new additions, but the remaining terms are all present in the single's filter model. The contraction into the array (K_{CB}), expansion out of the array (K_{EB}), and resistance through the slot(s) (K_S) are all functions of element count and not functions of pleat count. Thus, the optimal pleat count is computed in the same manner as presented in Chapter III.

$$\Delta P_T = \frac{1}{2} \rho [(K_{CB} + K_{EB})V_2^2 + K_S V_3^2 + 2K_G V_3^2 + (K_{CP} + K_{EP} + K_P)V_5^2] + AV_6 + BV_6^2$$

IV.3.4. Influence of Design Parameters

The model was employed to examine the variation of parameters and the resulting effects on resistance in order to better understand the design space and behaviors of a MESA. Media constants, media thickness, filter depth, and face velocity were identified as important design parameters in the single filter section. These factors remain critical in the MESA design as well as factors unique to MESAs such as element width and number of elements.

1. Effects of Filter Element Count

The filter element count is the most important design factor in a Multi-Element Structured Array. An array's main resistance is created by flow through the slot as seen in Figure 4.18B. This resistance is primarily a function of element count. The element count also has a significant influence on the impact of other design parameters. The incorporating of two to eight elements will reduce the face velocity into each individual element by 50% to 87.5% respectively. This substantial reduction in velocity allows an array to essentially eliminate or considerably hinder any influence created by pleat count, grating contribution, media thickness, or media constants.

The model was used to study various element counts by calculating resistance data for 20"x20"x1" deep filter elements in five configurations. Media properties were set at a thickness of 1.5 mm with constants $A = 10 \times 10^{-4}$ and $B = 15 \times 10^{-7}$. The results were plotted in Figure 4.19.

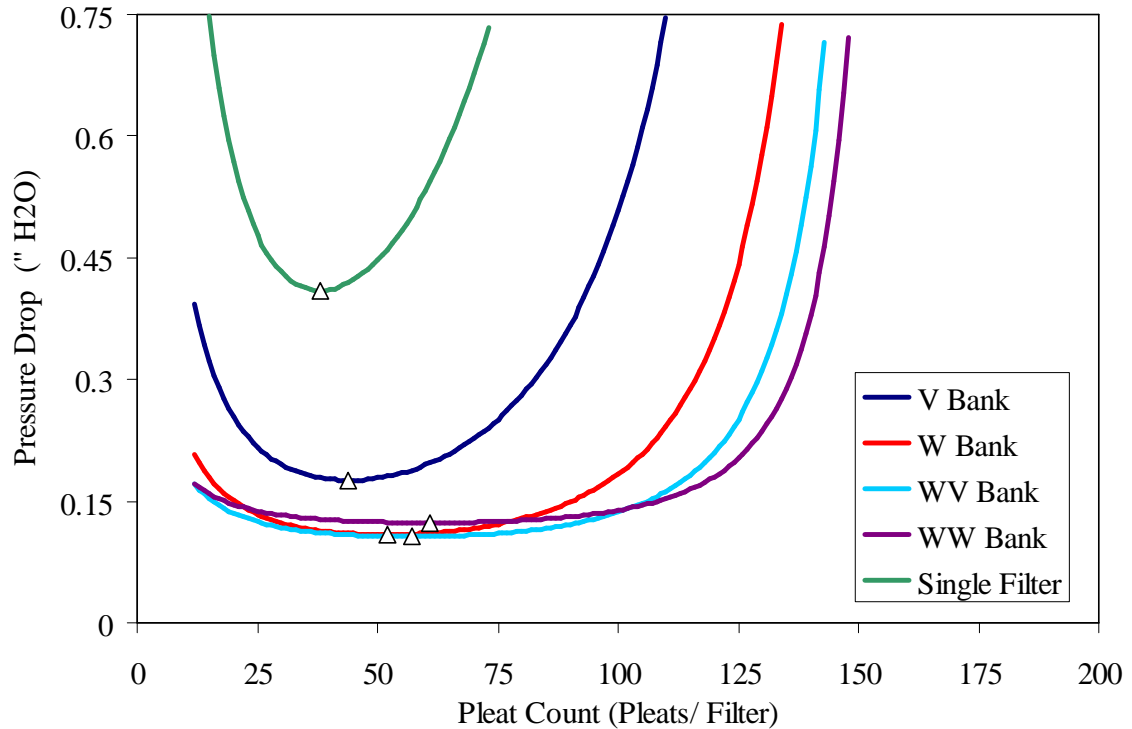


Figure 4.19: Effects of Element Count on MESA Pleating Curve

The pleating curves lose their distinctive “U” shape and adopted an “L” shape as the total number of filter elements increased due to the reduction of the face velocity encountered by each element. The presence of the media-dominated regime in higher element arrays was essentially removed due to the array’s ability to incorporate a substantial media area even at low pleat counts. The viscous-dominated regime still existed; however, the pleating had to be taken to an unusually high count before the viscosity-induced resistance could become relevant.

The optimal pleat count shifted right as element count increased since the viscosity resistances were more impeded in higher element arrays. The lowest obtainable resistance experienced a minimum and then began to rise (see Figure 4.20). This rise was due to the incremental increase in the fixed resistances. Each additional element further

enhanced the friction for flow within the slots as well as increased the resistances created by a larger expansion and contraction within the array. After the “WV” configuration, the minor decrease in media and pleat resistances were not able to compensate for the subsequent increase in fixed resistances. The charts below present each term’s individual contribution to the total pressure drop as the number of elements increased.

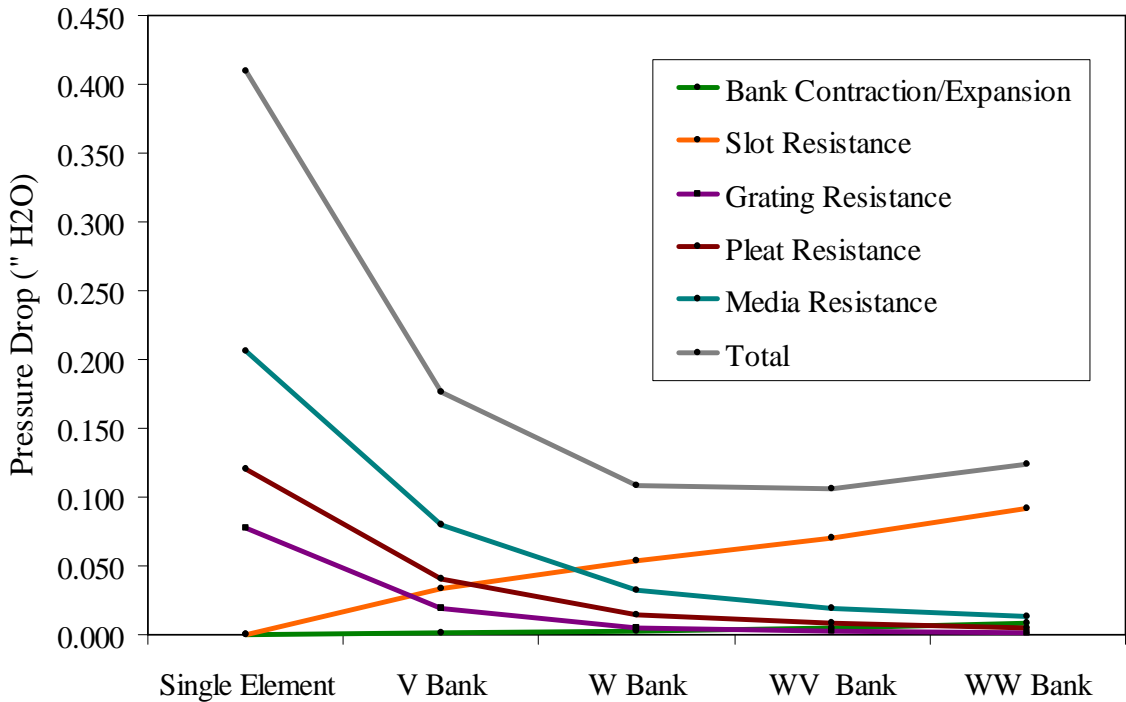


Figure 4.20: Effect of Element Count on Contribution

Although the extra elements help to reduce the operational pressure drop, the major advantage of the MESA designs was the vast increase in available filtration area. The pressure drop data from Figure 4.19 was plotted below versus their corresponding available filtration area. Table 4.5 presents the optimal pleat count of each system, available filtration area, and lowest obtainable resistance (LOR). Each array was compared to the available filtration area and LOR of the 20”x20”x1” filter system

composed of an identical media. The arrays, at the very minimum, were able to double the available filtration area while operating at fifty percent of the pressure drop.

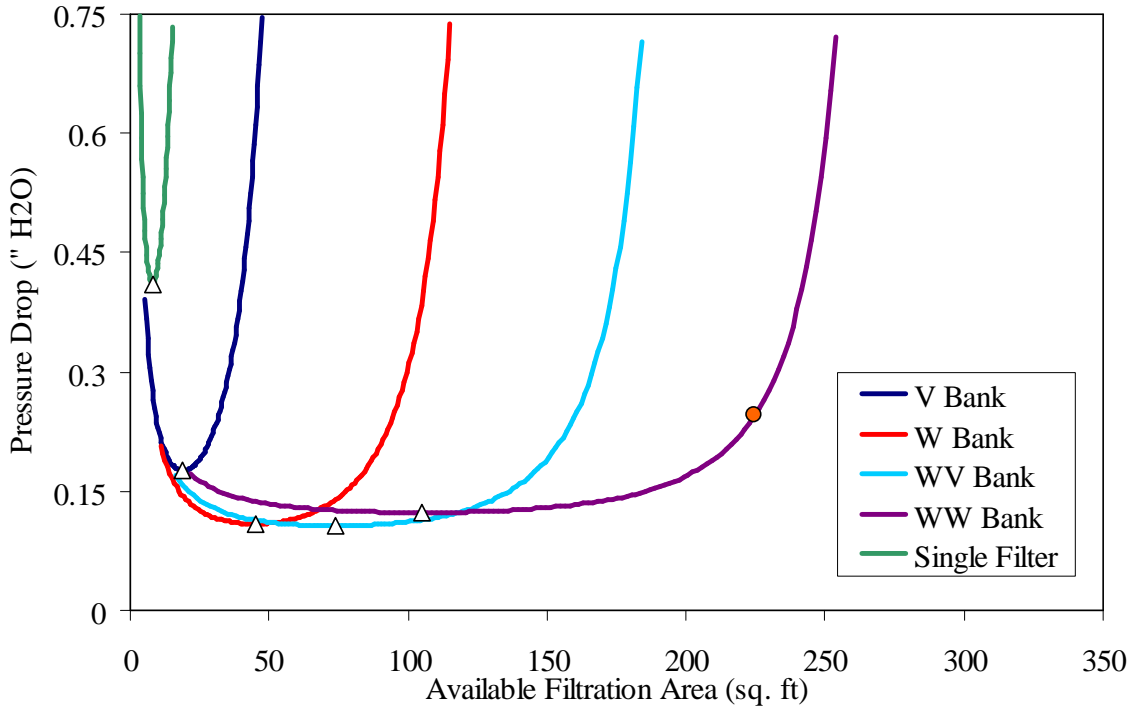


Figure 4.21: Effects of Element Count on MESA Performance Curve

Table 4.5: MESA vs. Single Filter Comparison

System (-)	Optimal Count (Pleats/Filter)	Media Area (sq. ft)	Lowest ΔP (\" H ₂ O)	Area Increase (%)	ΔP Reduction (%)
Single	38	8.0	0.410	n/a	n/a
V	44	19.0	0.176	237.9	42.9
W	52	44.9	0.109	561.2	26.5
WV	57	73.7	0.106	921.8	25.9
WW	61	105.2	0.123	1314.4	30.1

The orange circle represents the most area that can be incorporated into a system before going over the 0.25\" H₂O mark. This mark is heuristically considered the maximum acceptable starting resistance of an HVAC filter. A single 20\"x20\"x1\" filter composed of this media would not be constructed due to its high pressure drop. The

media would be manufactured into a 2” or 4” deep filter. Employing the single filter model for a quick computation, a 4” filter with 27 pleats could be built with the same media and maintain a resistance of 0.25” H₂O. The filter would possess slightly less than 25 square feet of available filtration area. A “WW” array would still be able to incorporate nine times the media and operate at the same resistance.

2. Effects of Filter Element Width

Filters with shorter widths were modeled as MESA’s to study to the impact of shallower slots depths. Theses systems mimic the commercially available products such as V-Banks. Arrays composed of shorter element widths provide a lower obtainable resistance than their wider counterparts at low filtration areas, but lose their competitive advantage at higher media areas due to increased pleat resistances. The shallower slot depth decreased the coefficient of friction for flow within the slot and decreased the fixed resistances of the system. The shorter-width filters were unable to handle the additional material as pleat count and the amount of packaged media increased. The pleat openings essentially close and the friction within the pleat rose. The filter elements with longer widths were able to better accommodate the additional pleats leading to increased filtration area.

The effects of element width were observed while constructing Figure 4.22. Three widths were modeled at 500 fpm using “WV” arrays composed of 20”x20”x1” depth element. Each element was modeled with 1mm thick media and constants of $A = 15 \times 10^{-4}$ and $B = 20 \times 10^{-7}$.

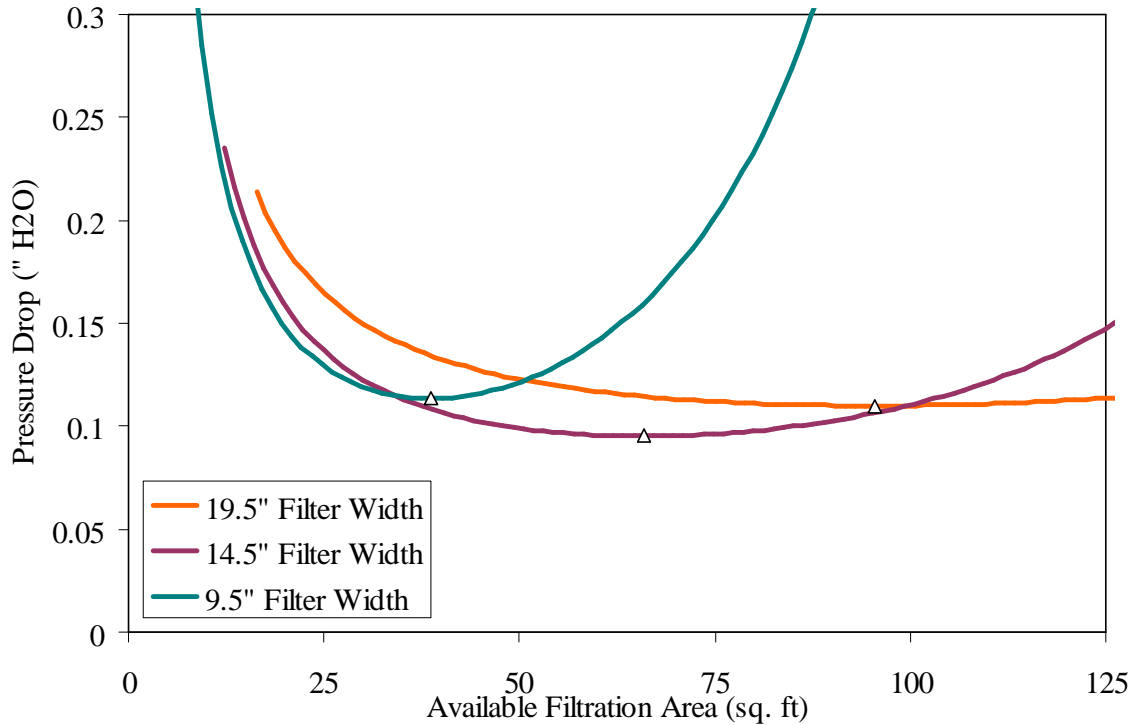


Figure 4.22: Effects of Element Width on MESA Performance Curve

The plot's behavior for arrays composed with shorter filter widths acted as a hybrid between single filters and 19.5" width arrays. A shallow array had more of the traditional "U" shape than the deeper slotted arrays. As the width of the elements increase, the graph began to flatten out as more of the overall pressure drop was comprised from fixed resistance instead of media and pleat pressure drops. Below was a plot of the contribution of each terms resistance to the total pressure drop at the optimal pleat count. The pleat and media terms were the dominate resistances in the single filter accounting for nearly eighty percent of the total pressure drop combined. They remained the prevalent resistances in the 9.5" width array, but as the widths were further increased their effects were reduced to less than thirty percent of the total pressure drop in 19.5" wide arrays.

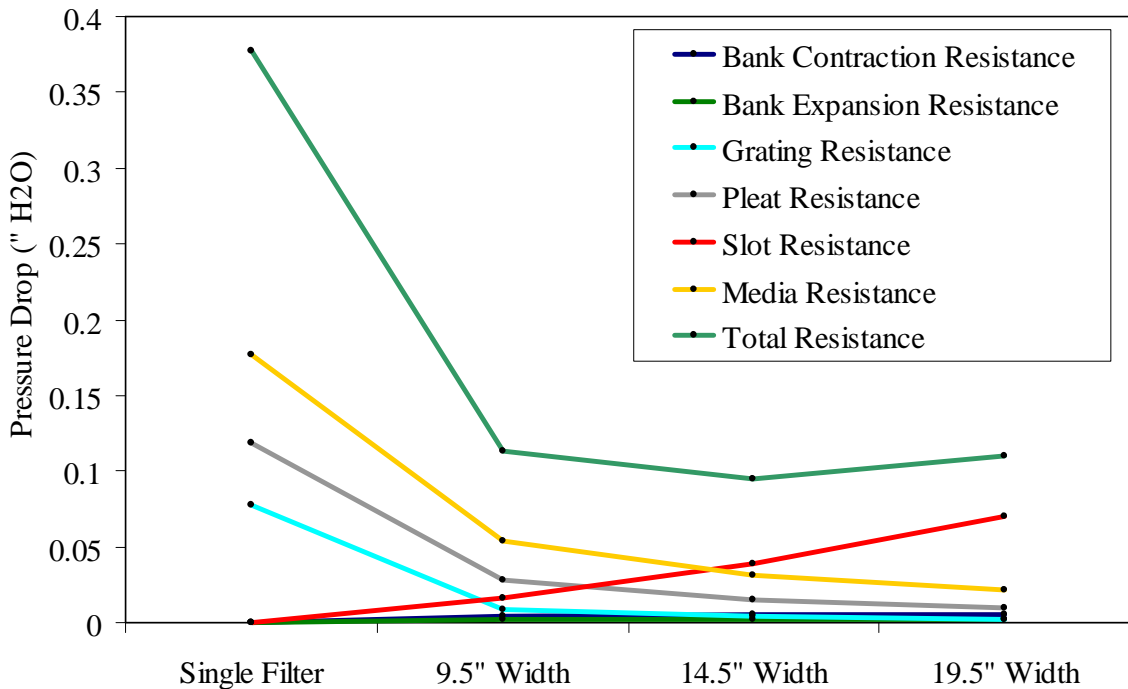


Figure 4.23: Effect of Element Width on Contribution

3. Effects of Filter Element Depth

A larger filter depth equated to a lower pressure drop and a higher available filtration area in single filter, yet the same did not hold true for Multi-Element Structured Arrays. Naturally, deeper elements increase the blockage resistance by creating a larger contraction and expansion into and out of the array. More significant though is the increase in slot resistance due to the decrease of the slot's pitch. The slot's pitch has to be decreased in order to accommodate the deeper elements into the array. The synergy of these effects leads to an increase in the fixed resistances that rendered a deeper element array less efficient.

Figure 4.24 and 4.25 were composed to illustrate these claims by modeling a "V" array configuration of various elements depths at 500 fpm. Each element was modeled with 1 mm thick media and constants of $A = 15 \times 10^{-4}$ and $B = 20 \times 10^{-7}$. The effects lead

to a 0.05" H₂O increase in the fixed resistances of the 4" filter array over the 2" filter array. This allowed the 2" element array to operate at a lower pressure drop for most of the curve.

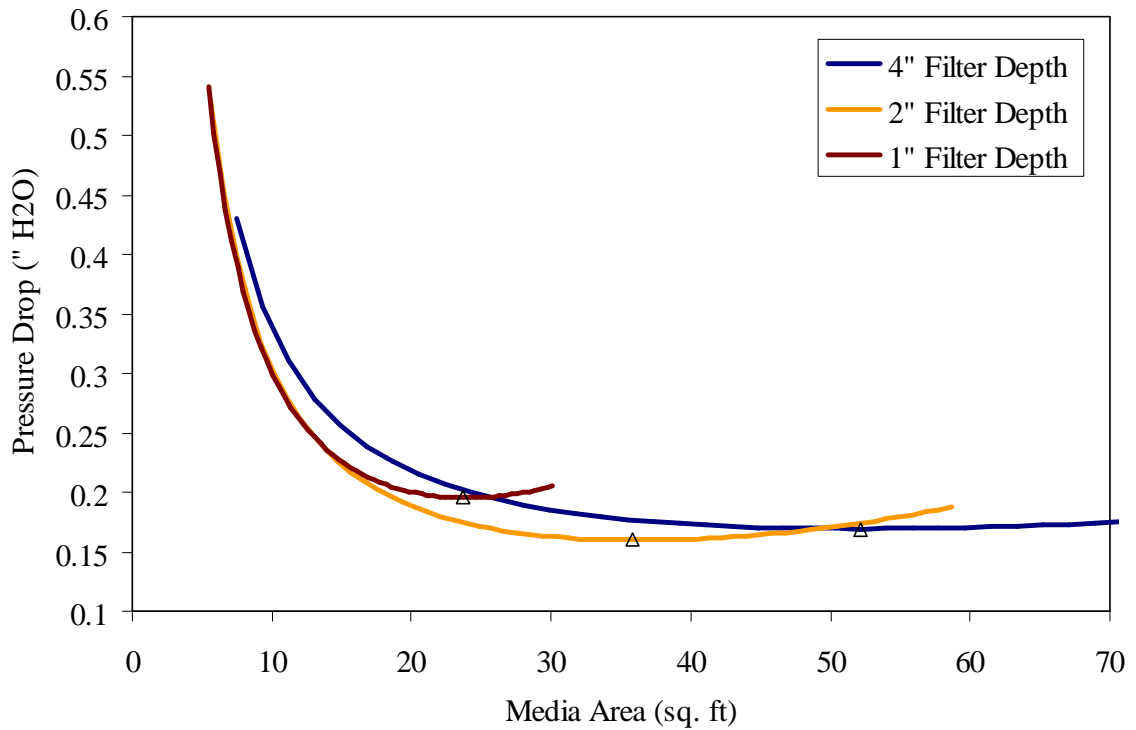


Figure 4.24: Effects of Element Depth on MESA Performance Curve

Figure 4.25 displays the individual contribution of each term at the lowest obtainable resistance. Just as seen in a single filter, the media and pleat resistances decrease as the element depth increases. The net decrease of the media and pleat, however, can not compensate for the rise in fixed resistances of the array.

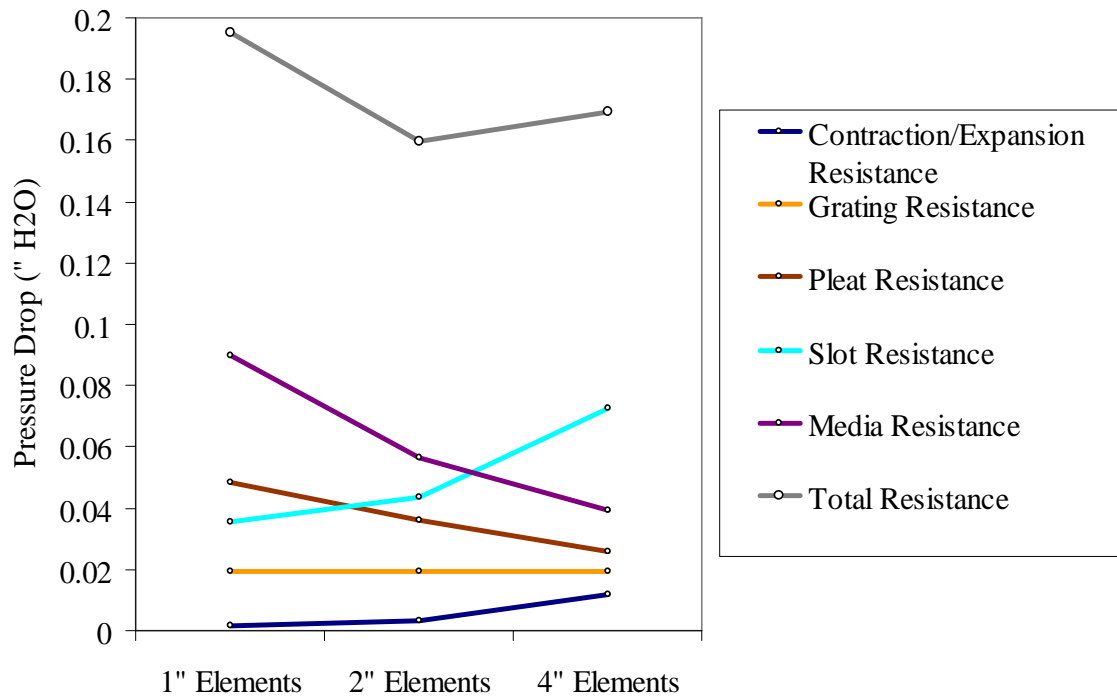


Figure 4.25: Effect of Element Depth on Contribution

Although not the case for V MESA’s modeled above, 1” deep filter elements typically outperform deeper-element arrays at higher element counts because they minimize contraction/expansion resistances and possess larger slot pitches. These geometric advantages reduce the fixed resistances that serve as the primary resistance in higher-element count arrays. Two and four inch deep elements are only able to package more media at a lower resistance than the 1” elements when the element count is low.

5. Effects of Media Constants

An increase in the media constants within a Multi-Element Structured Array will heighten the resistance of the media and raise the overall pressure drop of the system, but the magnitude of resistance rise depends heavily on the number of elements. The effects of media constants on a MESA are similar to those seen in a single filter, but the overall extent of their influence is diminished.

The lowest obtainable resistance of a 2" deep single pleated filter varied from 0.13" H₂O to 0.46" H₂O as the media constants changed from $A=1 \times 10^{-4}$ and $B=1 \times 10^{-7}$ to $A=30 \times 10^{-4}$ and $B=30 \times 10^{-7}$. Figure 4.26 modeled the same filter elements (2" deep and 1 mm thick media) in a V configuration at 500 fpm. The LOR changed from 0.09" H₂O at $A=1 \times 10^{-4}$ and $B=1 \times 10^{-7}$ to 0.21" H₂O at $A=30 \times 10^{-4}$ and $B=30 \times 10^{-7}$. The media-dominated regime showed a large increase, yet an array should not be constructed in this regime. Since the onset of pleat resistances are delayed in a MESA, the system was ultimately able to incorporate a large quantity of pleats to reduce the high-resistance media effects. The same outcome could have been obtained by employing an array with more elements. This makes MESAs an appealing platform for high resistance materials since their resistances can be eliminated by various design techniques.

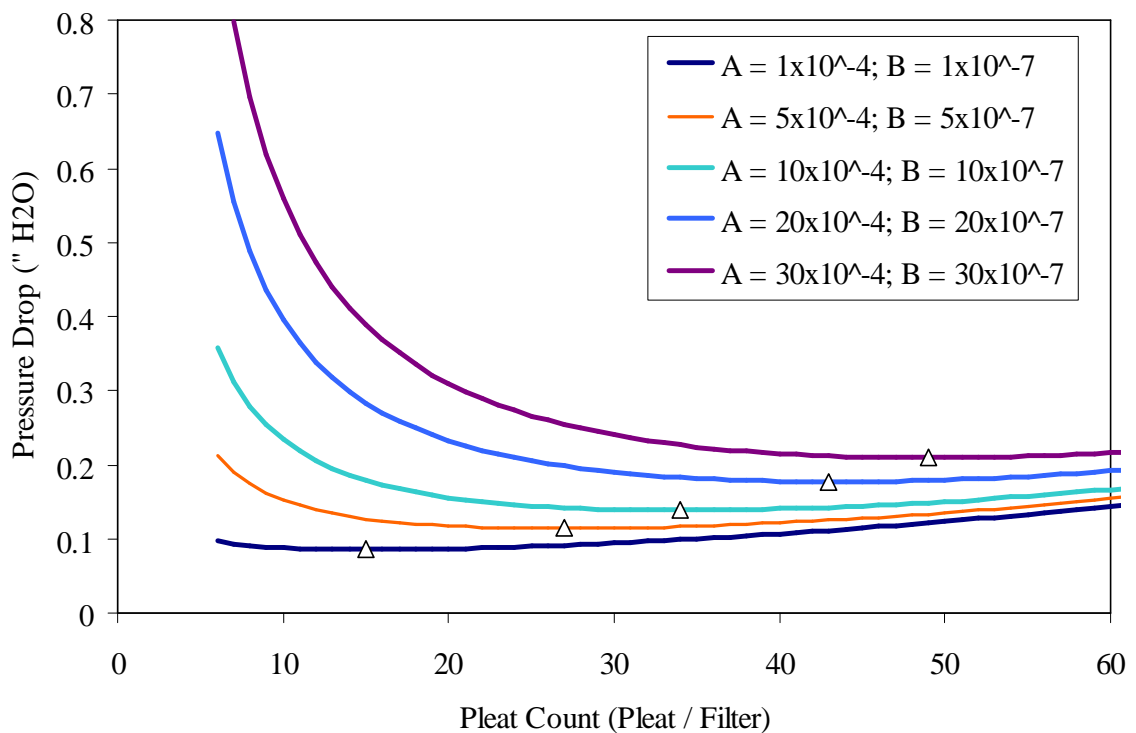


Figure 4.26: Effects of Media Constants on MESA Pleating Curve

5. Effects of Media Thickness

Media thickness has a unique ability to influence the viscous-dominated region of the pleating curve and possesses the potential to hinder the maximum available filtration area of an array. The resistance in the viscous-dominated regime increases as additional tip blockage is added and as the flow in the pleats becomes constrained. A thicker media accelerates both of these factors, but the constricted flow due to a bulkier media is the major inhibiting effect. This hastens the rate of pleat closure and limits the quantity of pleats that can be incorporated into an array. The overall effect of a thicker media shifts the viscous-dominated regime from a quasi-flat line into a more traditional, steep slope.

To illustrate the effects of media thickness, Figure 4.27 was composed by modeling various media thickness within a “W” array at a face velocity of 500 fpm. The array housed 2” elements containing media with constants of $A = 15 \times 10^{-4}$ and $B = 20 \times 10^{-7}$. Similar to the results obtained for a single filter, a thicker media shifts the optimal pleat count left and to a higher lowest obtainable resistance.

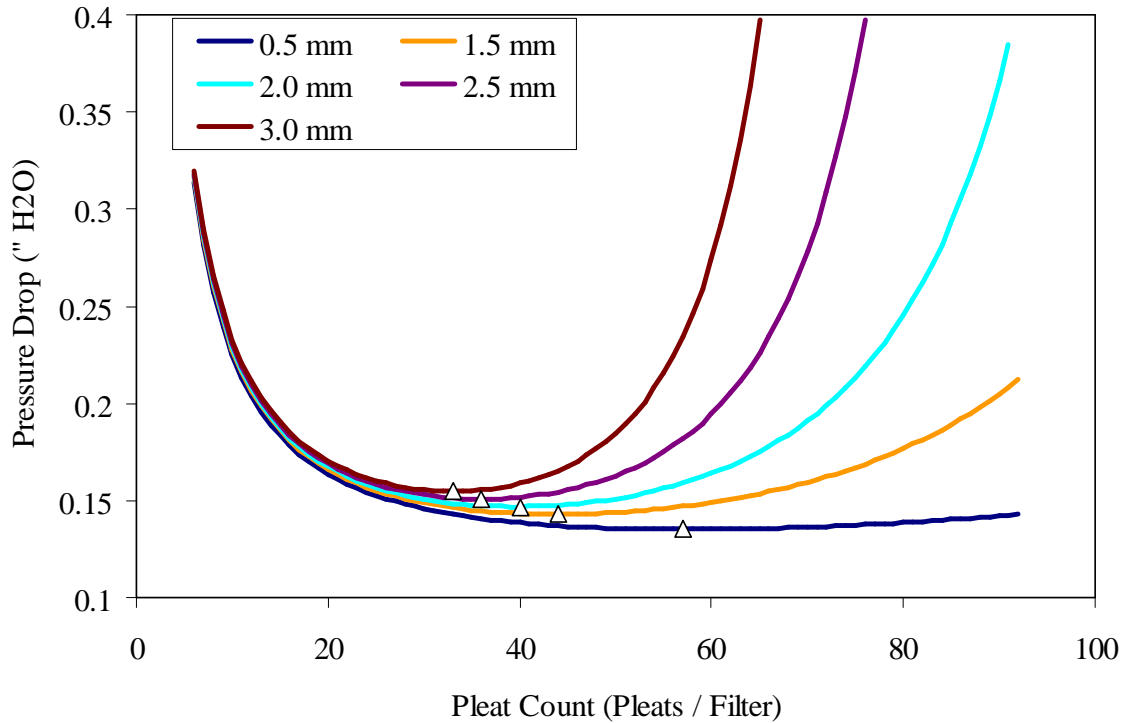


Figure 4.27: Effects of Media Thickness on MESA Pleating Curve

6. Effects of Face Velocity

Increasing the velocity within a Multi-Element Structured Array raises the overall resistance of the pleating curve. The media-dominated regime and viscous-dominated regimes in particular have a tendency to rise at an exaggerated rate. This produces the curling effects that give rise to a more distinct “U” shape. The degree of curl principally depends on the number of elements within the array being examined.

The plot below is a computation done on 2” elements loaded into a “W” array. The media possessed constants of $A = 15 \times 10^{-4}$ and $B = 20 \times 10^{-7}$ and had a thickness of 1 mm. The overall resistance grows in response to an increase in velocity. The main difference between the effects seen below and the ones observed in the single filter section is the lack of response in the viscous-dominated region. As stated earlier, the face

velocity in a “W” array is reduced by one-fourth resulting in a one-sixteenth reduction in the resistance of viscous terms. The media-regime may experience anywhere from a one-fourth to a one-sixteenth reduction depending on the magnitude of A and B. Thus, a large increase in velocity does not have the same pronounced effect on the viscous terms in an array as it does in a single pleated filter. The face velocity’s ability to curl the media and viscous regions would be further enhanced when fewer elements are utilized and diminished when more filters are employed.

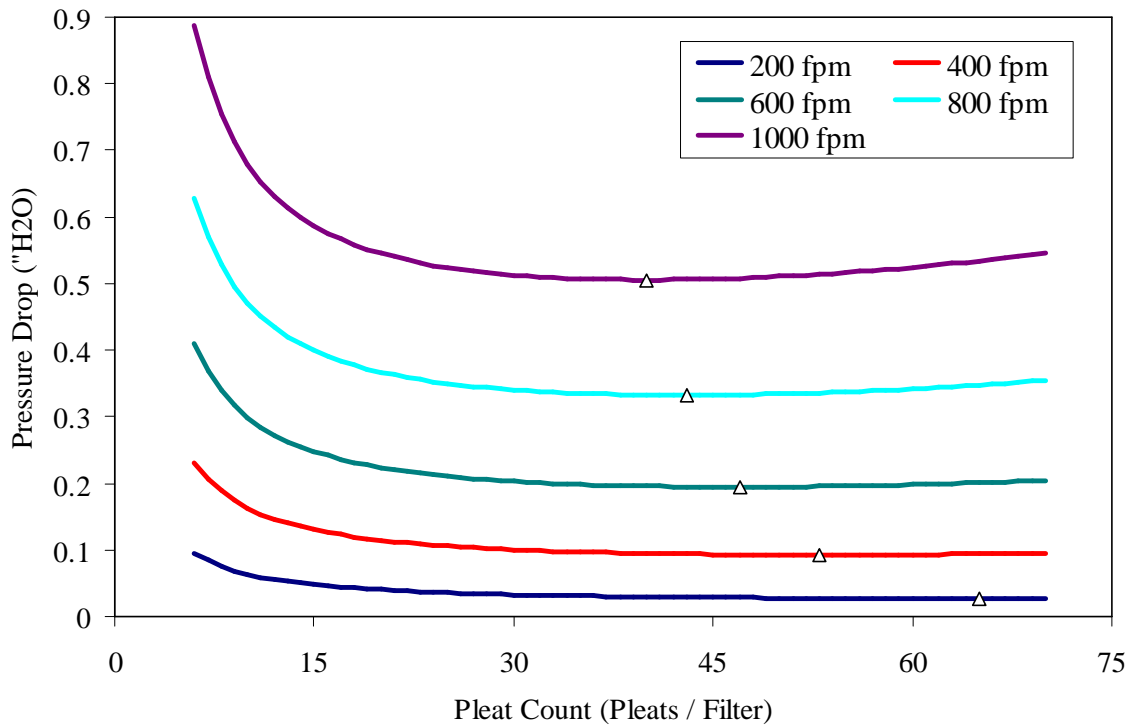


Figure 4.28: Effects of Velocity on MESA Pleating Curve

7. Influence Summary

Table 4.6 was compiled based on data and observations made during simulations ran with the model. The table is a general reference to indicate the net effect (“+”: increased resistance;

“-”: decrease in resistance) that an increase in the design parameter will have on a particular resistance. A single filter can be optimized with respect to pleat count by balancing the media and viscous terms. A MESA can be optimized with respect to element count, element width, and element depth. The optimization arises from balancing the traditional pleat and media resistances versus the fixed resistances of the system.

Table 4.6: Summary of Design Parameters and Effects due to their Increase

Design Variable	Array Edges	Slot	Pleat Tip	Pleat	Media
Element Count	+	+	-	-	-
Element Width	+ (minor)	+	-	-	-
Element Depth	+	+	-	-	-
Media Thickness	n/a	n/a	+	+	- (minor)
Media Constants	n/a	n/a	n/a	n/a	+
Pleat Count	n/a	n/a	+	+	-

CHAPTER V: THEORY AND EXPERIMENTAL FOR AIR FILTRATION PERFORMANCE

V.1. Introduction

The previous chapters identified novel packaging designs such as higher pleat counts and utilization of multiple elements that provided a means to increase the available media area while maintaining or lowering the initial resistance. The aim of the remaining chapters is to investigate these pleating and design arrangements to determine the influence of increasing pleat count, pleat height, and element count on initial pressure drop, aging profiles, and removal efficiency. This was accomplished by testing commercially available and custom-order 24"x24" filters with an in-house rig modeled after the ASHRAE 52.2 Standard (ASHRAE 2007). The filtration designs were then analyzed for energy consumption, quality factor, and useful lifetime based on the empirical data. The background information provide in this chapter will highlight key terms and models of filtration theory as well as equipment and procedures to carry out the experimentations.

V.2. Theory

V.2.1. Previous Research concerning Dirt Loading of Air Filters

The initial pressure drop of a filter only serves as the baseline for the overall power consumption. A reduction in the initial resistance is important because it translates into a net reduction of energy across the lifetime of the filter, yet it at times represents

only a fraction of the overall working pressure drop. The filter's pressure drop increases due to the accumulation of dirt over its operational lifetime. The capture of dirt is referred to as aging or loading of the filter while the pressure increase per weight of dirt catch is known as the aging or loading rate. The operational pressure drop and power consumption will therefore be a function of the initial pressure drop and the dirt loading [Novick et al. 1992.]

$$\Delta P_{\text{filter}} = \Delta P_{\text{initial}} + \Delta P_{\text{load}} \quad (5.1)$$

The rate of filter resistance increase with dirt loading has been the subject of extensive research [Novick et al. 1992, Lebedev & Kirisch 1995, Walsh et al. 1996, Japuntich et al. 1997, Davis and Kim 1999, Bémer and Callé 2000]. As a filter is challenged with particulate matter, the pressure drop will undergo two distinct regions of aging. Initially, the filter's resistance will increase marginally with the additional of dirt. This region is known as the depth filtration region because the dirt is being accumulated within the depth of the fibers during this period. The dirt, at first, acts as single particles adhered to the surface of the fibers. Subsequent particles will then begin to adhere to the initial particles forming agglomerate chains on the surface of the fibers. These dendrite chains act as secondary fibers capable of capturing additional dirt. Eventually, the pores of the filter become clogged and particles no longer load within the depths of the fibrous material [Thomas et al. 1999, Song et al. 2006].

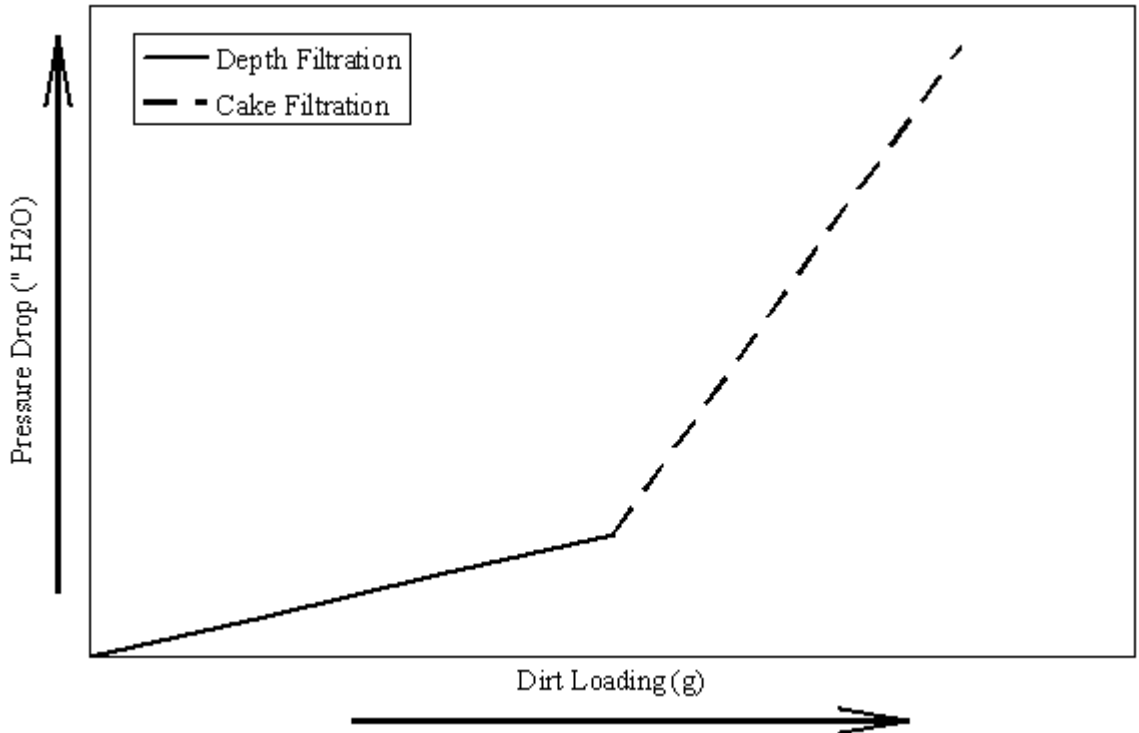


Figure 5.1: General Trend in Filter Loading

At this point, the filter transitions from the depth loading to surface loading.

Surface loading is characterized by a steep increase in resistance per weight of particles loaded. A layer, known as the cake, is formed on the surface of the filter since the dirt is no longer able to penetrate into the filter. Subsequent particles load onto the cake causing the thickness of the filtering media to increase. By Darcy's Law, the resistance will increase proportionally with the thickness of the porous media [Thomas et al.1999].

V.2.2. Particulate Removal Efficiency by Fibrous Media

A filtration system's foremost responsibility is the removal of particulate matter from the air stream. Medium and high efficiency filters accomplish this through a series of mechanisms that act in conjunction to remove particles much smaller than the average pore size of the filtration medium. These mechanisms are as followed: sieving, inertial impaction, interception, Brownian motion, electrostatic deposition, and settling [Davis

1973, Brown 1993]. The probability of a particle passing through a filter of thickness (h) composed of fibers with length (L) and radius (R) can be modeled from the single fiber theory as:

$$\text{Penetration} = 100\exp(-2 \eta LRh) \quad (5.2)$$

The collection efficiency of the fiber (η) is a summation of the individual collection efficiency of each mechanism. Sieving and settling are only effective at removing large particle from the air stream, and particles of this size usually settle out in the ductwork before reaching the filter. Electrostatic deposition is of importance in filters employing a charged surfactant coating to draw particles out of the air streams. Impaction, interception, and Brownian motion account for the majority of particle removal; thus, the collection efficiency can be described as (Davis1973):

$$\eta = \eta_{\text{DIFFUSION}} + \eta_{\text{IMPACTION}} + \eta_{\text{INTERCEPTION}} \quad (5.3)$$

The theories behind each mechanism are quite complex and not precisely understood. Discussion of the multitude of theories is beyond the scope of this research, yet a general assessment of each mechanism is presented below.

Inertial impaction is used to describe particulate capture by means of physical contact with the filtration fiber due to deviations from the streamlines. As the air flow approaches a filter fiber, the streamlines will diverge and flow will be channel around the fiber. Larger particle with significant momentum are not capable of making this direction change. The particle's inertia causes it to deviate from the streamline and collide with the front side of the fiber. The efficiency of this mechanism increases with larger particle size and faster approach velocities [Brown 1993]. The mechanism is sketched as:

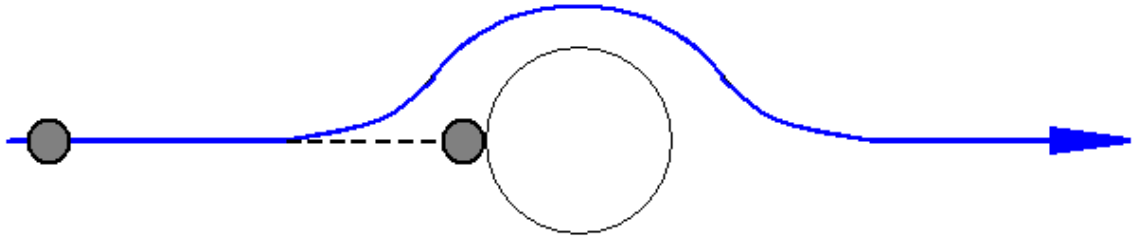


Figure 5.2: Impaction Mechanism for Particulate Capture

Interception occurs when a particle is following on a streamline and that passes close to a fiber. The particulate is captured if the streamline is within one particle radius of the fiber. The particle will deposit on the front half of the fiber by this mechanism. The efficiency is primarily dependent on the packing density of the fibers and diameter of fiber [Brown 1993].

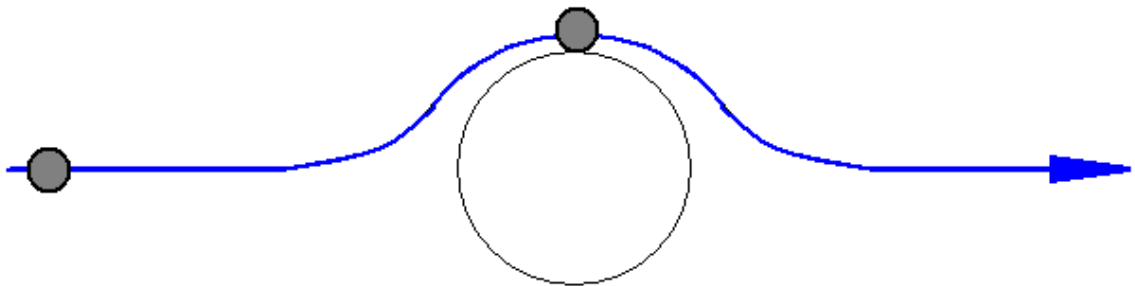


Figure 5.3: Interception Mechanism for Particulate Capture

Very small particles are carried by the air flow, but they do not strictly follow the streamlines. As the particles randomly move through the filter due to Brownian motion, there is a probability that they will encounter a fiber and adhere. This is referred to as capture by Brownian motion or diffusion. The probability of capture increases with increasing packing density of fibers, decreased diameter of fiber, and increased resident time within the fiber mesh [Brown 1993]. Particles will be deposited on all sides of the fiber when this mechanism is prevalent.

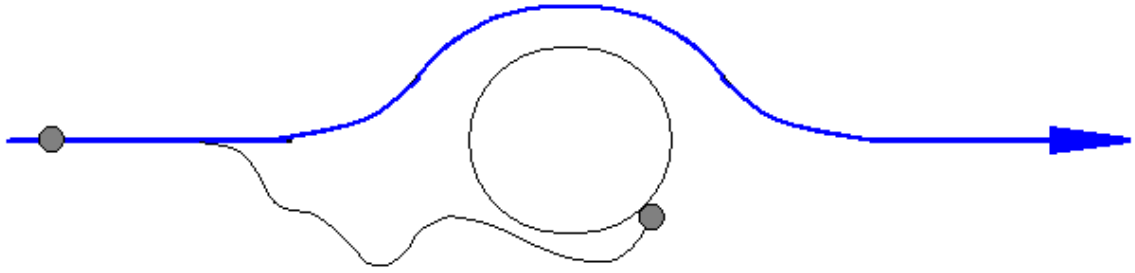
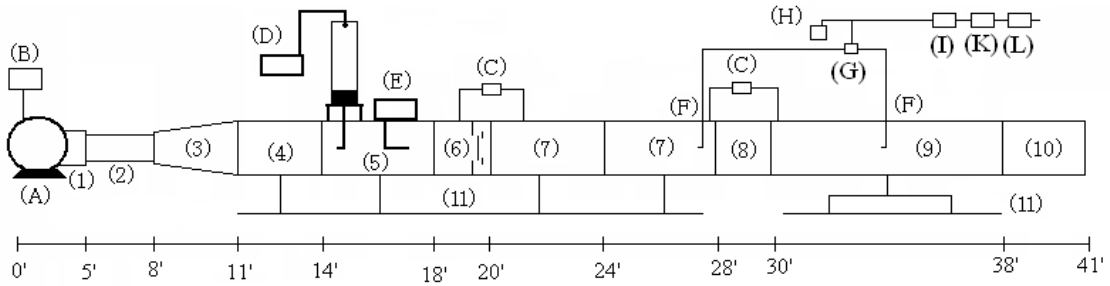


Figure 5.4: Particulate Capture by Brownian Motion

V.3. Experimental

V.3.1. Test Rig and Equipment

Performance for 24" x 24" face dimension filtration units were conducted on a test rig modeled after the ASHRAE 52.2 Standard [ASHRAE 2007]. Modifications were made to reduce the cost, simplify the overall design, and remain compatible with previously purchased in-house equipment and materials. The system was engineered to delivery 2000 cfm of specifically tailored air for evaluation of air-cleaning devices in regards to pressure drop, particulate removal efficiency, and dirt holding capacity. Provided below was a full schematic of the rig, a general description of the equipment, and an overview of the test procedures used throughout the remainder of the dissertation.



<u>Equipment</u>	<u>Segments</u>
(A) Blower	(1) Outlet Sleeve
(B) Frequency Drive	(2) Connector Sleeve
(C) Differential Pressure Transmitter	(3) Upstream Expansion
(D) Aerosol Generator	(4) Upstream Filter Box
(E) Dirt Loader	(5) Aerosol Inlet
(F) Isokinetic Probe	(6) Upstream Mixer
(G) Three-Way Valve	(7) Upstream Duct
(H) Particle Counter	(8) Test Section
(I) Inline HEPA Filter	(9) Downstream Duct
(J) Mass Flow Controller	(10) Downstream Filter
(K) Dessicant	(11) Railing System
(L) House Air	

Figure 5.5: Schematic of Full Scale Test Rig

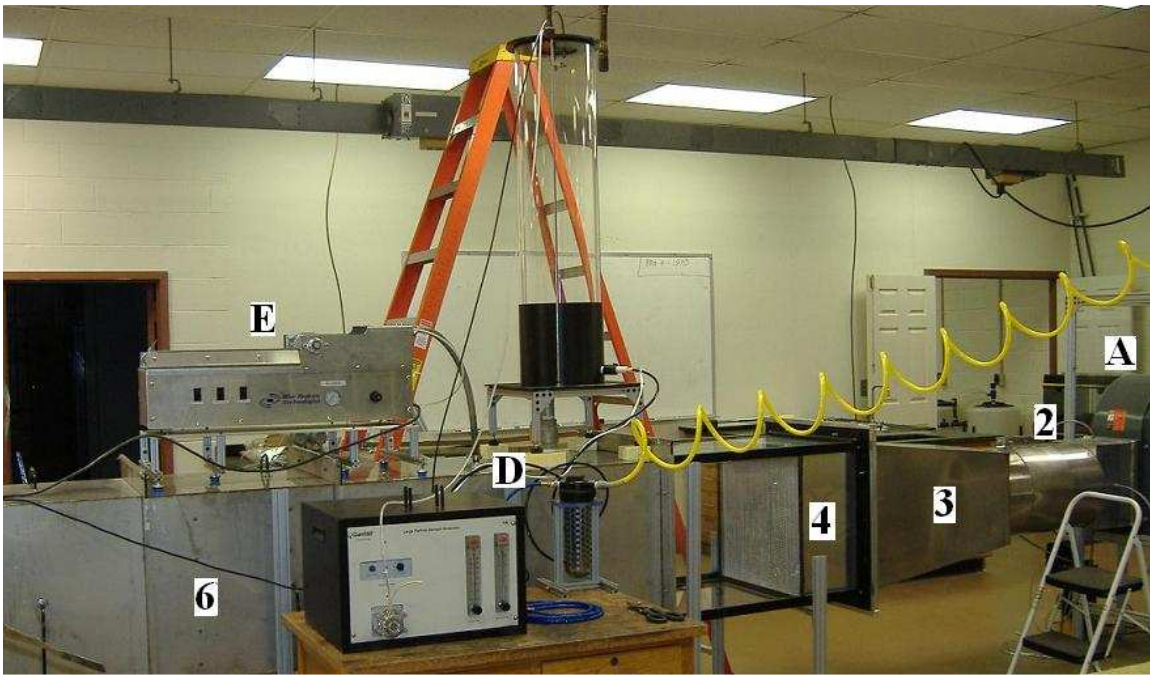


Figure 5.6: Upstream Picture of the Test Rig

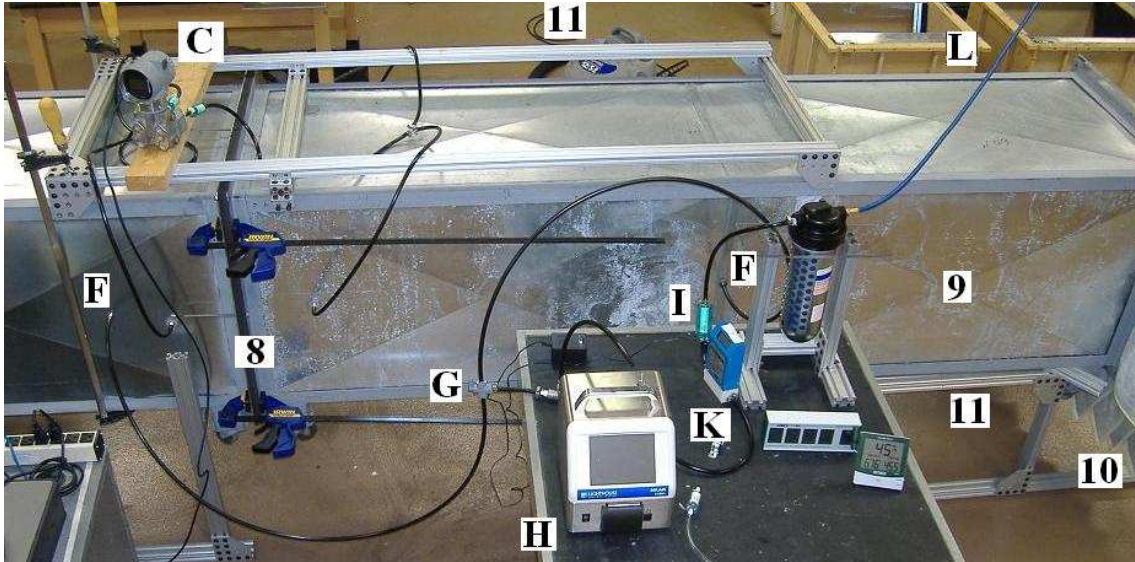


Figure 5.7: Downstream Picture of the Test Rig

The rig was set up in a positive displacement arrangement. Room air was introduced into the test duct by a Dayton systems blower driven by a 3 HP motor. The blower could deliver the required 2000 cfm correlating to a 500 fpm face velocity with up to 4.4" H₂O of static head. The motor was controlled by a Hitachi frequency drive with a range of zero to sixty hertz at 0.1 Hz increments. The frequency drive could be programmed to ramp up or down at a controlled rate.

The air exited the blower via a stainless steel four-way expansion that increased the cross section area of the rig to 24" x 24". The transition led directly to an upstream filtration box that is capable of holding a HEPA air filter or a 36" deep pocket bag filter. All dirt loading and efficiency tests employed the HEPA filter while initial pressure drop tests utilized the bag filter. The HEPA filter [American Air Filter's (AAF) Astrocel] removed 99.97% of 0.3 micron diameter particulate matter. This particle size is considered the most penetrating; therefore, the removal rate of all other particle sizes would be greater than 99.97%. The high removal efficiency was needed to remove

background contamination and provide a uniform baseline during efficiency testing.

Figure 5.5 below demonstrates the removal efficiency of the HEPA compared to the MERV 15 bag filter (AAF DriPak 2000).

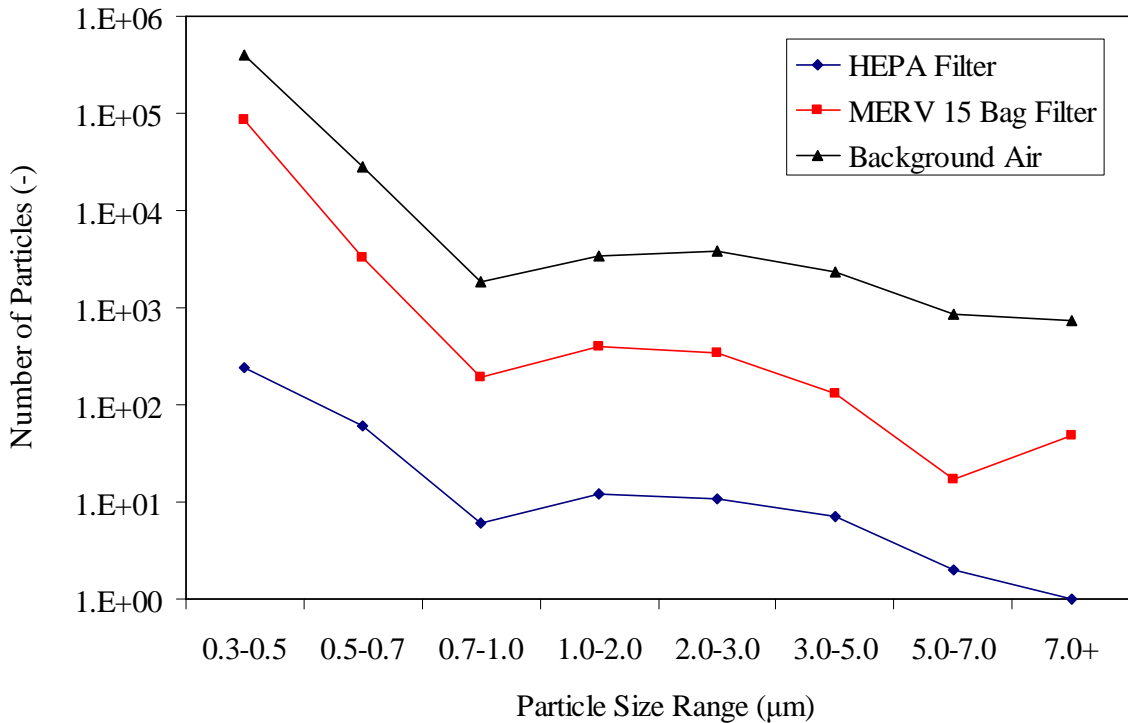


Figure 5.8: Removal Efficiency of Upstream Filters

The bag, or pocket, filter was used when large volumetric flow rates were needed, yet high purity background air was not necessary. The pocket filter allowed the system to achieve higher face velocities because of its low pressure drop (0.45” H₂O at 500 fpm). The filter prevented background air from artificially aging the test filter while being capable of supplying a sufficient volume of air that a HEPA filter would not allow.

The clean air passed from the filtration box into the aerosol inlet section. The rig was capable of challenging filters with particulate matter ranging from 0.01 µm to 100 µm. In order to create challenge particles spanning three orders of magnitude, the system

was equipped with a TSI 8108 Large Particle Generator and a Blue Heaven custom-built dust loader.

The TSI 8108 system was built to output a polydispersed challenge of KCl salt particles in the range of 0.1 to 10 μm . The particles were created by pumping a 30% KCl solution at 1.2 mL/min into a spray nozzle where it was mixed with 1 cfm of atomizing air. The nebulized particles were dispersed into a 12" diameter by 5' high plenum where the droplets were dried with 4 cfm of preheated air. A Kr- air ionizer neutralized any charges present on the aerosol. Charge removal was necessary to prevent the particle from being artificially captured by electrostatic deposition within the ductwork or the test filter. The KCl particles exited the plenum via a 1.5" NPT pipe. The pipe delivered the particles into the center of the ductwork facing the direction of flow. Distribution was enhanced by introducing the particles in this manner. The manufacturer's schematic is below.

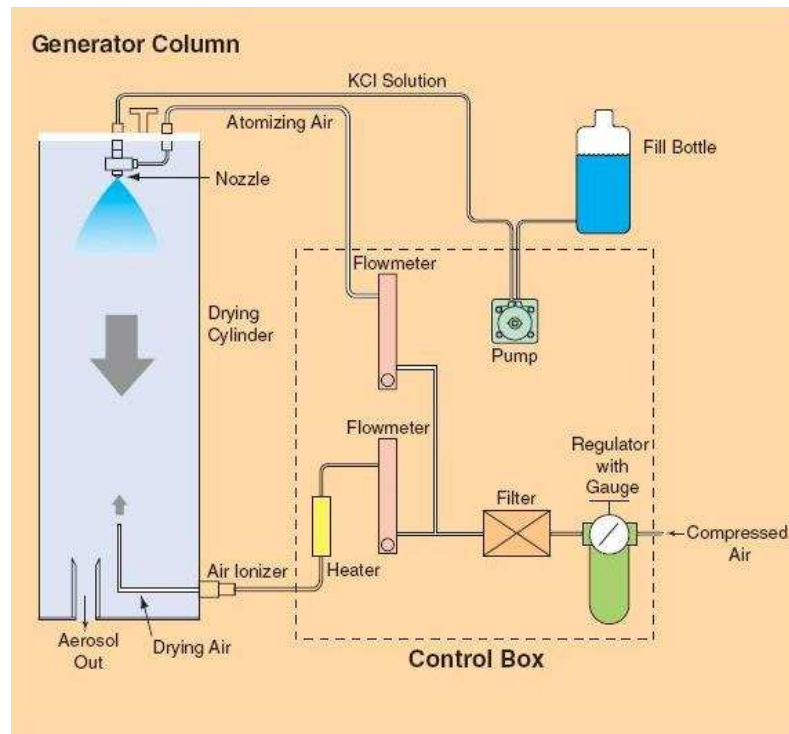


Figure 5.9: TSI 8108 Large Particle Generator Schematic

The generator produced a stable concentration of 600 particle/cm³ of 1 micron and 10 particle/cm³ of 10 micron aerosol when nebulizing the KCl solution. The unit can also be employed to nebulized other material such as monodispersed polystyrene latex (PSL) spheres in the size range of 0.01 to 20 microns.

Unlike the TSI 8108, the Blue Heaven unit was designed to artificially age the test filter with a high concentration of particulate matter. The loader was designed to meet the ASHRAE 52.2 Standard, and the critical dimension for the unit may be found there [ASHRAE 2007]. The loader was designed to introduce dirt into the rig by a venturi pump. House air was sent through a desiccant bowl to dry the air to a dew point of -45°F before being supplied to the unit at 80 PSI. The air throttling through the venturi pump caused a vacuum to be formed on the feed tray. The belt driven feed tray brought the challenge dirt into proximity of the vacuum at a steady linear rate of 0.5 ft/min. The height of the challenge on the feed tray determined the particulate concentration in the test rig.

A common artificial aging material is ASHRAE synthetic test dirt. ASHRAE dirt is a conglomeration of ASTM ISO fines (73%), carbon black (23%), and milled cotton linters (4%). ASTM ISO fines are a mixture of alumina oxide and silica dioxide. The carbon black is Raven 411 and is commonly used in toner ink. Table 5.1 denotes the manufacturer's reported size distribution for the ISO fines. The carbon black cotton linters both possessed dimensions larger than 10 microns.

Table 5.1: ASHRAE Dust Size Distribution

Particle Size micron	Composition % Less Than
1	2.5 - 3.5
2	10.5 - 12.5
3	18.5 - 22.0
4	25.5 - 29.5
5	31.0 - 36.0
7	41.0 - 46.0
10	50.0 - 54.0
20	70.0 - 74.0
40	88.0 - 91.0
80	99.5 - 100
120	100

The challenge particulates were mixed and distributed throughout the cross section of the system by the upstream static mixer. The three-part mixer began by contracting and concentrating the loaded air with a 12” circular opening orifice plate. To expand and distribute the mixed air, a 12” circular disk built from a 50% blocked perforated stainless steel was located one foot behind the orifice plate. A 50% blocked perforated stainless steel ring (outside diameter of 18” with inner diameter of 12”) followed six inches behind the disk and further distributed the loaded air. The test air reached the filtration system via two, four foot long sections designed to allow the air to further distribute and self correct. The mixer, in conjunction with the upstream duct, provided a uniform flow into the filtration test section. Table 5.2 shows that the coefficient of variances (CoV) for delivered airflow to the filtration section was less than 10% as mandated by ASHRAE Standard 52.2. The CoV measurements were performed with an Extech vane-anemometer using the method highlighted in Section II.5.1.

Table 5.2: Average Velocity and Coefficient of Variation within Test Rig

Setting (Hz)	15	20	30	40	50	60
Average Velocity (m/s)	1.05	1.39	2.04	2.80	3.49	4.22
Standard Deviation	0.06	0.11	0.11	0.21	0.29	0.32
Coefficient of Variance	6.18	8.03	5.52	7.53	8.32	7.60

The upstream duct also houses an isokinetic probe used during removal efficiency testing. The probe was located 12 inches in front of the filtration unit positioned in the center of the ductwork.

The test section was an adjustable region that can accommodate filtration units up to 36” in depth. This was accomplished through a linear motion track created out of 80/20 aluminum extrusion on which the downstream ductwork and final filter rest. The filtration units were custom built for each filter design. Further information concerning their construction can be found in the Appendix.

The air passed through the test section and traveled into the downstream ductwork. The downstream duct was an 8’ long section that housed a second isokinetic probe. The final filter, a 36” 95% efficiency pocket filter (AAF DriPak 2000), was located at the end of the duct work to capture any challenge particulate that passed through the tested filter.

The transitions between sections were outfitted with a clamping system to seal the rig and prevent the loss of volumetric flow and challenge particulates. Each section possessed a 3 inch wide flanged joining plate. Closed cell foam with a thickness of 3/8” was added to the width of each flange. The seal between the sections was created by compressing the foam to a minimum of 75% of its original thickness. The compression was created by outfitting the flange with bolt assemblies and specialized tracks. The extruded aluminum U-channel tracks doubled as a second enclosing mechanism and ran

the width of the flange. A schematic and picture of the sealing mechanism is shown below.

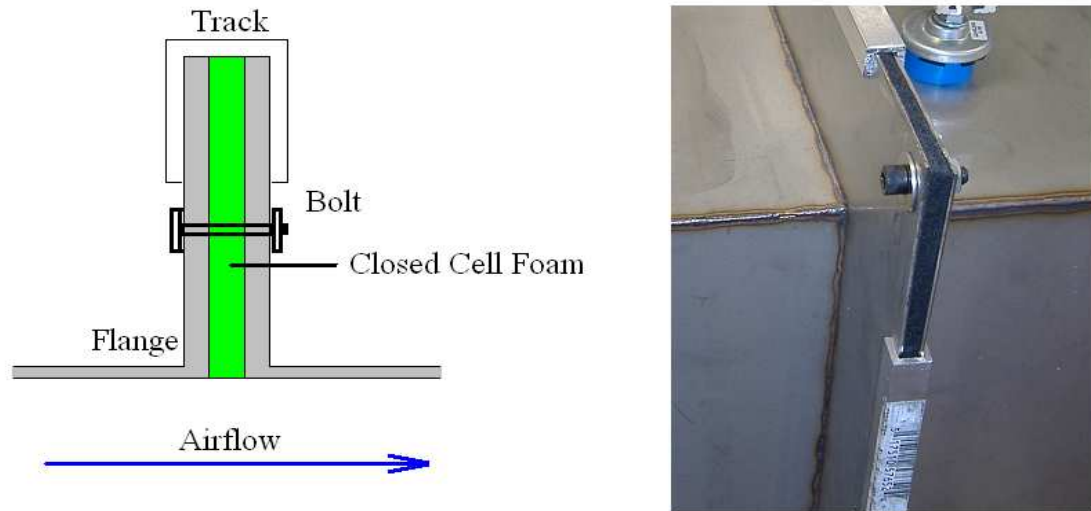


Figure 5.10: Schematic and Picture of Sealing System

V.3.2. Experimental Data Acquisition

The rig was designed to measure pressure drop, face velocity, and upstream/downstream particle count for a given filter unit. From these measurements, the filter's performance could be assessed for power consumption, dirt holding capacity, and particle removal efficiency. The following sections detail how each individual measurement was made as well as the general procedure for each test.

V.3.2.1. Volumetric Flow

Volumetric flow measurements were derived from the pressure drop across the orifice plate. The resistance to flow created by the orifice can be directly related to the face velocity by the following equation (Perry and Green 1997).

$$V = ((2\Delta P / \rho C_d))^{1/2} \quad (5.3)$$

The pressure drop across the orifice plate was measured by an Invsys differential pressure transmitter. The meter has a programmable span to include differential pressures up to 30.00" H₂O. The span was set at 3.500" H₂O because this was slightly higher than the maximum achievable resistance across the orifice with the current blower configuration. The meter transmits a 4-20 mA signal which was converted to a 1-5 V signal via a precision resistor. The voltage drop across the resistor was monitor by a Personal Measurement System PMS1208LS data logger. The data logger communicated with a PC through a USB cord where the TracerDAQ software recorded the signal.

The differential pressure was measured 6 inches upstream and downstream of the plate. To minimize error associated with flow maldistribution, a four tap configuration was employed. Each tap was located 90 degrees apart from one another and was stationed flush to the test rig. The lines running from each tap were connected together via a manifold.

The positioning of the taps included the resistance created by the flow distributors as well. This meant that previous published coefficient of discharge (C_d) could not be used; thus, the coefficient had to be determined experimentally. Experimental determination of the coefficient was achieved by creating a calibration curve formulated through two methods. The first method utilized a vane-anemometer to gather face velocity measurements at set frequencies. The coefficient was calibrated against these measurements. For thoroughness, a second calibration method was employed based on the manufacturer's blower curves.

The vane anemometer method was based on the ASHRAE 52.2 Standard technique for verifying flow distribution within a duct. The outlet to the filtration rig was

sectioned off into a 3x3 grid. The blower was set to the desired frequency, and the face velocity was allowed to equilibrate. An Extech vane anemometer was positioned at one the nine points and was allowed to reach a steady velocity. The anemometer's recorder was turned on, and a running average of the face velocity through that point was gathered over a one minute period. The procedure was conducted three times for all nine points, and an average face velocity for this technique (V_T) was computed. This value can then be used with the resistance measured at the orifice plate to compute the coefficient value calculated by:

$$C_d = \frac{1}{2} \rho V_T^2 / \Delta P_{\text{ORIFICE}} \quad (5.4)$$

The second method to verify the flow rate utilized the manufacturer supplied blower curves to compute the face velocity over the range of blower frequencies. An Omega pressure transducer measured the pressure differential at the inlet to the blower and the immediate outlet of the blower as shown below.

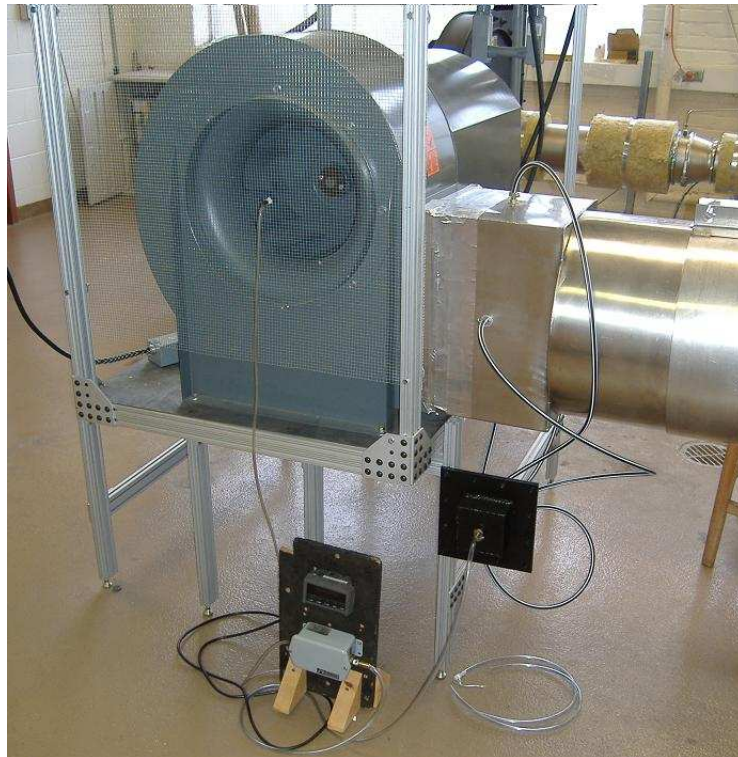


Figure 5.11: Blower and Tap Configuration

The pressure at the blower's outlet was measured by a four-tap configuration. Each tap was located 90 degrees apart from each previous tap. The taps were connected together by a manifold to get an average resistance at the exit of the blower.

The volumetric flow rates were calculated for each frequency based on the recorded pressure drop at the blower and the blower curve equations presented in Chapter II.5.1. The coefficient was computed using Equation 5.4 and a face velocity (V_T) derived from the blower curve equations. The graph below is the calibration curve created for the orifice plate based on both the vane anemometer readings and the computed blower curve values. The coefficient of discharge was determined to be 44.

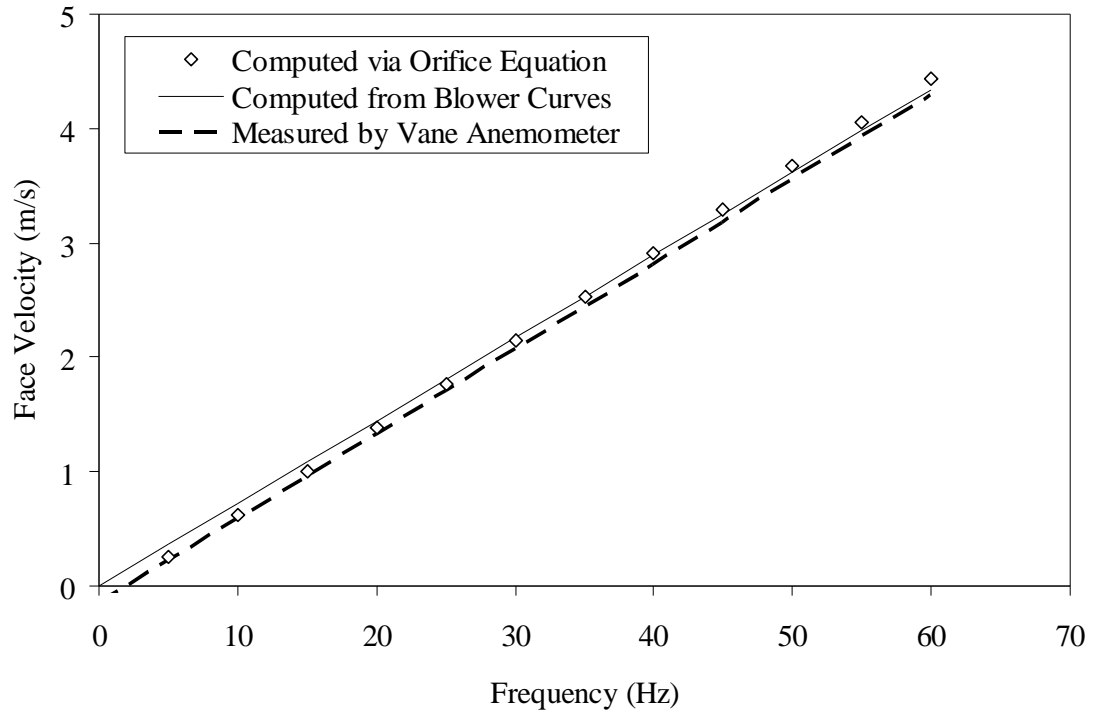


Figure 5.12 Face Velocity Calibration Curve for Test Rig's Orifice Plate

V.3.2.2. Pressure Drop across Filtration Section

The pressure drop across the filtration test section was measured with a second Invsys differential pressure transmitter. The meter also had a programmable span to include differential pressures up to 30.00" H₂O. The span was set at 1.500" H₂O because this represented the upper working limit for most air filters. The transmitter possessed a resolution of 0.001" H₂O and transmitted to the data logger in the same manner as discussed before. A two tap system was employed with mountings located on the right and left walls six inches before and after the test section. The taps were fashioned flushed with the ductwork to prevent eddies from forming at the point of measurement. Each pair of taps was then joined by a tee junction before being connected to the pressure transducer. The length of tubing used to connect each tap to the tee and each tee to the

meter were identical in length. The two tap configuration was employed to minimize error associated with flow maldistribution. A 4-tap configuration was unneeded since flow maldistribution should be at a minimal with a CoV for the rig being less than 10% over all flow rates.

V.3.2.3. Particle Count

Particle Counting was conducted with a Lighthouse Solair 3100+ light scattering optical particle counter. The system pulled a constant 1 cfm of sample air into the unit via a vacuum pump. Based on the light scattering principle, the equipment sized and counted the airborne particulate matter into the following eight distributions: 0.3-0.5 μm , 0.5 – 0.7 μm , 0.7-1.0 μm , 1.0 – 2.0 μm , 2.0-3.0 μm , 3.0- 5.0 μm , 5.0 -7.0 μm , and 7.0+ μm .

Samples were pulled from the isokinetic probes located at the center line of the ductwork 1 foot before and 4 feet behind the test section. The isokinetic probes were connected via Bev-a-Line XX tubing to a three way valve. Bev-a-Line XX tubing was chosen because of its low occurrence of particle adhesion in the line. The three-way valve allows samples to be taken from the upstream and downstream probes without moving the particle counter.

The incoming sample had to be diluted down with clean, house air before being counted because the TSI 8108 generated an overall particle concentration (10^7 particle/ft³) well beyond the counting limit of the Solair 3100+. Clean air was obtained by running compressed air through two, inline HEPA filters and a desiccant dryer. The clean air was mixed with the sample air from the ductwork before being connected to the particle counter. The dilute ratio was chosen as 21 LPM clean air and 7 LPM challenge air. This

ratio brought the concentration within a countable domain while keeping the resident time in the tubing to a minimal (0.75 seconds) to prevent particle from settling in the line.

In order to use upstream and downstream dual probe configuration as described above, it had to be determined that there was no deviation in sample counts between the two locations. Figure 5.13 below shows that the two probes show similar counts when monitoring a baseline concentration without the present of a test filter.

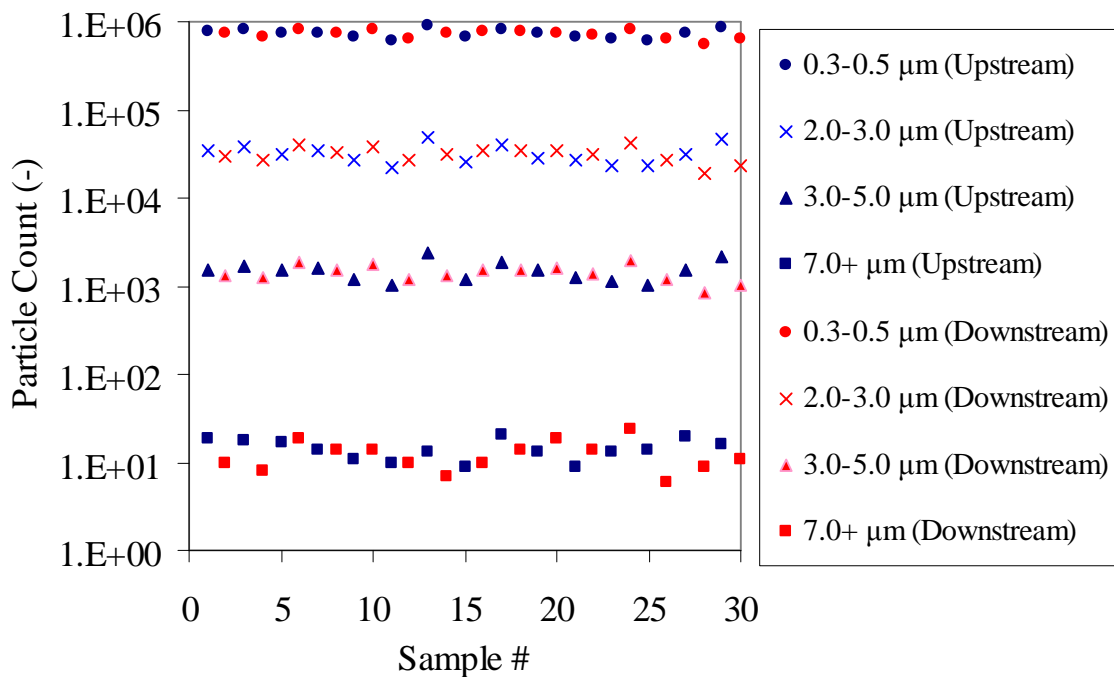


Figure 5.13: Comparison of Upstream and Downstream Counting Probes

V.3.3. Testing Procedures

V.3.3.1. Initial Pressure Drop

The initial, or clean, resistance to flow for a filtration unit was achieved by measuring the pressure drop across the orifice plate and filtration section over the entire range of frequencies. The filtration unit, either a single filter or a multi-element

structured array, was first loaded into its appropriate housing unit. The housing was secured within the test rig by bolt assemblies and quick-grip clamps. When tightened, the bolts aligned perpendicular to the flanges. This allowed the filtration units to reproducibly mate with the flanges in the desired, flushed position to ensure the elimination of flow disturbances due to misalignment. The 8 quick grip clamps were positioned equal-distance around the perimeter of the test section. Each clamp provided 300 pounds of force equating to 15.7 PSI of pressure on the foam seals.



Figure 5.14: Alignment and Clamping System

The room temperature, dew point, and atmospheric pressure were recorded with an Extech 445815 Hygrometer and a Conex JDB1 digital barometer. Based on the dew point, the partial pressure of water (P_{H_2O}) in the air was computed. The partial pressure of the air (P_{AIR}) was calculated using the computed partial pressure of water and the barometric pressure (P_{ATM}). The air density was calculated from the ratio of the

components using the ideal gas law. The equations to perform these calculations are shown below.

$$P_{H_2O} = (6.1078 \times 10^{\frac{7.5 \cdot (\text{Dew Point (K)} - 2048.625)}{(\text{Dew Point (K)} - 35.85)}}) \times 100$$

$$P_{AIR} = P_{ATM} - P_{H_2O}$$

$$\text{Air Density (in kg/m}^3\text{)} = P_{AIR} / (287.05 \cdot T(K)) + P_{H_2O} / (461.50 \cdot T(K))$$

The pressure transmitters were then turned on and zeroed. The data acquisition software was then initiated. The software recorded a 12-bit signal from each pressure transmitter at a rate of 5 data points per second. The blower was turned on and allowed to automatically ramp up to 60 Hz over the course of 420 seconds. A ramp rate of 420 seconds was chosen to eliminate trailing effects due to the transmitters not being in equilibrium at the same point in time. Further information regarding this behavior can be found in the Appendix. Once the blower reached 60 Hz, the system was shut down and the data-logging software was stopped.

A text data file was generated from the software that was further processed in Excel. The transducer's readings, which were recorded as a 1 to 5 volt signal, was changed to the corresponding pressure drop measurements. Face velocity was determined from the orifice plate calibration curve utilizing the current air density.

V.3.3.2. Testing Procedure for Dirt Loading

Dirt loading tests were performed to artificially age the filter at an accelerated rate in order to evaluate filter performance. The face velocity used during dirt loading was 500 fpm (2000 cfm). This velocity was chosen because it is a one of two common set points in the HVAC industry. It was preferred over the second set point (300 fpm)

because the larger particles in the ASHRAE dust tend to settle in the ductwork due to longer resident times.

The procedure began by weighing the test filter element(s) with a DENVER Instruments S2002 scale. The scale has a top capacity of 2000 g with a resolution of 0.01g. The filter elements were prepped for the dirt loading test in the same manner as the initial resistance. The specially design filter encasements and clamps held and positioned the filter element in the correct arrangement. Pressure transmitters were zeroed and atmospheric conditions recorded. The blower was initiated and set to deliver 1985 cfm of house air into the rig.

The clean air was mixed with a known concentration of dirt introduced into the system by the Blue Heaven dust loader. The concentration was fixed by assuring that a uniform height of dirt was evenly distributed across the tray. This was accomplished with a leveling tool shown below. Challenge dirt was first dried out in an oven at 110°C (230°F) for 30 minutes to promote dispersion of the material when subjected to the shearing forces of the venturi pump. The dirt was then loaded into the feed tray and gradually spread out to achieve a uniform layer.



Figure 5.15: Loading Tray with leveling Tool

The tray was loaded to a height of 0.25” with a tray width of 4.5”. The chain feed rate was 0.5 linear inches per minute. This equated to 0.56 in^3 of challenge per minute. When picked up and mixed with the 15 cfm of air supplied by the venturi pump and the 1985 cfm of clean air, the volumetric concentration delivered to the filter was $1.6 \times 10^{-7} \text{ ft}^3 \text{ dirt per ft}^3 \text{ air}$. A fully loaded tray (272.0 cm^3 volumetric loading dirt) was experimentally determined to weigh 82.9 grams. This equated to an apparent packing density of 0.30 g / cm^3 of tray volume. The mass load to the rig was computed to be 2.81 g / min equating to a delivered concentration of $1.4 \times 10^{-3} \text{ g ASHRAE dust per ft}^3 \text{ air}$.

Data acquisition took place by turning on the pressure transmitter when the dirt loader was turned on. There was a one minute lag between the time the dirt load started and when the tray delivered the first amount of challenge dirt to the venturi pump. This lag could easily be identified and removed from the gathered data.

Although the rig loaded the filter at a uniform rate, the blower will not continue to output the desired volumetric flow. The blower's volumetric output steadily dropped as the static head in the system increased due to the filter's loading. In order to keep the blower set at 1985 cfm, the frequency drive was manually incremented to maintain a set point resistance across the orifice plate. The rate at which the filter loads was quite low; thus, it was very easy to maintain the flow within ± 20 cfm.

The filter was aged with ASHRAE dirt until a resistance of 1.0" H₂O across the filter unit was achieved. The test was stopped and the filter unit was removed and weighed to determine the amount of dirt loaded. It was possible to periodically pull and weigh the filter, but it was determined to be unnecessary for data processing since the system loads at a uniform rate. Chapter VI showcases the uniformity of the loading rate in context with other results. Periodically pulling the filter introduces errors into the data collection due to potential disturbances of the cake formation on the filter's surface. Additionally, it ran the risk of dropping the filter and ruining the test.

V.3.3.3. Removal Efficiency Testing

A filtration removal efficiency test was performed to identify the ability of the filter to remove particles based on their diameter. The test began by loading the desired filters into their respective filtration unit. The units were then clamped and sealed within the ductwork in the same manner described for the initial resistance testing and loading test. The blower was initiated and allowed to reach a face velocity of 500 fpm. The TSI nebulizer was then started and the challenge KCl particle concentration was allowed to equilibrate over a five minute period before data collection started.

Data collection was conducted with a Solair 3100+ particle counter. The process was initialized by taking a 20 second sample count from the upstream isokinetic probe. The three-way valve was then switched to allow a sample from the downstream isokinetic probe to be obtained. Before the downstream sample was gathered, the counter performed a 10 second self-purge to remove any remaining particles out of the line from the previous sample. The counter then measured a 20 second count of the downstream particles. The process was repeated until 50 counts were taken from the upstream and downstream probes.

The data from the Solair 3100+ was downloaded via Lighthouse LMS Exchange software. The data was transferred to Microsoft Excel where it was further processed. The removal efficiency for a given size range was calculated based on the differential of the downstream count to the average of the before and after upstream count. This is shown in the formula below:

$$\text{Penetration} = [0.5(U_{i-1} + U_{i+1}) - D_i] / [0.5(U_{i-1} + U_{i+1})] \quad 5.5$$

CHAPTER VI: FILTRATION PERFORMANCE OF NOVEL, SINGLE FILTER DESIGNS

VI.1. Introduction

Section III.3 showed that by pleating beyond the initial acceptable resistance, a filter could be constructed that incorporates more media while decreasing the initial pressure drop. The capture of dust and debris by the filter increases the resistance of the media and power consumption of the filter. Common notation would assume that an increase in media area would result in a reduction of the rate that the filter loads and an extension of the useful operational life of the filter. This assumption must be verified before these novel designs can be utilized to their maximum potential. The following chapter examines these packaging designs to determine how the additional media area translates into enhanced energy performance.

VI.2. Materials and Methods

The filters utilized during this project were specially order from Quality Filters in Robertsdale, AL. The elements possessed depths between 1” and 4” and employ pleating strategies that span the media- and viscous-dominated regimes of the U curve. The media used was Kimberly Clark Intrepid® 411SF and Type 355H. The following table lists the filters, dimensions, and pleat counts. The filters were loaded with ASHRAE dirt purchased from Blue Heaven Technology. Each filter was analyzed for initial resistance and subjected to a loading test as outline before.

Table 6.1: Critical Parameters of Filters Utilized

Filter	Depth	Width	Height	Pleat Count	Media Type
1	13/16" (1")	23.75" (24")	23.75" (24")	20	411 SF
2	13/16" (1")	23.75" (24")	23.75" (24")	28	412 SF
3	13/16" (1")	23.75" (24")	23.75" (24")	36	413 SF
4	13/16" (1")	23.75" (24")	23.75" (24")	44	414 SF
5	13/16" (1")	23.75" (24")	23.75" (24")	52	415 SF
6	13/16" (1")	23.75" (24")	23.75" (24")	60	416 SF
7	1.75" (2")	23.375" (24")	23.375" (24")	15	417 SF
8	1.75" (2")	23.375" (24")	23.375" (24")	20	418 SF
9	1.75" (2")	23.375" (24")	23.375" (24")	25	419 SF
10	1.75" (2")	23.375" (24")	23.375" (24")	30	420 SF
11	1.75" (2")	23.375" (24")	23.375" (24")	35	421 SF
12	1.75" (2")	23.375" (24")	23.375" (24")	40	422 SF
13	3.5" (4")	23.375" (24")	23.375" (24")	10	423 SF
14	3.5" (4")	23.375" (24")	23.375" (24")	16	424 SF
15	3.5" (4")	23.375" (24")	23.375" (24")	22	425 SF
16	3.5" (4")	23.375" (24")	23.375" (24")	28	426 SF
17	13/16" (1")	23.75" (24")	23.75" (24")	20	355 H
18	13/16" (1")	23.75" (24")	23.75" (24")	28	356 H
19	13/16" (1")	23.75" (24")	23.75" (24")	36	357 H
20	13/16" (1")	23.75" (24")	23.75" (24")	44	358 H
21	13/16" (1")	23.75" (24")	23.75" (24")	52	359 H
22	13/16" (1")	23.75" (24")	23.75" (24")	60	360 H

VI.3. Results and Discussion

VI.3.1. Initial Resistance of 411SF Filters

Figure 6.1 through 6.3 demonstrated the initial “U” curves for each set of filter depths composed of 411SF media. In addition, the model presented in Chapter III was utilized to predict the initial resistance. The model was able to estimate the resistance quite well without the need for modification factors. One of the limitations discussed in Chapter IV was the potential inability to apply the model to filtration systems with face dimensions different than 20”x20”. The figures show that this is not the case for filter with dimensions of 24”x24”.

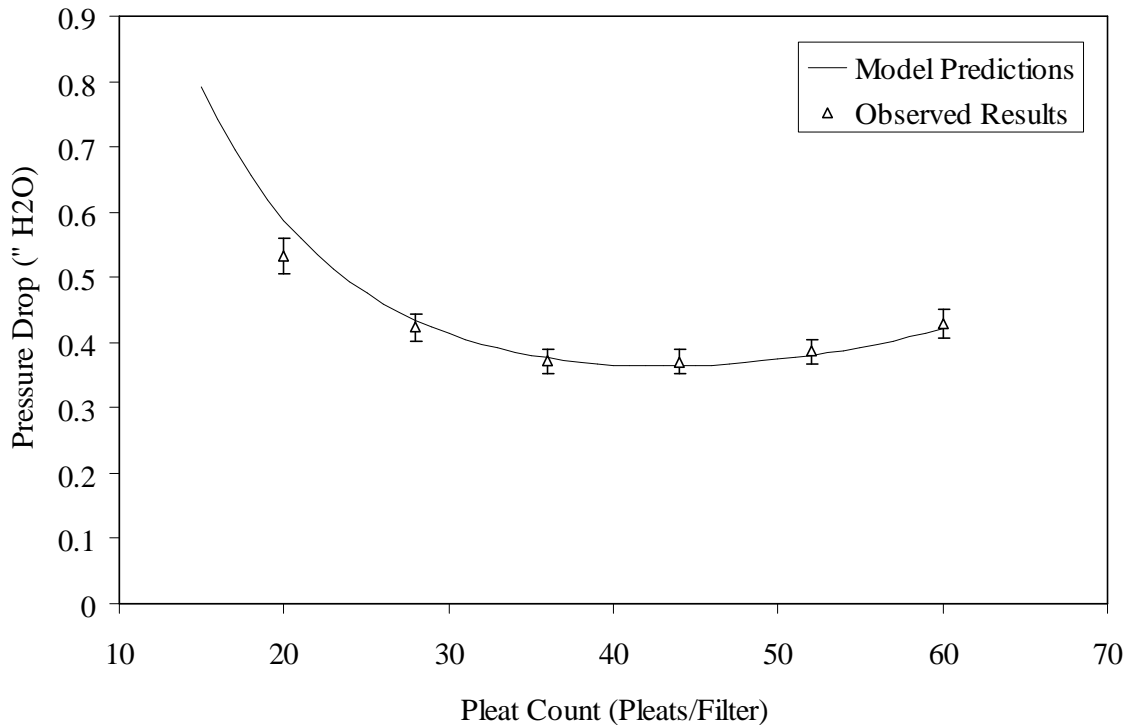


Figure 6.1: Pleating Curve for 24"x24"x1" Filters at 500 fpm
Filters composed of 411 SF media

Minor discrepancies were observed when modeling the 24"x24"x2" filters; however, the values for the most part fell within the $\pm 5\%$ error bars. Of particular note, the pressure drop of the 24"x24"x2" filter with 35 pleats could most certainly be attributed to improper construction. The pleating was erratic with several of the pleats very tightly spaced while others remained open. The deviation of the 24"x24"x4" 15 pleat filter is attributed to the variation in element housing. Quality filters constructed this filter with a different filter housing which possessed combs and a higher degree of blockage than the other 24"x24"x4" filters. The combs were removed prior to testing, but the filter still had a additional housing effects that could not be removed.

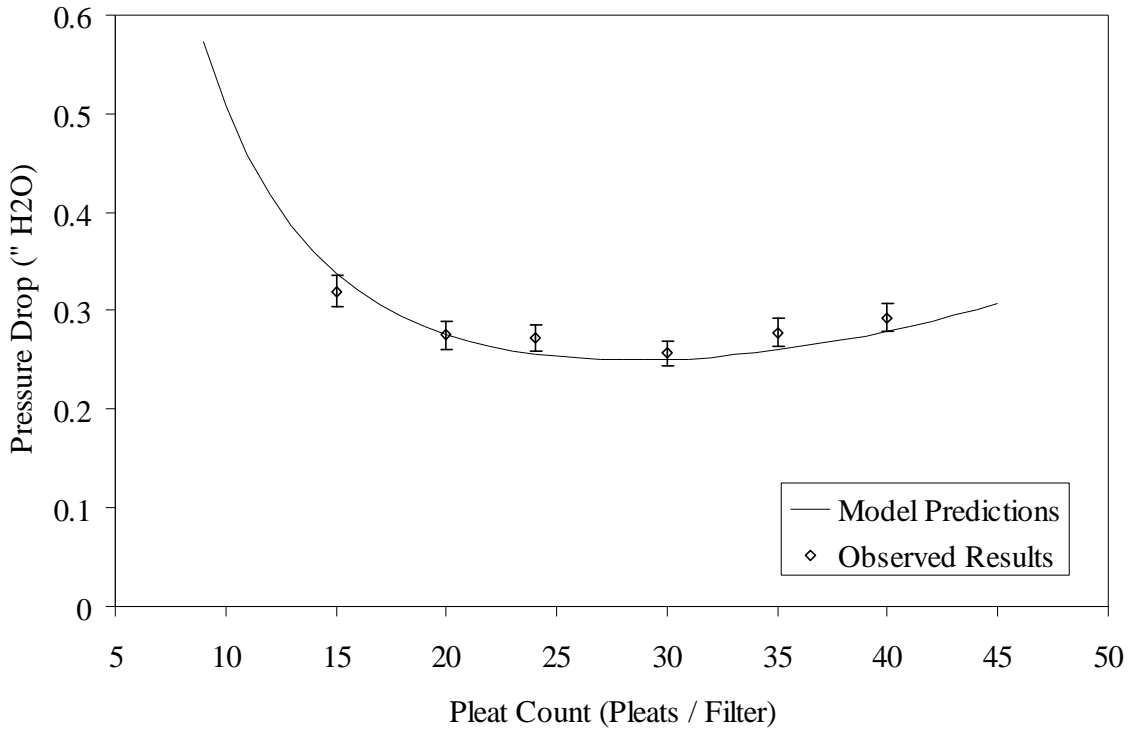


Figure 6.2: Pleating Curve for 24''x24''x2'' Filters at 500 fpm
Filters composed of 411 SF media

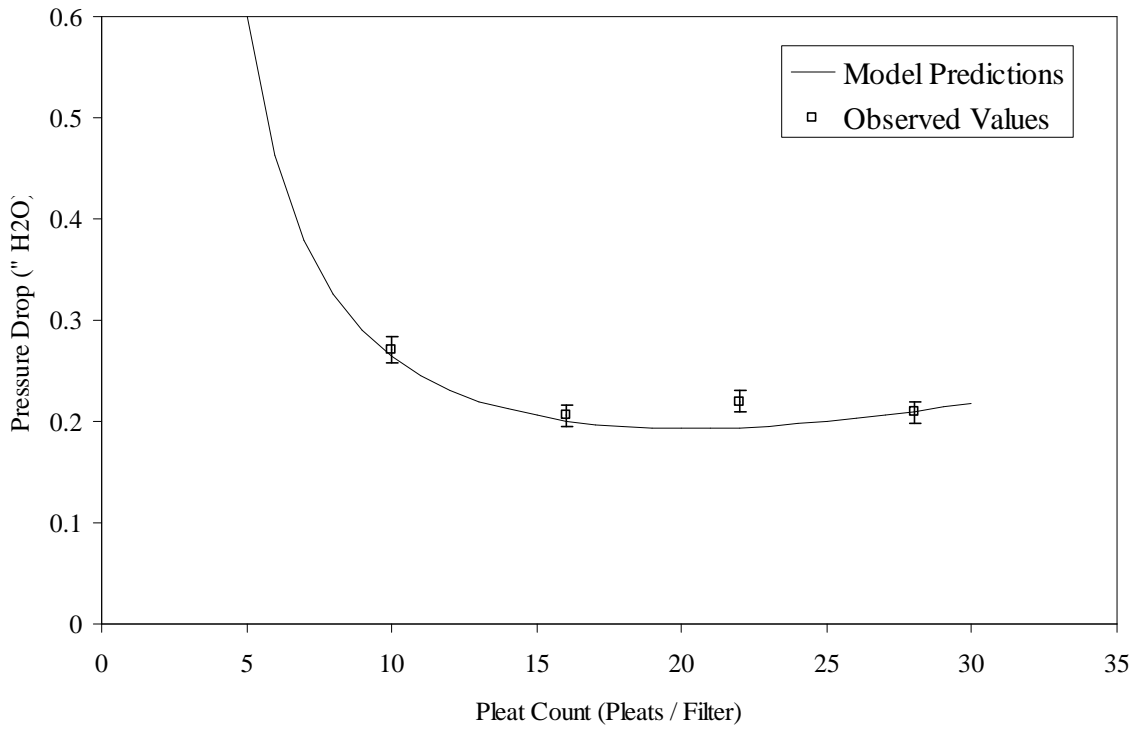


Figure 6.3: Pleating Curve for 24''x24''x4'' Filters at 500 fpm
Filters composed of 411 SF media

VI.3.2. Dirt Loading

Figure 6.4 presents the dirt loading results obtained on the 24"x24"x1" deep filters. It was presumed that the additional filtration media would allow an element to hold more dirt. It can be seen that the higher pleat counts do hold more dirt than the lower pleat counts. The 20, 28, 36, 44, 52, and 60 pleat filter were able to catch 22.8, 40.7, 52.0, 59.5, 64.0, and 58.4 grams of dirt respectively before reaching their final resistance of 1.0" H₂O.

The ability to capture more particulate matter, however, did not have a linear relationship with increasing available media. The effect can be seen when comparing the 52 pleat element to the 60 pleat element. The 60 pleat element not only started at a higher resistance, but it remained at a higher resistance over the course of the filter aging. If the dirt holding increased linearly with media, the 60 pleat should age slower and eventually operate at a lower resistance.

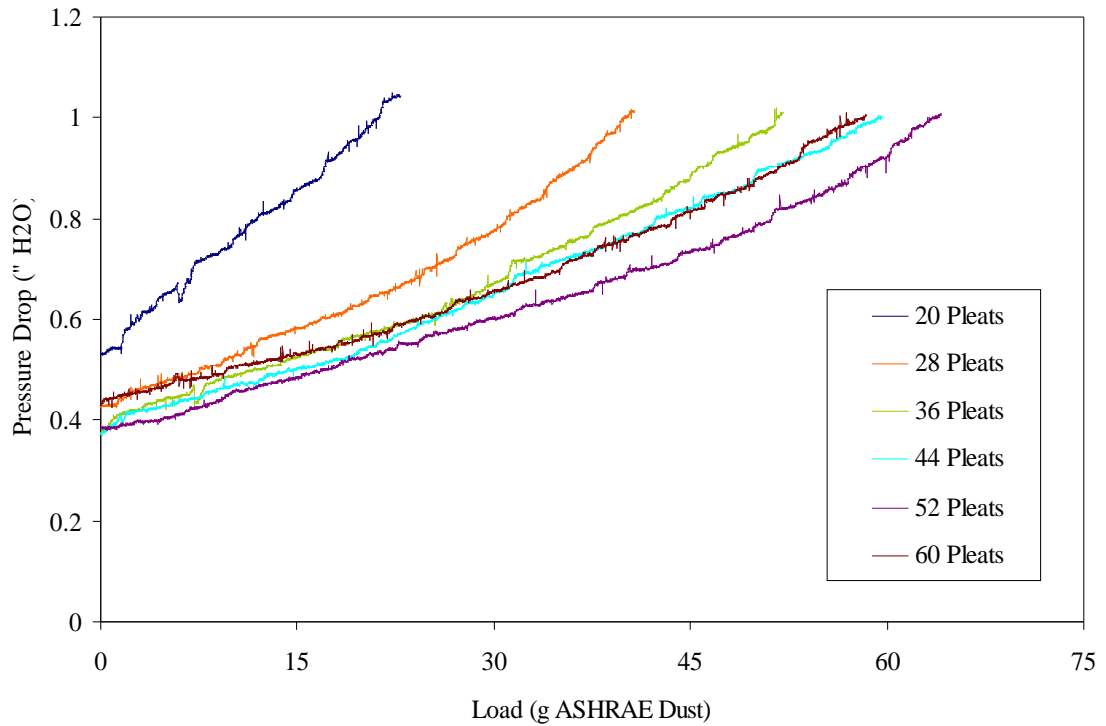


Figure 6.4: Dirt Loading for 24"x24"x1" Filters

Figure 6.5 better demonstrates this behavior by plotting the nominal increase in resistance versus the normalized loading per media area. The nominal increase in resistance is the current resistance minus the filter starting resistance, or more simply:

$$\Delta P_{\text{NOMINAL}} = \Delta P_{\text{FILTER}} - \Delta P_{\text{INITIAL}} \quad 6.1$$

The nominal resistance eliminates the discrepancies created by variations in the initial resistance and allows the data to be viewed as increase in pressure per unit of loading. The normalized dirt loading is defined as the weight capture divide by the available media. By plotting the data in this manner, the filter can be assessed based on the pressure performance and utilization of the media employed.

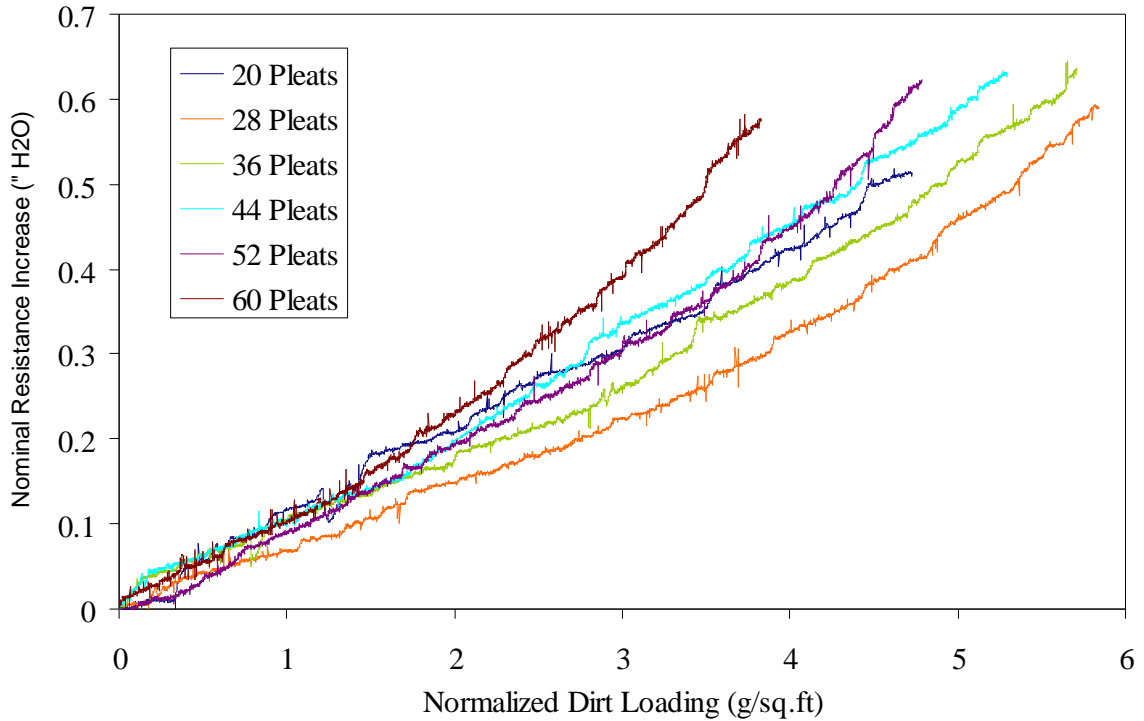


Figure 6.5: Normalized Loading Profiles of 24"x24"x1" Filters (411SF Media)

The normalized rate of loading between the various pleat counts is clearly affected by the degree of pleating. The incorporation of extra media lowered the rate of loading as seen by comparing the 20 pleat curve to the 28 pleat curve. This can be explained by Darcy's law. Previous research states that dirt loads within the filter and then on the surface. Both of these effects will influence the media or Darcian term of the filter's pressure drop by decreasing the permeability and increasing the thickness. The Darcian term is a first order function of media face velocity. The additional media area slows the face velocity through the media; thus, the resistance induced by a thicker, lower permeability media due to dirt clogging is reduced because of the lower media face velocity. The net outcome is a slower normalized aging of the unit.

This hypothesis is supported by examining the slopes of the 20 and 28 pleat filters while operating in the depth filtration regime. The slope of the 20 pleat filter, fitted by

Excel as shown below, was calculated at 0.1068” H₂O per g/ft² loaded. The slope of the 28 pleat filter was determined to be 0.0735” H₂O per g/ft² loaded. The normalized loading rate was thus reduced by 30%. The face velocity through the 20 pleat filter is calculated to be 93.3 fpm. The inclusion of extra 8 pleats into the design reduced the face velocity to 66.6 fpm. This equated to a 29% decrease in face velocity.

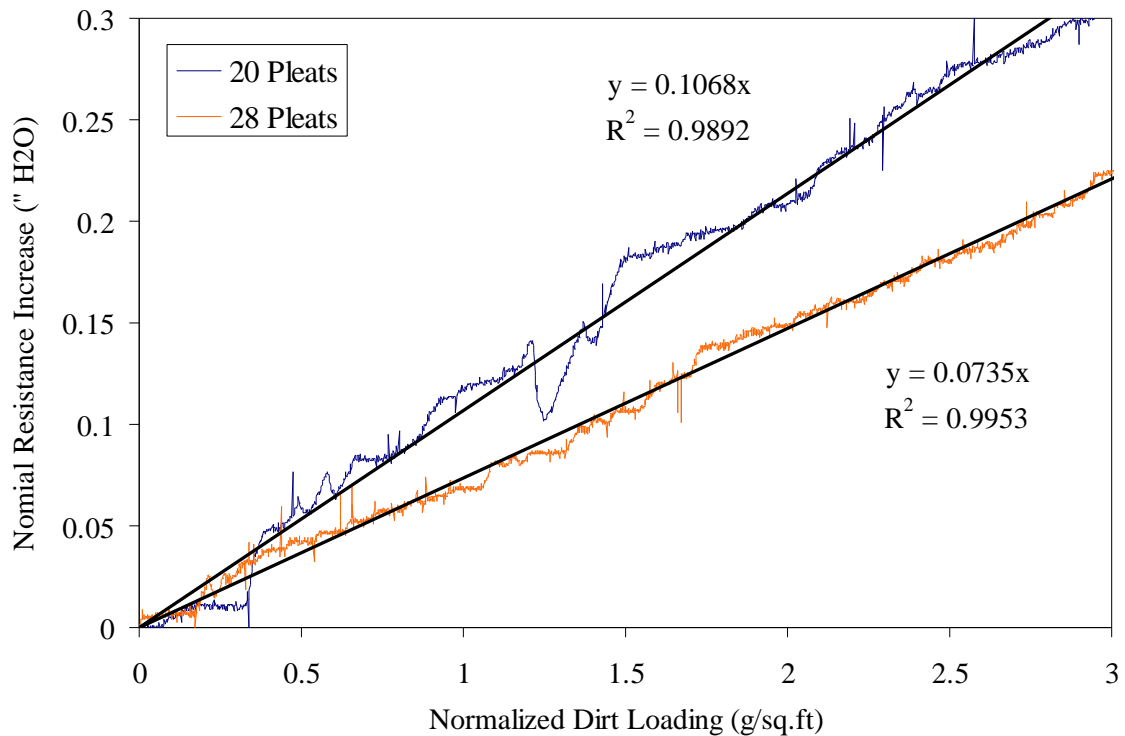


Figure 6.6: Depth Filtration Regime for 20 and 28 Pleat Filter

By this approach, increasing the pleat count further should result in an even greater reduction in media face velocity and subsequently normalized aging rate of the filter. Again, this was not observed. Counter intuitively, the normalized aging rate begins to increase after the 28 pleat filter. Although the 36 pleat filter still possessed a lower aging rate than the 20 pleat, all pleat counts above 36 have a faster normalized aging rate than the 20 pleat filter.

The one of two hypotheses for this effect is preferential blockage of the material brought on by an increase in the pleating angle beta (β). The media is more exposed to the incoming dirt challenge at lower pleating angles. An increase in the angle aligns the fibers to be more directly behind their upstream neighbor. Large particles, such as those found in ASHRAE dirt, cannot follow the streamlines and preferentially load on the surface fibers of the filter. This blocks the inner portions of the filter from subsequent particles, and the filter prematurely transitions to cake formation. Figure 6.7 demonstrates this hypothesis. The green circles represent the array of fibers within the filtration media. The black dots are large particulates that are captured by impaction or interception. The blue line represents the flight path of the particle. As can be seen in this simple schematic, the higher angled media eliminates the interiors of the media from being accessed by the particles. A shell builds on the front of the fiber causing the media to prematurely transition from depth to cake filtration.

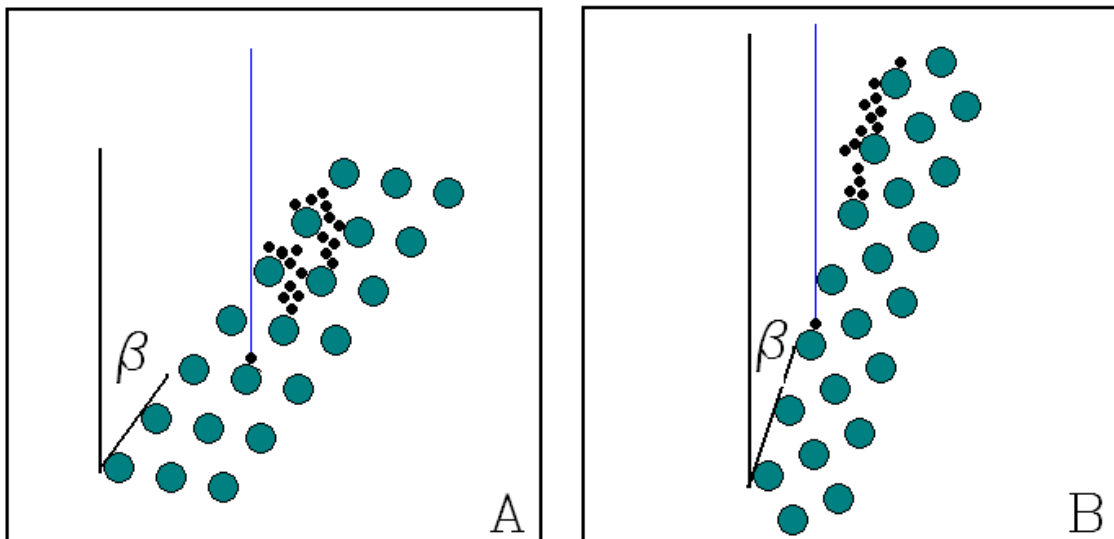


Figure 6.7: Schematic of Preferential Loading. (A) Low Beta Angle (B) High Beta Angle

Figure 6.8, which only re-graphs three of the six filters for clarity, indicates a premature transition from depth filtration to cake filtration does occur. The normalized loading rate of the 20 pleat filter is a linear line; thus, no transition occurs over the loading ranges explored (0 to 4.5 g/sq.ft). The 28 pleat filter shows a transition from depth to cake filtration at approximately 4 g/sq.ft. The higher angled 60 pleat filter transitions very quickly from depth to cake filtration at 1.75 g/sq.ft. Although difficult, it can also be deduced from Figure 6.5 that the transitions from depth to cake for the 36, 44, and 52 pleated filter occurs at 3.5, 3.0, and 2.75 g/ sq.ft respectively

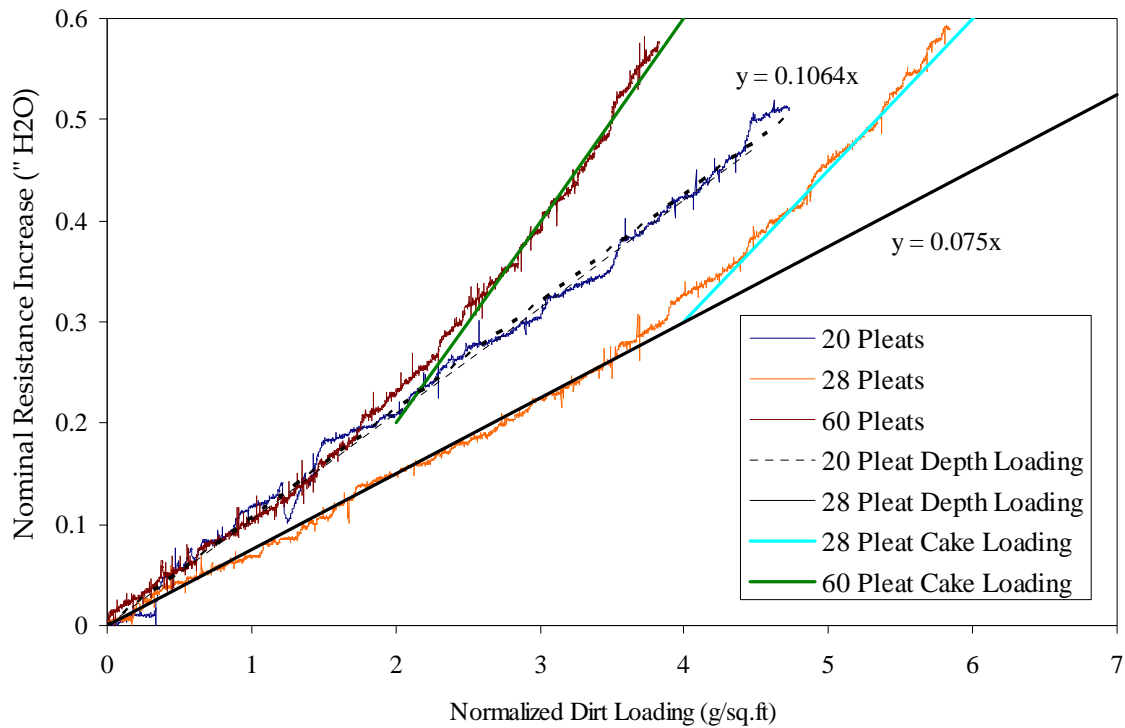


Figure 6.8: Normalized Loading Profiles of Select 24''x24''x1'' 411SF Filters with Transition Lines.

The loading results of filter composed of type 355H media were very similar to the results obtain with filter composed of type 411SF media. High pleat count filters

demonstrated a decrease in the normalized loading rate in the depth regime, yet transition to cake loading prematurely.

The second hypothesis proposes that the premature transition to cake filtration is caused by the reduction in face velocity through the filter. The reduction allows the uppermost fiber layers to filter the incoming air with a higher efficiency. The topmost layers thus become clogged more rapidly.

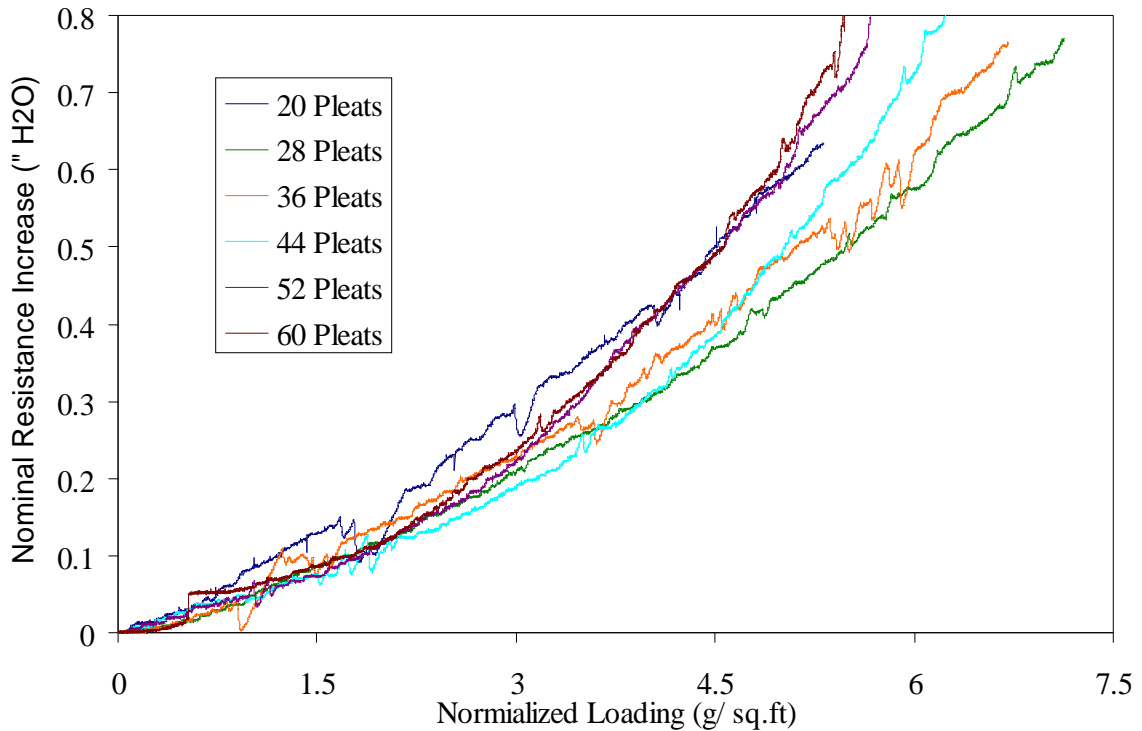


Figure 6.9: Normalized Loading Profiles of 24"x24"x1" Filters (355H Media)

The results were also similar when the analysis was performed on deeper pleated filters. In Figure 6.10, higher pleat counts display more dirt holding capacity than their lower pleat count counterparts. The only exception is the 35 pleat count filter; however, this is most likely a result of its poor construction. The benefits of pleating into the viscous-dominant regime can be visualized by comparing the 30 pleat count to the 40. Although

the 40 pleat filter has a higher initial resistance, the overall pressure drop is lower throughout most the course of operation.

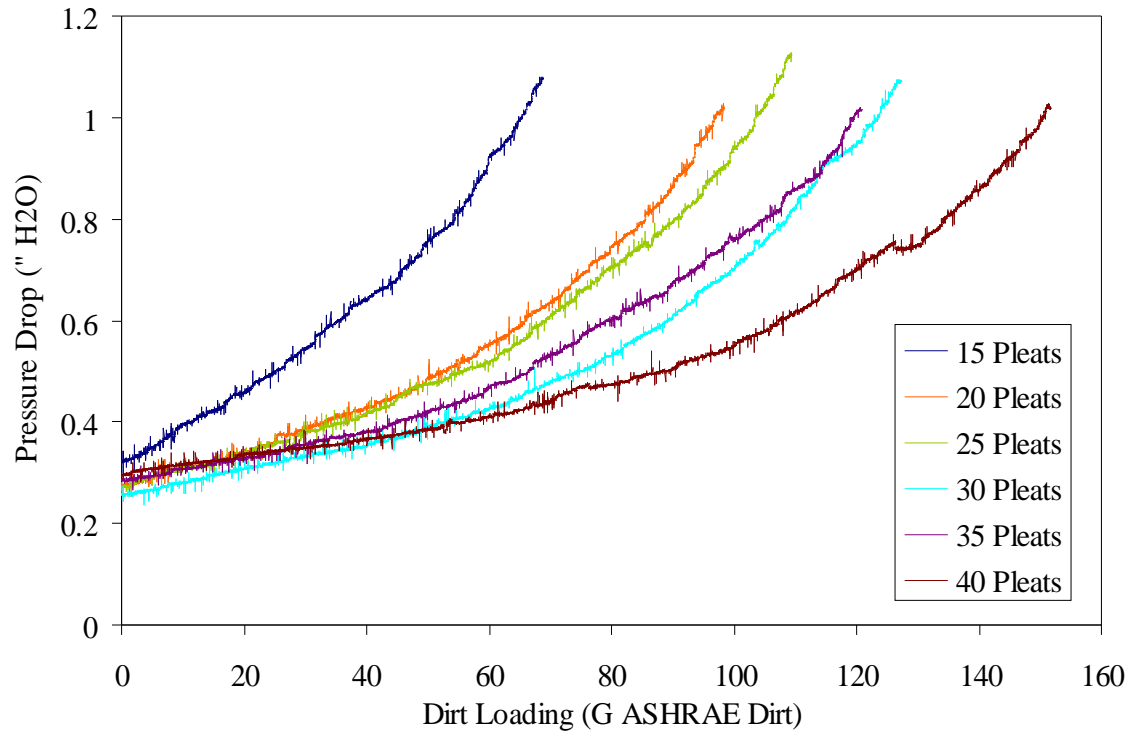


Figure 6.10: Dirt Loading for 24"x24"x2" Filters (411SF Media)

Looking at the normalized dirt loading of the 2" filters, all higher pleated filters show a slightly slower rate of aging in the depth filtration regime; however, all of these filters transition to the cake regime sooner than 15 pleat filter. This observation correlates to the discussion above. The 15, 20, 25, 30, 35, and 40 pleat filters transition out of the depth regime respectfully at the 5.5, 4.5, 4.0, 3.75, 2.5, and 3.0 g/ sq.ft

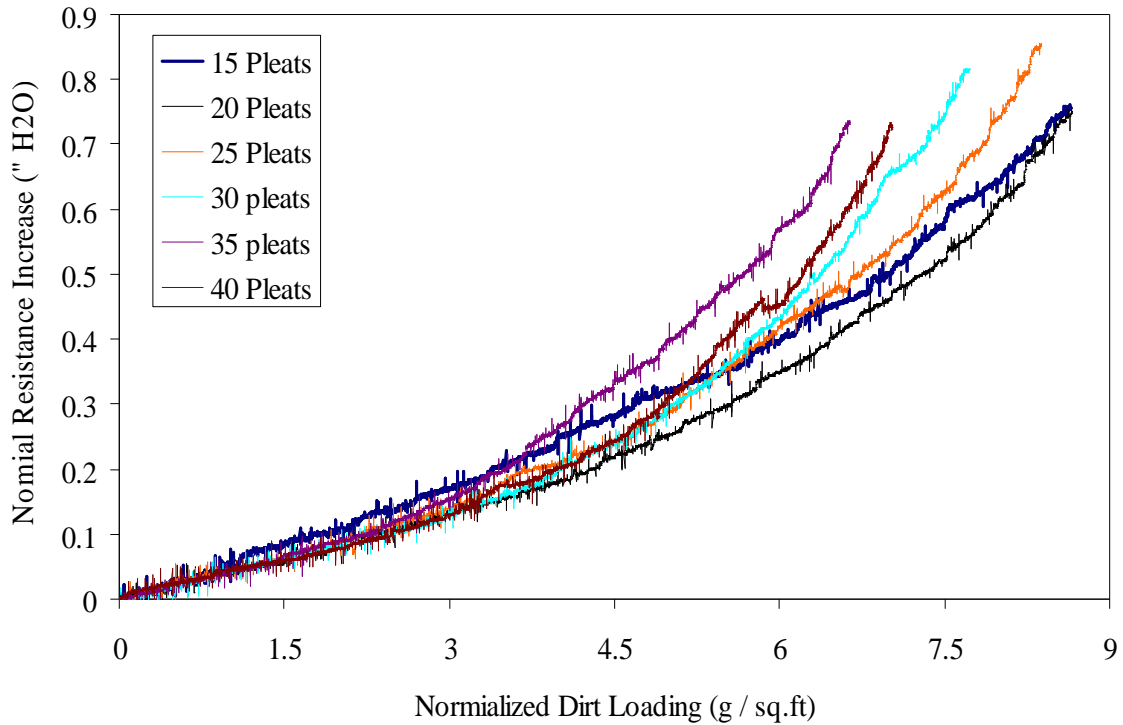


Figure 6.11: Normalized Dirt Loading for 24\"x24\"x2\" Filters (411SF Media)

Figure 6.12 and 6.13 shows that the 4 inch deep filters exhibit the same trends.

Another interesting behavior is well displayed in the normalized dirt loading of the 4 inch filters. The slope of the aging rate is nearly identical during the depth filtration regime; however, once the filters transition to the cake regime their slopes become much greater at higher pleat counts. The 10 pleat filter shows a cake slope of 0.28\" H₂O increase per g/sq.ft loaded. The 28 pleat filter shows an increase of 0.46\" H₂O per g/sq.ft. Thus, it is very important when utilizing higher pleat counts to change the filter sooner after the transition has occurred.

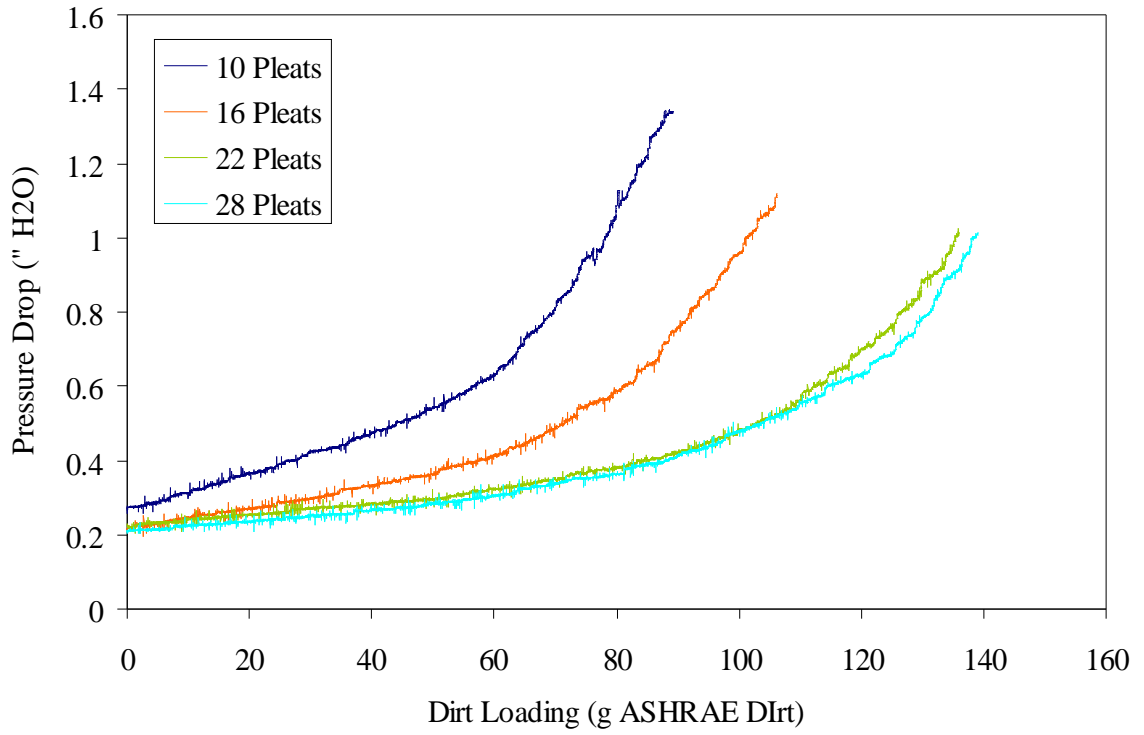


Figure 6.12: Dirt Loading for 24"x24"x4" Filters (411SF Media)

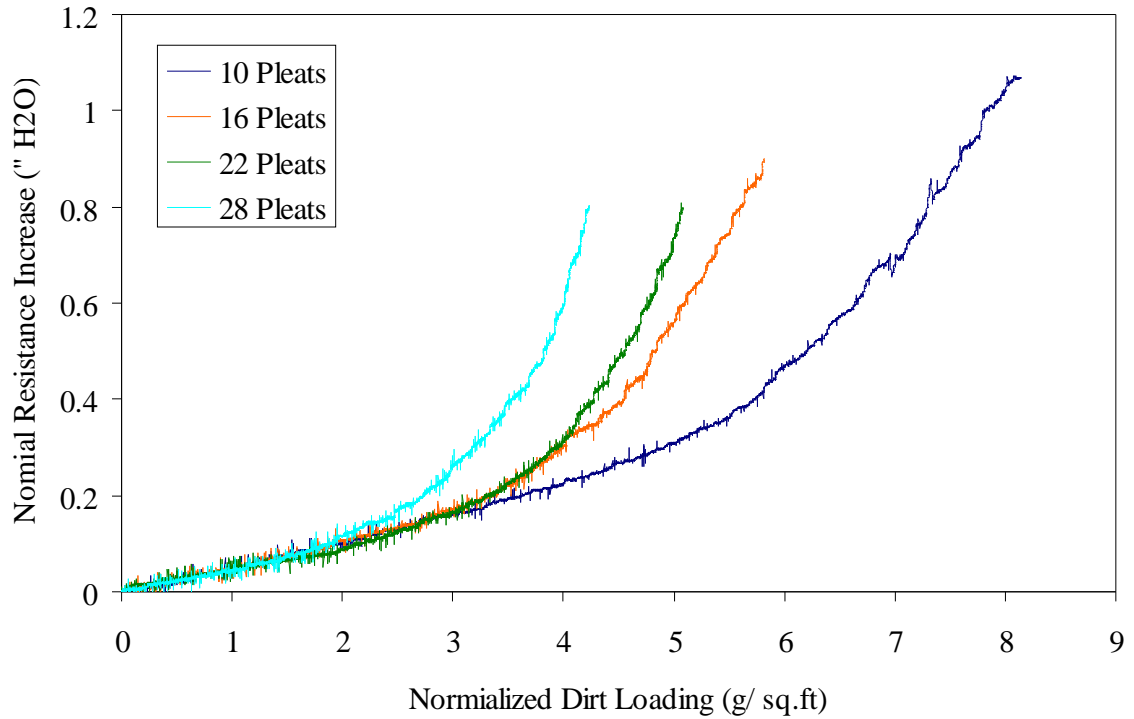


Figure 6.13: Normalized Dirt Loading for 24"x24"x2" Filters (411SF Media)

Figure 6.14 examines all 22 filters to see if there is a relationship between the transition point and the pleating angle. The data indicates that there is a general trend between increasing pleat angle and delaying the onset of the transition point. The graph also indicates that the depth of the filter plays a role with the onset of the transition point. In general, filters with deeper pleats transition at a higher media utilization for a given pleating angle.

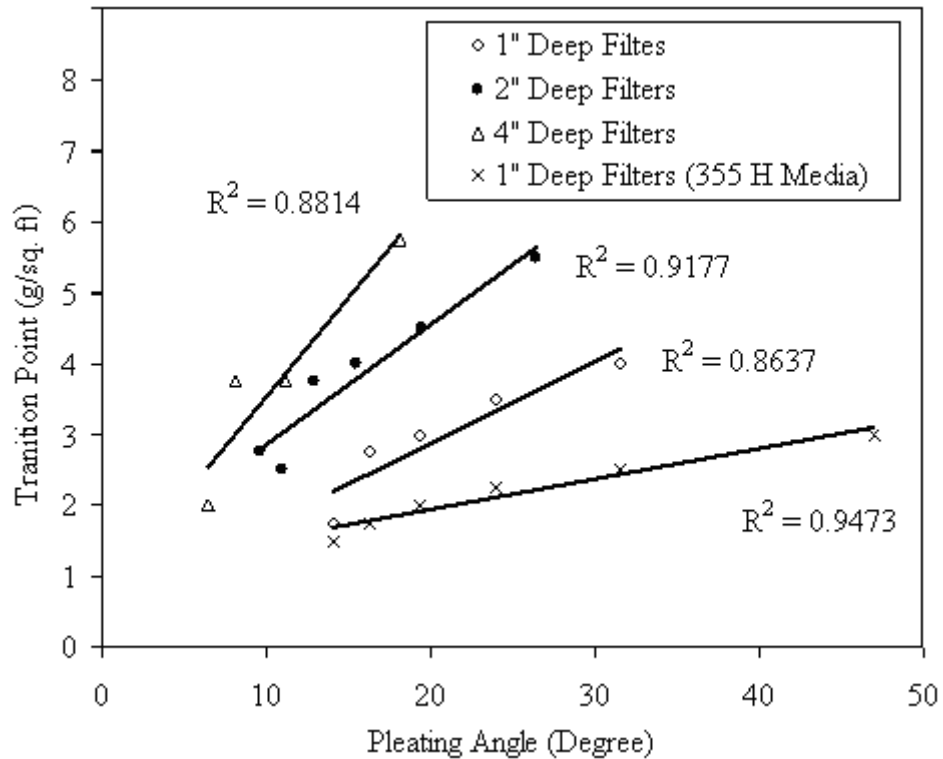


Figure 6.14: Relationship between Pleating Angle and Transition Point

Initially, there was some concern that the observed results were actually an artifact of the measurement process. Filters, unlike sieve trays, can not capture 100% of the test dirt. The two media (411SF and 355H) types utilized in this experimentation are only rated for removing >95% and >90% of ASHRAE dust. As discussed, a filter becomes more efficient at removing dirt as it ages. Since the filters were only weighed at the start and end of the test and believed to load at a uniform rate, in theory the majority of dirt could have been captured in the cake regime when the filtration efficiency is at its highest. This would artificially skew the results so that the steep increase in resistance looks to be the caused by only a small amount of dirt.

To eliminate this possibility, the 24"x24"x2" 411SF filter were not loaded continuously from start to finish. The filters were loaded from their initial resistance

until a resistance of 0.5” H₂O was reached. The filters were removed, weighed, and reinserted to be loaded again. This process was continued with stopping points of 0.75 and 1.0” H₂O. The results of the loading rates for the 15, 20, and 40 pleated filters are shown in Tables 6.2 through 6.4.

Table 6.2: Interval Loading Rate for 24”x24”x2” 411SF Filter with 15 Pleats

Time (min)	Filter Weight (g)	Loading Interval (min)	Loading (g)	Load Rate (g/min)
0	383.52	n/a	0	n/a
11.41	411.08	11.41	27.56	2.42
20.06	435.63	8.65	24.55	2.84
26.42	452.28	6.36	16.65	2.62

Table 6.3: Interval Loading Rate for 24”x24”x2” 411SF Filter with 20 Pleats

Time (min)	Filter Weight (g)	Loading Interval (min)	Loading (g)	Load Rate (g/min)
0	462.79	n/a	0	n/a
19.91	516.06	19.91	53.27	2.68
30.44	543.32	10.53	27.26	2.59
37.34	561.15	6.9	17.83	2.58

Table 6.4: Interval Loading Rate for 24”x24”x2” 411SF Filter with 40 Pleats

Time (min)	Filter Weight (g)	Loading Interval (min)	Loading (g)	Load Rate (g/min)
0	701.92	n/a	0	n/a
24.99	773.16	24.99	71.24	2.85
45.37	825.25	20.38	52.09	2.56
56.69	853.52	11.32	28.27	2.50

The three filters showed that they did not age at a faster rate as they were loaded with dirt and their efficiency increased. The average loading rate for each filter was 2.62, 2.62, and 2.63 g/min with coefficients of variance of 8.1, 2.0, and 7.2 %.

VI.3.3. Estimations of Useful Lifetime and Power Consumption

Based on the loading data obtained, estimations for the useful lifetime and the average energy consumption of these filters were made. The analysis had to make several assumptions before the values could be calculated. A filter was assigned a useful life of 6 months or until 1" H₂O pressure drop was reached. The filter was changed at this point. The operational conditions were set at 2000 cfm with an average run time of 12 hours per day.

The total atmospheric dust concentration was estimated to be 30 ug/m³ of air with the filter capturing a third of the dirt concentration. Total atmospheric dirt concentration will vary widely based on the environment. Remote conditions can possess less than 5 ug/m³. At the other end of the spectrum, dirt concentrations of 100 ug/m³ and above have been recorded in urban settings (Bouchertall 1989, Kim et al. 2002). The rate of loading is highly dependent on the composition of the incoming particle challenge, but it was assumed that the loading rate based on the previously presented data held valid. The national average power cost was taken from the Department of Energy's Energy Information Agency website as \$0.11/kWh (April 2009 estimate). Energy consumption only accounted for the pressure volume work to move air across the filter. The blower efficiency and the losses due to power conversion were estimated at 70%. Filter costs listed below were price paid to procure the filters from Quality Filters during the Fall of 2007. The power and energy analysis shown in Figure 6.15 through 6.17 and Tables 6.5 through 6.7 were prepared base on these assumptions.

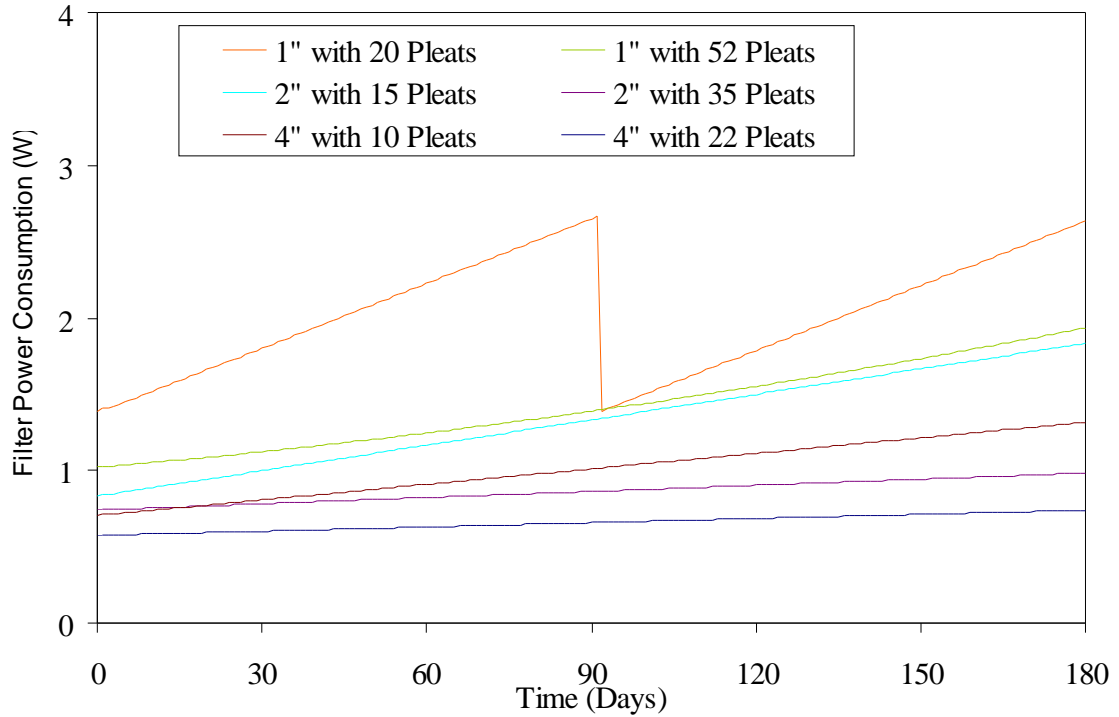


Figure 6.15: Average Power Consumption of 24"x24"x1" Filters

Table 6.5: Estimated Lifetime Costs for 24"x24"x1" Filters

Filter Type	Pleats (#)	Filter Cost (\$)	Energy Usage (kWh)	Energy Cost (\$)	Total Cost (\$)
Standard 1" Deep	20	\$3.42	566	\$62.33	\$65.75
Premium 1" Deep	28	\$4.79	508	\$55.95	\$60.74
Custom 1" Deep	36	\$6.14	438	\$48.22	\$54.36
Custom 1" Deep	44	\$7.52	422	\$46.48	\$54.00
Custom 1" Deep	52	\$8.89	398	\$43.84	\$52.73
Custom 1" Deep	60	\$10.26	436	\$47.96	\$58.22

The analysis demonstrated that using higher pleat counts will result in a decreased energy usage. The energy reduction will more than offset the initial increase in procurement costs. For example, an additional upfront cost of \$5.47 to purchase a 52 pleat filter instead of a 28 filter decreased the energy requirement by 168 kWh over the course of six months. This translated into a reduction in energy cost of \$18.49.

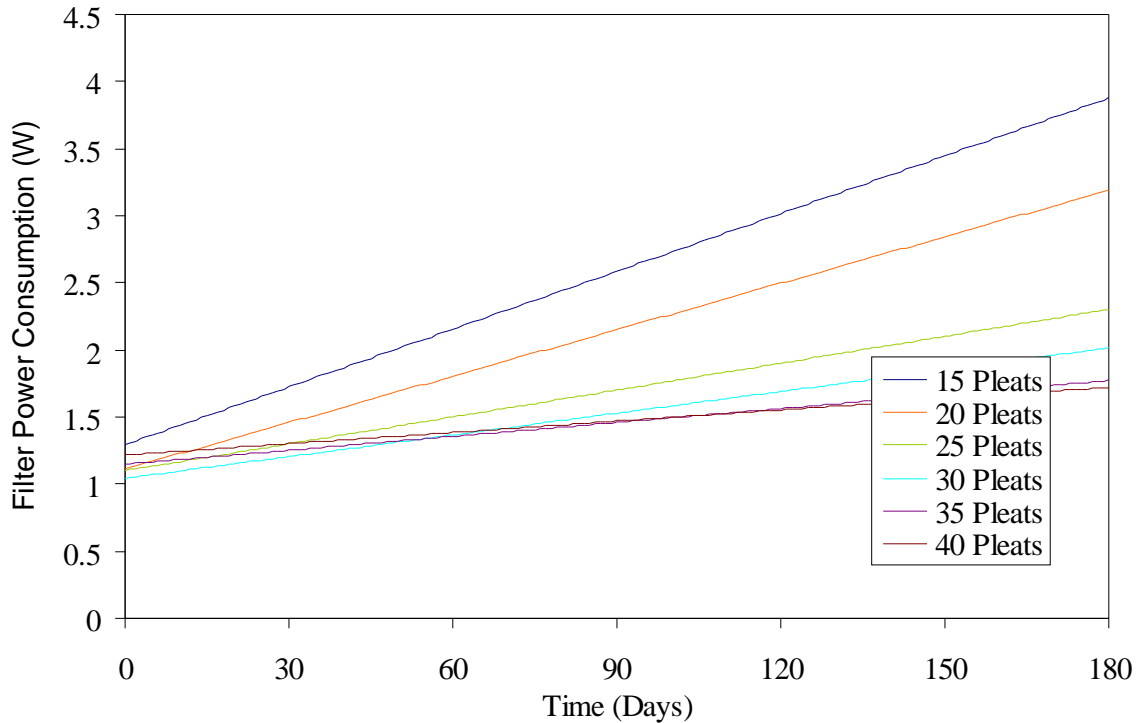


Figure 6.16: Average Power Consumption of 24''x24''x2'' Filters

The power analysis performed on the 24''x24''x2'' demonstrated the benefit of simply adding a marginal amount of additional media. The increase in media area from 15 to 20 pleats is enough to maintain the filter in the depth filter regime during the full six months of operation. This results in a reduction of 80 kWh in energy.

Table 6.6: Estimated Lifetime Costs for 24''x24''x2'' Filters

Filter Type	Pleats (#)	Filter Cost (\$)	Energy Usage (kWh)	Energy Cost (\$)	Total Cost (\$)
Commercial 2" Deep	15	\$4.65	468	\$51.49	\$56.14
Custom 2" Deep	20	\$6.20	389	\$42.84	\$49.04
Custom 2" Deep	25	\$7.44	307	\$33.87	\$41.31
Custom 2" Deep	30	\$9.25	276	\$30.44	\$39.69
Custom 2" Deep	35	\$10.85	264	\$29.08	\$39.93
Custom 2" Deep	40	\$12.40	266	\$29.27	\$41.67

The employment of an even deeper-pleated filters results in a further reduction in energy consumption. The best case energy scenario for a 1” and 2” deep filter has estimated consumptions of 398 kWh and 264 kWh, yet a 4” filter can operate as low as 196 kWh over the same time span.

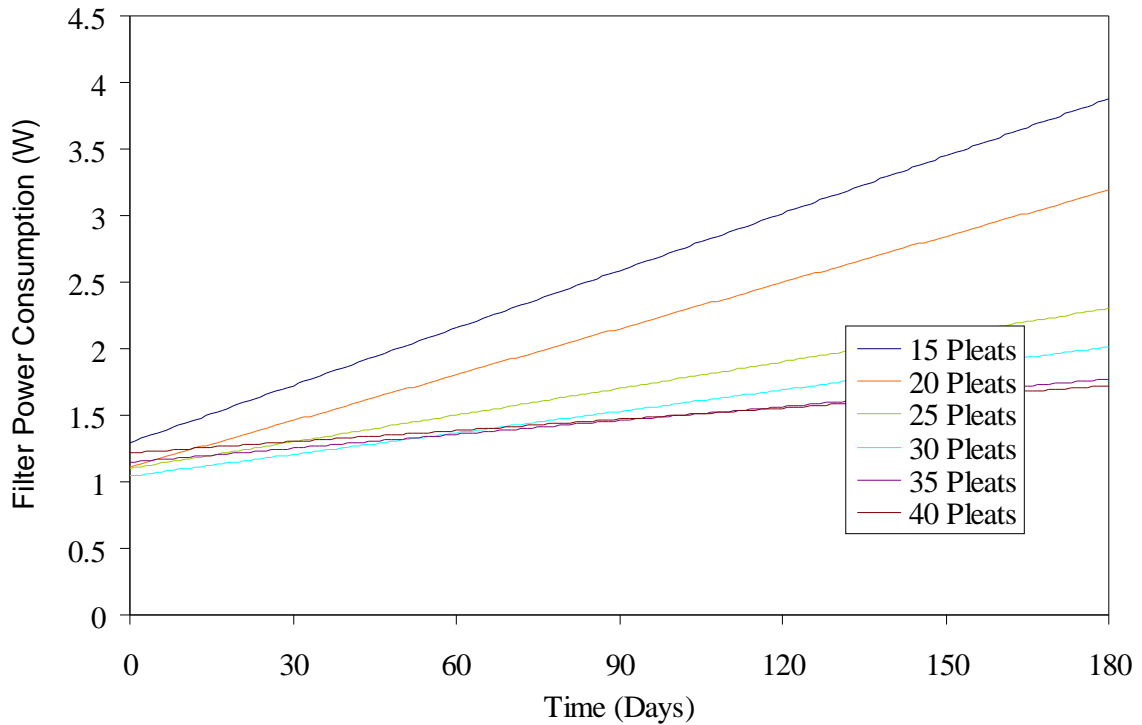


Figure 6.17: Average Power Consumption of 24”x24”x4” Filters

Table 6.7: Estimated Lifetime Costs for 24”x24”x4” Filters

Filter Type	Pleats (#)	Filter Cost (\$)	Energy Usage (kWh)	Energy Cost (\$)	Total Cost (\$)
Standard 4" Deep	10	\$6.40	340	\$37.49	\$43.89
Custom 4" Deep	16	\$10.24	237	\$26.08	\$36.32
Custom 4" Deep	22	\$14.09	200	\$21.96	\$36.05
Custom 4" Deep	28	\$17.92	196	\$21.63	\$39.55

The above analysis shows the effectiveness of the novel design in reducing the energy consumption of a filtration unit. By utilizing a custom pleated 24”x24”x4” deep filter over a standard 24”x24”x1” (Table 6.5), the energy consumption is reduced by 66%

resulting in an estimated energy savings of almost \$40. The net upfront cost to procure the 4” filter is a mere \$11.08 more.

A 66% reduction in HVAC Pressure-Volume work would have a major impact on the annual energy consumption of the United States. The Department of Energy estimates that 60 million American households utilize some form of central air. These households consume 356 billion kWh annually to power these air units (DOE 2009). Of that 356 billion kWh, roughly 15% goes to the Pressure-Volume work required to move air across the filter units. The deployment of a more efficiently designed filter would reduce this consumption and could lead to a 35.7 billion kWh reduction in annual energy consumption within the United States.

CHAPTER VII: FILTRATION PERFORMANCE OF MULTI-ELEMENT STRUCTURED ARRAYS

VII.1. Introduction

Multi-Element Structured Arrays are capable of decreasing the initial pressure drop of a filtration system by incorporating numerous filter element into a single configuration thereby decreasing the face velocity through each element. The reduction in resistance is often greater than 50% when compared to the precursor single elements. As with a single filter, the initial pressure drop is just one of many criteria on which performance can be based. The aspects of removal efficiency and dirt loading must be assessed in order to evaluate the overall performance of a MESA. The following chapter performs head-to-head comparison between MESA's and the single elements that comprise them to determine the deviations in removal efficiency and dirt holding capacity. Modifications within the MESA design are also tested to verify enhancements on the overall filtration performance.

VII.2. Particulate Removal Efficiency of a MEPFB

Since the removal efficiency of a filter is primarily dependent on the media design and particulate challenge, a MESA should not suffer from any major reduction in its ability to capture particles. There is a concern though that a MESA might decrease the removal efficiency of the impaction mechanism due to the large reduction in media velocity. If a MESA is not capable of removing particulate matter at the same efficiency as the elements from which it is built, then the overall benefit of the unit will be greatly

decreased. This assessment depends entirely on the MESA being properly sealed into place.

VII.2.1. Materials

A particulate removal evaluation was performed on a single 24"x24"x1" pleated filter and on a V bank built with identical 24"x24"x1" elements. The filter elements used were commercially available from Quality Filters. Each element possessed 28 pleats and was composed of Kimberly Clark Intrepid® filtration media (Type 355H). A general description of the test rig and procedure used for the experimental can be found in Chapter V.

VII.2.2. Results and Discussion

The MESA filtration unit demonstrated a removal efficiency that was comparable with the single filter's removal efficiency. Figure 7.1 was the observed results for the removal efficiency testing. The removal efficiencies of the two systems essentially overlapped or fell within the standard deviation error bars for particulate sizes greater than 1 micron. Of note, the removal efficiency of the MESA units in the sub-micron regime was higher than the single filter. The primary removal mechanism for particles of this size range is Brownian diffusion. Since the air velocity through the MESA's media was one-half the value of the single filter, the resident time in the filter was increased. It was quite reasonable to expect the removal efficiency to improve in this regime since capture by Brownian motion increased with increased resident time.

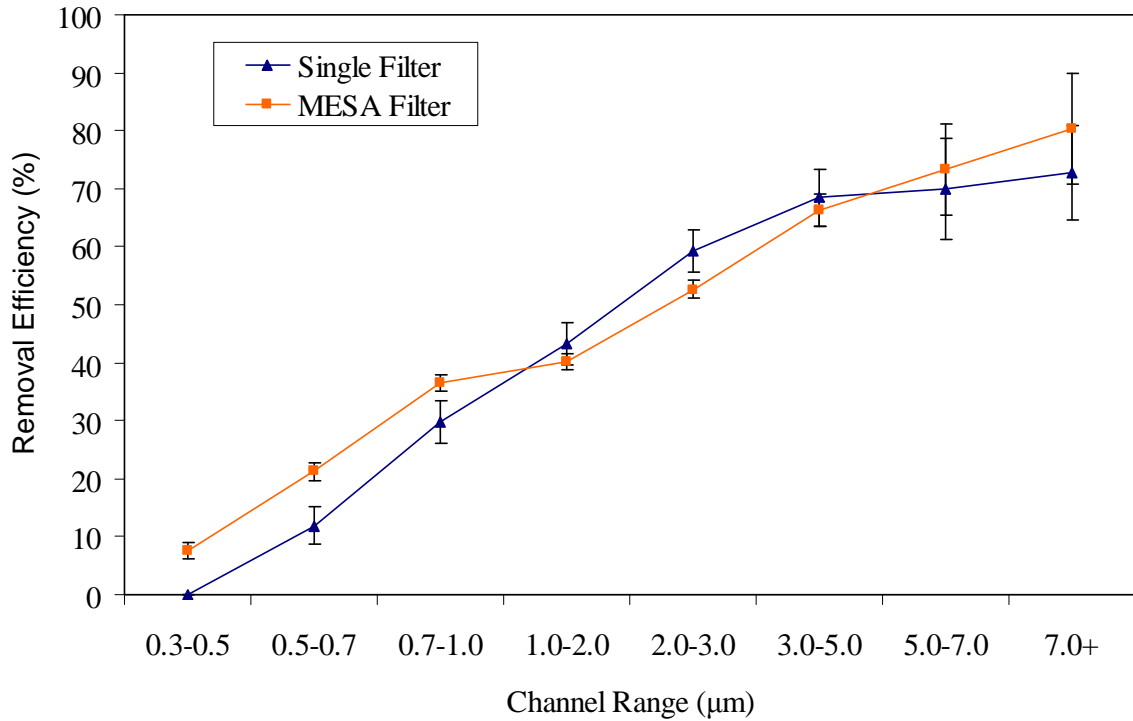


Figure 7.1: Removal Efficiency of a Single Filter and MESA

Figure 7.2 & 7.3 demonstrates the increase in removal efficiency with increasing dirt loading for the single filter as well as the MESA unit. This behavior is very common in depth loading filters and has been well reported in the literature (Japuntich et al. 1994, Stenhouse and Trottier 1991, Podgorski and Grzybowski 2000). The removal efficiency of a depth filter increases with loading because of the formation of dendrites within the fibrous media. The dendrites act as additional fibrous onto which the particles are captured. The major exception to this behavior occurs with electrostatic filter. As these particular filters clog, the charge on the fibers neutralizes with the loaded dirt and the removal efficiency drops.

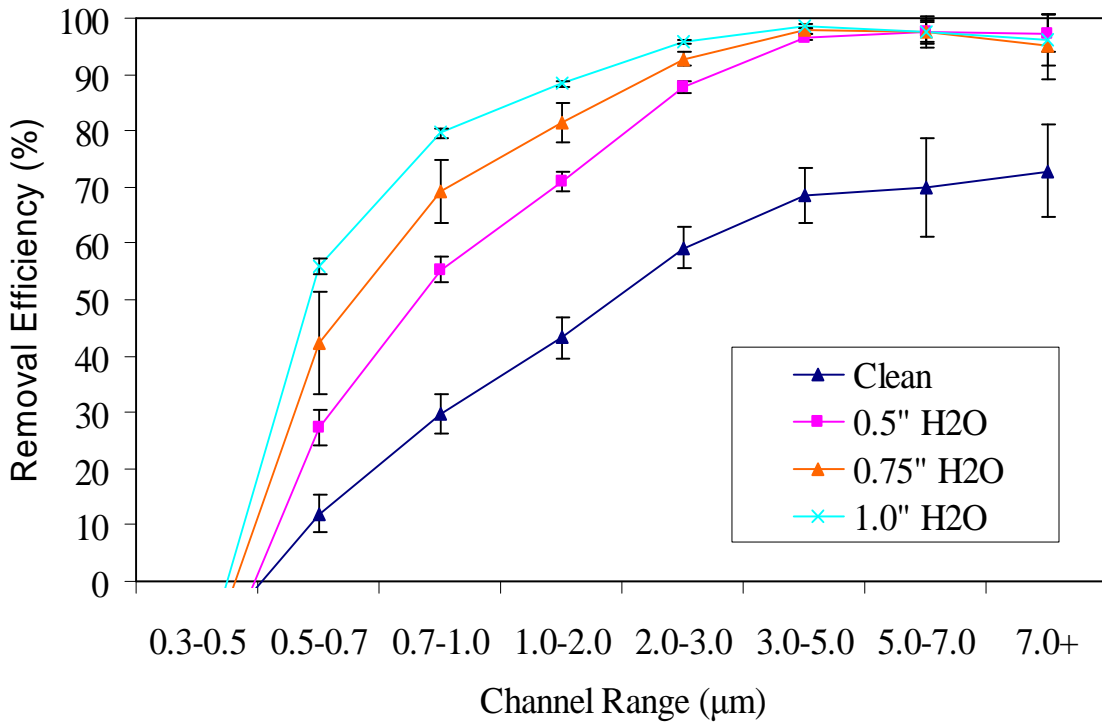


Figure 7.2: Removal Efficiency of a Single Element during Loading Conditions

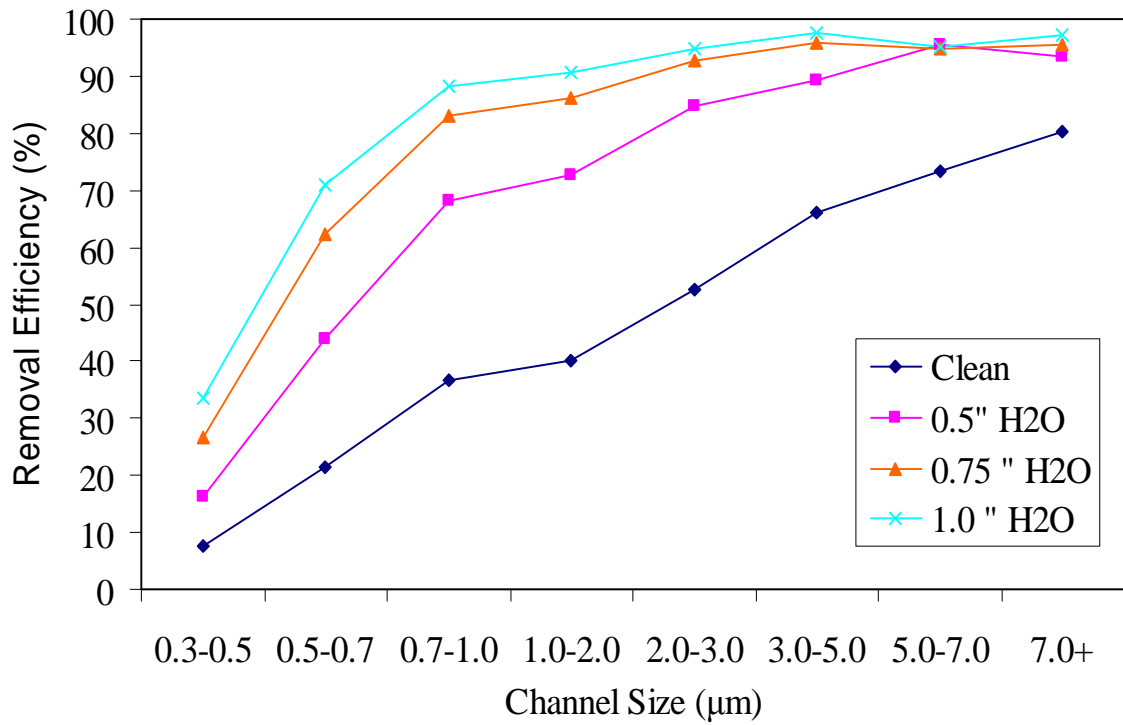


Figure 7.3: Removal Efficiency of a MESA during Loading Conditions

Both filter systems were capable of removing particles 2.0 micron and larger with an efficiency of >90 % once loaded. The single filter, however, significantly lagged behind the MESA's efficiency in the lower micron regime. In particular, the single filter was never able to successfully remove particles in the 0.3 to 0.5 micron range.

The real benefit of a MESA style unit can be seen when comparing the systems with a performance versus costs filters metric such as the quality factor. The quality factor is the log removal efficiency divided by the pressure drop [Brown 1993, Matteson and Orr 1987].

$$QF = \ln(\eta) / \Delta P \quad 7.1$$

The chart below compared the MESA to a single filter based on this parameter. The MESA's boosted a quality factor at least double that of the single filter's factor over the parameter spaced explored.

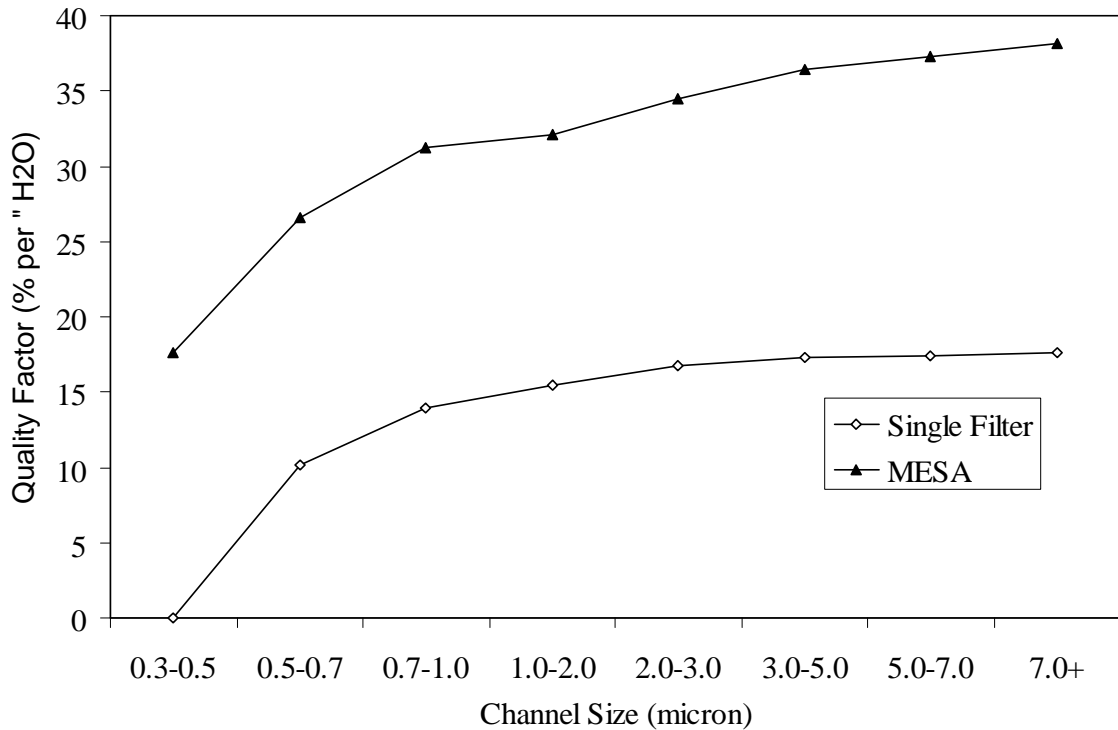


Figure 7.4: Quality Factor Analysis

VII.3. Dirt Loading of MESA's

MESA's have been demonstrated to perform at an equal or better removal efficiency compared to single filter element, yet they do so at a reduced initial pressure drop while providing additional available media. Chapter VI demonstrated that an increase in media area did not automatically translate into an increase in dirt holding capacity. MESA comprised of various elements and pleat counts were investigated to obtain a working knowledge of their dirt holding capacities. The results of the tests were used to evaluate MESA for useful lifetime, power consumption, percent media utilization, and performance enhancement over single filters.

VII.3.1. Materials

The experimentation utilized custom ordered 24"x24"x1" purchased from Quality Filters. The filters were constructed with Kimberly Clark Intrepid® filtration media Type 355H. The filters were subjected to a loading analysis with ASHRAE synthetic dirt procured from Blue Heaven Technologies.

VII.3.2. Results and Discussion

VII.3.1.1. Influence of Pleat Count within an MESA

V MESA units were employed to study the effect of increasing the element pleat count while holding all other variables constant. The result (Figure 7.5 and 7.6) showed that the general trends observed were similar in nature to the trends observed in the single filter elements. MESA's constructed with higher pleated element demonstrated the capacity to hold more dirt before reaching their final resistance of 1.0" H₂O.

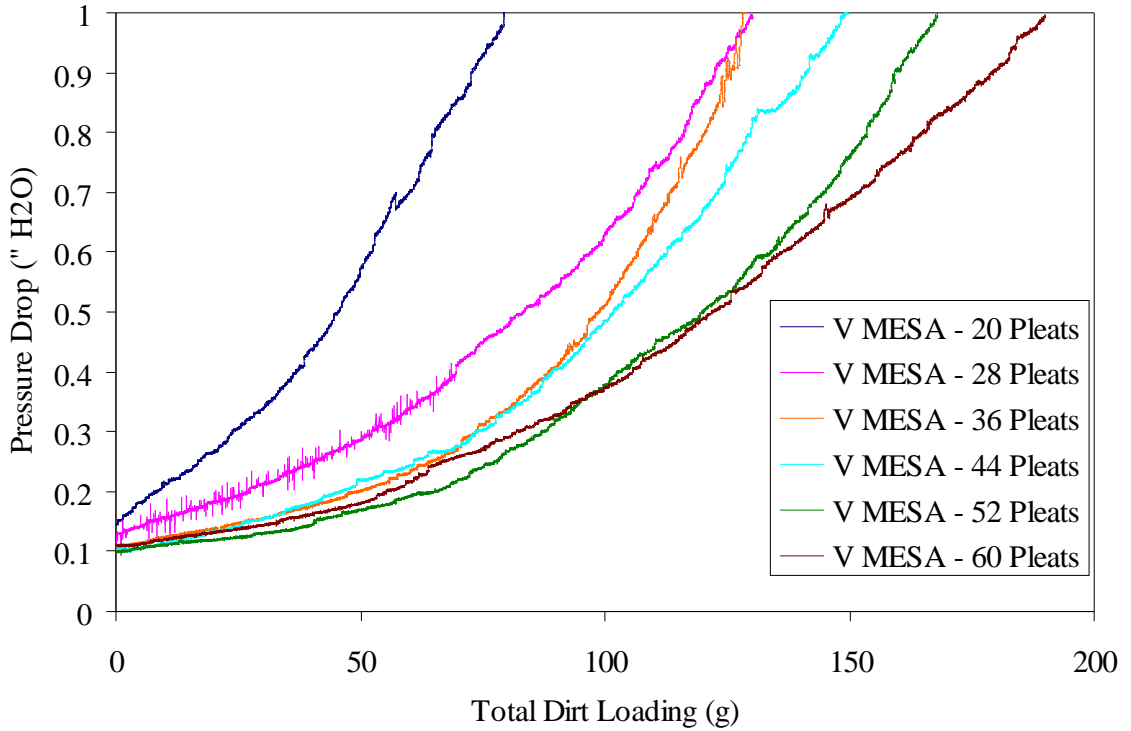


Figure 7.5: Total Dirt Holding Capacity of V MESA with Various Pleat Counts

The additional area provided by increasing the element pleat count in a MESA did not show a linear relationship with dirt loading. The normalized dirt loading showed that the elements still underwent a preferred media utilization pattern with a 28 pleat count MESA demonstrating the highest utilization. This pattern was very similar to the one present in Chapter VI.

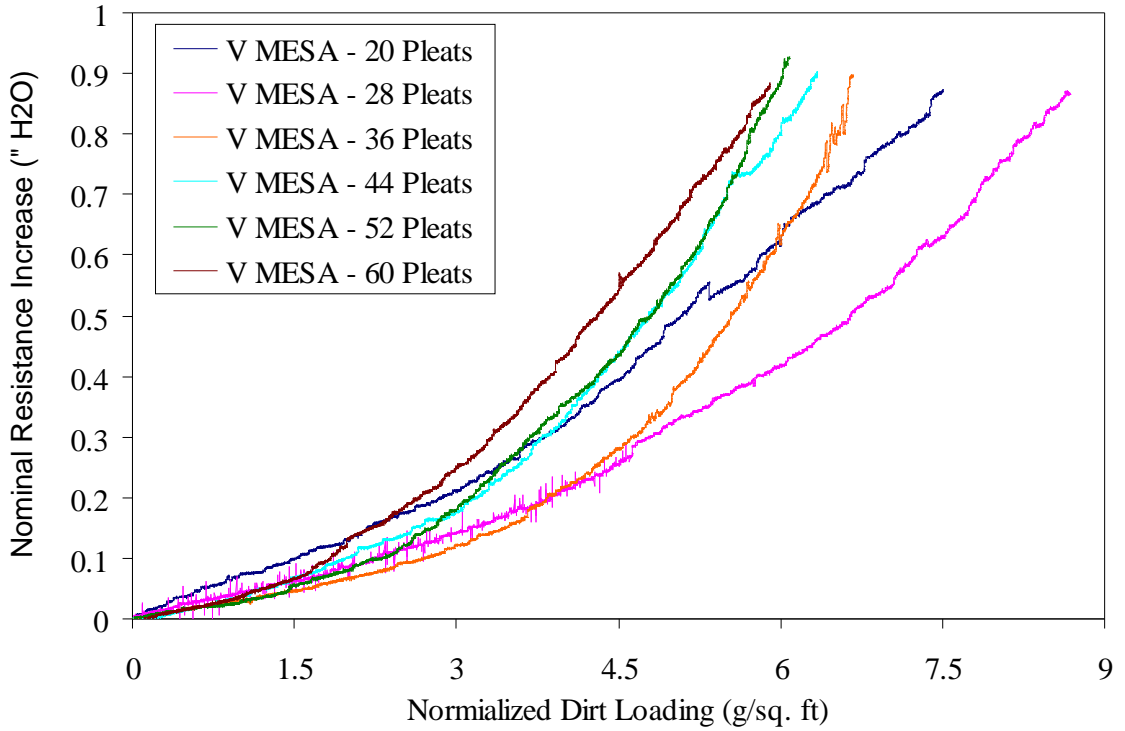


Figure 7.6: Normalized Dirt Holding Capacity of V MESA with Various Pleat Counts

Table 7.1 was constructed by locating the transition point of all pleat counts of the V Mesa and the precursor single elements that were ensemble into the MESA's. As seen, the lower pleat count elements of each designs showed similar utilization of the media before transitioning out of the depth regime. This trend did not continue as the elements are pleated higher. Higher pleated MESA showed a lower media utilization than their single element counterparts.

Table 7.1: Transition Point of V MESA and Single Elements

Pleating Pleats / Element	Single Filter Transition (g / sq. ft)	V MESA Transition (g / sq. ft)
20	3.0	3.0
28	2.8	2.8
36	2.75	2.5
44	2.5	1.75
52	2.25	1.75
60	2.0	1.5

VII.3.1.2. Influence of Element Count within an MESA

V and W MESAs' constructed out of 24"x24"x1" filter elements were compared to their single filter precursor to determine the influence of increasing the element count of a filtration system. The elements possessed 28 pleats and were made from Kimberly Clark 355H fibrous media. Both arrays were able to operate at a lower resistance level than the single filter when subjected to the filtration loading. Due to the decreased initial resistance, the V MESA was able to be loaded with 42 grams of ASHRAE dust before it even reaches the initial pressure drop of the single filter. The W MESA further outperformed the other systems and was capable of operating below their initial pressure drop until it captured 75 grams and 125 grams of dirt respectively. The total dirt holding achieved by the W MESA (241.3 g) before reaching the final resistance was significantly greater than both the single filter (53.5g) and V MESA (130.3 g).

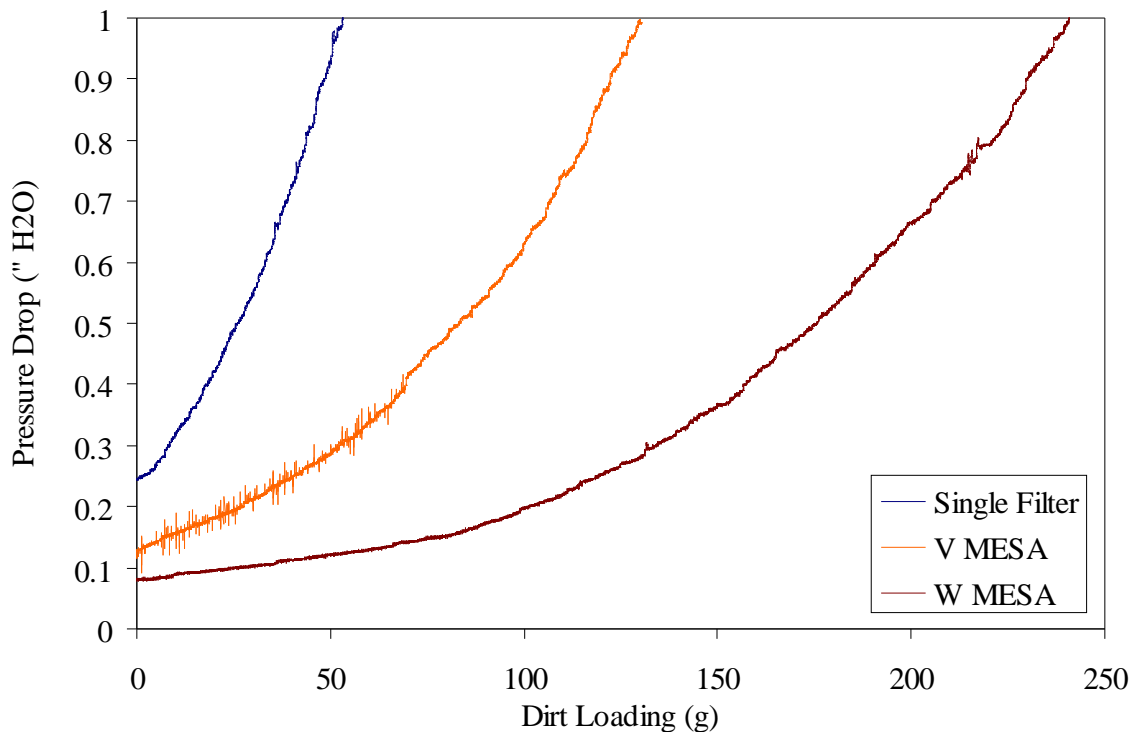


Figure 7.7: Total Dirt Loading of Various Element Count Systems

The MESA did not show the same aging rate or media utilization that a single element displays. In the depth filtration regime, the V and W MESA aged at a slower rate (0.042” H₂O per g/ft² and 0.02” H₂O per g/ft²) than the single filter (0.064” H₂O per g/ft²). This corresponded to a 34% and 69% reduction in the aging rate while in the depth regime. The most likely explanation for the decreased loading rate was the 50% and 75% reduction of face velocity achieved with utilizing more elements within the MESAs’.

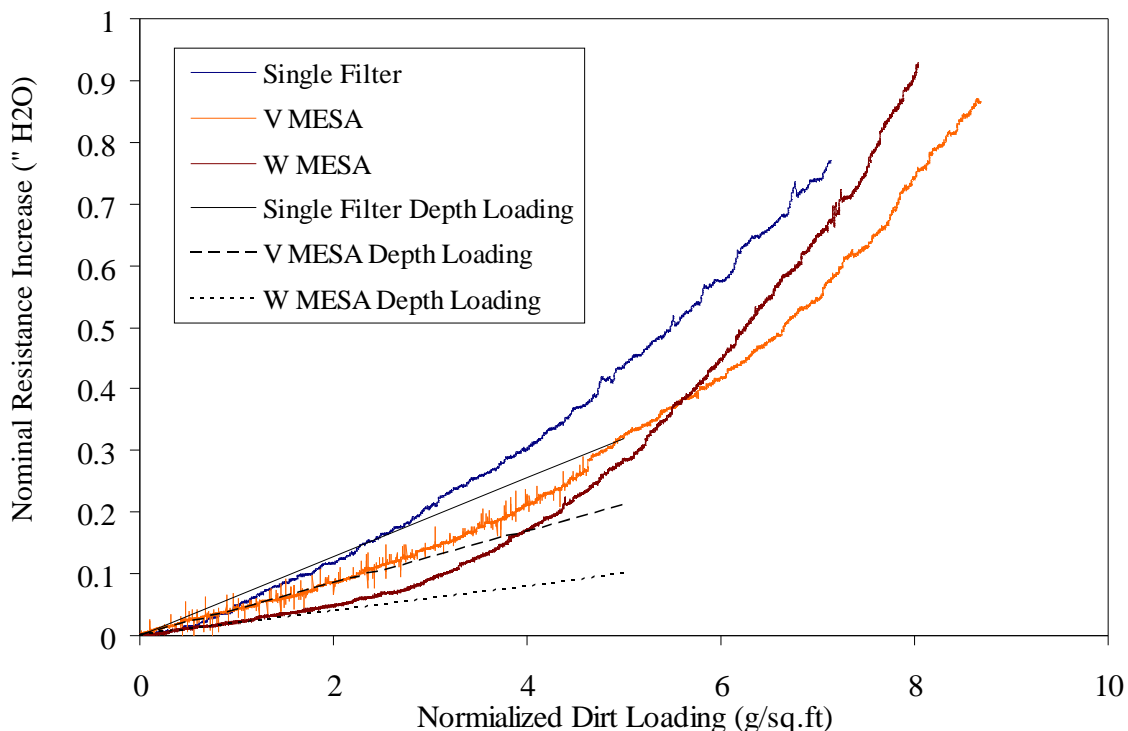


Figure 7.8: Normalized Loading Profile of a Various Element Count Systems with emphasis placed on the Depth Loading Regime

The transition to cake filtration occurred at approximately 2.8 g/ft² for both the single element and the V MESA, yet the W MESA transitions sooner at 2.2 g/ft². Based on the hypothesis of preferential surface loading postulated for the single filter element, this was expected since the elements are aligned more directly with the incoming

challenge dirt as well as subjected to a slower media velocity. This theory was backed by the increased normalized loading rate in the cake regime of both MESA's. In particular, the W MESA loaded at a 67% quicker rate than the single element once it had transitioned to cake filtration. This is important to realize because a MESA will very quickly increase in power consumption once cake filtration is reached; thus, appropriate change out measures must be implemented.

The shape of the transition region of the MESA was also interesting because it occurs over a broad range. Figure 7.9 below graphed the above plot with the V MESA removed for clarity. The single filter had two, very pronounced slopes indicating depth and surface filtration with a sharp transition point. The MESA had a gradual, intermediate slope between the depth close and the cake slope. The exact reason for this broad transition is unknown.

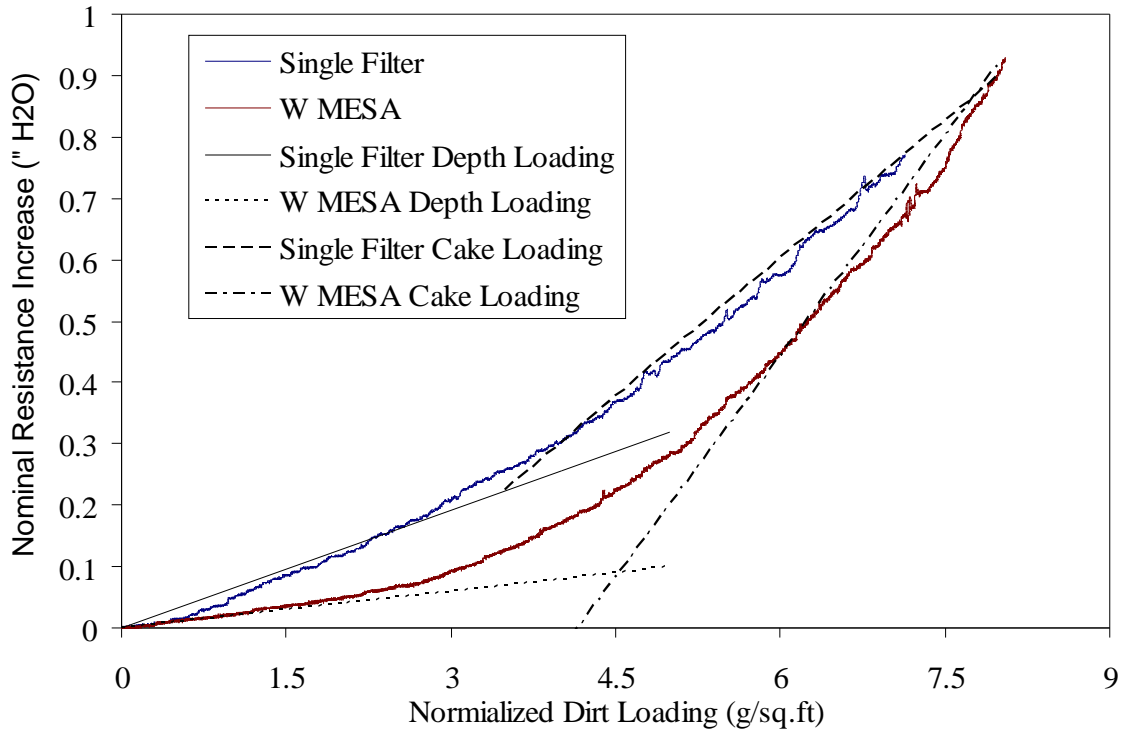


Figure 7.9: Normalized Loading Profile of a Various Element Count Systems with emphasis placed on the Cake Loading Regime

VII.3.1.3. Power Consumption Analysis

A power consumption analysis similar to the one performed in Chapter VI was reused to demonstrate the power consumption and associated cost of a MESA system compared to a single filter. Over the six month period, both MESAs' were able to operate significantly below the initial power consumption of the single filter. The employment of a V MESA instead of a traditional, flat filter resulted in a 40% reduction in energy consumption. The saving to the end user was an estimated \$19.83 over the six month period. A W MESA, with its decreased loading rate in the depth regime, barely aged and had a power consumption that was essentially a function of its initial pressure

drop. The net decrease in energy consumption was almost 80% resulting in a savings of \$38.96.

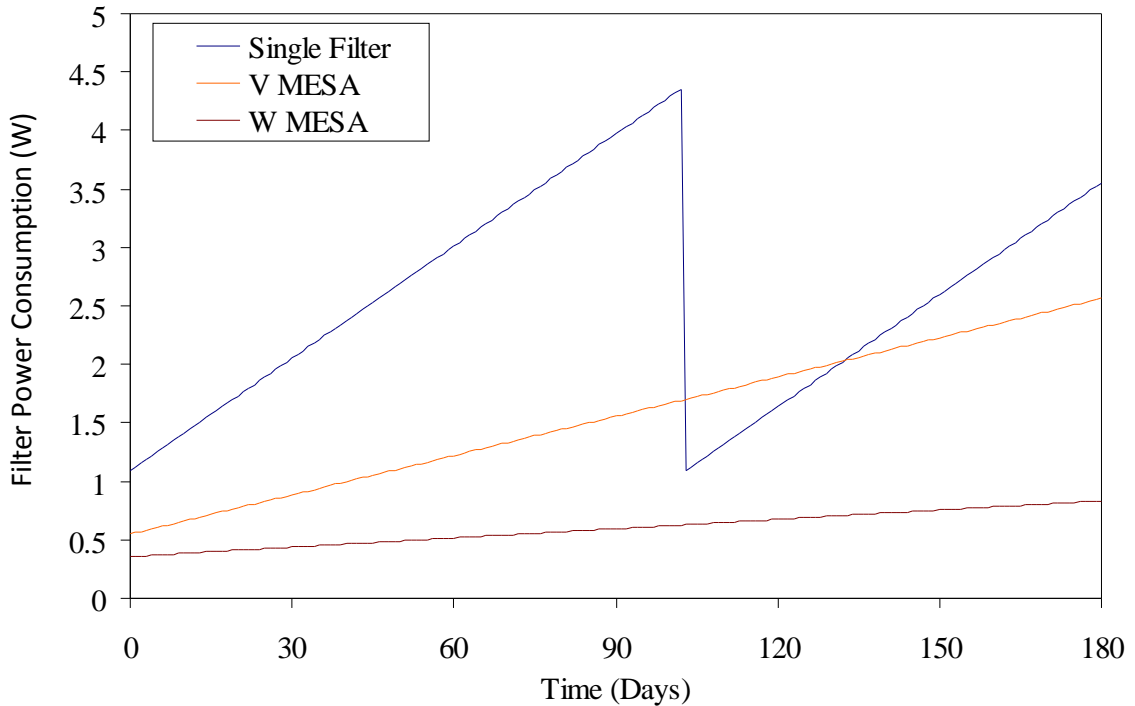


Figure 7.10: Power Consumption of MESAs' and Single Filter

Table 7.2: Associated Costs

Filter Type	Pleats (#)	Filter Cost (\$)	Energy Usage (kWh)	Energy Cost (\$)	Total Cost (\$)
Std. 1" Deep	28	\$3.98	462	\$50.81	\$58.77
V MESA	28	\$7.96	281	\$30.98	\$38.94
W MESA	28	\$15.92	107	\$11.85	\$27.77

VII.4. Preferential Element Alignment within a MESA

Pleated filter elements can be loaded into a MESA in two manners: horizontally-oriented pleats (left side) or vertically-oriented pleats (right side). The effect of alignment on performance was examined since the variation could affect the pressure drop, dirt loading capacity, and aging profile of an array.



Figure 7.11: Horizontally-Oriented (Left) & Vertically-Oriented (Right) Banks

VII.4.1. Materials and Methods

Two filter types employed in MESA architectures were utilized to determine if there was a performance deviation between the different pleat alignments corresponding to a preferred configuration. Each MESA was evaluated for initial pressure drop and loading profile. The first MESA unit was composed of DP 4-40 air filters from Airguard. DP 4-40 elements possessed dimensions of 24"x24"x4" (23.375"x23.375"x3.75") and were rated as MERV 8 filters. The filters were tested in a vertical and horizontal alignment pattern within a V MESA housing. The second MESA unit employed Airguard DP 95 filters. The 24"x24"x2" (23.375"x23.375"x1.75") filters were loaded into a W MESA. The manufacturer's reported MERV rating for the DP 95 unit was 13.

It was necessary that all elements used in this experiment were identically made because defects within a single element can translate into misperceived performance variations between the pleat alignments when loaded into a bank. It was assumed that all elements purchased from a commercial manufacturer would have similar initial resistances and be free from defects. This assumption was verified by testing each filter

for initial pressure drop while oriented perpendicular to flow. Only slight variations totally less than 5% were observed in the clean resistances and no physical defects were seen among the filter sets.

VII.4.2. Results and Discussion

VII.4.2.1. Initial Pressure Drop

The initial pressure drop of the DP 4-40 and DP 95 MESA's with pleats aligned in both configurations are shown in Figure 7.12 and 7.13. Figure 7.12 demonstrates that there were only minor variations within the initial resistance of the MESA units composed of DP 4-40 filter. The horizontally-aligned MESA did operate at a slightly reduced resistance above 500 fpm, but the magnitude of the decrease was small. This also occurred in a flow rate regime in which filters traditionally do not operate. The MESA composed of DP 95 filters displays no difference in initial resistance except for some minor fluctuations due to noise in the measurement devices. These observances were to be expected because air can access the same amount of media in both configurations.

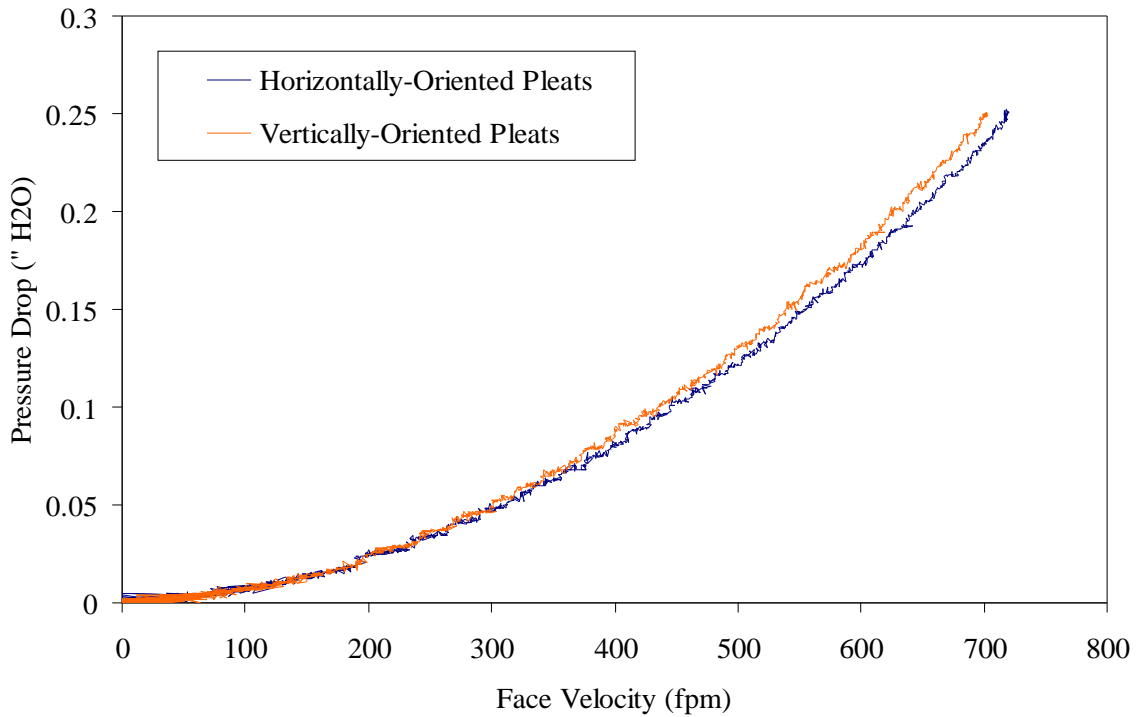


Figure 7.12: Clean Resistance of DP 4-40 Elements Loaded Vertically and Horizontally into a V MESA Configuration

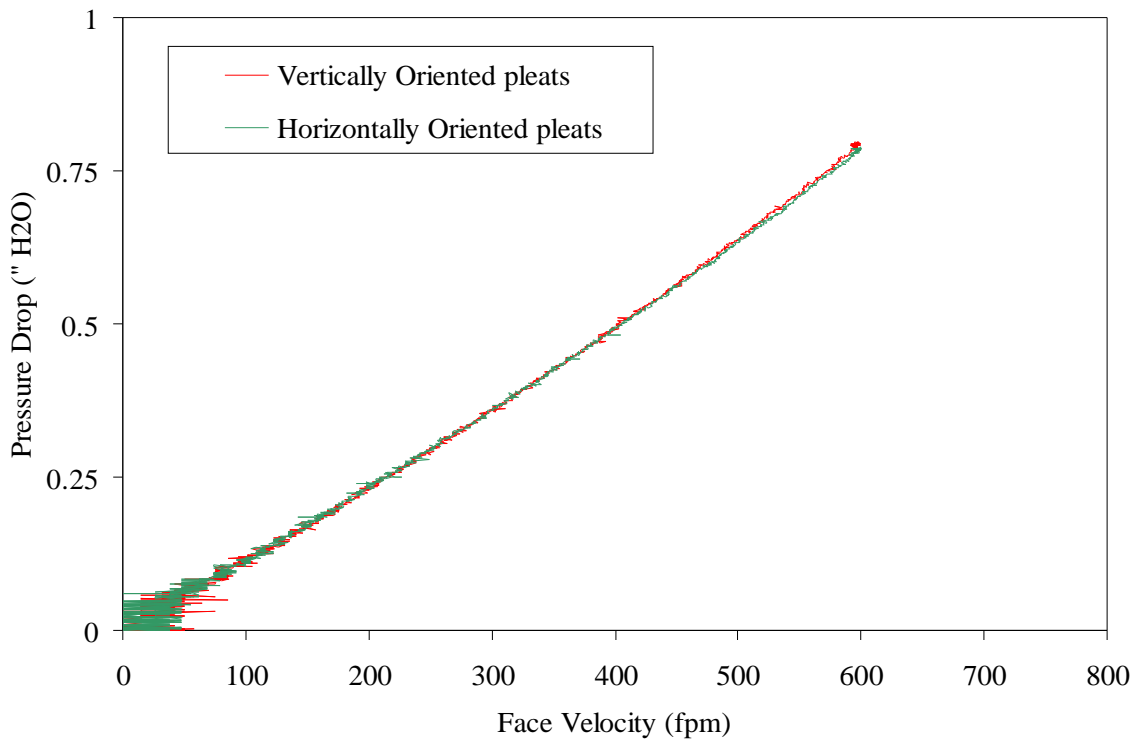


Figure 7.13: Clean Resistance of DP 95 Elements Loaded Vertically and Horizontally into a W MESA Configuration

VII.4.2.2. Dirt Loading

Although the initial resistance did not indicate much benefit between the two alignments, the MESA's with horizontally-oriented pleats did show a slight improvement in filtration performance over the vertically aligned under dirt loading conditions. These results can be seen in Figures 7.14 and 7.15.

In the case of the DP 4-40 filters, the performance was roughly the same throughout the test; however, the vertically-oriented filter transitioned from depth-to-cake filtration regime slightly sooner than in the horizontally-oriented filter. For the DP 95 filter based MESA's, the horizontally oriented filter units showed a slower rate of growth across the entire loading curve. The gap between the two orientations grew as the filters were further aged. Of note, the filters were not able to transition from depth to cake filtration because of the high initial resistance resulting in a shorten lifetime. Further loading of the DP 95 units could have possibly indicated a larger deviation in the units' performance; however, the test had to be stopped because of blower limitations.

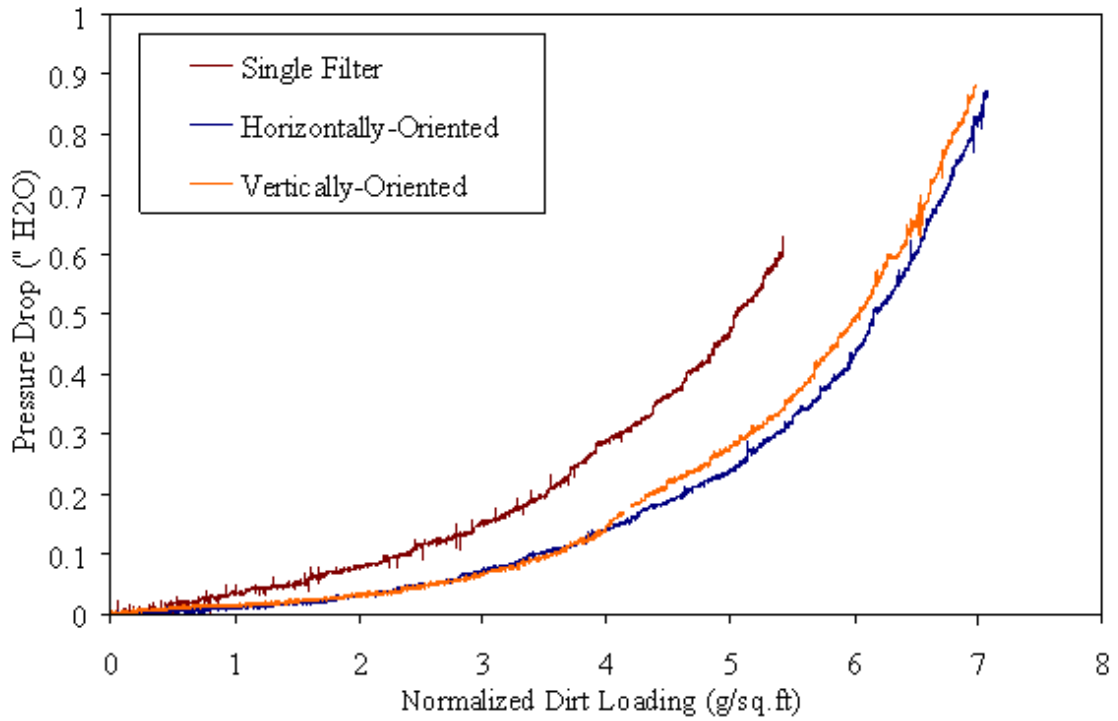


Figure 7.14: Aging of DP 4-40 Elements Loaded Vertically and Horizontally into a V MESA Configuration

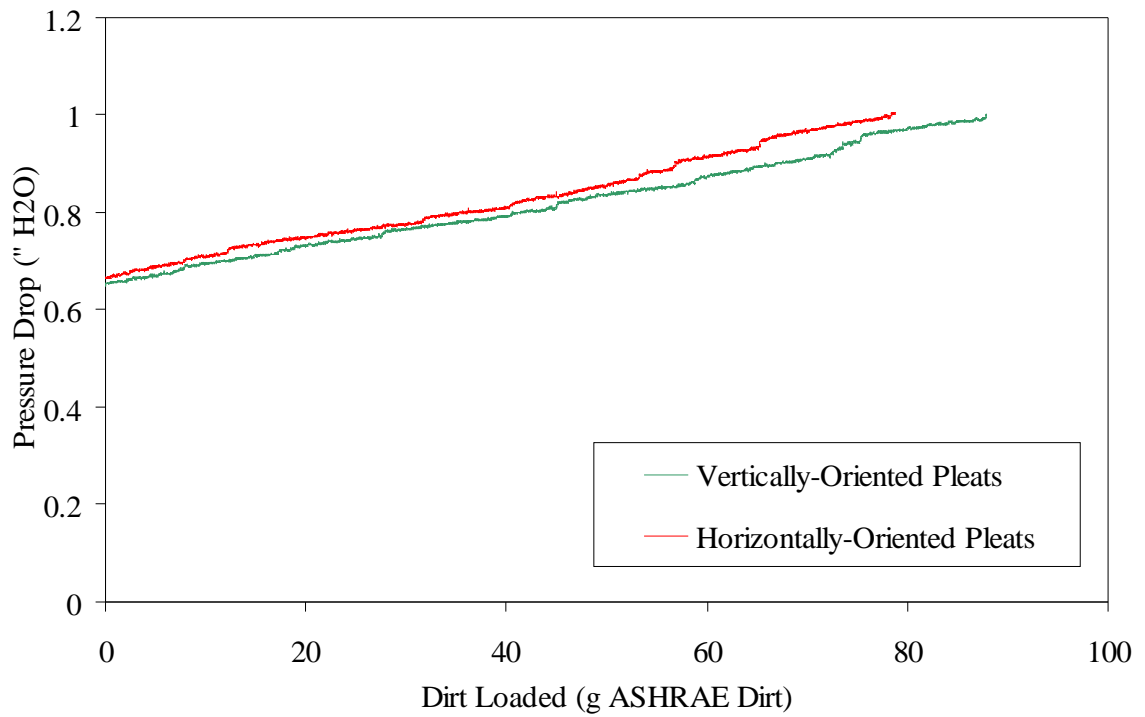
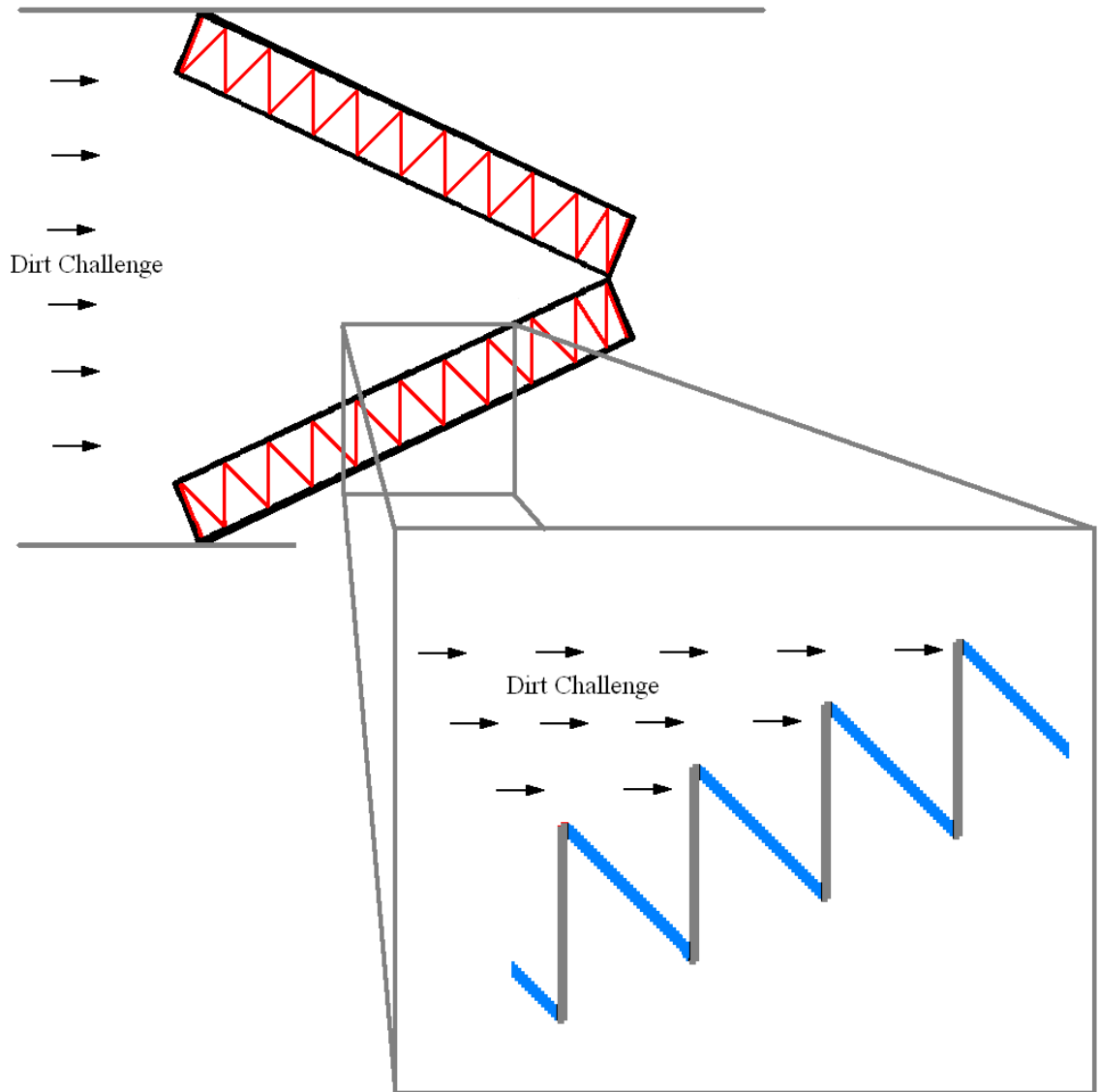


Figure 7.15: Dirt Loading of DP 95 Elements Loaded Vertically and Horizontally into a W MESA Configuration

It was postulated that the horizontally align bank elements achieve this slight performance advantage over the vertically align elements because of the media being preferentially loaded. The horizontally-oriented elements have both sides of the pleats equally exposed to the incoming dirt challenge. The vertical-oriented pleats were not equally exposed to the challenge dirt. The front side of the pleat was more inline with the dirt as shown in Figure 7.12. For future reference, the pleat shaded grey below will be referred to as the “inline side” and the blue pleats are known as the “shielded side”.



7.16: Schematic of Pleat Nomenclature

Although a preferential cake formation could be visually seen, it was very difficult to quantitatively assess its influence and presence. The cake could not be photographed because the opacity of the carbon black in the ASHRAE dirt obscured any distinguishing contrasts or shadows. Figure 7.17 and 7.18 below were the best representations that could be captured with the available digital camera. The inline side pleats were solid black indicating complete coverage of the filtration media with the

carbon black. The shielded side pleats were primary black indicating that challenge dirt was reaching the media, but small portions of the filter media remained the original green color.



Figure 7.17: View of Inline Loaded pleats



Figure 7.18: View of Shielded Loaded pleats

To determine the degree of loading, two techniques were attempted. The initial approach was to obtain basis weights at various intervals. This approach proved inadequate because the media could not be dissected without distributing the cake formation. Although the cake layer was destroyed, an air permeability test was still conducted on the samples cut. The air permeability was conducted using the calibration rig discussed in the Appendix.

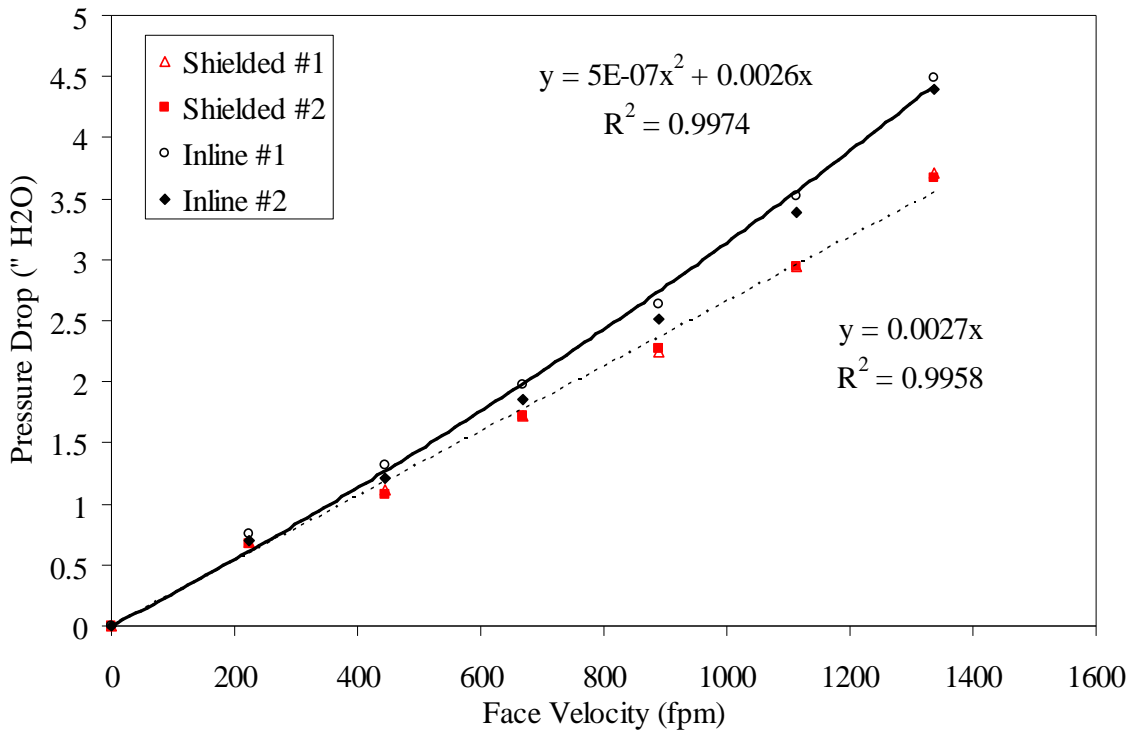


Figure 7.19: Air Permeability of Sample Obtained from Vertical MESA

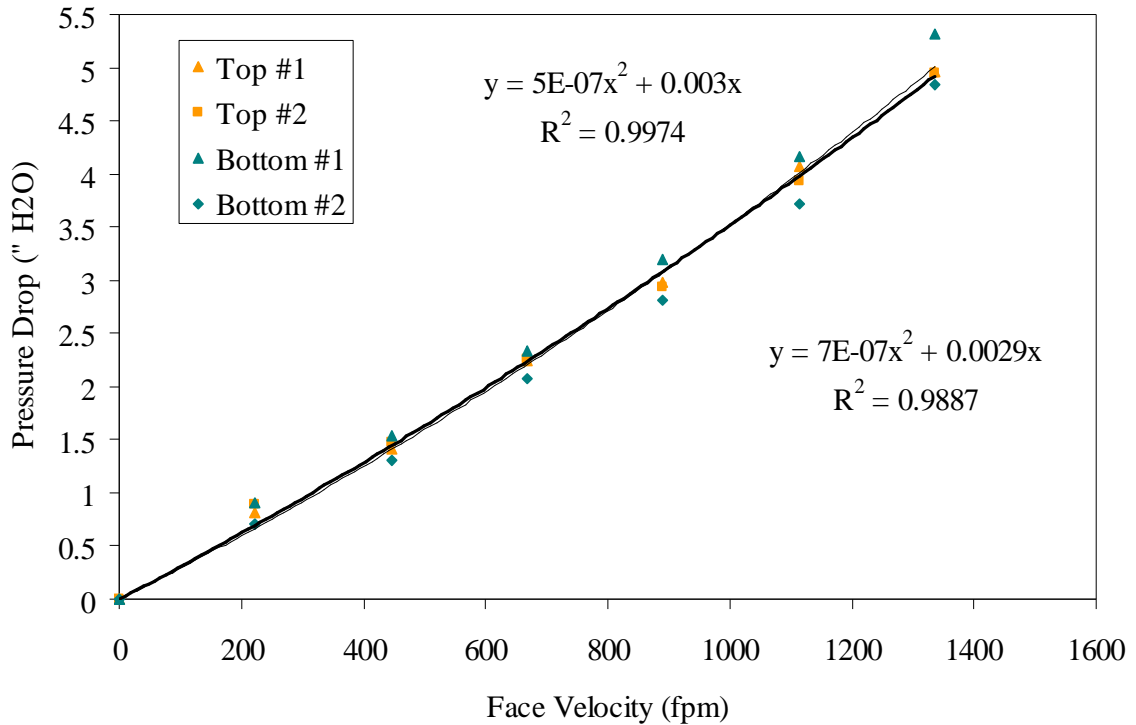


Figure 7.20: Air Permeability of Sample Obtained from Horizontal MESA

Figure 7.19 and 7.20 were created by dissecting the DP 4-40 filters and running two samples from each filter. Figure 7.19 demonstrates that the pleat's inline with the incoming dirt showed a higher resistance than the pleats that have been shielded. This would indicate that the filter was being loading unequally on the inline side. The samples obtained from the horizontally aligned unit show resistances that were very similar. The Excel-fitted trendlines indicated that the top and bottom pleats aged by the same degree.

A comparison between the two plots showed that the equally loaded horizontal pleats had a higher resistance than both the inline and shielded pleats of the vertical MESA. This was unique because the horizontal MESA operated at a lower resistance; however, the result is most likely due to errors in the measurement technique. It would be expected that the shield pleats have a higher permeability than the horizontal pleats

because they received less loading. The inline pleat, by the same mindset, should have a lower permeability due to additional dirt loading. This was not seen because the cake layer present on the inline side was disturbed when the samples were cut. It was believe the inline pleat's permeability was much lower during operating because of the cake layer that accumulates on the surface. Thus, this technique was not valid.

The next approach adopted was to measure the flow resistance in situ at select location to determine the magnitude of loading without disturbing the cake layer. This technique proved unusable because of difficulties aligning a pressure probe within the pleats as well as obtaining a good seal for an accurate measurement. Future work should focus on improving the viability of the technique.

The third approach, known as the peeling technique, gently dissected the filtration media utilizing adhesive squares (Thomas et al. 1999). Each square possessed two sides of equal adhesive material. The square was attached to a wooden backing and an initial weight as measured using a Citizen CX265 scale. The scale had a top weight of 60 g and a precision of 0.0001 g. The square was then situated above the desire test spot, and then pressed down with a 10 pound-force clamp. The clamp was then loosed, and the square was then reweighed to determine the amount of dirt removed. The process was continued until the square began to pull the fibers from the filter. Unlike the other techniques, the cake layer was captured and removed from the surface in a manner gentle enough to maintain its structural integrity.

The layering technique was preformed twice for each pleat side configuration. Figure 7.21 through 7.23 showed the resulting squares after the analysis was performed

on the different pleat sides. Figure 7.24 graphed the averaged removed dirt per layer of adhesive square.

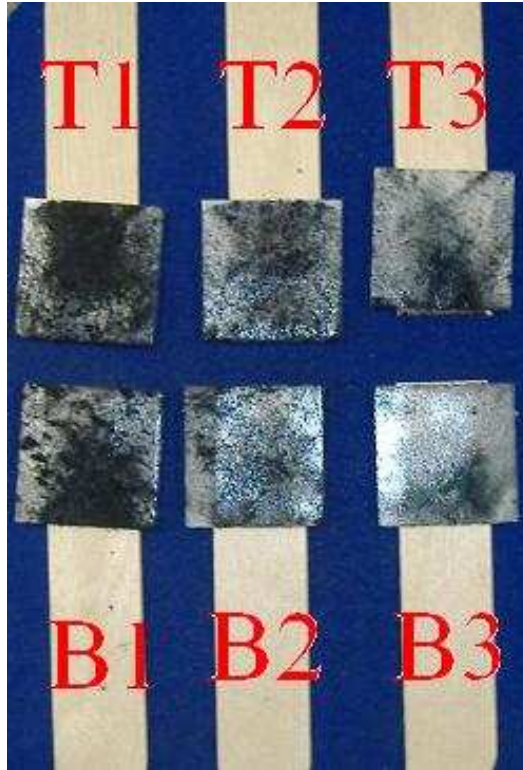


Figure 7.21: Adhesive Squares and Removed Dirt from top and bottom Pleat Sides of a Horizontally Oriented MESA after Dirt Loading

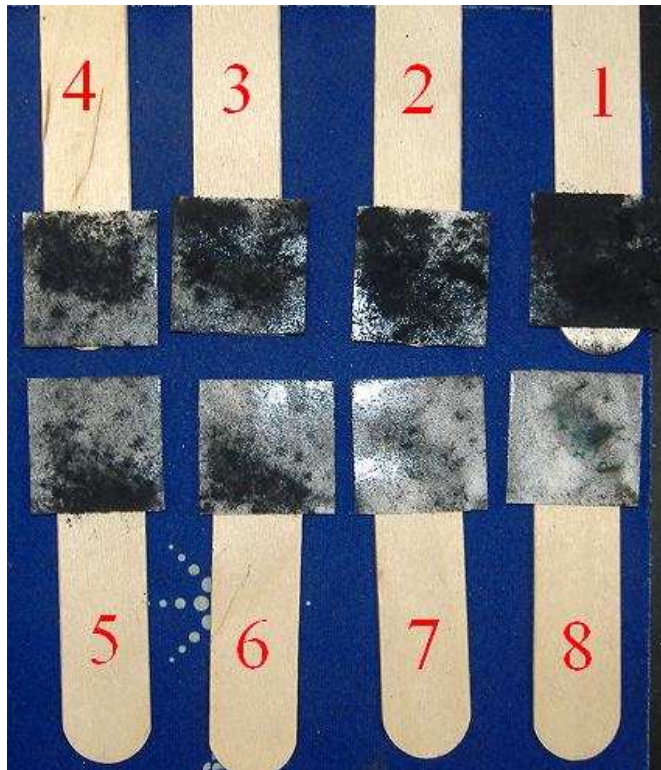


Figure 7.22: Adhesive Squares and Removed Dirt from inline Side of Vertically Oriented MESA after Dirt Loading

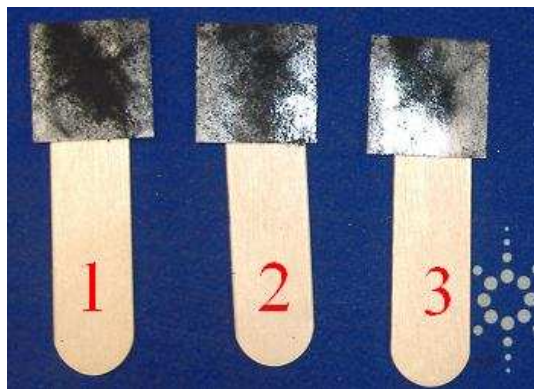


Figure 7.23: Adhesive Squares and Removed Dirt from Shielded Side of Vertically Oriented MESA after Dirt Loading

As seen in the pictures and the graph, the inline pleat side preferentially loads with dirt more readily than its shielded counterpart. The results also backs the assumption that the filtration media within the horizontally aligned MESA were exposed to the dirt in an equal manner since the same amount of cake was deposit on the top and

bottom pleats. It was odd that the degree of difference between the quantities of dirt loaded in the two orientations translates into a rather small difference in actual filtration performance. The cake formation of the inline pleat surface was roughly ten times greater than the shielded counterpart and five times greater than the horizontally oriented pleat sides. Future research needs to be performed in order to more readily identify the flow patterns and loading profiles within the two MESA orientations.

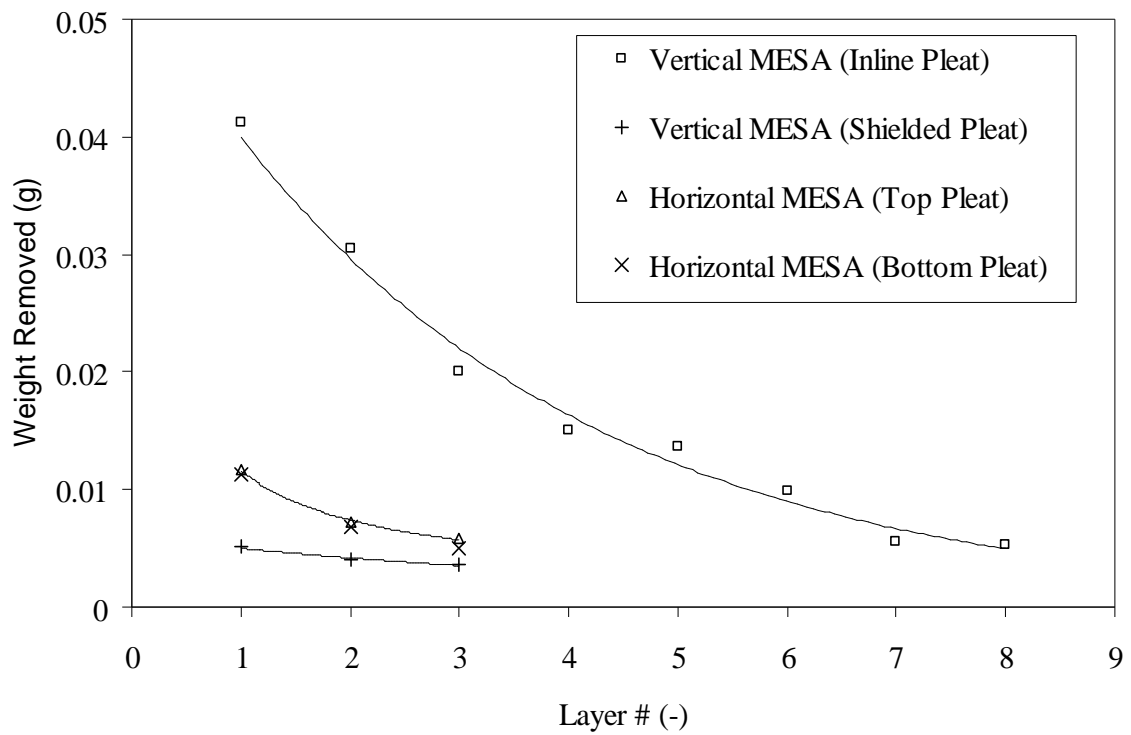


Figure 7.24: Weighed Pulled per Layer of Adhesive Backing

VIII. CONCLUSIONS AND FUTURE WORK

VIII.1. Conclusions

Novel packaging designs created by incorporate more pleats, elements, or deeper pleats demonstrated a substantial boost in energy performance over traditional filter designs. The incremental upfront cost to procure the filters is easily offset by the reduction of energy cost associated with operation. These design could be operated on the same maintenance schedule and essentially show no signs of aging before they are replaced.

The addition of more pleats and elements each showed an optimal count resulting in the lowest energy consumption. This optimal is brought about due to a gradually decline in media utilization as more pleats and elements are sequentially used. For single pleated filters, this optimal setting corresponded to a pleat count slightly higher than the optimal count needed to obtain the lowest initial resistance. Further experimentation and modeling efforts need to be employed to verify if this is a general trend among all filters or a coincidence within these filter sets.

The most unique aspect of the aging test was the prematurely transitioning from depth-to-cake as more pleats and element were added to the system. This is extremely important because most filtration research assumes that the results obtained on a flat piece of media will directly correlate to the performance characteristics when pleated. An example of this is Raber (1982) who was unsuccessfully in attempting to model the aging

evolution of filter by extending the results deduced on the loading of a flat sheet to the loading of a pleated filter. Location of the transition point is a high priority of interest to the engineering community because it marks the time that the filter needs to be changed. During the depth regime, the rise in pressure drop is low thus the filter is operating at a high quality factor. Once the filter transition to cake region, the quality factor quickly drops and the filter needs to be replaced.

VIII.2. Future Work

The robust worldwide market and the IAQ demands driving its growth provide a strong incentive for further exploration of multi-element structured arrays as a platform for dual-functioning microfibrous media. The recommendation for future work centers on continuation of the current research as well as potential areas of deployment of microfibrous media within newly devised packaging designs.

The utilization of microfibrous media as a dual functioning media needs to be accessed in a full scale experimentation to determine the influence of fiber diameter, particulate size, and porosity on pressure drop, particle removal efficiency, support retention, dirt holding capacity, breakthrough time for a given contaminant, and degradation of breakthrough time due to dirt blinding. A few potential areas of deployment are cathode air filters for solid oxide or PEM fuel cells; air filtration masks for biological or fire personal protection; remove of particulate matter and chemicals due to cigarette smoke; and utilization in clean room or semiconductor environment.

As an extension of the current work, additional experimentation is foremost needed to determine the exact mechanism causing the premature transition of the pleated filters and MESA's. Further investigation should also be conducted to determine the

influence of increasing element count in MESA composed of deeper pleated elements. All experimentation performed to this point could be further investigated through the use of CFM modeling as well as flow visualization employing fluorescent tracers particulates.

VIII.2.1 Utilization of Fairings

MESA modifications, such as the addition of fairings to reduce eddies created by the front edge, should be investigated to lower the initial resistance of the system and potentially extend the useful lifetime. Chapter IV demonstrates that the addition of a gradual contraction to the front of the bank and a gradual expansion out of the bank should eliminate the pressure drop associated with the blockage. Figure 4.20 indicated that the addition of the fins should reduce a WW configured MESA's initial pressure resistance by approximately 10%. The effect on dirt capacity and removal efficiency should be negligible, but this needs to be assessed.

VIII.2.2 Media Compression versus Permeability

Although unconventional for a pleated filter design standpoint, a MESA unit might be better served by compressing the media and incurring a higher media resistance. Once beyond the media-dominated regime, the only drawback to increasing the pleat count is the heighten resistance due to flow in tighter pleats and additional pleat tip blockage. The utilization of a thin media reduces both of these resistance influences. A bank can then be built with a higher pleat count leading to a low media velocity and higher filtration areas. The heighten media resistance will be offset by the substantially lowered media velocity given ample media area. Thus, a bank can be packaged with more media without drastically increasing the overall pressure drop.

VIII.2.3 Pyramid Filter

Higher element MESAs suffer from increased fixed resistance due to front edge blockage. The utilization of fairing might offset this resistance; however, a second approach is to design the filter units with a pyramid shape. The pyramid design would effectively remove all resistance created by flow blockage. In addition, it also has the potential to load more media into a give volume of ductwork than a MESA.

REFERENCES

- Arnold, B.D, Matela, D., and Veeck, A. 2005. Life-Cycle Costing of Air Filtration. ASHRAE Journal 47: 30-32
- ASHRAE. 2007. Method of Testing General Ventilation Air-Cleaning Devices for Removal Efficiency by Particle Size. ASHRAE Standard 52.2-1999. Atlanta: American Society
- Bémer, D., Callé, S. 2000. Evolution of the Efficiency and Pressure Drop of a Filter Media with Loading. Aerosol Science & Technology 33: 427-439
- Bird, R., Stewart, W., and Lightfoot, E. 2001. Transport Phenomena 2nd Edition New York: John Wiley & Sons, Inc.
- Bouchertall, Fathallah. 1989. Concentration and Size Distribution of Atmospheric Particle Matter at a Costal Site on the Baltic Sea. Atmospheric Environment. 23(10): 2241-2248
- Caesar, T., Schroth, T. 2002. The influence of Pleat Geometry on the Pressure Drop in Deep-pleated Cassette Filters. Filtration and Separation 39: 48-54
- Cahela, Donald, Tatarchuk, Bruce. 2001. Permeability of Sintered Microfibrous Composites for Heterogeneous Catalysis and other Chemical Processing Opportunities. Catalysis Today. 69: 33-39
- Chen D.R., Pui, D., and Tang, Y.M.1996. Filter Pleating Design for Cabin Air Filtration 960944 In:SAE Technical Paper Series pp 93-100 SAE Publications Group
- Chen, D.R., Pui, D., and Liu, Y.H. 1995. Optimization of Pleated Filters Designs Using a Finite-Element Numerical Model. Aerosol Science & Technology. 23:579-590.
- Del Fabbro, L., Laborde, J.C., Merlin, P., and Ricciardi, L. 2002. Air Flows and Pressure Drop Modeling for Different Pleated Industrial Filters. Filtration and Separations 39: 34-40
- Department of Energy (DOE). 2009. Energy Information Agency. <http://www.eia.doe.gov/>

- Dickenson, T. Christopher. 1992. Filters and filtration handbook. Oxford, U.K.: Elsevier Advanced Technology
- Environmental Protection Agency (EPA). 2009. Indoor Environmental Asthma Triggers. www.epa.gov/asthma/triggers.html
- Fried, Erwin, Idelchik, I.E. 1989. Flow resistance : A Design Guide for Engineers. New York: Hemisphere Pub. Co.
- Godish, Thad. 2001. Indoor Environmental Quality. Boca Raton: Lewis Publishers
- Harris, Daniel, Cahela, Donald, Tatarchuk, Bruce. 2001. Wet layup and sintering of metal-containing microfibrinous composites for chemical processing opportunities. *Composites*. 32: 1117-1126
- Idelchik, I.E. 1994. Handbook of Hydraulic Resistance 3rd Edition. Boca Raton: CRC Press, Inc.
- Japuntich, D.A., Stenhouse, J.I.T., Liu, B.Y.H. 1994. Experimental results of Solid Monodisperse particle Clogging of Fibrous Filters. *Journal of Aerosol Science*. 25 (2): 385-393
- Lebedev, M. N., Kirsch, A.A. 1995. Pressure Drop of Loaded Fibrous Filters. *Journal of Aerosol Science*. 26 (S1): S735-S736
- Lee, J., Kim, S. Liu, B.Y.H. 2001. Effect of Bi-Modal Aerosol Mass Loading on the Pressure Drop for Gas Cleaning Industrial Filters. *Aerosol Science & Technology* 35: 805-814
- Liu, David H.F., Lipták, Béla G. 2000. Air Pollution. Boca Raton: Lewis Publishers
- Kalluri, R. 2008. Microfibrinous Entrapped Catalyst and Sorbents: Microstructured Heterogeneous Contacting Systems with Enhanced Efficiency. Doctoral Dissertation. Auburn University, Auburn, AL
- Kay, Jack, Keller, George, Miller, Jay 1991. Indoor Air Pollution: Radon, Bioaerosols, and VOC's. Chelsea: Lewis Publishers
- Karanjjikar, M. 2005. Low Temperature Oxidation of Carbon Monoxide Using Microfibrinous Entrapped Catalysts for Fire Escape Mask Application. Doctoral Dissertation. Auburn University, Auburn, AL
- Kennedy, Daniel. 2007. Fuel Cell Cathode Air Filters: Methodologies for Design and Optimization. Masters Thesis. Auburn University, Auburn, AL

- Kim, S., Shen, S., Sioutas, C., Zhu, Y., and Hinds, W., (2002) Size Distribution and Diurnal and Seasonal Trends of Ultrafine Particulate in Sources and Receptor Sites the Los Angeles Basin. *Journal of Air and Waste management*. 52: 297-307.
- Marrion, Christopher J., Cahela, Donald R., Ahn, Soonho, Tatarchuk, Bruce J. 1994. Composite fiber structures for catalysts and electrodes. *Journal of Power Sources*. 47: 297-302
- Matteson, Michael J., Orr, Clyde. 1987. *Filtration Principles and Practices 2nd Edition*. New York: Marcel Dekker, Inc.
- Meckler, Milton 1991. *Indoor Air Quality Design Guidebook*. Lilburn: The Fairmont Press, Inc
- Moffat, Donald W. 1997. *Handbook of Indoor Air Quality Management*. Englewood Cliffs: Prentice Hall
- Novick, V.J., Monson, P.R., Ellison, P.E. 1992. The effect of Solid Particle Mass Loading on the Pressure Drop of HEPA Filters. *Journal of Aerosol Science*. 23 (6): 657-665
- Perry, Robert H., Green, Don W. 1997. *Perry's Chemical Engineers' Handbook 7th Edition*. New York: McGraw-Hill
- Podgorski, A. Grzybowski, P. 2000. Loading of Mechanical Fibrous Filters with Solid Polidisperse Aerosols: Mathematical Model and Experimental Verification. *Journal of Aerosol Science*. 31 (S1): S458-S459
- Queen, A.P. 2005. High efficiency adsorption filter via packed bed and polishing sorbent architecture for regenerable collective protection equipment. Masters Thesis. Auburn University, Auburn, AL
- Raber, Robert. 1982. Pressure Drop Optimization and Dust Capacity Estimation for a Deep-Pleated Industrial Air Filter Using Small Sample Data. *Filtration and Separation* 19:508-511
- Rivers, R., Murphy D. 2000. Air Filter Performance Under Variable Air Volume Conditions In: *ASHRAE Transactions Vol. 106, Part 2* pp 131-144
- Robinson, T. J., Ouellet, A. E. 1999. *Filters and Filtration*. *ASHRAE Journal* 41: 65-70
- Rudnick, S. 2004. optimizing the Design of Room Air Filters for the Removal of Submicrometer Particles. *Aerosol Science & Technology* 38: 861-869

- Scheidegger, A. 1974. The physics of flow through porous media 3rd Edition. Toronto: University of Toronto Press
- Stenhouse, J.I.T., Trottier, R. 1991. The Loading of Fibrous Filters with Submicron Particles. *Journal of Aerosol Science*. 22 (S1): S777-S780
- Tatarchuk, B.J. 1992. Method of Optimizing Composite Preparation for Electrical Propoeriuates: Maximum Capacitance Electrodes. US Patent #5,102,745.
- Tatarchuk Bruce J., Rose M.R, Krishnagopalan, A., Zabasajja, J.N. Kohler D. 1992. Mixed Fiber Composite Structures. US Patent #5,096,663.
- Tatarchuk Bruce J., Rose M.R, Krishnagopalan, A., Zabasajja, J.N. Kohler D. 1992. Preparation of Mixed Fiber Composite Structures. US Patent #5,080,963.
- Tatarchuk Bruce J.,Rose M.R, Krishnagopalan, A., Zabasajja, J.N. Kohler D. 1994. Mixed Fiber Composite Structures High Surfaces Area High Conductivity Mixtures US Patent #5,304,330.
- Thomas, D., Contal, P., Renaudin, V., Penicot, P., Leclerc, D., Vendel, J. 1999. Modelling Pressure Drop in HEPA Filters during Dynamic Filtration. *Journal of Aerosol Science*. 30 (2): 235-246
- Tronville, P., Sala, R. 2003. Minimization of Resistance in Pleat-Media Air Filter Designs: Empirical and CFD Approaches. *HVAC&R Res* 9: 95-106
- Valmari, T., Lehtimaki, M. Taiple, A. 2006. Filter Clogging by Bimodal Aerosol. *Aerosol Science & Technology* 40: 255-260
- Walsh, D.C., Stenhouse, J.I.T., Scurrah, K.L., Graef, A. 1996. The Effect of Solid and Liquid Aerosol particle Loading on Fibrous Filter Material Performance. *Journal of Aerosol Science*. 27 (S1): S617-S618
- Waring, M.S., Siegel, J. A. 2008. Particle Loading Rates for HVAC filters, heat exchangers, and ducts. *Indoor Air* 18:209-224

APPENDIX A

A.1. Rotameter Calibration

The rotameters used to supply air to the media test rig were calibrated by a timed, volumetric displacement technique. A container of known volume (9.2 liters) was submerged in a large basin of water. The rotameters were set to the desired volumetric flow rate. The rotameters' discharge was then positioned into the submerged container, and the time to displace the 9.2L of water from the container was recorded. The volumetric flow rate could be calculated by dividing the container's volume by the recorded time to displace the water. Fifteen different rotameters setting were examined, and the test was performed twice at each setting. The rotameters were showed to be properly calibrated.

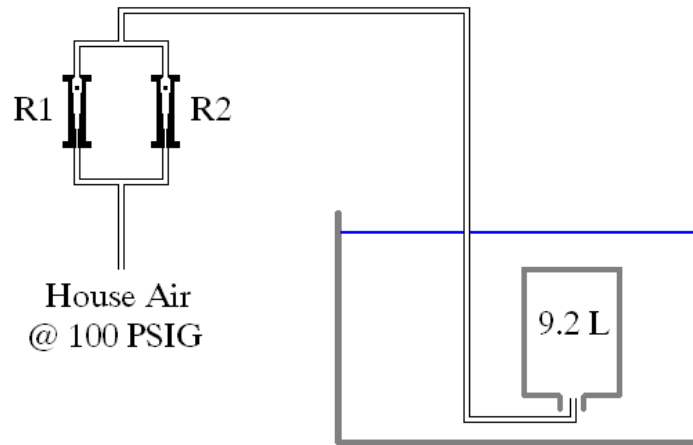


Figure A1: Rotameter Calibration Set-Up

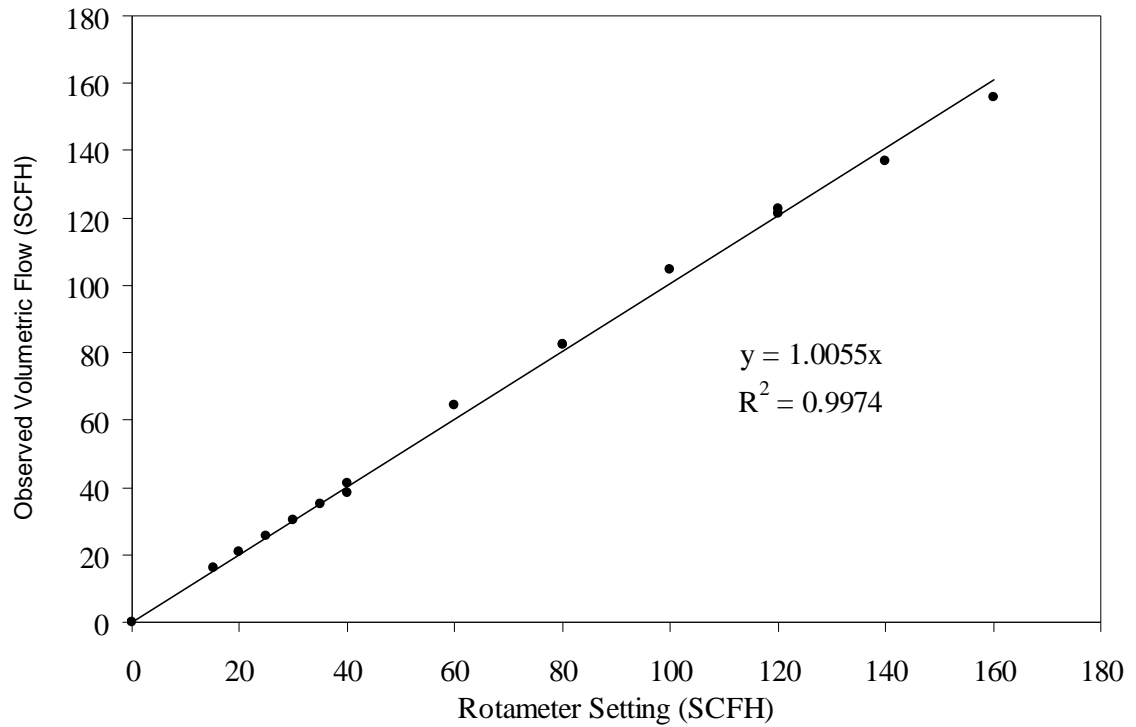


Figure A2: Rotameter Calibration Curve

Table A1: Experimental Data

R1 (scfh)	R2 (scfh)	Total Flow (scfh)	Time 1 (s)	Time 2 (s)	Observed Flow (scfh)	Deviation (%)
0	0	0	0	0	0.00	0.00
15	0	15	72.14	72.05	16.22	7.54
20	0	20	55.59	55.48	21.06	5.04
25	0	25	46.07	45.95	25.42	1.66
30	0	30	38.6	38.73	30.25	0.83
35	0	35	33.41	33.3	35.07	0.19
40	0	40	30.5	30.12	38.59	3.66
0	40	40	28.63	28.03	41.29	3.11
20	40	60	18.28	18.1	64.30	6.69
40	40	80	14.2	14.16	82.48	3.01
0	80	80	14.05	14.41	82.19	2.67
20	80	100	11.15	11.16	104.85	4.63
40	80	120	9.51	9.53	122.86	2.33
0	120	120	9.68	9.63	121.14	0.94
20	120	140	8.57	8.5	137.04	2.16
40	120	160	7.5	7.5	155.95	2.60

A.2. Calibration of Pressure Transducers

The pressure transducers utilized in the research were verified to be accurately working by testing their measurements against a known pressure drop. The test apparatus consisted of a 20' long $\frac{1}{2}$ " internal diameter PVC tube. Using the rotameters calibrated above, a known volumetric flow rate was delivered to the tube. The pressure drop across the tube was measured 1' foot the air inlet and 18' downstream. The measured resistance could then be compared to the theoretical resistance calculated by Darcy's Weisbach equation for flow through a tube. The results and schematic are shown below.

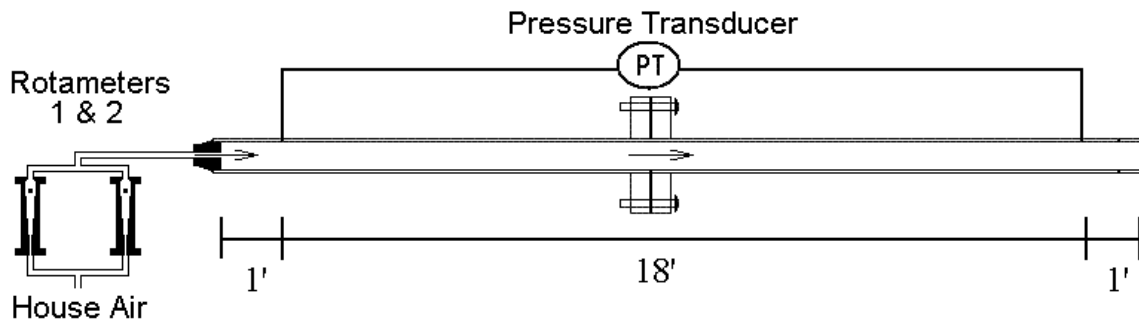


Figure A.3: Calibration Tube

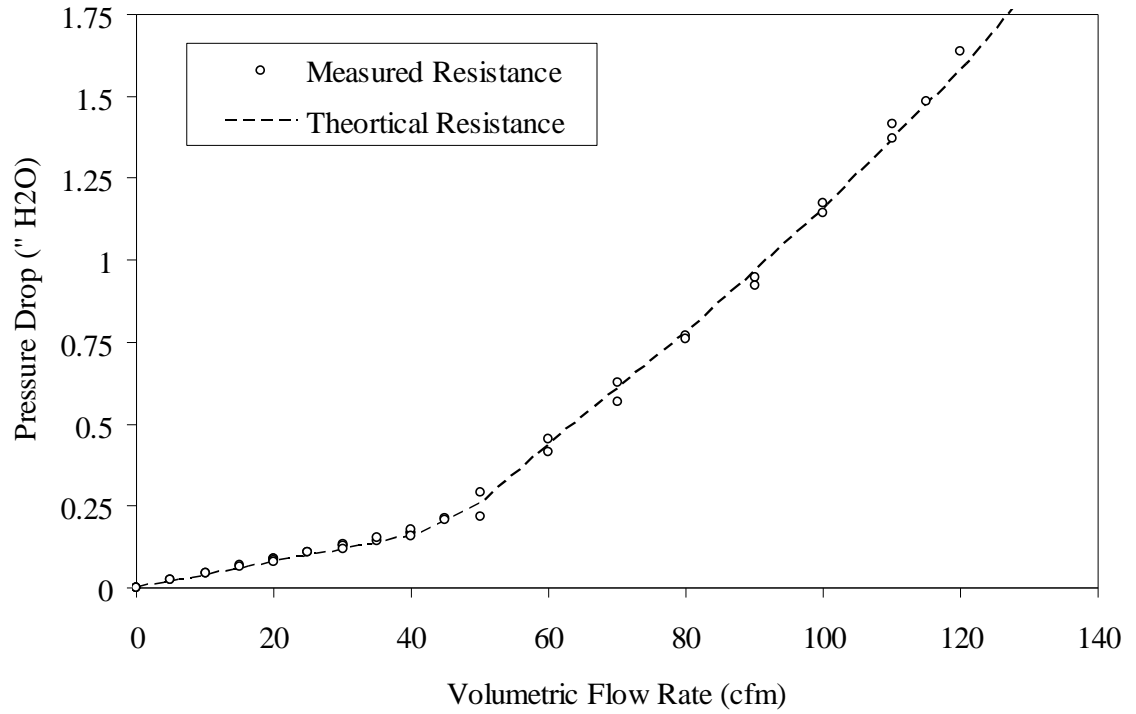


Figure A4: Calibration Curve for Pressure Transducer #1

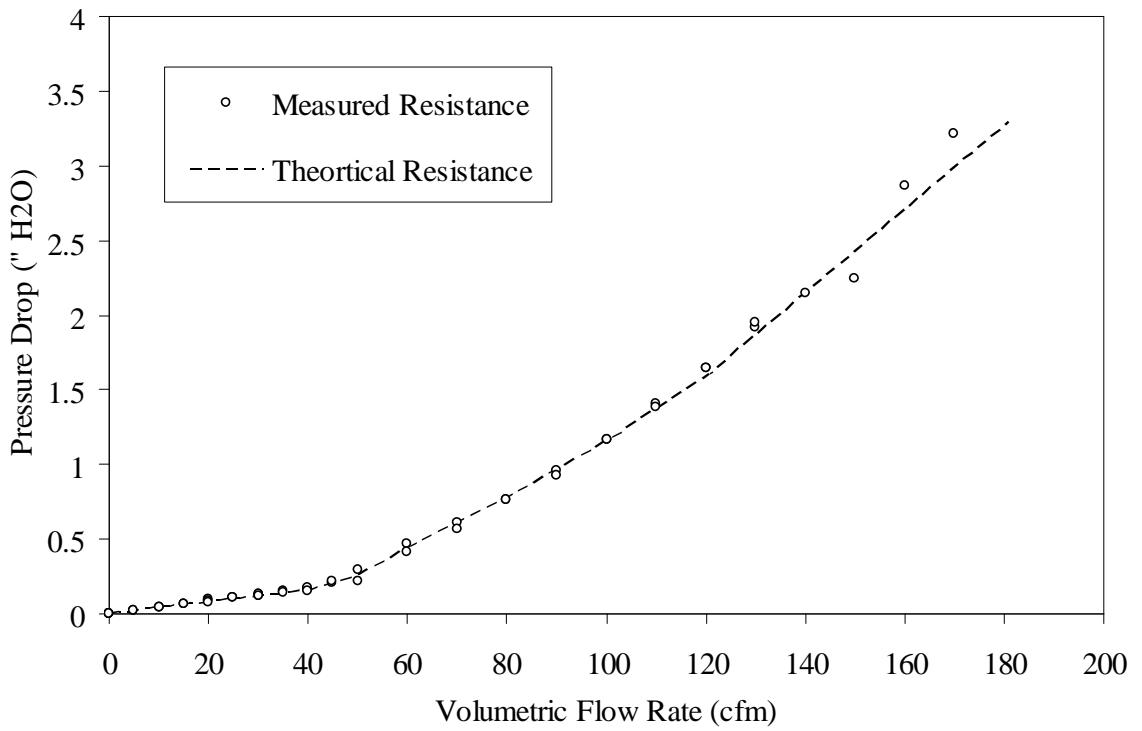


Figure A5: Calibration Curve for Pressure Transducer #2

A.3. Construction of Filter Holders

Single 24" x 24" filter holders were constructed out of aluminum bars cut to precisely fit the nominal dimensions of the filter. Three units were constructed to fit the three filter depths used in this dissertation. The bars were outfitted with upstream and downstream flanges that partially blocked the filter's grating. The flanges were equipped with closed cell foam creating a solid seal and preventing edge leak around the filter. Reinforcing brackets were added to prevent the flanges from deforming when subjected to the pressure of the clamps.

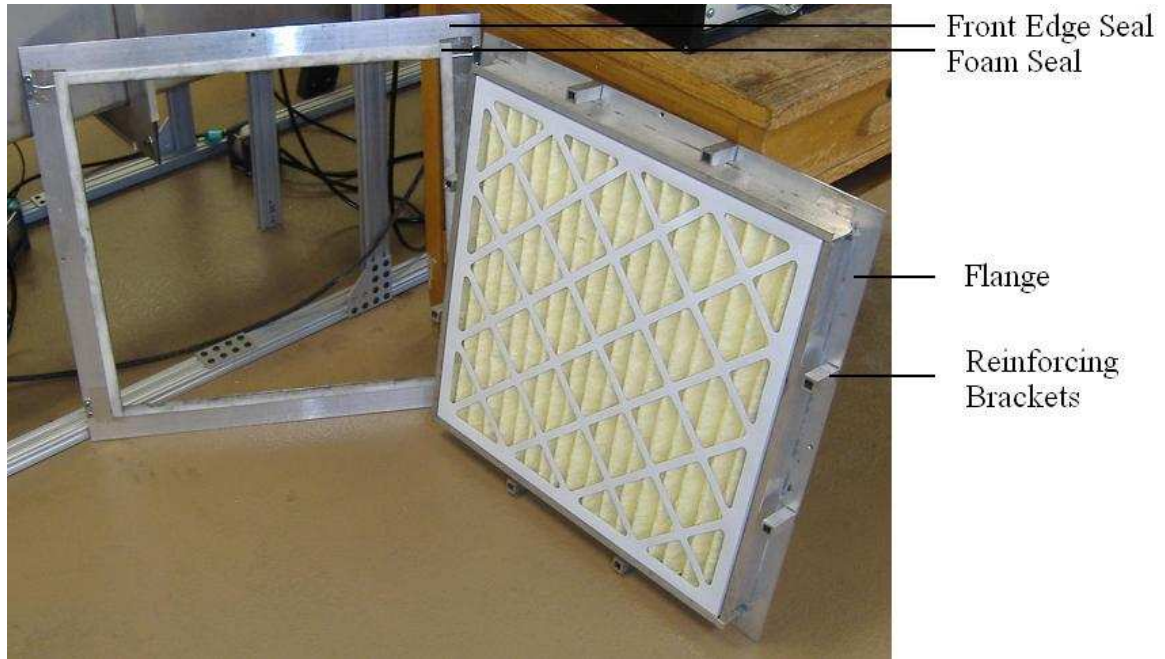


Figure A6: 24"x24"x2" Filter Holder

A.4. Construction of MESA Unit

MESA units were constructed primarily out of 5/8" particle board. The boards were obtained as 48" x 24" rectangular pieces. They were then cut down into 24" x 24" and 28" x 24" sections. The 28" x 24" squares serve as the top and bottom walls for the MESA. The 24" x 24" side walls were positioned into place using 24" spacer molds, and

then they were fastened to the extended squares using drywall screws. L brackets were added to all eight corner to further strength the MESA unit.

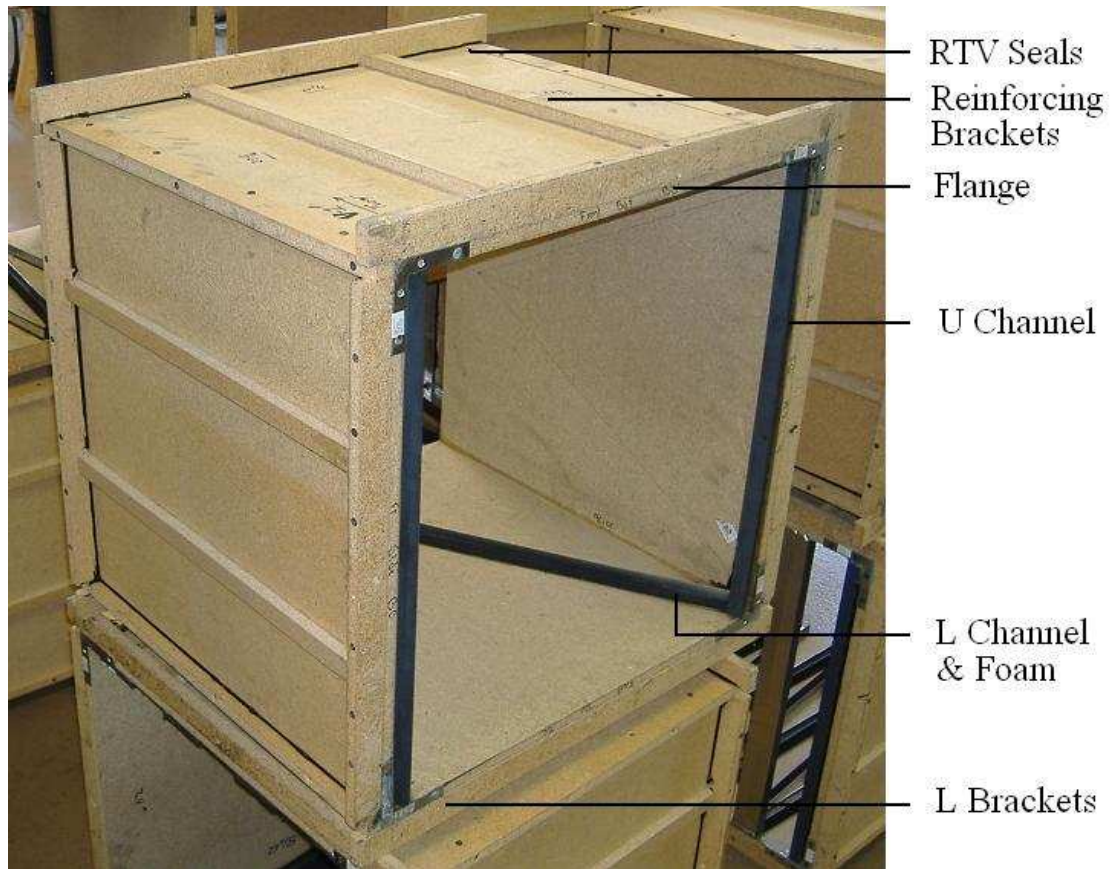


Figure A7: MESA Housing Schematic

The units were outfitted with 1.5” flanges in order to mate up with the ductwork and form a tight seal. The flanges were reinforced with 1” wide strips of particle board. The reinforcing brackets were necessary to prevent the flanges from failing when subjected to the 1800 pounds of force created by the clamping system. All cracks and joints were sealed with RTV silicone gasket sealant. The flexible RTV gasket was both air and water impermeable.

The filter elements were held in the MESA units by a combination of mechanisms. The front edges were created by custom cutting aluminum or plastic

extruded U channel. The U channel fit tightly between the top and bottom walls to serve as an anchor for the filter element. L channel were add to the top and bottom walls to serve as support and provided additional seals for the filters. A solid seal is created between the L bracket and the MESA unit through the use of closed-cell foam.

A.5. Weight Increase of ASHRAE Dirt under Atmospheric Conditions

The ASHRAE dirt is dried in an oven at 110°C (230°F) for 30 minutes prior to being placed onto the dirt loader. The dust is dried to prevent agglomerations from forming. The dirt is composed of three materials (AL₂O₃, SiO₂, and Carbon black) usually associated with high surface area. This could lead to water adsorption over the course of the test would cause the errors in the associated weight of dirt loading. The constituents of ASHRAE dirt, however, have very low pore volume to negate this phenomenon from occurring. The graph below demonstrates the average uptake of the synthetic challenge dust over the course of 90 minutes. Ninety minutes was chosen because it represents the maximum time from leaving the oven to end weighing.

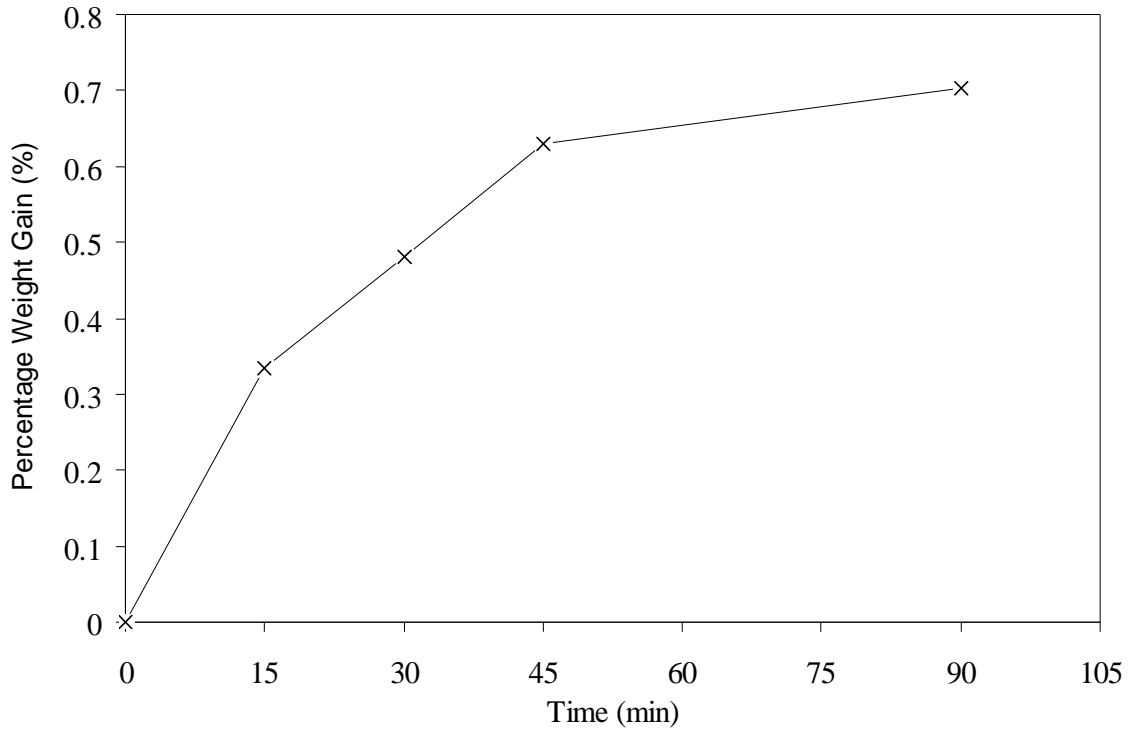


Figure A.8: ASHRAE Dust Water Uptake over Time

A.6. Observed Flow Channeling due to Pleat Tip Blockage

The models are based on the assumption that air is channeled around the pleat tips due to an increase in Darcy's constant. The carbon black present in the ASHRAE dust stains the media when it comes into contact. Figure () and () below shows that incoming challenge dirt was channeled away from the tips. Figure () is the upstream pleat tips after a low dust loaded. Subsequent loading will turn the tips black; however, the downstream tips retain their original white coloration even after the filter has been fully loaded.

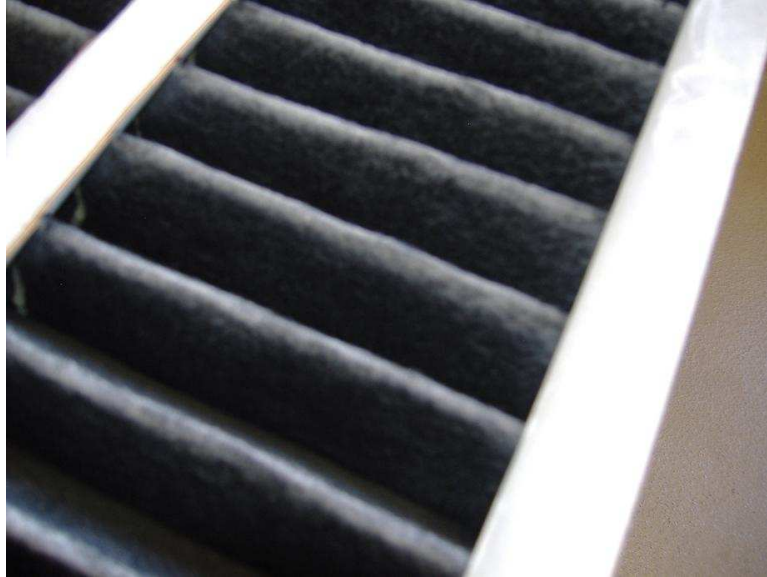


Figure A.9: Upstream Pleat Tip after Dust Loading

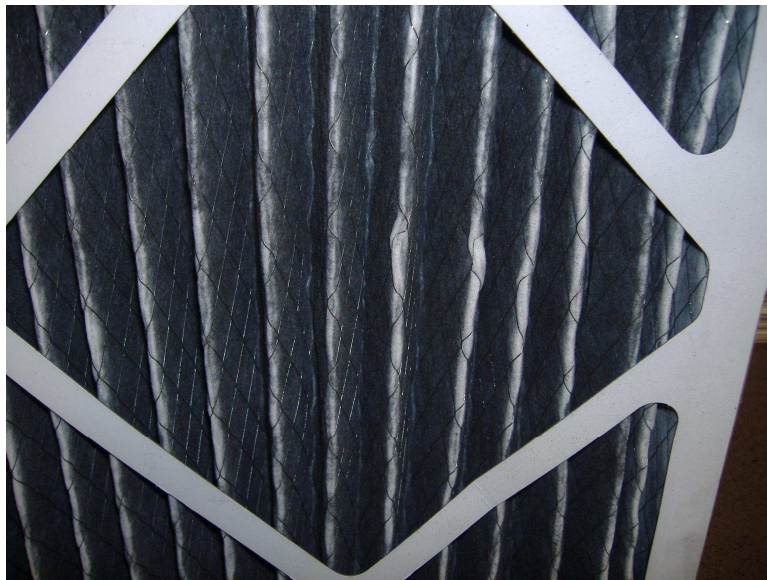


Figure A.10: Downstream Pleat Tip after Dust Loading

A.7. Determination of Ramping Rate

The Hitachi inverter can control the frequency of the blower as well as the frequency's rate of change. This function, when coupled with the data logging capabilities of the pressure transmitters, allows flow versus pressure drop measurements to be collected over the entire operational frequency range instead of at certain set points.

The inverter's ramping rate, however, does affect the measurement readings. A fast ramping rate causes the data to be artificially skewed towards a lower resistance at a given face velocity. This occurs because the resistance data being recorded by the upstream orifice's transmitter is not in equilibrium at same point in time with the data signal being recorded by the downstream filter's transmitter.

It was necessary to determine an appropriate ramp rate in order to eliminate this data lag. First, steady state data was gathered at various increments throughout the frequency range. This data shows the actual pressure drop versus face velocity relationship of the filter. Figure A11 illustrates the significant lag between a ramp rate of 120 Hz/min and steady state values. The lag in equilibrium between the two pressure meters can be clearly seen at the end of the curve. The face velocity, which is measured via the orifice transmitter, reaches equilibrium at 60 Hz several seconds before the filter's transmitter reaches equilibrium. This causes the final section of the graph to resemble a vertical line. It was determined that a rate of 8.57 Hz/min was the fastest the system could be ramped without created deviations between the set points and a continuous graph.

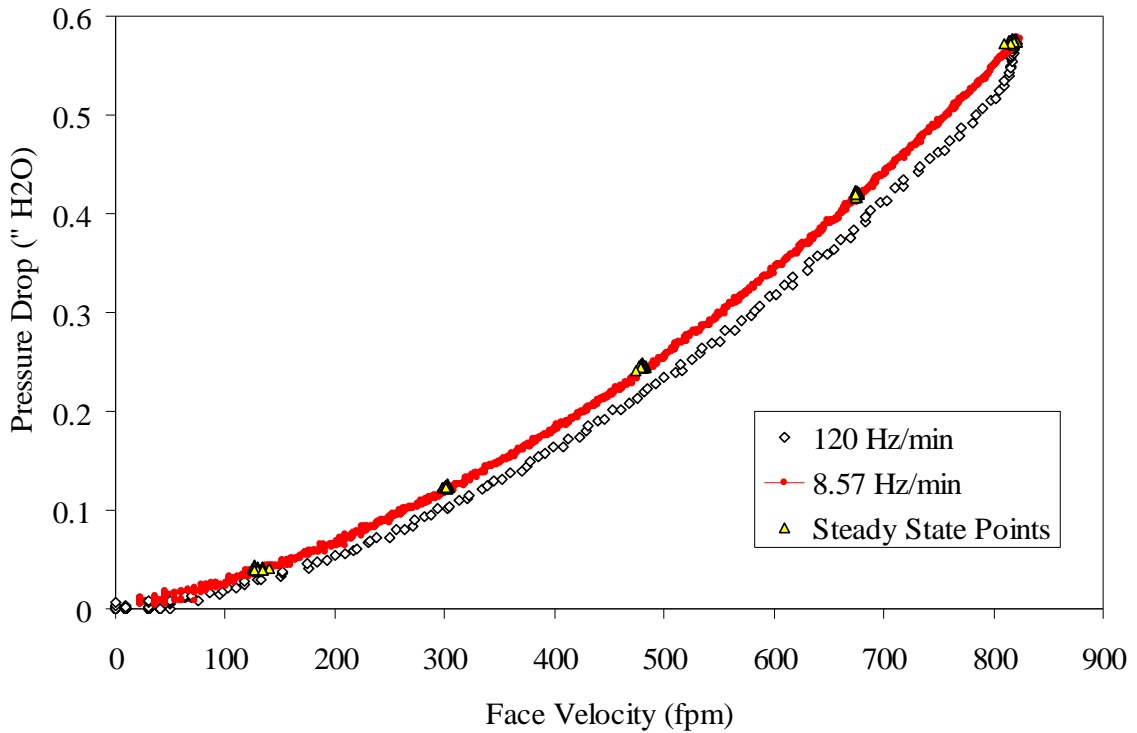


Figure A.11: Variation in Pressure Measurements due to Incrementing Rate

Figure A.11 was generated by performing consecutive runs on the same filter arrangement. The 95% efficiency pre-filter ensured that the filter did not age over the course of the experimental tests. Before and after weight on the filter confirm this statement. The tests were conducted by setting the inverter to the desired ramping rate and allowing the system to auto-ramp to 60 Hz while the pressure transmitters data-logged the measurements. The following ramping rates were investigated: 120 Hz/min, 60 Hz/min, 30 Hz/min, 20 Hz/min, 15 Hz/min, 12 Hz/min, 10 Hz/min, 8.57 Hz/min, 7.5 Hz/min, and 6 Hz/min. The additional data was not plotted for clarity reasons. The set points were gathered by setting the frequency to a desired point, and then allowing the system to remain static over the course of 30 seconds. The data for the last tens seconds was gathered, processed, and then plotted.

APPENDIX B: NOMENCLATURE

B.1. Arabic Symbols

A_i	=	Area at Point i, ft ²
A	=	Media (Darcy's) Constant, " H ₂ O•min/ft
A_T	=	Pleat Tip Media Loss, ft ²
B	=	Media Constant, " H ₂ O•min ² /ft ²
D_c	=	Pore Hydraulic Diameter, ft
D_H	=	Duct Height, ft
D_h	=	Hydraulic Diameter, ft
D_i	=	Downstream Particle Count at time i, -
D_W	=	Duct Width, ft
E	=	Energy, W•hr
E_C	=	Element Count, -
F_B	=	Front Edge Blockage, ft ²
F_D	=	Filter Depth, ft
F_H	=	Filter Height, ft
F_i	=	Force in Direction i, lb _f
F_s	=	Force of surfaces on fluid, lb _f
F_W	=	Filter Width, ft
g	=	Gravity, ft/min ²
h	=	Height, ft
K_i	=	Friction Coefficient, -
Kn	=	Knudsen number, -
L	=	Length, ft
L_V	=	Viscous Losses, W•hr
m	=	mass, lb _m
M	=	Dust Load, lb _m
M_T	=	Media Thickness, ft
N	=	Empirical Constant,
P_i	=	Pressure at Point i, " H ₂ O
P_c	=	Pleat Count, -
P_H	=	Pleat Height, ft
P_L	=	Pleat Length, ft
ΔP	=	Pressure Drop
Q	=	Volumetric Flow Rate, ft ³ /min
QF	=	Quality Factor, %/"H ₂ O
R	=	Fiber Radius, ft
Re	=	Reynolds number, -

S_O	=	Slot Opening, ft
S_D	=	Slot Depth, ft
S_H	=	Slot Height, ft
t	=	Time, min
U_i	=	Upstream Particle Count at time i, -
u_i	=	Vector in Direction I, -
V_i	=	Velocity at Point I, ft/min
W	=	Mass Flow Rate, lb_m/s
Δz	=	Filter Thickness, ft

B.2. Greek Symbols

α	=	Slot Pitch, radian
α_V	=	Velocity Ratio, -
α_{SM}	=	Solid Mass Fraction, -
β	=	Pleat Pitch, radian
γ	=	Gamma Pleat Angle, radian
δW_s	=	Mechanical Energy Added, $W \cdot hr$
Γ	=	Momentum, $lb_m \cdot ft/min$
η	=	Pleat Coefficient Term, -
η_i	=	Efficiency of Term I, -
λ	=	Tube Friction Coefficient, -
μ	=	Viscosity, $Pa \cdot s$
ρ	=	Density, lb_m/ft^3
σ	=	Pleat Count, -
χ	=	Pleat Coefficient Term, -

B.3. Subscripts

geo	-	geometry
m	-	media
f	-	filter
g	-	grating
e	-	expansion
c	-	contraction
t	-	tube
p	-	pleat
s	-	slot
a	-	array
d	-	discharge
T	-	technique
B	-	blower